
THE UNIVERSITY *of* EDINBURGH

# Consideration of Atmospheric Stability in Wind Energy Modelling

Doctoral Thesis

Michael Blair

University of Edinburgh

2019



# Lay Summary

*Computer simulations of wind flow are routinely used as part of the wind farm design process and better simulations can lead to more efficient wind farm designs. One way to improve wind flow simulation is to consider how air flows differently when it is being heated by the ground during the day or cooled by the ground at night.*

*The amount of heating and cooling varies from place to place and can be quantified by taking simultaneous measurements of temperature both near the ground and higher up. For this research, such measurements were made at various sites in the UK and Ireland. It was demonstrated that, to avoid the expense of making these measurements, weather models can be used instead.*

*When the heating and cooling effects were included, the wind flow simulations were shown to more accurately represent real-life conditions. It was shown that designing wind farms using the improved simulations would result in 0.5% more electricity being generated.*

# Abstract

*Improvements in wind flow modelling accuracy can impact positively on wind farm business cases and therefore contribute towards meeting national and global energy decarbonisation targets. 'Atmospheric stability' is a meteorological phenomenon which is often disregarded in conventional wind flow modelling practice but which can have significant impact on wind farm energy predictions. The concept relates to the reaction of the near-surface atmosphere to diurnal and seasonal variation in the heating and cooling influences of the Earth's surface.*

*This thesis details a demonstration of incorporating atmospheric stability effects into Computational Fluid Dynamics (CFD) wind flow modelling methodology to improve wind farm energy yield assessment and layout design.*

*Measurements of virtual potential temperature differential between 10m and 60 - 100m above ground level (a proxy for atmospheric stability) were made at ten onshore and two offshore sites. A comparison was then made between these measured data and commercially available 'Vortex' Weather Research & Forecasting (WRF) mesoscale data and the latter was shown to be a viable, cheaper and more readily accessible input data source.*

*A new technique for parametrising stability data was developed as part of a streamlined CFD-based wind flow modelling approach. CFD simulations of key wind flow parameters (wind shear, turbulence intensity and wind speed ratio) were made using both a 'neutral' assumption (a widely used industry-standard approach) and a more sophisticated 'diabatic' assumption, which incorporated site-specific inputs. These predictions were compared against on-site measurements, demonstrating an overall improvement in modelling accuracy when the diabatic assumption was implemented.*

*Energy yields for onshore wind farms with fixed layouts calculated using neutral and diabatic flow modelling were shown to differ from one another by 1.4% on average (0.1 to 4.8%). Further, onshore wind farm layouts optimised based on the diabatic flow modelling method showed an average increase in predicted energy yield of 0.5% (0.1 to 1.1%) compared to those optimised based on neutral flow modelling. For a mature energy technology such as onshore wind, energy yield uplifts in this range can significantly impact project viability.*

# Declaration

*I declare that this thesis has been composed solely by myself and that it has not been submitted, in whole or in part, in any previous application for a degree. Except where stated otherwise by reference or acknowledgment, the work presented is entirely my own.*

*Michael Blair*

*17th October 2019*

# Contents

# Table of Figures

# 1 Background

## 1.1 Introduction

### 1.1.1 Climate Change

The root of this PhD research project lies in the global effort to transition to clean energy, reduce greenhouse gas emissions and therefore stem the worst of the potential effects of climate change.

In its Fifth Assessment Report [1], published in 2014, the Intergovernmental Panel on Climate Change reported an observation that global mean surface temperature has already increased by 0.85°C in the period 1880 – 2012. It was stated to be *extremely likely* that this change was driven by emissions related to human activity and that to keep temperature increase to less than 2°C compared to pre-industrial levels would require the concentration of $CO_2$ equivalent gases in the atmosphere to stabilise at no greater than 450 parts per million.

In December 2015, 196 UN member states agreed and adopted the Paris Agreement: a resolution to keep global temperature rise this century below 2°C and to pursue efforts to limit the temperature increase even further to 1.5 degrees Celsius [2]. This agreement obliges member states to set, track and report on ever-increasing emissions reduction targets in order to achieve the stated goal.

### 1.1.2 The Changing Face of the Energy Sector

Scotland's response to this challenge has been among the most robust in the world. In 2011, the Scottish Government set a target of 100% of electricity demand to be met by renewable sources by 2020 [3]. In 2018, 74.6% of Scotland's electricity demand was met by renewables [4] and the expectation is that the 2020 target will be met and exceeded.

However, electricity demand makes up just a quarter of total energy demand in Scotland. As set out in the 2017 Scottish Energy Strategy, the focus is now firmly shifting towards the de-carbonisation of heat and transport, which together make up the other three quarters of energy demand [5].

The Scottish Energy Strategy considers two potential future scenarios: one in which the heat and transport sectors are predominantly electrified (e.g. electric vehicles, air-source heat pumps, pumped-hydro storage) and one in which there is a transition to using low-carbon gas (e.g. hydrogen boilers, fuel-cell vehicles). In both scenarios, renewable energy retains a pivotal role: either by generating electricity for direct transmission to end-users or by powering conversion systems (such as hydrogen electrolysers) to convert renewable electricity into clean gas.

Specifically, the Scottish Government is now targeting 50% of total energy demand to be met by renewables by 2030 [4] which could see the contribution of renewables reaching 140% of current electricity demand (or a total of 19GW of installed capacity in Scotland alone). The long-term legally binding target, as legislated by MSPs in the Scottish Parliament on 25$^{th}$ September 2019, is to achieve net-zero carbon emissions by 2045 [6].

For the foreseeable future, the momentum is likely to continue to lie with onshore and offshore wind which together made up the vast majority of new electricity generating plant installed in Scotland in recent decades. In September 2019, BEIS (the UK Government department for Business, Energy and Industrial Strategy) announced the results of the third Contracts for Difference (CfD) renewable energy subsidy auction. The auction cleared at a price of £39.65 per MWh (2012 real prices) [7] or £45.45 per MWh in 2019 prices which, when compared against wholesale power price forecasts for the 15 year contract duration, makes the winning projects close to subsidy-free. This marks a cost reduction for offshore wind of 65% compared to the first CfD auction held in 2015.

Wind energy is now the cheapest form of renewable or non-renewable generation available in the UK (albeit, not including system balancing costs). Furthermore, advances in turbine technology and supply chain efficiency mean that costs are still coming down rapidly, both on- and offshore.

### 1.1.3 Challenges for Wind Energy

Significant challenges in wind energy remain to be addressed if the anticipated penetration of wind energy into the UK market is to be realised.

Firstly, despite falling costs, the financial margins of wind energy development have never been tighter. For onshore wind, the withdrawal of government subsidy for new-build projects in 2015 means that developers are currently weighing up the prospect of building out projects which will be paid the wholesale electricity price only, entailing significant risk and revenue volatility. In addition, wind farms cannot fully exploit schemes such as the Capacity Mechanism, which offers other more flexible generators a steady income stream.

All of this means that, now more than ever, developers need to know accurately how much revenue prospective wind farms will bring in. The accuracy of wind resource assessment feeds directly into the viability of a wind farm business case: lower costs of borrowing can be achieved with greater certainty in energy yield assessment. Not only that, but developers juggling a portfolio of multiple options need to be certain of which are the more attractive investment opportunities and, for CfD entrants, the right strike price to bid.

Secondly, the variability of wind energy presents a challenge to the Transmission System Operator (TSO - National Grid) in terms of balancing the supply and demand of electricity on the timescale of hours to days. Advances in energy storage and grid inter-connection will help to facilitate a future high penetration of renewables – but this situation can be improved further with highly accurate short-term wind forecasting.

Electricity generators connected to the transmission network (i.e. most large wind farms) are obliged to notify the TSO of their anticipated level of output ahead of delivery and are financially incentivised to forecast accurately. This allows the SO to ensure that there is adequate generation capacity online to meet demand, as well as controlling the risk of grid frequency deviations through the appropriate use of spinning reserve and other frequency response measures.

The problem for wind farm operators is that short-term forecasting is highly complex: it is generally possible to predict total wind farm energy output with higher certainty over ten years than over a single hour. The reason for this is that the meteorological conditions which drive wind farm power output, such as synoptically driven wind speed and direction, are changing significantly from hour to hour as pressure systems pass over, whereas average conditions do not change very significantly from decade to decade.

Thirdly, advances in turbine technology are allowing ever-larger wind turbines which will interact with the atmosphere significantly differently from a typical turbine installed today. It is foreseeable that turbines with rotor diameter of 250m could be deployed offshore in the next 5-10 years. These rotors will span multiple sub-layers of the atmosphere, regularly exposing them to vertical wind speed gradients well in excess of those experienced by the largest turbines of today. This presents a challenge for wind turbine manufacturers, in terms of designing turbines which can withstand these relatively extreme loadings and also for wind farm developers, who must take their own view on how this interaction will affect turbine power performance, operability and lifetime.

All three of these challenges can be partly addressed by developing a more sophisticated understanding of the wind climate at a prospective wind farm site. This is the pursuit of teams of wind analysts, working for manufacturers, developers, operators and consultancies, whose job it is to assess long-term energy yield, forecast short-term power output and design wind farms to operate safely and efficiently.

### 1.1.4 Wind Resource Assessment

Wind analysis, as a discipline, has advanced considerably over the past twenty years. Early resource assessment campaigns for large wind farms were based on measurements from 10 metre masts and only very basic wind flow modelling, or none at all. We now know this to be insufficient to gain the level of understanding of the wind climate required to design a wind farm in 2018, particularly in the often challenging topography of Scotland.

To meet this need, improved measurement techniques (e.g. tall masts and remote sensing devices) and sophisticated flow modelling practices (e.g. computational fluid dynamics (CFD)) have been implemented. It is now common practice to commission aerial laser ranging surveys to accurately assess terrain features and forestry canopy heights, in order to better predict their effect on the wind flow. Three revisions have been made to the international standard for wind turbine power performance testing [8] which has stood for many years as an authoritative guide to various aspects of wind analysis. This is soon to be joined by a dedicated standard for wind resource assessment (IEC-61400 Part 15).

Despite this progress, wind analysis remains a highly active area of research, supporting a steady stream of literature, multiple conferences world-wide and various cross-industry groups.

## 1.2 Research Aims

This thesis focusses on boundary layer atmospheric physics and, specifically, 'atmospheric stability': an aspect of the wind climate which has arguably been de-prioritised by the wind analysis community until recent times. The research aims align with the questions most relevant to wind farm developers:

- To what extent is atmospheric stability a significant factor on the incident wind speed distribution?
- Are site-specific measurements required and, if so, where is the optimal balance between accuracy and cost?
- What opportunities and risks does atmospheric stability present, in terms of wind farm design, appraisal and operation?

In answering these questions, this thesis will address specific outstanding questions in the field of wind analysis. The intended impact of this research project is to increase the value of onshore wind farm projects, via improved energy yield assessment and layout design.

Following on from the research aims presented here, section 3.3 presents some more specific research objectives. The impact of this work is summarised in section 8.2.

## 1.3 Thesis Structure

This document is structured as follows: in **Chapter 2**, the physics of atmospheric stability is summarised and some technical concepts surrounding wind analysis are introduced. In **Chapter 3**, a synthesis of some relevant literature is presented and some context is put forward as to how this PhD project fits into the wider research landscape.

In **Chapter 4**, an analysis of data from the Weather Research and Forecasting (WRF) mesoscale model is presented and a methodology is set out to calculate virtual potential temperature differential and categorise atmospheric stability. Distributions of atmospheric

stability for various UK/Ireland and world-wide sites are analysed and their properties assessed with reference to the literature. Also, mesoscale data is used to generate atmospheric stability maps of the UK and Ireland.

In **Chapter 5**, measured virtual potential temperature differential data from various onshore and offshore sites are analysed. The dependence of key wind flow parameters, such as wind speed, shear and turbulence intensity, are shown to correlate strongly with temperature differential. Then, measured data are compared against mesoscale data in order to validate the use of the latter in CFD flow modelling.

In **Chapter 6**, atmospheric stability distributions derived from WRF data are employed in a re-designed CFD modelling process and this is shown to lead to an increase in modelling accuracy. In **Chapter 7**, the impact of this increase in flow modelling accuracy is assessed; both in terms of improvement in wind farm energy yield assessment accuracy and layout design.

**Chapter 8** provides conclusions and presents conclusions, key recommendations and next steps.

# 2 Theory

## 2.1 The Earth's Atmosphere

This section gives a brief and simplified overview of some general large-scale meteorological concepts which are necessary to understand aspects of the UK/Ireland climate, for example, why the region experiences relatively very high average wind speeds.

The Earth's atmosphere extends to approximately 100km from the surface; broadly comprising the troposphere (spanning 0-10km), stratosphere (10-50km), mesosphere (50-80km) and thermosphere (80-100km) [9]. Figure 2.1 (not to scale) depicts this structure.

The atmospheric boundary layer (ABL), which is the focus of this research, is a subdivision of the troposphere, and can loosely be defined as the layer of atmosphere which directly interacts with the Earth's surface.

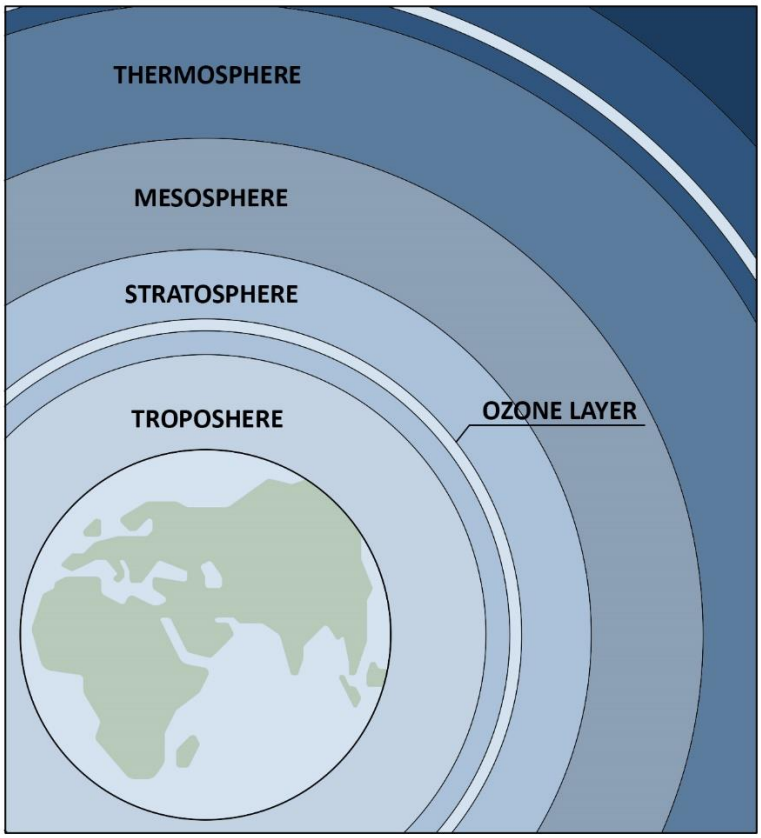


*Figure 2.1: Diagram showing the structure of Earth's atmosphere (illustrative).*

### 2.1.1 The Troposphere

Owing to hydrostatic equilibrium and the consequent rapid thinning of the atmosphere with increasing height, the troposphere (0 to ~10km) makes up the vast majority of the mass of the Earth's atmosphere.

Due to thermal and mechanical interaction with the surface, the troposphere can be broadly regarded as highly variable in nature. This is in contrast with the stratosphere above which exhibits a very consistent trend of increasing temperature with height; a phenomenon which suppresses vertical air movements, resulting in a relatively non-turbulent and predictable atmospheric layer and a 'cap' on the turbulent troposphere below. So, the regions of interest to weather modelling are the troposphere, which encapsulates everything we know as 'weather' and the tropopause (the boundary between the troposphere and stratosphere).

The first principle of any consideration of weather patterns on Earth is the concept of the atmosphere as a layer of fluid on an unevenly heated rotating sphere [10]. This leads to atmospheric circulation and the system of six belt-like circulation cells, wrapping the planet longitudinally: two 'Hadley' cells at 0 ˚ to +30 ˚ and 0 ˚ to -30 ˚ latitude; two 'Ferrel' cells at +30˚ to +60 ˚ and -30 ˚ to -60 ˚ and; two Polar cells at +60 ˚ to +90 ˚ and -60 ˚ to -90˚. This model of the atmosphere at planetary level is far too simplified to explain site-specific weather patterns but it does serve to explain some general trends correctly. Figure 2.2 illustrates these circulatory cells.

At the equator (the boundary between two Hadley cells), which experiences the highest magnitude of solar heating, air heated near the surface rises and is circulated northward/ southward to less intensely heated regions, with this transfer occurring near the top of the troposphere at ~10km above the surface. This creates low average surface pressure at the equator, facilitating higher precipitation, and high average surface pressure at the tropics (+30 ˚ and -30 ˚ latitude), leading to generally more settled weather. At the surface, air naturally then flows from the high-pressure zone created at the tropics back to the low pressure zone at the equator (the 'Trade Winds'), thus completing the circulation cells.

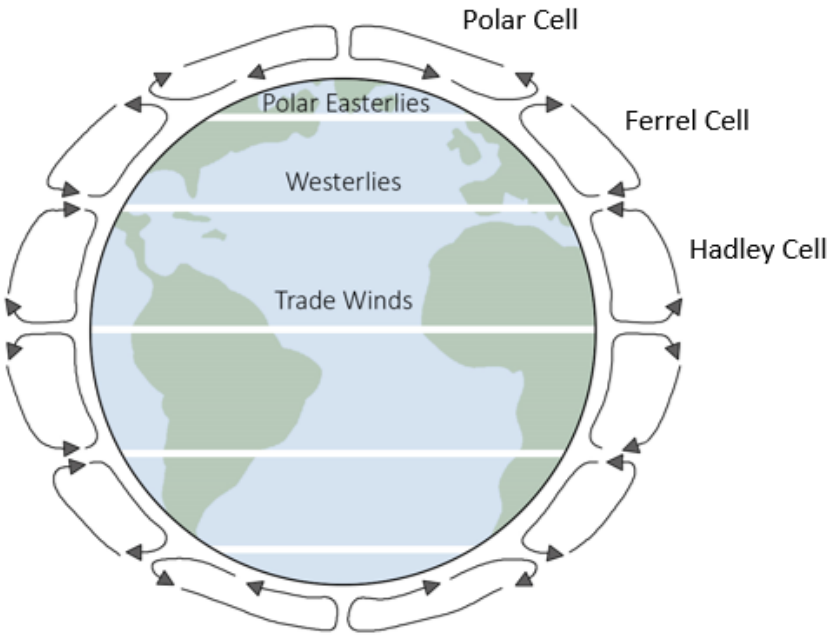


*Figure 2.2: Diagram showing the atmosphere's circulatory cells and indicating the localised dominant wind patterns at different latitudes: trade winds, westerlies and polar easterlies (illustrative).*

Due to the Coriolis effect, for an observer on the east-west rotating planetary surface, this near-surface returning air flow is diverted to the right in the northern hemisphere and to the left in the southern hemisphere, so that the Trade Winds actually present as north-easterlies in the northern hemisphere and south-easterlies in the southern hemisphere.

Similarly, at the boundary between the northern-hemisphere Ferrel and Polar cells (around the latitude of the UK/Ireland) a low average surface pressure zone is created (partly explaining relatively high rainfall). The wind climate in the UK/Ireland is mostly driven by the northern-hemisphere Ferrel cell which comprises northerly winds at high altitude and southerlies (diverted by the Coriolis force into south-westerlies) at the near-surface, explaining the predominant wind direction in the region.

An interesting complication in this respect is that the relative sizes of the Ferrel and Polar cells, and therefore the location of the inter-cell boundary and the jet stream, can shift north- and south-ward, leading to highly variable weather.

### 2.1.2 The Atmospheric Boundary Layer (ABL)

This section gives a general overview of the ABL and the physical nature of atmopsheric stability. The governing physics is then set out in detail in the following section 2.2.

A boundary layer develops when the velocity of a fluid is affected by the drag effects of nearby surfaces. The effect is negligible at sufficient distance from the object and becomes more significant towards the surface, at which point the velocity is reduced to zero. This equally applies when considering the flow of air over the Earth's surface: a gradual decrease in wind velocity from the upper atmosphere downwards towards the surface is observed. This provides an alternative, more precise, definition of the ABL: the layer of the troposphere within 1-2km of the surface in which the wind velocity is significantly affected by surface drag.

The ABL can be further sub-divided into the 'surface layer' (defined as the lowest 10% of the ABL) and the 'Ekman layer' (the ABL above the surface layer) [9]. At the transition between the ABL and the troposphere above is a potential temperature inversion. Figure 2.3 illustrates the structure of the troposphere, including the sub-structure of the ABL.

In the case of wind flow there is an additional consideration: the Earth's rotation drives a daily cycle of solar-driven heating and cooling at the surface. This leads to a progression of near-surface atmospheric conditions within the ABL, broadly classifiable as 'stable', 'unstable' and 'neutral', which have important consequences for wind flow.

Stable conditions, generally observed at night and more often at low wind speed, are mainly a result of radiative surface cooling. As the surface cools, the layer of air immediately above the surface cools by conduction. This cooled layer is denser than the layer above and therefore remains at the surface. This effect cascades up through the atmosphere, leading to a 'stratified' atmosphere: a positive 'potential temperature' gradient (increasing with height), high wind shear (rapidly increasing horizontal wind speed with height) and low turbulence. The term potential temperature refers to normalised temperature for a pressure of 1000hPa – explained further in 2.2.3.

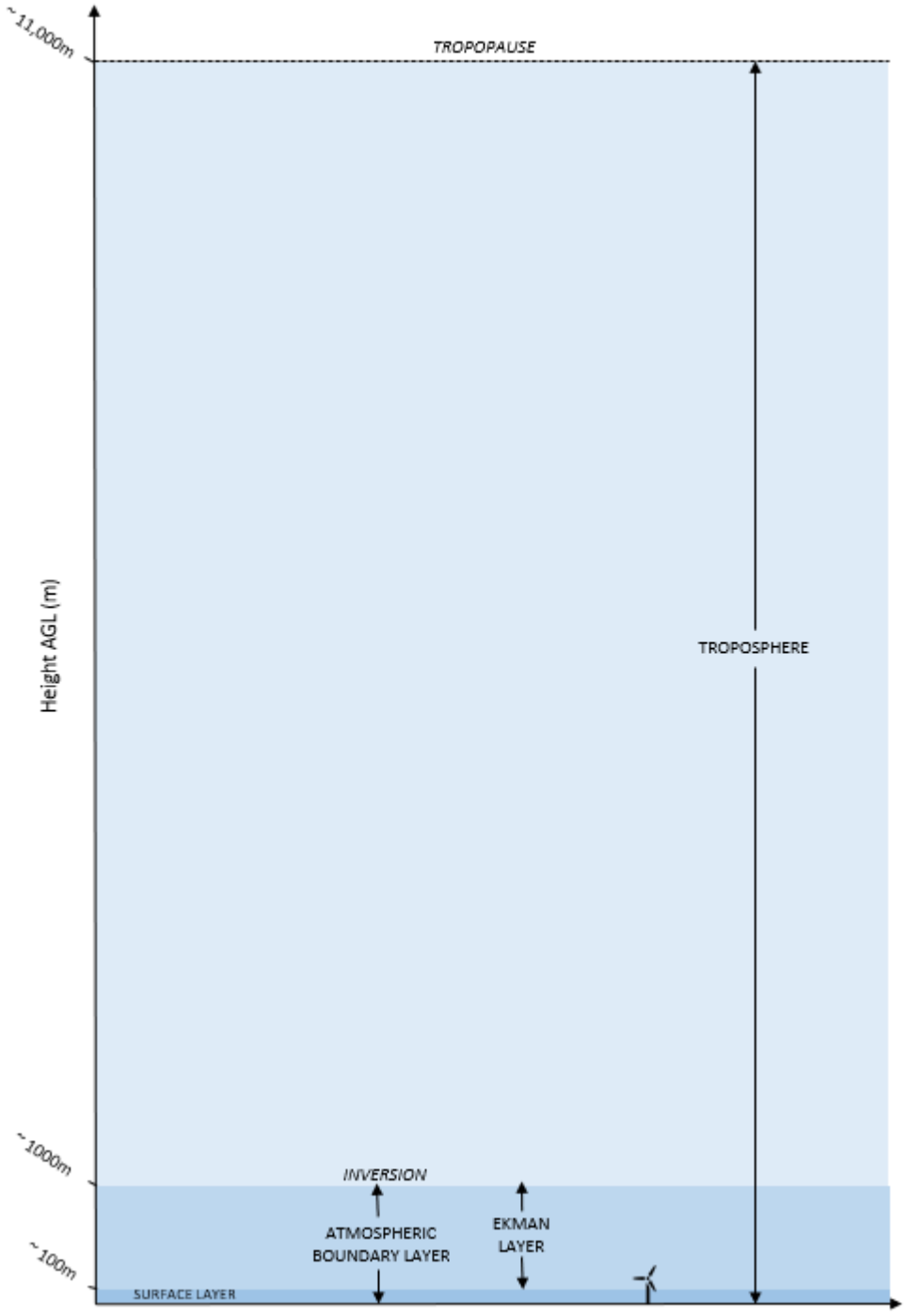


*Figure 2.3: Diagram showing the sub-layers of the troposphere (not to exact scale). An indicative wind turbine is included for context.*

Unstable conditions, more often occurring during the day, arise as a result of the onset of convection during solar heating of the surface. As the layer of air above the surface heats up by conduction, air packets become less dense than in the layer above and will therefore rise, leading to the development of a convective, 'well-mixed' boundary layer. Unstable conditions are characterised by a negative potential temperature gradient, relatively low wind shear and high turbulence.

Neutral conditions, generally occurring as a transitional state, are characterised by unchanging potential temperature with increasing height and wind conditions (shear and turbulence) which lie between stable and unstable conditions.

There are two broad ways to measure and classify the atmospheric state: direct measurement of vertical heat flux and inference of vertical heat flux using vertically distributed temperature, relative humidity and pressure sensors to measure the virtual potential temperature gradient. This is an important differentiation: in this research, the latter approach of inferring rather than directly measuring atmospheric stability is taken.

Figure 2.4 shows frequency distributions for all (black), neutral (green), stable (blue) and unstable (red) atmospheric stability, binned by concurrent wind speed. This plot is based on data from an SSE site, where stability has been defined by ranges of measured virtual potential temperature gradient (as will be discussed in greater detail in Chapter 4). It can be observed that non-neutral conditions dominate at this site below around 10m/s and neutral dominates above 10m/s. This is due to the fact that high wind speed (and increased turbulent kinetic energy) has the effect of disrupting thermal processes, such as those which result in stable and unstable conditions.

Importantly, industry-standard wind flow modelling practice is conventionally to model the atmosphere as 'purely neutral' with uniform potential temperature throughout the ABL and troposphere above. With reference to Figure 2.4, this is to assume that modelling only the neutral component (green) of the overall distribution will result in an adequate simulation of the mean wind flow, neglecting to model either the stable (blue) or unstable (red) components explicitly.

In this research, this assumption is challenged: the full range of site-specific neutral, stable and unstable conditions are modelled and the resulting wind flow is compared to a neutral-only simulation.

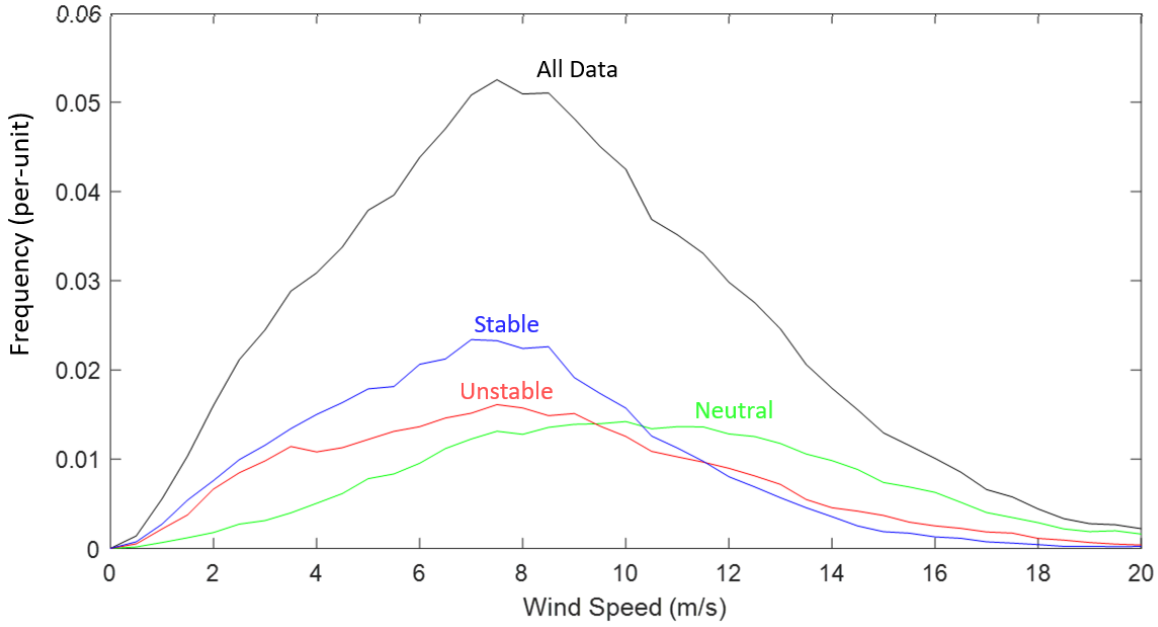


*Figure 2.4: Wind speed frequency distributions corresponding to all data (black), neutral atmosphere (green), stable atmosphere (blue) and unstable atmosphere (red).*

## 2.2 Atmospheric Thermodynamics

A useful starting point is to describe the atmospheric boundary layer as an ideal gas at rest and in hydrostatic equilibrium. This provides the theoretical framework for atmospheric stability, which is of interest to wind flow modelling, to be related to temperature gradient which can be easily measured.

In this section, first a description of the atmosphere as an ideal gas in hydrostatic equilibrium is set out and the adiabatic temperature lapse rate is calculated. Then, the effect of non-adiabatic lapse rates, such as those caused by ground heating and cooling effects, is considered, in terms of the tendency for air parcels to vertically accelerate or decelerate. The derivations here are mostly adapted from [9] and [10].

It is useful to consider the atmosphere to be made up of stacked 'parcels' of air with some arbitrary length, width and height which interact with their environment (e.g. adjacent parcels) at their outer surfaces.

In this analogy, the pressure of a parcel is taken to be equal to that of its environment (i.e. all surrounding parcels). However, the density, temperature and composition (i.e. moisture content) may differ from surrounding parcels, which impacts on how parcels interact with one another.

### 2.2.1 Hydrostatic Balance Equation

The atmosphere, or each mole of the atmospheric mixture of gases, as approximated to an ideal gas obeys the ideal gas law :

$$pV_m = R^*T \tag{1}$$

where $p$ is pressure (Pa), $V_m$ is the molar volume, $R^*$ is the universal gas constant (8.314 J $K^{-1}$ $mol^{-1}$) and $T$ is the absolute temperature (K) [10]. Substituting $V_m = \rho/M_m$, where $\rho$ is the density of air, $M_m$ is the mass of one mole of air, and $R^* = RM_m$, where $R$ is the gas constant per unit mass, we get:

$$p = RT\rho \tag{2}$$

which is an alternative expression of the ideal gas law [10]. The value of $R$ depends on the exact composition of the atmosphere – especially in terms of the concentration of water vapour – which is an important consideration, as will be explored in 2.2.4.

Hydrostatic equilibrium is reached when the upwards and downwards forces on a parcel of air cancel out and the parcel remains at rest. A parcel at height above ground level, $z$, with mass, $m$, height, $\Delta z$, and top/bottom area, $\Delta A$, will experience a downwards force due to gravity ($F_g = mg$), an additional downwards force due to pressure from the atmosphere

above ($F_{p(top)} = p(z + \Delta z) \cdot \Delta A$) and an upwards force due to pressure from the atmosphere below ($F_{p(bottom)} = p(z) \cdot \Delta A$). Therefore, for these forces to cancel:

$$g\rho \cdot \Delta A \cdot \Delta z = p(z) \cdot \Delta A - p(z + \Delta z) \cdot \Delta A \quad (3)$$

$\Delta A$ can be cancelled in this equation and $p(z + \Delta z)$ can be substituted for the Taylor expansion:

$$p(z + \Delta z) = p(z) + \frac{dp}{dz}\Delta z \quad (4)$$

This leads to the hydrostatic balance equation:

$$\frac{dp}{dz} = -g\rho \quad (5)$$

This equation defines the vertical pressure gradient ($\frac{dp}{dz}$) in terms of air density ($\rho$) and gravitational acceleration, which is taken to be constant. For a standard atmosphere with $\rho = 1.225\text{kg/m}^3$ [10]:

$$\frac{dp}{dz} = -g\rho = -9.8\ x\ 1.225 = -0.12\ hPa/m \quad (6)$$

### 2.2.2 Dry Adiabatic Lapse Rate

Predominantly, temperature decreases with height in the troposphere, including in the boundary layer ($\frac{dT}{dz} < 0$). In cases where temperature increases with height ($\frac{dT}{dz} > 0$), this is known as an 'inversion'. This rate of change of temperature with height, $\frac{dT}{dz}$, has important consequences for the vertical transfer of heat, moisture and vertical momentum [9], which is central to this research.

The 'lapse rate' $\Gamma$ is defined as negative of the temperature gradient, so that a positive lapse rate indicates a decrease in temperature with height:

$$\Gamma_e = -\frac{dT}{dz} \tag{7}$$

$\Gamma_e$ denotes the 'environmental' lapse rate: the actual, measurable lapse rate of the atmosphere [10].

The Dry Adiabatic Lapse Rate (DALR), denoted $\Gamma_a$, is the theoretical lapse rate of a section of atmosphere made up of *dry* air in hydrostatic equilibrium. It also describes the temperature change, $dT$, that an air parcel will undergo if vertically displaced through height, $dz$. 'Adiabatic' indicates that no heat is transferred between the parcel and the environment, whereas 'diabatic' is the converse. This equivalence is important: if an air parcel is displaced vertically within an atmosphere with $\Gamma_e = \Gamma_a$, then its temperature, and therefore density, will remain equal to that of its surroundings and it will remain at its displaced height ('neutral' atmosphere).

For $\Gamma_e > \Gamma_a$, an upwardly displaced air parcel will find itself with greater temperature and lower density than its surroundings: it will be buoyant and will continue to rise ('unstable' atmosphere). For $\Gamma_e < \Gamma_a$, the displaced air parcel will have lower temperature/higher density and will sink back to its original height ('stable' atmosphere).

To substantiate this point, consider a parcel at equal temperature $T$ with its surroundings, displaced from height z to height (z + $\delta z$) and developing adiabatically. Its displaced temperature $T_p{}'$ will be:

$$T_p{}' = T - \Gamma_a \delta z \tag{8}$$

where T is the original, un-displaced temperature. Similarly, the environmental temperature $T_e{}'$ of the parcel's new surroundings will be:

$$T_e' = T - \Gamma_e \delta z \quad (9)$$

By use of the ideal gas law (2), it can be seen that the density of the parcel and its surroundings are:

$$\rho_p' = \frac{p_p'}{RT_p'} \quad \text{and} \quad \rho_e' = \frac{p_e'}{RT_e'} \quad (10)$$

The parcel remains at equal pressure with its surroundings as it is displaced so $p_p' = p_e'$. So, the parcel will have greater density than its surroundings ($\rho_p' > \rho_e'$), causing it to sink when its displaced temperature is less than the environmental temperature ($T_p' < T_e'$ or $\Gamma_e < \Gamma_a$). The converse is true for $\Gamma_e > \Gamma_a$, in which case the parcel density is lower than the environmental density.

Knowing the value of $\Gamma_a$ is, then, of key importance to identifying when neutral, unstable and stable conditions might occur. Deriving $\Gamma_a$ starts with an expression of the First Law of Thermodynamics which relates a change in enthalpy $H$ to temperature $T$, volume $V$, and changes in entropy and pressure, $\delta S$ and $\delta p$:

$$\delta H = T\delta S + V\delta p \quad (11)$$

$V$ is expanded using the ideal gas law (2) and the relation $V = 1/\rho$:

$$\delta H = T\delta S + \frac{RT}{p}\delta p \quad (12)$$

Now, $\delta H = \delta U + V\delta p$ where $U$ is internal energy and for unit mass $\delta U = c_v \delta T$, where $c_v$ is the atmospheric specific heat capacity at constant volume [10]:

$$c_v \delta T + V \delta p = T \delta S + \frac{RT}{p} \delta p \quad (13)$$

We again apply the ideal gas law (2) and the assumption $\delta T = \frac{T \delta p}{p}$ to the ($V \delta p$) term to get:

$$c_v \delta T + R \delta T = T \delta S + \frac{RT}{p} \delta p \quad (14)$$

Then make the substitution $c_p = c_v + R$, where $c_p$ is the specific heat capacity at constant pressure to get:

$$c_p \delta T = T \delta S + \frac{RT}{p} \delta p \quad (15)$$

Now we state that for an adiabatic process, there is no change in entropy ($\delta S$ = 0):

$$c_p \delta T = \frac{RT}{p} \delta p \quad (16)$$

As we are concerned with changing conditions with height, we can convert $\delta T$ and $\delta p$ to $\frac{dT}{dz}$ and $\frac{dp}{dz}$. Again, making use of the ideal gas law (2) and the hydrostatic equation (5), we get:

$$\frac{dT}{dz} = \frac{RT}{c_p p} \frac{dp}{dz} = \frac{g}{c_p} \cong 9.8\ K/km \quad (17)$$

So, the Dry Adiabatic Lapse Rate $(DALR), \Gamma_a \cong -9.8\ \mathrm{K/km}$ and whether $\Gamma_e$ is greater or less than this value will dictate whether the atmosphere is stable or unstable [10].

### 2.2.3 Potential Temperature

An alternative description of the DALR is the temperature change that a displaced parcel will undergo as a result of the effects of changing environmental pressure as it rises or sinks. It is useful to define the potential temperature, $\theta$, as the resultant temperature of a vertically displaced air parcel developing adiabatically (i.e. equal to $T_p{}'$ in equation (8)). Equation 16 can be re-expressed as:

$$c_p \cdot \delta ln(T) = R \cdot \delta ln(p) \qquad (18)$$

Integration with $T = \theta$ and $p = p_0$ (the end-state pressure) leads to:

$$c_p \cdot ln\left(\frac{\theta}{T}\right) = R \cdot ln\left(\frac{p_0}{p}\right) \qquad (19)$$

This leads to an important definition of potential temperature:

$$\theta = T\left(\frac{p_0}{p}\right)^{\kappa} \qquad (20)$$

where the Poisson constant, $\kappa = \frac{R}{c_p} \approx \frac{2}{7}$ has been introduced. $p_0$ is the end-state pressure and is taken to be $p_0 = 1000\ \mathrm{hPa}$ by convention [9].

When $\Gamma_e = \Gamma_a$ (i.e. neutral atmosphere) then $\frac{\mathrm{d}\theta}{\mathrm{dz}} = 0$ by definition. $\frac{\mathrm{d}\theta}{\mathrm{dz}} > 0$ and $\frac{\mathrm{d}\theta}{\mathrm{dz}} < 0$ correspond to stable and unstable atmospheres, respectively.

### 2.2.4 Saturated Adiabatic Lapse Rate (SALR)

Sections 2.2.2 and 2.2.3 described a method for determining the behaviour of a vertically displaced air parcel in an atmosphere comprising entirely dry air. In reality, the atmosphere

may contain some fraction of both water vapour and liquid water – both of which have a bearing on the onset of convective processes.

Water vapour is less dense than dry air, meaning that an air parcel containing a high concentration of water vapour will be less dense and will tend to rise in an environment comprising dry air. Liquid water is more dense than dry air and, similarly, an air parcel with a high liquid water concentration will tend to sink in an environment comprising dry air. When evaluating whether a vertically perturbed air parcel will rise or sink, it is therefore necessary to take into account the relative concentrations of dry air, water vapour and liquid water in the parcel and in the environment.

The temperature of an air parcel rising adiabatically, will eventually reach its dew point temperature, at which point it becomes 'saturated' and condensation of water vapour into liquid water becomes the dominant process. The parcel, being composed of a greater concentration of liquid water, therefore becomes heavier and sinks. This can be seen as having a counter-active effect to the convective process.

The saturated adiabatic lapse rate (SALR) can be described in a similar way to the DALR (full derivation given in [10]):

$$\Gamma_s = \frac{g}{c_p} \cdot \frac{\left(1 + \frac{\Lambda \mu_s}{RT}\right)}{\left(1 + \frac{\Lambda^2 \mu_s}{c_p T^2 R_v}\right)} = \Gamma_a \cdot \frac{\left(1 + \frac{\Lambda \mu_s}{RT}\right)}{\left(1 + \frac{\Lambda^2 \mu_s}{c_p T^2 R_v}\right)} \qquad (21)$$

Here $\Lambda$ is the latent heat of vaporisation of water; $\mu_S$ the saturation mixing ratio; $c_p, T$ and $R$ have their previous definitions and $R_v$ is the specific gas constant for water vapour. It can be observed that $\Gamma_s$ is equal to $\Gamma_a$ multiplied by an adjustment factor which depends strongly on temperature, $T$. Typical values for $\Gamma_s$ are in the range 5.0 – 8.0 K/km.

### 2.2.5 Virtual Potential Temperature

Virtual temperature $T_v$ is the temperature that an air parcel with non-zero moisture content would need to reach to have the same density and pressure as a dry air parcel. Converting potential temperature $\theta$ into virtual potential temperature $\theta_v$ therefore provides a concise

means of accounting for the effects of moisture content while retaining a simple (single-variable) description of the atmosphere.

It is possible to define $T_v$ as a function of absolute temperature, $T$, and relative humidity (*RH*) which can be readily measured [10].

Let $m_d$, $m_v$ and $m_L$ be the masses of dry air, water vapour and liquid water in an air parcel with volume, $V$ (note that the subscript, v, has a different meaning here than in $T_v$). We can then calculate the total density and then 'partial densities' ($\rho$') of the air parcel as:

$$\rho = \frac{m_d + m_v + m_L}{V} \tag{22}$$

$$\rightarrow \quad \rho = \rho'_d + \rho'_v + \rho'_L \cong \rho'_d + \rho'_v \tag{23}$$

In the above equation, the partial density of liquid water is low enough as to be negligible for our purposes, which is why the right-hand side can be reduced to two terms.

Now we apply the ideal gas law (2) to both the partial densities, $\rho'_d$ and $\rho'_v$ :

$$\rho'_d = \frac{p'_d}{R_d T} \qquad \textit{and} \qquad \rho'_v = \frac{p'_v}{R_v T} \tag{24}$$

In this case, both the partial density of dry air $(\rho'_d)$ and water vapour $(\rho'_v)$ have been defined in terms of partial pressures $(p'_d)$ and $(p'_v)$. Consequently, we can make use of Dalton's law of partial pressures:

$$p = p'_d + p'_v \tag{25}$$

Combining equations (1), (23), (24) and (25) yields:

$$\rho = \frac{p - p'_v}{R_d T} + \frac{p'_v}{R_v T} \tag{26}$$

$$\rightarrow \quad \rho = \frac{p}{R_d T} - \frac{p'_v}{R_d T} + \frac{p'_v}{R_v T} \tag{27}$$

$$\rightarrow \quad p = R_d \rho T \left[1 + \frac{p'_v}{R_d T \rho} - \frac{p'_v}{R_v T \rho}\right] \tag{28}$$

$$\rightarrow \quad p = R_d \rho T \left[1 + \frac{p'_v}{R_d T \rho} - \frac{p'_v}{R_d T \rho} \cdot \frac{R_d}{R_v}\right] \tag{29}$$

We can now make the substitution $\varepsilon = \left(\frac{R_d}{R_v}\right) \cong 0.622$ for the relative gas constants of dry air and water vapour, an approximation which is appropriate for the mixture of gases which comprise dry air in Earth's atmosphere [9].

$$p = R_d \rho T \left[1 + \frac{p'_v}{R_d T \rho} - \varepsilon \frac{p'_v}{R_d T \rho}\right] \tag{30}$$

Now, we can make the substitution $R_d T \rho = p$, which is a re-expression of the ideal gas law (2) and also the definition of relative humidity $(\mathrm{RH})$, $\mathrm{p'_v} = \mathrm{RH} \cdot \mathrm{p_{sat}(T)}$ [10].

$$p = R_d \rho T \left[1 + \frac{RH \cdot p_{sat}(T)}{p} \cdot (1 - \varepsilon)\right] \tag{31}$$

We now have an equation of the form of the ideal gas law, where the temperature term is the absolute temperature multiplied by a scalar quantity. Therefore, we can express $T_v$ as:

$$T_v = T \cdot \left[1 + \frac{RH \cdot p_{sat}(T)}{p} \cdot (1 - \varepsilon)\right] \quad (32)$$

In this case, $T_v$ is the temperature that a dry parcel of air would need to attain in order to have equal density and pressure to an air parcel with relative humidity, $RH$, when the saturation vapour pressure is $p_{sat}$ and pressure is $p$.

The saturated vapour pressure ($p_{sat}$) can be calculated using a range of empirical and non-empirical methods. The Tetens equation [11] is a fairly simple approach for calculation of $p_{sat}$, commonly used in boundary layer applications because it agrees well with more sophisticated methods within the likely boundary layer temperature range. The Tetens equation is:

$$p_{sat} = 6.1078 \times 10^{7.5T/(237.3+T)} \quad (33)$$

Equation (32) can similarly be applied to potential temperatures, referring back to equation (20):

$$\theta_v = \theta \cdot \left[1 + \frac{RH \cdot p_{sat}(T)}{p} \cdot (1 - \varepsilon)\right] \quad (34)$$

*or*

$$\theta_v = T \left(\frac{p_0}{p}\right)^{\kappa} \cdot \left[1 + \frac{RH \cdot p_{sat}(T)}{p} \cdot (1 - \varepsilon)\right] \quad (35)$$

NB. In the literature [9], the more common form of this equation is expressed as a function of the mixing ratio, $\mu_s$:

$$\theta_v = \theta \cdot [1 + 0.61\mu_s] \tag{36}$$

This gives a simpler form of the relation but does not allow for a single expression which relates $T_v$ directly to the measured values, $RH$, $p_{sat}$ and $p$. This equation is only applicable to unsaturated air.

### 2.2.6 Brunt-Väisälä Frequency

The Brunt-Väisälä frequency describes the vertical force on a displaced air parcel, which is a very useful quantity in terms of linking atmospheric stability to wind flow. The upward buoyancy force can be equated to the product of its mass and acceleration (as per Newton's Second Law):

$$gV'\left(\rho'_e - \rho'_p\right) = \rho'_p V' \left(\frac{d^2(\delta z)}{dt^2}\right) \tag{37}$$

$$\rightarrow \quad \frac{d^2(\delta z)}{dt^2} = g\left(\frac{\rho'_e}{\rho'_p} - 1\right) \tag{38}$$

$$\rightarrow \quad \frac{d^2(\delta z)}{dt^2} = g\left(\frac{T'_p}{T'_e} - 1\right) \tag{39}$$

$$\rightarrow \quad \frac{d^2(\delta z)}{dt^2} = g\left(\frac{T - \Gamma_a \delta z}{T - \Gamma_e \delta z} - 1\right) \tag{40}$$

$$\rightarrow \quad \frac{\mathrm{d}^2(\delta \mathrm{z})}{\mathrm{dt}^2} = -\frac{\mathrm{g}}{\mathrm{T}}\left(\frac{\mathrm{dT}}{\mathrm{dz}} + \frac{\mathrm{g}}{\mathrm{c_p}}\right) \delta \mathrm{z} \tag{41}$$

We introduce the Brunt- Väisälä frequency, $N$, such that:

$$N^2 = \frac{g}{T}\left(\frac{dT}{dz} + \frac{g}{c_p}\right) \tag{42}$$

So that:

$$\frac{d^2(\delta z)}{dt^2} = -N^2(\delta z) \tag{43}$$

And it can further be shown that $N$ relates to the potential temperature gradient [10]:

$$N^2 = \frac{g}{\theta}\frac{d\theta}{dz} \tag{44}$$

Applying equation (44) to an air parcel displaced upwards (e.g. due to flow over a terrain feature) this results in the following cases:

- $\frac{d\theta}{dz} = 0$ (neutral). The displaced air parcel remains at the same temperature as the surrounding environment as it rises and therefore does not accelerate or decelerate.

- $\frac{d\theta}{dz} > 0$ (stable). The displaced air parcel will experience a restorative downwards force as a result of being heavier than its surroundings, resulting in simple harmonic motion of the parcel with period $2\pi/N$.

- $\frac{d\theta}{dz} < 0$ (unstable). The displaced air parcel will continue to accelerate upwards due to being lighter than its surroundings until such time as it enters a region with $\frac{d\theta}{dz} > 0$. In this case, the atmosphere is conducive to vertical motion and in equation (44) above, the value of $N$ is non-real.

It is important to distinguish between atmospheric states and the conditions which precede them. For example, an observation of $\frac{d\theta}{dz} < 0$ does not necessarily mean that the atmosphere is in an unstable state: an initial perturbation is required to trigger the convective process. However, for onshore sites, flow over complex terrain or mechanically induced turbulence will often provide this trigger, making this generally a safe assumption.

### 2.2.7 Surface heating and cooling

Sections 2.2.1 to 2.2.6 set out how the atmosphere reacts to potential temperature gradients ($\frac{d\theta}{dz}$) greater than and less than zero. This section introduces thermodynamic heating and cooling processes at the surface which lead to variation in ($\frac{d\theta}{dz}$). In the simple case, the interaction we need to understand is between the surface and the atmosphere at the geographical site of interest. In more complex cases, it becomes necessary to include surface-atmosphere interactions occurring upstream, with the resulting changes to the atmospheric profile being advected towards the site of interest.

The basic concepts of surface heating and cooling processes will be introduced in order to provide theoretical context and understanding of the processes which result in different stability climates at different sites.

A simple method for examining surface heating and cooling is to imagine a thin layer at the surface, at which all energy fluxes to and from the atmosphere above and the surface below must balance. This 'heat budget' can be expressed as:

$$Q^* + Q_G + Q_H + Q_E + \Delta Q_S = 0 \qquad (45)$$

where $Q^*$ is the net radiative heat flux; $Q_G$ is the heat flux into the surface; $Q_H$ and $Q_E$ are the sensible and latent heat fluxes out of the surface into the air and; $\Delta Q_S$ is heat stored in the surface layer. The convention in this case is that all fluxes are positive when acting upward, away from the Earth. Therefore $Q^*$ will generally be negative as it is dominated by downward solar irradiance, whereas $Q_H$ and $Q_E$ can be both negative (heat flux into surface) or positive (heat flux into atmosphere), depending on the relative temperatures of the atmosphere and surface.

$Q^*$, the net radiative heat flux can be further broken down into its short-wave ($K$) and long-wave ($I$) upward and downward components:

$$Q^* = K\downarrow + K\uparrow + I\downarrow + I\uparrow \quad (46)$$

$K\downarrow$ is the attenuated solar irradiance. The Earth is heated by radiation from the sun at a rate of 1360-1380 W/m$^2$ [9]. However, this gross heat flux is attenuated by various factors including cloud cover and solar elevation angle ($\Psi$), which is itself a function of time of day, time of year and latitude. Specifically,

$$K\downarrow = S \cdot T_K \cdot sin(\Psi) \quad (47)$$

where $S$ is the gross solar irradiance (take $S$=1370 W/m$^2$) and $T_K$ is the transmissivity of the atmosphere which can be approximated by [12]:

$$T_K = (0.6 + 0.2\,sin(\Psi)) \cdot (1 - 0.4\sigma_{C_H}) \cdot (1 - 0.7\sigma_{C_M}) \cdot (1 - 0.4\sigma_{C_L}) \quad (48)$$

where $\sigma_{C_H}$, $\sigma_{C_M}$ and $\sigma_{C_L}$ are the spatial coverages of high, medium and low-level clouds respectively. $\sin(\Psi)$ is given by [13]:

$$sin(\Psi) = sin(\phi) \cdot sin(\delta_S) - cos(\phi) \cdot cos(\delta_S)\, cos\left[\left(\frac{\pi t_{UTC}}{12}\right) - \lambda_e\right] \quad (49)$$

where ø and $\lambda_e$ are the latitude and longitude co-ordinates (in radians) of the site of interest, $t_{UTC}$ is the hour of the day and $\delta_S$ is the solar declination angle:

$$\delta_S = \phi_r cos\left[\frac{2\pi(d - d_r)}{d_y}\right] \quad (50)$$

where $\phi_r$ = 0.409; $d_r$=173; $d_y$= 365.25 and $d$ is the day of the year.

$K\uparrow$ in equation (46) is that short-wave radiation which is reflected at the surface. The fraction of heat which will be reflected at the surface is the albedo, *a*, so that:

$$K\uparrow = -a \cdot K\downarrow \tag{51}$$

The albedo is an important site-specific property as it has a significant bearing on the amount of solar irradiance reaching the surface. Some approximate values of *a* are given in *Table* 2.1 from [9].

| *Surface* | *Albedo (a)* |
|---|---|
| *Dark Wet Soil* | *0.05* |
| *Coniferous Forest* | *0.1* |
| *Crops* | *0.2* |
| *Grass* | *0.2* |
| *Dry Soil* | *0.4* |
| *Snow* | *0.95* |
| *Water* | *0.05 - 1* |

*Table 2.1: Some typical values of surface albedo from* [9]*. For water, a depends on solar elevation angle.*

$I\downarrow$ and $I\uparrow$ is even more simply approximated by [12]:

$$I\downarrow + I\uparrow = I^* = 0.08 \cdot \left[1 - 0.1\sigma_{C_H} - 0.3\sigma_{C_M} - 0.6\sigma_{C_L}\right] \tag{52}$$

So that the net radiative heat flux can be expressed as:

$$Q^* = (1-a) \cdot S \cdot T_K \cdot sin(\Psi) \cdot I^* \tag{53}$$

According to [14], equation (45) can be re-written as:

$$C_{GA}\frac{\partial T_G}{\partial t} = -Q^* - Q_H - Q_E + Q_G \qquad (54)$$

where the term relating to heat stored in the surface ($\Delta Q_S$) has been related to an equivalent term describing the surface temperature change over time ($\frac{\partial T_G}{\partial t}$). This substitution is made possible by a two-layer model of the surface and ground below. The constant $C_{GA}$ incorporates molecular conductivity and heat capacity coefficients which are specific to the type of surface.

This equation yields some relevant solutions:

- When the right-hand side sums to > 0, surface temperature will increase. (e.g. at sunrise, when $Q^*$ is suddenly large and negative and dominates over the other fluxes). This will result in heating of the atmosphere at the surface, leading to a positive lapse rate ($\Gamma_e > \Gamma_a$) and an unstable atmosphere.
- When the right-hand side sums to < 0, surface temperature will decrease. This will result in cooling of the atmosphere at the surface, leading to a negative lapse rate ($\Gamma_e < \Gamma_a$) and a stable atmosphere.

Evaluating the relative magnitudes of $Q_H$, $Q_E$ and $Q_G$ is the subject of numerous parametrisation models (for example, [14] [15]) of various levels of sophistication and – although of key importance – is outside of the scope of this thesis. A couple of key points:

- The ratio of $Q_H$ to $Q_E$ is determined by both the temperature difference between the surface and air *and* the difference in moisture content.
- $Q_G$ will differ greatly in onshore/offshore cases due to the relatively huge effective heat capacity of deep water.

The use of mesoscale data to analyse heat fluxes and related temperature gradients is discussed in Chapter 4.

### 2.2.8 Section Summary

This section has introduced the concept of the dry adiabatic lapse rate (DALR), which acts as a threshold between stable and unstable conditions. Potential temperature ($\theta$) and virtual potential temperature ($\theta_v$) have been introduced, so that a simple relation between virtual potential temperature and atmospheric state has been established which takes into account the important factors of pressure gradient and latent heat transfer.

The meteorological effects (solar irradiation, reflection and heat exchange) which can lead to variation in $\frac{d\theta}{dz}$ have been presented, laying the ground for a discussion of how this variation might be different depending on time of day, time of year and location on Earth. This will be taken up in Chapter 4.

## 2.3 Flow Parametrisation

So far, priority has been given to deriving and describing the atmosphere in terms of $\frac{d\theta}{dz}$, the potential temperature gradient or $\frac{d\theta_v}{dz}$, the virtual potential temperature gradient. In subsequent chapters, $\frac{d\theta_v}{dz}$ (or actually, $\Delta\theta_v$) will be used to characterise the atmosphere – not as a direct representation of atmospheric stability, but as a proxy.

However, it is useful to briefly mention two other quantities which are more direct descriptors of the atmospheric state: Richardson Number and Obukhov Length.

### 2.3.1 Gradient Richardson Number

The Gradient Richardson Number ($Ri$) is a property of any moving fluid which can readily be applied to the atmosphere, where the rate of change of temperature ($\frac{\partial\theta_v}{\partial z}$) and wind speed ($\frac{\partial U}{\partial z}$) with height are known:

$$Ri = \frac{\left(\frac{g}{\theta_v}\right) \cdot \left(\frac{\partial \theta_v}{\partial z}\right)}{\left(\frac{\partial U}{\partial z}\right)^2} \quad (55)$$

The term $\theta_v$ denotes the virtual potential temperature, as derived earlier (equation (35)). Essentially, $Ri$ gives an indication of the relative magnitudes of temperature gradient and wind speed gradient. Therefore, $Ri$ will be large and negative for very unstable conditions ($\frac{\partial \theta_v}{\partial z} < 0$); large and positive for very stable conditions ($\frac{\partial \theta_v}{\partial z} > 0$) and close to zero for neutral conditions ($\frac{\partial \theta_v}{\partial z} \cong 0$).

### 2.3.2 Obukhov Length

The Obukhov Length depends on the vertical heat flux and friction velocity, $U_*$ [17]. Friction velocity is an expression of the shear stress between the ground and the geostrophic wind speed above the boundary layer [18]. The Obukhov Length is given by:

$$L = \frac{-U_*^3}{\kappa \cdot \left(\frac{g}{\theta_v}\right) \cdot \overline{(\omega' \theta')}} \quad (56)$$

$\overline{\omega' \theta'}$ is the co-variance of fluctuations (deviations from the respective mean values) in potential temperature, $\theta'$, and vertical wind speed, $\omega'$. The covariance of two variables is a measure of the extent to which they have a positive correlation, i.e. the covariance is positive when large values of one variable are co-incident with large values of the other and negative when large values of one variable are co-incident with small values of the other.

So, when $\overline{\omega' \theta'}$ is large and positive, this indicates that temperature fluctuation is positively correlated with vertical wind speed fluctuation: there is strong upward vertical heat flux. When $\overline{\omega' \theta'}$ is large and negative, this indicates the opposite: there is strong downward vertical heat flux. When $\overline{\omega' \theta'}$ is close to zero, vertical wind speed and temperature fluctuations are non-correlated.

The Obukhov Length is a length scale: it is the height above which buoyancy overtakes wind shear as the primary cause of turbulent kinetic energy (TKE). So, when $\overline{\omega'\theta'}$ is large and positive (daytime unstable atmosphere), $L$ is small and positive: buoyancy dominates in most of the boundary layer. When $\overline{\omega'\theta'}$ is small and positive, $L$ is large and positive and wind shear ('mechanical' TKE) will dominate for much of the boundary layer, from the surface upwards. When $\overline{\omega'\theta'}$ is close to zero, $L$ becomes infinite and when $\overline{\omega'\theta'}$ is negative (night time stable atmosphere), $L$ is also negative (i.e. no buoyancy-generated TKE in the boundary layer).

Ultrasonic anemometers can be used to measure both $U_*$ and $\overline{\omega'\theta'}$, although this can come with significant technological challenges. For practical purposes, such as for making corrections to vertical wind speed profiles (such as in [19]) $L$ can also be related to $Ri$ (which is easier to measure), using an empirical relationship such as [20]:

$$Ri > 0 \qquad L = \frac{z}{Ri} \qquad (57)$$

$$0 < Ri < 2 \qquad L = \frac{z(1-5Ri)}{Ri} \qquad (58)$$

The application of calculating $L$ to adjust vertical wind speed profiles is discussed in section 2.4.3. $L$ is a well-established metric for classifying atmospheric stability (Table 2.2).

| | |
|---|---|
| *Very Stable* | *0 < L < 200m* |
| *Stable* | *200 < L < 1000m* |
| *Near Neutral* | *\|L\| > 1000m* |
| *Unstable* | *-1000 < L < -200m* |
| *Very Unstable* | *-200 < L < 0m* |

*Table 2.2: Classification of five atmospheric stability states by Obukhov Length, L* [21].

Argyle [22] used this flux-profile relationship to convert measurements of temperature and wind speed gradient to Obukhov length at two offshore UK sites, resulting in clear annual and diurnal trends being observed.

## 2.4 Shear

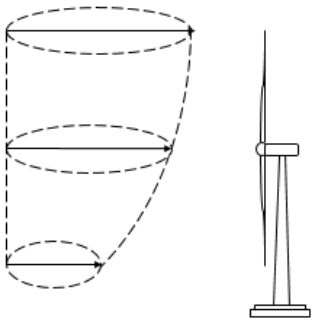

*Figure 2.5: Illustration of changing wind speed with height (wind shear) incident on a wind turbine.*

Wind shear describes the rate of change of horizontal wind speed with height above ground level. Fundamentally, wind shear exists because of the 'no slip' condition: the fact that the velocity of any fluid moving parallel to a solid surface will be reduced to zero at the boundary due to frictional forces. Figure 2.5 is a simple diagram of incident wind shear on a wind turbine.

Wind shear is of interest to wind energy developers for multiple reasons: first, wind turbine generator power curves are generally defined as electrical power output as a function of wind speed *at hub height.* So, it is important for accurate energy yield prediction that wind speed can be accurately extrapolated to hub height from measurement height, which may be different.

Second, wind shear affects the amount of kinetic energy passing through the rotor, which in turn affects electrical output: two identical wind turbines experiencing the same hub-height wind speed may not therefore exhibit the same power production. Alternatives to hub-height wind speed for defining power curves are therefore becoming more common in analysis pratice, such as Rotor Equivalent Wind Speed (REWS) and Rotor Average Wind Speed (RAWS), which take wind shear into account.

Third, the mechanical impacts of wind shear in wind turbine structures must be considered. A wind turbine rotor passing through uniform wind speed during one full rotation will suffer far less onerous bending moments than a rotor passing through a significant vertical wind speed gradient. Wind turbine manufacturers will generally stipulate limits for wind shear that cannot be exceeded at a proposed turbine location, in order to preserve long-term structural integrity.

Current industry best practice is to estimate wind shear from measured or CFD-modelled data from two or more heights using the power law, described below - this is the approach taken in this research for validation of measurements against CFD-modelled results.

However, when such measurements are not available, wind shear can be estimated by an assessment of ground and atmospheric conditions, using the log law. The log law and the various adjustments to it to account for the effects of atmospheric stability still constitute an active area of research so this topic is also covered below, for background information.

### 2.4.1 Power Law

The most commonly encountered expression of wind shear is the power law, the simplest expression of which is:

$$\left(\frac{U_1}{U_2}\right) = \left(\frac{z_1}{z_2}\right)^{\alpha} \tag{59}$$

In this equation, the ratio of wind speeds at two heights, $U_1$ and $U_2$, is expressed as the ratio of their vertical heights, $z_1$ and $z_2$, raised to the power $\alpha$, the 'shear exponent'. This relationship is particularly useful when wind speed measurements at two heights are available and $\alpha$ can be calculated as:

$$\alpha = \frac{ln(U_1 \,/\, U_2)}{ln(z_1 \,/\, z_2)} \tag{60}$$

Or, for the generalised case where three or more wind speeds, $U_i$, are available at measurement heights, $z_i$:

$$\alpha = \frac{d(ln(U_i))}{d(ln(z_i))} \tag{61}$$

In the latter case, a straight-line fit can be utilised to find a value of α which best represents the observed data.

The power law may also be suitable when wind speed at only one height is known but accuracy is not of great importance (e.g. if being used to extrapolate over a relatively very small vertical distance). In this case, reference values of $\alpha$ are available. For example, α = (1/7) ≈ 0.14 is a commonly used approximation in wind turbine suitability assessment or, alternatively, lookup tables (such as Table 2.3 from [23]) can be consulted.

| ***Stability*** | ***Offshore*** | ***Flat Onshore*** | ***Urban*** |
|---|---|---|---|
| ***Unstable*** | *0.06* | *0.11* | *0.27* |
| ***Neutral*** | *0.10* | *0.16* | *0.34* |
| ***Stable*** | *0.27* | *0.40* | *0.60* |

*Table 2.3: Reference values of α from* [23].

### 2.4.2 Log Law

In some instances, it may be necessary to estimate the effects of wind shear over significant vertical distances without having knowledge of wind speed at two or more heights. In this case, the log law, first developed in 1925 by Ludwig Prandtl [24], is known to perform better than the power law at estimating wind shear in the near-surface atmosphere. It is expressed as:

$$U = \frac{u^*}{\kappa} ln\left(\frac{z}{z_0}\right) \tag{62}$$

In this case, $U$ is the unknown wind speed at height, $z$, above ground level. $\kappa$ is the Von Karman constant ($\kappa \approx 0.4$). $u^*$ is the friction velocity, which is given by [18]:

$$u^* = \sqrt{\frac{\tau_0}{\rho}} \tag{63}$$

where $\tau_0$ is the surface stress and $\rho$ is mean air density [12]. $z_0$ is a length-scale known as the surface roughness: the tendency of the surface to exhibit drag on wind flow or, more

specifically, the height above ground at which wind speed *theoretically* equals zero according to logarithmic extrapolation downwards from above the boundary layer.

Smooth, uniform surfaces such as open ground and sea, exhibit less drag on wind flow than more irregular surfaces – some examples of surface types and their associated estimated values are given in Table 2.4.

| ***Terrain description*** | $z_0$ **(m)** |
|---|---|
| *Open sea (>5km fetch)* | *0.0002* |
| *Mud flats, snow; no vegetation, no obstacles* | *0.005* |
| *Open flat terrain; grass, few isolated obstacles* | *0.03* |
| *Low crops; occasional large obstacles* | *0.1* |
| *High crops; scattered obstacles* | *0.25* |
| *parkland, bushes; numerous obstacles* | *0.5* |
| *Regular large obstacle coverage (suburb, forest)* | *1* |

*Table 2.4: Some examples of $z_0$ values corresponding to various surface types, ranging from least rough to most rough* [25].

An alternative expression of (62), developed later by Paeschke [26], for flow over a large obstacle is:

$$U = \frac{u^*}{\kappa} ln\left(\frac{z-d}{z_0}\right) \qquad (64)$$

In this case, $d$ is the displacement height: the distance by which the flow is displaced above ground level by the obstacle. For a solid obstacle, such as a large man-made structure, $d$ equals the height of the structure. For non-solid obstacles, such as forestry compartments, $d$ will take some value between zero and the height of the obstacle, depending on the obstacle's density.

### 2.4.3 Monin-Obukhov Similarity Theory

The log law detailed above – and the alternative for flow over obstacles – are known to predict wind profiles well in neutral conditions [27]. However, for flow over an un-changing surface (e.g. constant $z_0$), neither of these equations allow for any time-variation in wind shear (except due to some variation in $u^*$). This is at odds with observations which generally show daily and seasonal variation in the wind profile due to atmospheric stability effects. It is therefore necessary to introduce a corrective term to make the log law more generally applicable.

Monin and Obukhov addressed this issue in their 1954 paper, introducing Monin-Obukhov Similarity Theory (MOST) [28].

Section 2.3.2 introduced the concept of the Obukhov Length, $L$, a length scale which can be used to characterise surface layer turbulent fluxes. Essentially, MOST describes a flux-profile relationship, wherein vertical profiles of potential temperature ($\theta$), humidity ($q$) and horizontal wind speed ($U$) can be defined as universal functions ($\phi_m$, $\phi_t$ and $\phi_q$) of the dimensionless stability parameter, ($z/L$) [29]:

$$\frac{\kappa z}{u^*} \cdot \frac{\partial U}{\partial z} = \phi_m \left(\frac{z}{L}\right) \tag{65}$$

$$\frac{\kappa z}{\theta^*} \cdot \frac{\partial \theta}{\partial z} = \phi_t \left(\frac{z}{L}\right) \tag{66}$$

$$\frac{\kappa z}{q^*} \cdot \frac{\partial q}{\partial z} = \phi_q \left(\frac{z}{L}\right) \tag{67}$$

These flux-profile relationships are an important link between heat flux (the important component of Obukhov Length, $L$) and vertical profiles of wind speed, potential temperature and humidity.

Integrating the above results in a further alternative expression of the log law (equation (62)) which applies to flow in neutral and none-neutral conditions, assuming no obstacles (i.e. neglecting displacement height, $d$):

$$U = \frac{u^*}{\kappa}\left[ln\left(\frac{z}{z_0}\right) - \Psi\left(\frac{z}{L}\right)\right] \quad (68)$$

where the term $\Psi$ is the stability correction to wind speed calculated using the original (neutral) log law. Refining the function $\Psi$ has been the work of many empirical studies over decades, ranging from Kansas in 1968 [20] to the North Sea in 1990 and 2009 [29] [30] to Antarctica in 2003 [31], where flux and/or temperature gradient measurements are used to parametrise the flux-profile relationships.

The parametrisation derived by Beljaars [32] is defined distinctly for stable and unstable conditions ($L > 0$ and $L < 0$). For stable conditions ($L > 0$):

$$\Psi = -5\left(\frac{z}{L}\right) \quad (69)$$

For unstable conditions ($L < 0$):

$$\Psi = 2 \cdot ln\left(\frac{1+x}{2}\right) + ln\left(\frac{1+x^2}{2}\right) - 2\,tan^{-1}x + \frac{\pi}{2} \quad (70)$$

$$x = \left[1 - 16\left(\frac{z}{L}\right)\right]^{-1/4} \quad (71)$$

Barthelmie [27] used this parametrisation of MOST to adjust predictions of wind speed at 48m from measurements at 20m, resulting in a significant correction of around 0.1-0.2 m/s and demonstrating increased prediction accuracy when comparing against measured data from the greater height. (Although possibly not as accurate as if the power law were used

with measurements from two or more lower anemometers. Newman [33], using measured data from site in Oklahoma, showed that estimating hub-height wind speed using the power law in conjunction with lower-level measurements outperforms the stability-adjusted log law, presented here).

So, MOST offers a means to convert temperature gradient measurements to vertical flux measurements or vice versa and to use either to make corrections to vertical wind speed extrapolation calculations, using an extended version of the log law.

It is worth making clear at this stage that validation of MOST does not form part of this research. Although this would be of interest, sufficient such studies appear in the literature and the focus here is instead on improving and validating CFD modelling rather than empirically derived relationships.

## 2.5 Turbulence Intensity

Turbulence intensity (TI) describes the variation in wind speed within a given averaging period (10-minute averaging periods with 1Hz sampling frequency are generally used in wind analysis by convention). TI is simply related to standard deviation, $\sigma$, and mean wind speed, $U$, according to:

$$TI = \frac{\sigma}{U} \qquad (72)$$

TI is another important factor in terms of wind turbine design, suitability assessment and energy resource assessment. Similarly to wind shear, turbine suppliers prescribe limits on the value of TI which can be borne by a given wind turbine.

Specifically, the IEC guidelines stipulate that long-term representative TI must not exceed 14% for a Class Ib/IIb certified turbine or 16% for a Class Ia/IIa certified turbine [34]. These limits are designed to ensure that turbines can withstand the mechanical stress on the rotor and drive-train resulting from variable wind loading.

Where measured turbulence data is concerned, various definitions of TI are used for different applications: 'mean TI' is generally taken to be the average across all wind speed bins, $N$.

$$TI_{mean} = \sum_{1}^{N} \left(\frac{\sigma_n}{U_n}\right) / N \quad (73)$$

This is the metric that is used in this research, unless otherwise stated. 'Characteristic TI', which is often used by turbine manufacturers as a greater (more conservative for structural design) value, is filtered for 15 ± 0.5 m/s and adjusted upwards by adding the standard deviation of all measurements in that wind speed bin to the mean.

$$TI_{char} = \sum_{1}^{N} \left(\frac{\sigma_n}{U_n}\right) / N + \sum_{1}^{N} \left(\frac{\sigma_n}{U_n} - \frac{\overline{\sigma_n}}{U_n}\right) / (N-1) \quad (74)$$

where the second term is used to denote the standard deviation of measured TI in the 15 ± 0.5 m/s wind speed bin (sometimes referred to as sigma-sigma; '$\sigma_\sigma$').

'Representative TI' is similar, except that the adjustment is 1.28 times the standard deviation (i.e. 90% confidence interval) of measured TI values.

$$TI_{rep} = \sum_{1}^{N} \left(\frac{\sigma_n}{U_n}\right) / N + 1.28 \sum_{1}^{N} \left(\frac{\sigma_n}{U_n} - \frac{\overline{\sigma_n}}{U_n}\right) / (N-1) \quad (75)$$

Wind flow in all environments exhibits turbulence to some extent. TI can be mechanically induced, for example, by flow in complex terrain or near forestry or induced by buoyancy in an unstable boundary layer.

## 2.6 Wind Farm Layout Design and Resource Assessment

This section sets out some key principles in the design and assessment of proposed wind farms. Wind farm developers conduct energy resource assessment in order to identify viable investment opportunities, with energy yield generally being the most influential factor in a wind farm business case. A yield estimate will comprise the following broad stages:

1. Layout Design
2. Wind Measurement

3. Flow modelling
4. Wake modelling
5. Energy conversion
6. Uncertainty analysis

Each of these stages is summarised briefly in this section, for context.

### 2.6.1 Layout Design

Wind farm layout design takes into account various factors. Primarily, turbines should be sited to take advantage of the windiest locations on the site – this is most applicable at onshore sites with complex terrain, where hilltops offer the highest wind speeds. However, near-shore offshore wind farms can also experience variation in wind speed from one part of the site to another, when the wind is coming from direction sectors with relatively short offshore fetch (distance to the coast line).

The spacing of wind turbines should be optimised for array efficiency: tighter layouts allow a greater number of turbines to be constructed within a constrained area but this allows less distance between turbines for the wind speed to recover downstream (wake effects), leading to overall lower efficiency. A further constraint here is that wind turbine rotors generate turbulence which affects the fatigue loading on downstream turbines. The recommendations of mechanical loading assessments will often result in a minimum turbine spacing which might be sub-optimal in terms of maximising energy yield within a constrained area.

Finally, site constraints such as ground/seabed conditions, environmental exclusion areas, and landowner boundaries must be taken into account as well as impact of visual amenity and noise levels.

Layout design will often be undertaken as part of an iterative wake-optimisation process, using software packages such as WindFarmer, published by DNV-GL [35].

### 2.6.2 Wind Measurement

An ideal measurement campaign for a prospective wind farm would comprise measurements spanning the rotor disk of each proposed wind turbine, including at hub height.

Unfortunately, wind measurement is complex and expensive and not all proposed wind farm projects turn out to be viable (which might otherwise justify greater up-front spend in wind measurement), so compromises have to be made.

Wind measurement campaigns should span at least one year and preferably multiple years in order to capture intra-annual (seasonal) and annual variation from long-term mean conditions. Measurement masts should have anemometers at multiple heights (in order to measure wind shear), with the top-most measurement being as close as practically possible to the proposed wind turbine hub-height, so that any uncertainty introduced by extrapolating from measurement height to hub height is minimised.

The number of masts needed to reliably estimate energy yield depends on the size and complexity of the site. For a small, flat site, one mast would usually be expected to be satisfactory. For a large site with steep topography and/or forestry, additional masts should be utilised in order to capture sufficient measurements which are representative of proposed turbines' operational conditions.

Increasingly, developers are using remote-sensing devices such as LiDAR (Light Detection and Ranging) and SoDAR (Sonic Detection and Ranging) as alternatives to mast-based wind speed and direction measurements. These carry the advantages of being cheaper (at least for shorter deployments), more easily deployed and often have the ability to measure up to greater heights than masts.

### 2.6.3 Flow Modelling

For the usual case where a single mast is being used for the assessment of wind conditions at multiple proposed turbine locations, measured wind distributions at measurement locations must be extrapolated to proposed turbine locations, taking into account the effects of topography and forestry on the ambient wind flow (i.e. not accounting for the influence of the turbines themselves). Established linear flow solvers such as WAsP (DTU Wind Energy) [36] have become industry-standard tools in this field. These are termed 'linear' flow models, due to the fact that they use a simplified form of the governing Reynolds-Averaged Navier-Stokes (RANS) equations for fluid flow. Linear flow models have the advantage of being

computationally non-intensive but are not capable of simulating complex flow effects such as re-circulation in the lee of hills.

Over the past decade, Computational Fluid Dynamics (CFD) has gained traction within the mainstream wind industry as a more precise means for modelling wind flow – particularly in highly complex terrain. The main distinction from linear flow modelling is the evaluation of all terms of the RANS equations, leading to much greater computational requirements. The principles of CFD are set out in section 2.9 and the implementation of ANSYS CFX for flow modelling is detailed in 6.1.

A quantity of key importance is the ratio of average wind speed at one point on a site to another – often referred to as a 'speed-up' (although it will equally as often be a 'slow-down'). Energy yield analysis relies heavily on this concept, in that wind distributions at turbine locations are evaluated by scaling the wind distribution at a measurement location by the simulated speed-up between the two locations. It is therefore a useful measurement, along with shear and TI, for assessing the accuracy of predictions from flow modelling software.

It is this step in the energy yield assessment process which is under scrutiny in this research. The sophistication and flexibility of CFD modelling, allows for the simulation of non-neutral atmospheric processes (i.e. the effects of non-neutral atmospheric stability). Incorporating this new physics will lead to changes in the interaction of wind flow with topography and forestry and therefore the evaluated free-stream wind distributions at turbine locations.

### 2.6.4 Wake Modelling

For developments constituting more than one wind turbine, the wake interaction between turbines must be considered.

Industry-standard practice still relies on models developed in the 1980s such as the PARK [37] and eddy viscosity [38] models, which model the interaction of turbines with wind flow as a wind speed deficit field which is then super-imposed on the ambient wind flow field. Both models can be said to be based on heavily simplified physics, although much has been done to validate their outputs against measured data from operational wind farms.

The WindFarmer (DNV-GL) software package [35] can be used to run both PARK and eddy viscosity models, with optional additional adjustments based on semi-empirical findings, such as the Large Wind Farm Correction. Similar to ambient flow modelling, CFD is increasingly being seen as a more accurate and physically realistic alternative to established methodologies.

### 2.6.5 Energy Conversion

The result of ambient flow and wake modelling is a set of hub-height wind speed distributions at turbine locations. These distributions are then multiplied by a power curve, giving the electrical power output as a function of wind speed at hub-height, and summed across all turbines to evaluate the gross energy yield. As an additional step, it may sometimes be desirable to adjust the stated power curve to match site-specific turbulence intensity (i.e. turbulence normalisation) or wind shear (i.e. Rotor Equivalent Wind Speed method), in order to better incorporate turbulent averaging effects and better represent energy flow through the rotor disk, respectively.

After gross annual energy yield has been calculated in this way, site-specific loss factors are applied to account for turbine downtime (typically, for example, 3%), electrical array losses (typically 2%) and control system inefficiency (variable).

### 2.6.6 Uncertainty Assessment

It is necessary to understand the level of confidence associated with any prediction of wind farm energy yield. Wind measurement, ambient flow modelling and wake modelling all incorporate uncertainties which can be expressed as standard errors and used to evaluate a standard deviation on the calculated energy yield. For bank-financed projects, lower costs of borrowing can be achieved if lower uncertainty can be demonstrated.

The relevance of uncertainty assessment in terms of this research is the potential to demonstrate increased ambient flow modelling accuracy via the incorporation of atmospheric stability effects and therefore reduce overall energy yield uncertainty.

## 2.7 Stability-Wind Phenomena

The physical changes that incorporating atmospheric stability will bring to wind flow simulations of real-world sites are not easily qualitatively stated: the various possible interactions of wind flow with the surface are too many.

However, it is useful to summarise some distinct stability-related flow features to give an indication of the kinds of processes that are being simulated and an impression of *why* the wind flow field should be expected to be different in non-neutral conditions, compared to neutral conditions.

### 2.7.1 Gravity Waves & Roll Vortices

Wind flow in stable conditions is more likely to go around rather than over obstacles or to be blocked altogether, compared to unstable or neutral conditions, essentially due to the resistive effect of the stable atmosphere to upward and downward motion. This effect is quantified by the Froude number [9]:

$$Fr = \frac{\pi\, U}{N\, W_T} \qquad (76)$$

In this equation, $U$ is the mean wind speed and $N$ is the Brunt- Väisälä frequency, as before (equation (42)). $W_T$ is the width of the obstacle disturbing the flow. So, $Fr$ relates the natural frequency of a displaced air parcel (via $N$) to the natural frequency of the obstacle (via $W_T$). It is evident that $Fr << 1$ for large $N$ (stable conditions), and $1 < Fr < 2$ for small $N$ (unstable conditions). Figure 2.6, adapted from [9], shows some visualisations of how wind flow changes with different values of $Fr$. Around $Fr = 0.1$, the obstacle causes significant upstream blockage and wind is more likely to flow around than over the obstacle. For greater values, such as $Fr = 0.4$, flow is more inclined to go over the obstacle, but will be perturbed by its presence.

At $Fr = 1.0$, resonant effects come into play: very pronounced lee-waves would be present downwind of the obstacle and rotors (re-circulating air flow) would form nearer the surface.

It is evident that a wind turbine placed downstream of the obstacle in Figure 2.6 would experience a wide range of flow conditions, depending on the value of $Fr$ and that no single value of $Fr$ is approximately representative of all conditions.

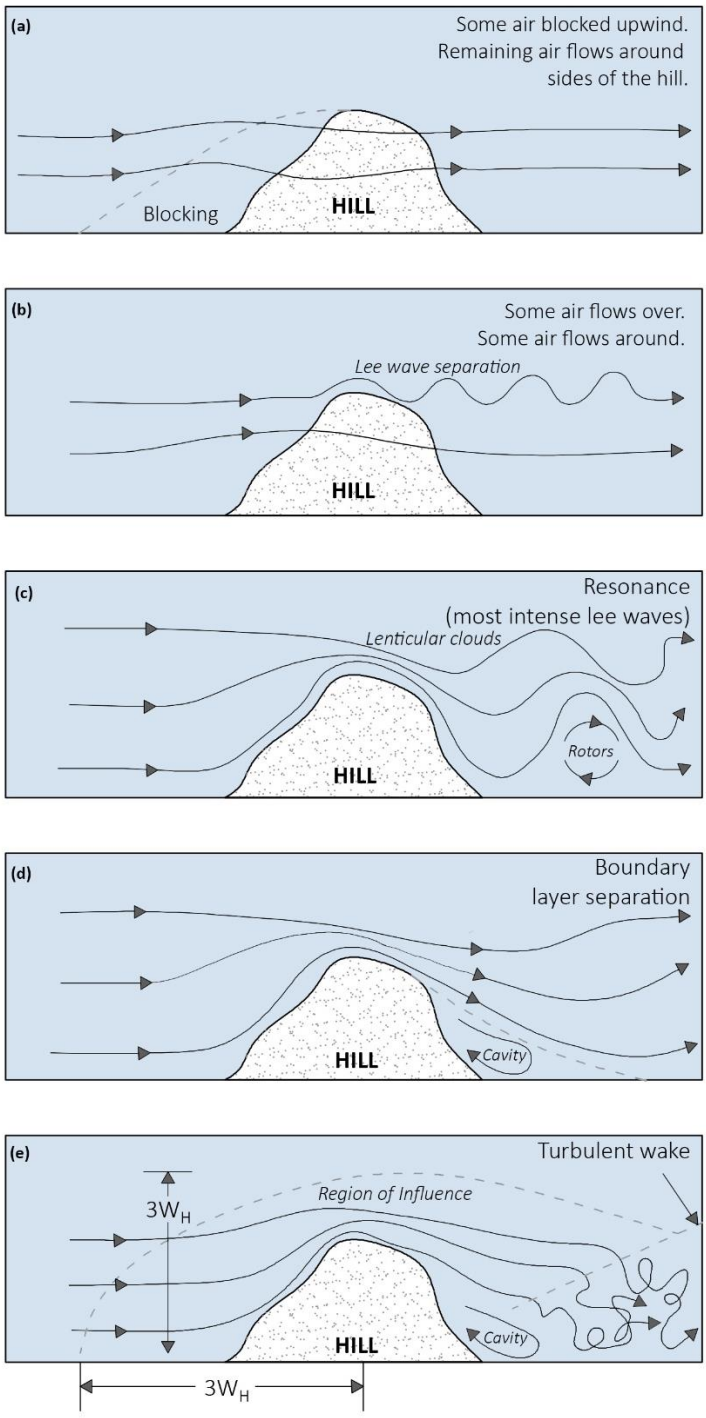


*Figure 2.6: Visualisations of wind flow in the region of an obstacle in (a) very stable conditions (Fr ~ 0.1); (b) stable conditions (Fr = 0.4); (c) slightly stable conditions (Fr = 1.0); (d) very unstable conditions (Fr = 1.7) and; (e) neutral conditions (Fr = ∞). Adapted from* [9].

### 2.7.2 Low-level Jets

The term 'low level jet' (LLJ) describes an atypical offshore vertical wind speed profile which increases abruptly at some height and reaches a maximum before decreasing at higher altitude to the geostrophic wind speed. Neither the technical definition of what constitutes a low-level jet nor its meteorological drivers are definitively established in the literature.

However, it has been proposed that a root cause in many cases is warm air being advected over cold sea surface (i.e. heated atmosphere over land being advected over cold sea in winter/spring) [39]. This leads to stable stratification and a de-coupling of the near-surface stable layer from the unstable atmosphere above. This discontinuity explains the extreme rates of change in wind speed with height. Non-neutral wind flow modelling is therefore required to predict the frequency of occurrence of such events, which presents challenges in terms of site suitability for very tall turbines.

Broadly speaking, the peak wind speed during a LLJ event will occur between 100 and 1000m AGL, will be tens to hundreds of metres in the vertical and will occur over a horizontal region of the order of ~100km [40].

## 2.8 Weather Modelling

Numerical modelling for spatially extrapolating and/or forecasting weather conditions can take place on the scale of hours (e.g. daily weather forecasts) or centuries (e.g. climate change research). All numerical models, including CFD, follow a basic design: a region of interest (domain) is split into a 3D lattice, or 'mesh', of horizontally and vertically distributed cells or nodes. Some start and/or boundary conditions are defined and the meteorological parameters of interest are evaluated numerically from the fundamental equations of state (i.e. the ideal gas law etc.) in the X, Y, Z and time dimensions.

Various models can also be applied across a wide range of spatial scales, each generalising different parts of the governing physics, in particular, the treatment of turbulence closure. This must be appropriate for the spatial scale under consideration as to have a single set of physics at all scales would make global modelling computationally unfeasible or micro-scale

modelling inaccurate. Table 2.5, taken from [41], outlines five broad categories of weather modelling.

| Scale | Primary Drivers | Tool | Spatial Scale | Time Scale |
|---|---|---|---|---|
| Planetary | Hadley Cells, Jet Stream, Rossby Waves | General Circulation Model (GCM) | 6000km | Days to months |
| Synoptic | Pressure Systems, Frontal Systems | GCM & Mesoscale Model | 2000km | Days to weeks |
| Mesoscale | Sea Breezes, Low Level Jets, Gap Winds | Mesoscale Model | 100km | Hours to days |
| Sub-Mesoscale | Thunderstorms, Dust Devils | Mesoscale Model & Large Eddy Simulation | 10km | Minutes to hours |
| Micro-scale (CFD) | Small Eddies, Tip Vortices | Computational Fluid Dynamics | 2m | Seconds |

*Table 2.5: A categorisation of five weather modelling scales and some key characteristics taken from* [41].

These models can be used in a nested form: output data derived from a larger-scale model can be used as inputs to a smaller-scale model. For example, the conditions at a site of interest can be extracted from a mesoscale model at a resolution of 3 x 3km and used to initiate a microscale (CFD) model, which evaluates conditions at a resolution of 25 x 25m.

### 2.8.1 General Circulation Models

General Circulation Models (GCMs) simulate synoptic atmospheric processes for a domain covering the entire planet. GCMs use real-time measured data from a global network of satellites, meteorological stations, weather buoys, radiosondes, aircraft and ships as initialisation for a computer model which might be run multiple times per day to forecast weather from the present time out to 1-2 weeks ahead.

The domain in a GCM model is typically made up of spatial cells of <1˚ of latitude/longitude (i.e. approx. 100km) and temporal resolution is usually output every 6 – 12 hours. There will

typically be 20-30 vertical layers in the simulated atmosphere and, in the case of ocean-atmosphere coupled models, 20-30 vertical layers below the surface. GCMs make use of some simplifications, notably the hydrostatic assumptions (i.e. very limited vertical momentum which is of importance in wind modelling).

The primary purpose of GCMs is, of course, for weather forecasting and most innovation in this area is driven by national weather agencies operating at the cutting edge of meteorological science and computational power. The 'Global Forecast System' (GFS) GCM, for example, is scheduled to be upgraded by the US National Oceanic and Atmospheric Administration (NOAA) in 2019 to have 128 vertical layers and a spatial resolution of 9km – significantly overlapping with what would usually be considered mesoscale modelling.

In addition to weather forecasts, another product of GCMs - useful for the purposes of weather and wind energy research - is reanalysis data sets. These give a series of snapshots of the global climate at the temporal resolution of the GCM (e.g. incorporating all measured data but no temporal forecasting – only spatial extrapolation). These data sets can be used to initiate weather models at smaller spatial scales and greater temporal resolution (i.e. nested models).

A key criterion of a reanalysis data set is consistency in the spatial extrapolation step (some variation in the data assimilation step is expected). Maybe for that reason, there is a fairly high degree of turnover in this area of research. Table 2.6 presents a summary of some well-established reanalysis data sets, in order to demonstrate the variety and general progression in precision observed over the past 2-3 decades.

| Reanalysis Data Set | Source | Year Commissioned | GCM | Indicative Spatial Resolution | Temporal Resolution | Vertical Atmospheric Layers |
|---|---|---|---|---|---|---|
| NCEP/ NCAR [42] | NCEP (NOAA) | 1996 | 3DVAR | 2.5˚ | 6 hours | 28 |
| MERRA [43] | NASA | 2009 | GEOS | 0.5 – 0.67˚ | 6 hours | 72 |
| CFSR [44] | NCEP (NOAA) | 2009 | 3DVAR | 0.5˚ | 6 hours | 64 |
| MERRA-2 [45] | NASA | 2014 | GEOS | 0.5˚ | Hourly | 72 |
| ERA-5 [46] | ECMWF | 2017 | 4DVAR | 0.25˚ | Hourly | 137 |

*Table 2.6: Summary of various publicly available reanalysis data sets.*

### 2.8.2 Mesoscale Modelling

Despite the creeping overlap between modelling categories, mesoscale modelling retains a place as a distinct step between planetary-scale and micro-scale weather modelling.

Unlike general circulation modelling, mesoscale modelling will always take into account parameters such as ground cover and its effect on meteorological conditions. Spatial resolution is generally of the order of 1-10 km.

Although numerous mesoscale models exist, the Weather Research and Forecasting (WRF) model stands out in terms of its breadth of use and acceptance across academia and industry [41]. WRF was developed in the late 1990s by various US institutions including the National Center for Atmospheric Research (NCAR) and the National Oceanic and Atmospheric Administration (NOAA) and has been regularly updated up to the latest version 4.0 in 2018.

WRF runs as a nested model: gridded time series GCM data for the region of interest are required inputs. The output parameters are generally more numerous and more detailed than can be extracted from GCMs. The model is normally operated in non-hydrostatic mode.

## 2.9 Computational Fluid Dynamics

Computational Fluid Dynamics (CFD) is increasingly the tool of choice of wind farm developers, consultants and turbine manufacturers because of its fundamental ability to more accurately and more precisely simulate the physical laws which govern wind flow.

Although essentially based on 19$^{th}$ century physics, implementing CFD did not become practical until the 1950s, with the advent of computer processing. At first, CFD mostly remained the preserve of the automotive and aeronautical industries but reductions in the cost of computational resource and the requirement to accurately model more complex problems led to its adoption by the wind energy industry over the last decade or so.

Not unlike the weather models discussed in section 2.8, CFD is based on establishing boundary conditions at the domain edge (the 'inlet') and then evaluating various physical quantities at each of a finite number of cells within the domain; usually a lattice-like mesh. The mesh can be irregularly spaced, so that the cell density can be greater in a region of interest (i.e. leading to greater accuracy nearer the surface or in and around wind turbines) than in other, less sensitive areas.

The CFD solver steps linearly through time; evaluating for time = t and then moving on to t+1, so that the evolution of physical systems can be deterministically modelled. In the case that the input conditions at the inlet are kept constant, the solver will eventually converge on an approximately unchanging solution ('steady-state' solution). Alternatively, if some time-dependent variation is applied at the inlet, the mean conditions can be evaluated by averaging across the time dimension. The latter is an example of a 'transient solution'.

### 2.9.1 CFD Physics

The umbrella term 'CFD' covers various sub-methodologies which are briefly described here. The lines of division are usually in terms of the amount of simplification of turbulent processes and spatial/temporal averaging.

Much fluid flow modelling is based on the Navier-Stokes equations: a set of continuity equations which describe the conservation of mass, momentum and energy in a continuous, non-discretised fluid. Direct numerical solving of the Navier-Stokes equations is not

theoretically impossible but absolutely impractical, in terms of computational resource, for most real-world applications.

This impracticality can be overcome by averaging. The first step is to average in space: it is not necessary to resolve the forces acting on each and every molecule in a fluid – some minimum spatial scale can be chosen which is appropriate for the application at hand.

The second step is to average in time. It is not sufficient to simply model mean flow conditions over a series of averaging periods, as this is to neglect the flow fluctuations within those periods, which are essential to simulating how the flow will develop. Reynolds decomposition is used to average without neglecting fluctuations, so that for instantaneous velocities $u$, $v$ and $w$ in the $x$, $y$ and $z$ directions respectively [10]:

$$u = \bar{u}(x) + u'(x,t) \tag{77}$$

$$v = \bar{v}(y) + v'(y,t) \tag{78}$$

$$w = \bar{w}(z) + w'(z,t) \tag{79}$$

where $\bar{u}$, $\bar{v}$ and $\bar{w}$ are the mean values of velocity over the averaging period and $u'$, $v'$ and $w'$ are the fluctuations from zero such that $\bar{u}' = \bar{v}' = \bar{w}' = 0$.

The 'Reynolds-Averaged' Navier-Stokes (RANS) equations can then be solved leaving the problem of what to do with the resulting turbulent (fluctuating) terms. The solutions to this problem are known as turbulence closure schemes.

In the simplest case, Prandtl's mixing length theory (along with other assumptions) can be used to arrive at linearised expressions of the Navier-Stokes equation [24]. These equations form the basis of simple flow modelling applications such as WAsP [36] (technically 'CFD' but to which the term is not usually applied).

The next step up in complexity (and computation requirements) is to introduce two-equation closure schemes which model horizontal, as well as vertical velocity gradients and incorporate the creation and dissipation of turbulent kinetic energy, $k$. Such models include $k-\epsilon$ [47], $k-\omega$ [48] and SST (shear-stress transport) [49], mentioned here in order of their date of development and relative sophistication. As a distinct alternative to RANS, Large Eddy Simulation (LES) is a much more computationally demanding but physically more realistic method, which involves simplifying the solution not so much by time-averaging but by filtering out the lower magnitude velocity fluctuations. Such simulations can be conducted at meso-scale as well as micro-scale.

### 2.9.2 Atmospheric Stability in CFD

Atmospheric stability effects can be integrated into CFD modelling, essentially by including those terms relating to the generation of turbulence from convection in unstable conditions and increased diffusion of turbulence in stable conditions in the Navier-Stokes momentum (80), turbulence (81) (82) and energy (83) equations [50]. These equations, showing the extra terms necessary for atmospheric stability modelling shaded yellow, are:

$$\frac{\partial}{\partial t}(\rho U_i) + \frac{\partial}{\partial x_k}(\rho U_k U_i) = \frac{\partial}{\partial x_i} p + \frac{\partial}{\partial x_j}\left[\mu_{eff}\left(\frac{\partial U_i}{\partial x_j} + \frac{\partial U_j}{\partial x_i}\right)\right] + g\beta\rho_{ref}(T - T_{ref})\delta_{i3} \qquad (80)$$

$$\frac{\partial}{\partial t}(\rho k) + \frac{\partial}{\partial x_j}(\rho U_j k) = \frac{\partial}{\partial x_j}\left[\left(\mu + \frac{\mu_T}{\sigma_k}\right)\frac{\partial k}{\partial x_j}\right] + P - \rho\epsilon - \frac{\mu_{eff}}{\sigma_H}\beta g\frac{\partial T}{\partial z} \qquad (81)$$

$$\frac{\partial}{\partial t}(\rho\epsilon) + \frac{\partial}{\partial x_j}(\rho U_j \epsilon) = \frac{\partial}{\partial x_j}\left[\left(\mu + \frac{\mu_T}{\sigma_\epsilon}\right)\frac{\partial \epsilon}{\partial x_j}\right] + C_{1\epsilon}\frac{\epsilon}{k}P - C_{2\epsilon}\rho\frac{\epsilon^2}{k} + C_{1\epsilon}\frac{\epsilon}{k}max\,(P_B, 0) \qquad (82)$$

$$\frac{\partial}{\partial t}(\rho H) + \frac{\partial}{\partial x_j}(\rho H U_j) = \frac{\partial}{\partial x_j}\left[\left(\frac{\lambda}{C_p} + \frac{\mu_T}{\sigma_H}\right)\frac{\partial H}{\partial x_j}\right] \qquad (83)$$

In order to express (83) in terms of potential temperature gradient, it is possible to make the substitution [50]:

$$dH = C_p d\theta \qquad (84)$$

$\theta$ is potential temperature, as defined earlier in section 2.2.3. A full explanation of the terms and adjustments to these equations is not given here but can be found in [50] (for ANSYS users) or [9] (for the general case).

# 3 Research Context

## 3.1 Literature Review

This section presents short critical reviews of key papers which form the landscape for this research. The summaries are grouped into three sections, based roughly on distinct technical disciplines with which they are primarily concerned: firstly, observations of the impacts of stability on measured wind flow and wind farm performance; secondly, the use of mesoscale modelling to define and categorise atmospheric stability and finally, the application of CFD to the problem of modelling the interaction of stability (whether modelled or measured) with complex terrain.

### 3.1.1 Impacts of Stability

In 2016, Mittelmeier et al [51] demonstrated a strong correlation between stability and wind farm array efficiency (i.e. wake effects) at Alpha Ventus offshore wind farm, in line with the conventional understanding that wind speed deficits downstream of turbines propagate further under stable conditions. The stability binning was based on a simple turbulence parameterisation (e.g. TI < 4% for stable conditions) taken from Dörenkämper [52]. The paper also describes a reasonably reliable substitute for mast-based TI measurements where only turbine SCADA measurements are available (i.e. standard deviation of power output divided by mean power output). The conclusions corroborated an earlier 2013 paper by Hansen [53].

In the same year, Holtslag et al [54] simulated lifetime fatigue loads on a theoretical 5MW turbine and compared three different methodologies for incorporating the effect of stability: a simple seven-category parametrisation, a computationally intensive thirty four-category parametrisation and the IEC standard approach [34] which neglects stability altogether.

For the first two methods, a generic frequency distribution of the stability parameter ($z/L$) was evaluated using the bulk-Richardson method in conjunction with sea and air temperature measurements from an offshore measurement site. Shear and TI were then estimated for multiple points along this distribution using the standard IEC approach with non-IEC stability corrections applied. The GH Bladed software [55] was then used to evaluate the lifetime fatigue loading for the simulated turbine in each stability state, also incorporating

wind speed as a third variable. Stability-induced variation in shear and TI was found to cause significant deviation between the three approaches.

The study concluded that the IEC approach was prone to over-estimating lifetime loads compared to the 34-category parametrisation due to the fact that a single high-shear, high-TI state is considered, which does not occur offshore with any significant frequency in reality. The intermediate seven-category parametrisation approach was found to under-estimate lifetime loads. However, this was due to the inadequacy of the stability bins used for the data set under consideration, rather than an indication that seven categories is necessarily too few. This backed up findings from 2007 by Sathe [21] where it had been shown that different wind speed profiles, as evaluated from estimations of Obukhov Length using the stability-adjusted log law, could result in significant differences in fatigue loadings.

Dörenkämper [56] demonstrated a link between wind turbine power performance in various atmospheric conditions, related to the impact of shear and TI on energy capture. Atmospheric conditions were defined based on measured shear and TI. The performance deviation between stable and unstable conditions was found to be up to 15-20%.

Wharton [57] compared wind shear and TI from SoDAR data against predictions evaluated from Obukhov Length and, at a wind farm of interest, found that neglecting stability would lead to an over-prediction of wind resource during unstable conditions and an under-prediction during stable conditions. For a different wind farm, Hansen [58] found the opposite trend: over-prediction in stable conditions and under-prediction in unstable conditions, showing the importance of taking into account site-specific considerations, such as turbine type and measurement configuration.

### 3.1.2 Mesoscale Modelling

Mesoscale models generally come into their own in two scenarios: when assessing geo-spatial trends over large areas (where attaining high accuracy at any one location is not of primary importance) and when correlating against short duration on-site measurements in order to exploit the typical long duration of mesoscale data.

In 2016, Clack et al [59] used data from the Rapid Update Cycle (RUC) mesoscale model to assess the impact of wind shear on wind resource assessment across the mainland United States. The data available covered the period 2006-14 with a 13km spatial resolution and hourly temporal resolution.

The wind energy resource was calculated at each grid point and time stamp using two methods: first, using only the hub-height wind speed then, by using wind speed from multiple heights in a more sophisticated approach whereby wind speed and wind direction at multiple heights are averaged to evaluate the rotor-equivalent wind speed (REWS). The discrepancy between these approaches was assessed spatially and temporally, revealing a diurnal variation of the order ±5% at one site in Texas which could be attributable to the influence of atmospheric stability on vertical wind speed gradient (shear) and wind direction gradient (veer).

### 3.1.3 CFD Modelling

CFD including atmospheric stability was first demonstrated twenty years ago by Montavon [60], using CFX4, a forerunner of ANSYS CFX, the CFD solver used in this project. The use of CFD for modelling stable conditions over a mountain range in Switzerland was validated.

Texier [61], in 2010, demonstrated an ability to accurately model non-neutral wind shear and turbulence intensity. Meteodyn CFD software was used to model wind conditions in the locality of two tall measurement masts in France, where stability was characterised by measured Richardson number.

More recently, Koblitz et al [62] at DTU performed some non-neutral wind flow simulations using a modified version of DTU's in-house CFD solver, Ellipsys3D. The modelled site was Benakanahalli Hill in India, at which highly sophisticated measurements (i.e. ultrasonic anemometers at multiple heights on five masts and measurements of soil temperature) had been made over a short two month period in 2010. The study used transient simulation, with time-varying CFD domain inlet conditions to simulate a typical diurnal cycle, where the inlet conditions are defined by on-site measurements of bulk Richardson Number at 10m AGL. An improved ability to model wind shear and veer at three mast locations was demonstrated, albeit for a much reduced subset of the data (the measured data was reduced down to three

days and comparison was only presented for two one hour periods: 1.00AM ('stable') and 12.00PM ('unstable')).

Hristov et al [63] at Vestas, working with the same modified CFD solver as above, described an improvement in energy yield prediction; validating wind flow modelling against an operational wind farm, rather than mast data. In this case, potential temperature at 10m and 80m distributions from WRF were used as a proxy to define stability in the CFD model. The stability distribution from the WRF model was indirectly validated against measurements from another site. CFD was run transiently (as above) for a nominal stability distribution and results were extracted from the simulation at regular time intervals throughout a diurnal cycle. Final results were then calculated by averaging across the simulation, weighting by the frequency of occurrence of each stability in the actual stability distribution (from WRF).

Also, in 2014, Montavon et al [64] used ANSYS CFX to simulate wind flow at site with complex terrain and forestry under various stability conditions, with stability defined as the potential temperature difference between the surface and the atmosphere above the surface layer (e.g. fixed potential temperature differentials of -2K, 0K, +2K etc). These simulations were compared against measurements from multiple masts and successfully validated some well understood concepts in terms of the dependency of shear and TI on stability.

An attempt was made to demonstrate improved wind speed ratio prediction, using a weighted average CFD approach, with the weighting informed by the distribution of Richardson Number from a WRF simulation. (The methodology for converting the $Ri$ distribution to potential temperature offset distribution was not explicit).

Desmond [17] [65] also used ANSYS CFX in a similar configuration to Montavon to model non-neutral flow at a site in France, focussing on the combined effects of stability and flow over the forest canopy. A statistical approach was developed to identify ranges of shear and TI parameters corresponding to stable and unstable conditions, making an assumption that flow can always be considered neutral at high wind speed as a filtering criterion. Stable and neutral CFD runs (using nominal potential temperature offsets) were then shown to give shear and TI predictions in the expected ranges – although unstable flow conditions could

not be similarly validated. This study also included a wind tunnel validation of the CFD model for stable and neutral flows.

In 2018, Alletto et al [66] at the turbine manufacturer, Enercon, used OpenFOAM to model non-neutral conditions and defined atmospheric stability as a potential temperature gradient profile at the inlet. The profiles were generated in a pre-simulation, whereby values of ground heat flux between -100 and 600 $W/\rho m^2$ were simulated and the resulting vertical potential temperature profiles extracted for use as inputs in the main simulations.

The relationship between the input heat flux values and the resulting potential temperature profiles in the pre-simulations was investigated and compared against Monin-Obukhov Similarity Theory (MOST) for various values of heat flux. CFD-simulated vertical wind speed gradient (shear) was found well to agree with MOST in the unstable and neutral cases. In the stable case, CFD was found to under-predict shear.

In terms of validation, a CFD simulation of Askervein Hill (South Uist, Scotland) was created and the resulting wind characteristics were compared against the measured flow field from a 1982-83 measurement campaign [67] (undertaken as part of International Energy Agency Task IV). This is an unexpected choice of validation data set in terms of:

- the length of the data set (approx.. 1 month covering Sep-Oct) and therefore the lack of seasonal balance
- the use of measured data from 35 years ago, since which time there has been much progress in terms of improving instrument accuracy and increased understanding of the importance of instrument installation techniques.
- the configuration of the measurements which, although pioneering for its time, included the use of mostly short (10m) measurement masts, as well as some hand-held anemometer readings and kite-based measurements.

The link between the CFD-simulated potential temperature gradient and the site-specific conditions during the measurement campaign, which would seem to be an obvious way to demonstrate the ability of the model to correctly model the effects of atmospheric stability, is not made clear.

The study also looked into the sensitivity to mesh resolution, concluding that 50m horizontal resolution is sufficient for accurately capturing attached flow. Increased resolution of 15m was found to be necessary for accurately modelling unattached flow, such as re-circulation in the lee of a hill.

Chang et al (2018) [68], using ANSYS Fluent, similarly used 1D pre-simulations (based on discrete values of Obukhov Length, $L$) to generate vertical profiles of potential temperature and then deployed these in primary simulations of flow over obstacles. Again, the authors demonstrated good qualitative agreement between the simulated vertical wind speed profiles and those expected from MOST for corresponding values of $L$.

The study further demonstrated an ability of the model to capture interesting stability-induced flow patterns downwind of a simulated cosine-shaped hill, such as gravity waves under slightly stable conditions ($L$=1000m).

Finally, the authors undertook a comparison against data from a 2017 measurement campaign, using a 200m mast in Germany. Mesoscale data from WRF was used to identify short (30 – 90 min) periods within the measured data corresponding to values of $L$ for which CFD simulations had been carried out. The simulated vertical wind speed profiles were found to compare well with measurements during the unstable and neutral periods but failed to capture the magnitude of wind shear during a strong stable period.

Temel et al (2018) [69] also conducted CFD (OpenFOAM) simulations of unstable, neutral and stable wind flow over the mainland USA. Stability was evaluated by running WRF, initiated using North American Reanalysis data. Two WRF simulations were run, incorporating different turbulence closure schemes ('YSU' and 'MYJ'). The resulting vertical potential temperature profiles (as well as humidity, wind speed and wind direction) were validated against weather balloon measurements for a site of interest and found to compare very well throughout a 15km vertical section (i.e. covering the entire troposphere) for both turbulence closure schemes.

Transient CFD simulations were then run, using the WRF data as inputs – specifically, stability effects were incorporated as time-varying surface temperature and heat flux. Simulations of 7-8 hour periods (covering four different stability categories) were produced and compared

to concurrent measurements of temperature (at 1.5m AGL), wind speed and wind direction (at 10m AGL). That the wind speed validation was conducted at 10m AGL is indicative of the fact that this research was not carried out with wind energy assessment in mind.

The results showed an ability of the model to capture general trends throughout the modelled periods. However, significant biases were observed in terms of wind speed predictions for both the daytime (unstable) and night-time (stable) cases.

## 3.2 Knowledge Gap

The previous section went some way to quantifying the impact of including atmospheric stability in wind flow modelling.

There is substantial precedent for measuring atmospheric stability and modelling its impact on wind flow and wind farms. It has been established that both measured and modelled heat flux and temperature gradient, as indicators of atmospheric stability, can be incorporated into CFD flow solvers, including ANSYS CFX and others.

However, in terms of the applicability to wind energy resource assessment, some key traits of the research conducted to date are:

- The link between the definition of atmospheric stability in a CFD model and the site-specific conditions is often indirect (e.g. [59], [62]) or non-existent (e.g. [66]).
- Validation of flow characteristics is often undertaken over an insufficiently long period (e.g. [62], [66], [69]) or only at a small number of locations (e.g. all of above). Validation over the course of at least one year at multiple locations is necessary to establish confidence for wind energy modelling.
- Validation is undertaken in terms of vertical profiles of wind speed and turbulence alone (e.g. [66], [68], [65]). Wind shear and TI validations are good accuracy indicators for CFD modelling, and of some importance to wind energy modelling in of themselves (as demonstrated by [54], [57],[58]).

However, it is also critical to validate the flow over complex terrain by validating against the wind speed ratio between multiple concurrent measurements on the same site.

- Validation is undertaken in terms of comparing simulated energy yield against measured (e.g. [63]). While this creates a link between stability and energy output, which is objectively attractive, it also introduces a lot of uncertainty due to the various other factors that can affect measured energy yield.

In addressing these limitations, this PhD will therefore make a novel contribution to the field.

Of key importance is deciding on how atmospheric stability will be defined. This research will focus on virtual potential temperature differential as a proxy for stability, with the relationship between the two well defined by MOST (see 2.4.3). This is in-keeping with much research conducted to date, where virtual potential temperature differential is either defined directly (e.g. [63], [70]) or profiles are generated in CFD pre-simulations, based on defined heat flux (e.g. [66], [68]).

## 3.3 Research Objectives

It is important to re-iterate that this research is being conducted as a joint academic/industry project and the needs of the industry partner, SSE Renewables, are central to defining the main objective: an ***efficient***, ***reliable*** and ***straight-forward*** methodology for incorporating the effects of atmospheric stability into wind flow modelling practice, which will form part of an improved process for evaluating long-term average wind farm energy yield. The intention is that this objective will be equally valuable to other, similar and smaller-scale, wind energy developers.

In order to be ***efficient***, this methodology should minimise the cost and maximise the ease of acquiring the necessary input data. The cost of using commercially available Vortex WRF data is essentially negligible compared to acquiring on-site measured temperature gradient and/or heat flux data – particularly considering that WRF data sets of up to 20 years length can be easily accessed. So, a major objective is to show whether or not Vortex WRF data are a suitable substitute for on-site measured data.

The methodology should also optimise the use of computational resource, in order that modelling the effects of atmospheric stability is not cost-prohibitive. It is therefore an objective to demonstrate whether CFD run-time can be reduced to a manageable level without compromising on flow modelling accuracy.

In order to be ***reliable***, the methodology should be validated using measured data from a large enough number of sites for the conclusions to considered widely applicable. Those sites should be representative of the kinds of sites to which the method will be applied, i.e. UK/Ireland onshore and offshore rather than elsewhere in the world, where stability regimes may be completely different. The input data sets should be site-specific and span multiple years, in order to eliminate the effects of seasonal variation. Also, the validation approach should be repeatable using a cost-effective instrument configuration, so that the validation data set can be extended to additional sites in future, as necessary.

In order to be ***straight-forward*** and easily-implementable, the methodology should use commercially-available software without requiring any complex adjustments. ANSYS CFX with the Windmodeller bolt-on, which is already routinely used in SSE, has the ability to model atmospheric stability effects by defining a virtual potential temperature differential between the ground and the top of the surface layer. Virtual potential temperature differential is a proxy for atmospheric stability, rather than a categorical stability parameter, such as Obukhov Length or Richardson Number. An objective is therefore to assess whether the use of virtual potential temperature differential as a proxy for stability results in the expected wind flow characteristics and flow modelling accuracy improvement.

In meeting these objectives, this research will address the key research questions posed in section 1.2:

- To what extent is atmospheric stability a significant factor on the incident wind speed distribution?
- Are site-specific measurements required and, if so, where is the optimal balance between accuracy and cost?
- What opportunities and risks does atmospheric stability present, in terms of wind farm design, appraisal and operation?

# 4 Mesoscale Analysis

## 4.1 Introduction

Mesoscale modelling, and the WRF model in particular, were briefly introduced in section 2.8. This chapter details the application of mesoscale modelling to the task of defining long-term atmospheric stability conditions, using virtual potential temperature gradient as a proxy, at various onshore and offshore sites in the UK/Ireland and overseas.

Two sources of processed WRF output data sets have been considered, both of which are introduced in more detail below.

### 4.1.1 Vortex

Vortex is a Barcelona-based commercial provider of processed WRF data, established in 2005 and aimed primarily at the wind development market. The draw for wind developers is easy access to reliable WRF data through an online interface without the requirement for in-house computational resource and technical knowledge to run the WRF model.

Vortex offers off-the-shelf data sets up to 20 years in length (longer data sets can be acquired by updating existing runs). The inputs to the WRF model can also be stipulated (e.g. MERRA, MERRA-2, CFSR and, recently, ERA-5). Time series data have a spatial resolution of 3km x 3km which is tied to the spatial resolution in the WRF model (although Vortex also offer a 'MAST' product which uses additional interpolation to produce wind distributions - not time series - at 1 x 1km resolution).

The data set used in this research comprises time series for 36 discrete modelling locations of up to 24 years in lengths, spanning the period 1994 to 2018. The parameters available are wind speed, wind direction, pressure, absolute temperature, relative humidity, Richardson Number, Obukhov Length, solar irradiance, sensible and latent heat flux. In most cases these are derived from the raw WRF outputs using post-processing algorithms. Table 4.1 resents a summary of key information relating to the Vortex data set and Table 4.2 shows the available meteorological outputs.

| ***Parameter*** | ***Vortex*** | ***UoE*** |
|---|---|---|
| ***Date Range*** | Approx. 1994 – 2018<br>(site-specific) | 01/01/2000 – 31/12/2010 |
| ***Time Resolution*** | Hourly | Hourly |
| ***Spatial Extent*** | 36 x discrete locations | 3km resolution grid covering the UK and Ireland |
| ***WRF Version*** | 3 | 2.2 |
| ***Run Date*** | 2016-18 | 2010 |
| ***Input Data*** | CFSR | NCEP GFS |
| ***Height AGL*** | 10 to 100m (10m resolution)<br>120 to 200 (20m res)<br>250 to 500 (50m res)<br>600 to 2000m (100m res)<br>2500 to 5000m (500m res) | 10m, 50m, 100m,<br>200m, 1000m. |
| ***Size*** | 30 GB | 3200 GB |

*Table 4.1: Specifications of both WRF data sets used.*

| *Parameter* | *Vortex* | *UoE* |
|---|---|---|
| *Brunt Väisälä Frequency* | | *x* |
| *Terrain Height* | | *x* |
| *Landmask (land/water)* | | *x* |
| *Pressure* | *x* | *x* |
| *PBL Height* | | *x* |
| *Water Vapor Mixing Ratio (q)* | | *x* |
| *Relative Humidity* | *x* | |
| *Inverse Obukhov Length (1/L)* | *x* | *x* |
| *Richardson Number* | *x* | |
| *Potential Temperature* | | *x* |
| *Absolute Temperature* | *x* | |
| *Turbulent Kinetic Energy (TKE)* | | *x* |
| *Surface Skin Temperature* | | *x* |
| *Wind Speed (x-direction) (U)* | | *x* |
| *Wind Speed (y-direction) (V)* | | *x* |
| *Horizontal Wind Speed (UV)* | *x* | |
| *Wind Direction* | *x* | |
| *Wind Speed (z-direction) (W)* | | *x* |
| *Friction Velocity (U*)* | | *x* |
| *Background Roughness Length ($z_0$)* | | *x* |
| *Sensible Heat Flux ($Q_E$)* | *x* | *x* |
| *Latent Heat Flux ($Q_H$)* | *x* | *x* |
| *Solar Irradiance (S)* | *x* | *x* |

*Table 4.2: Meteorological parameters available in both UoE and Vortex data sets.*

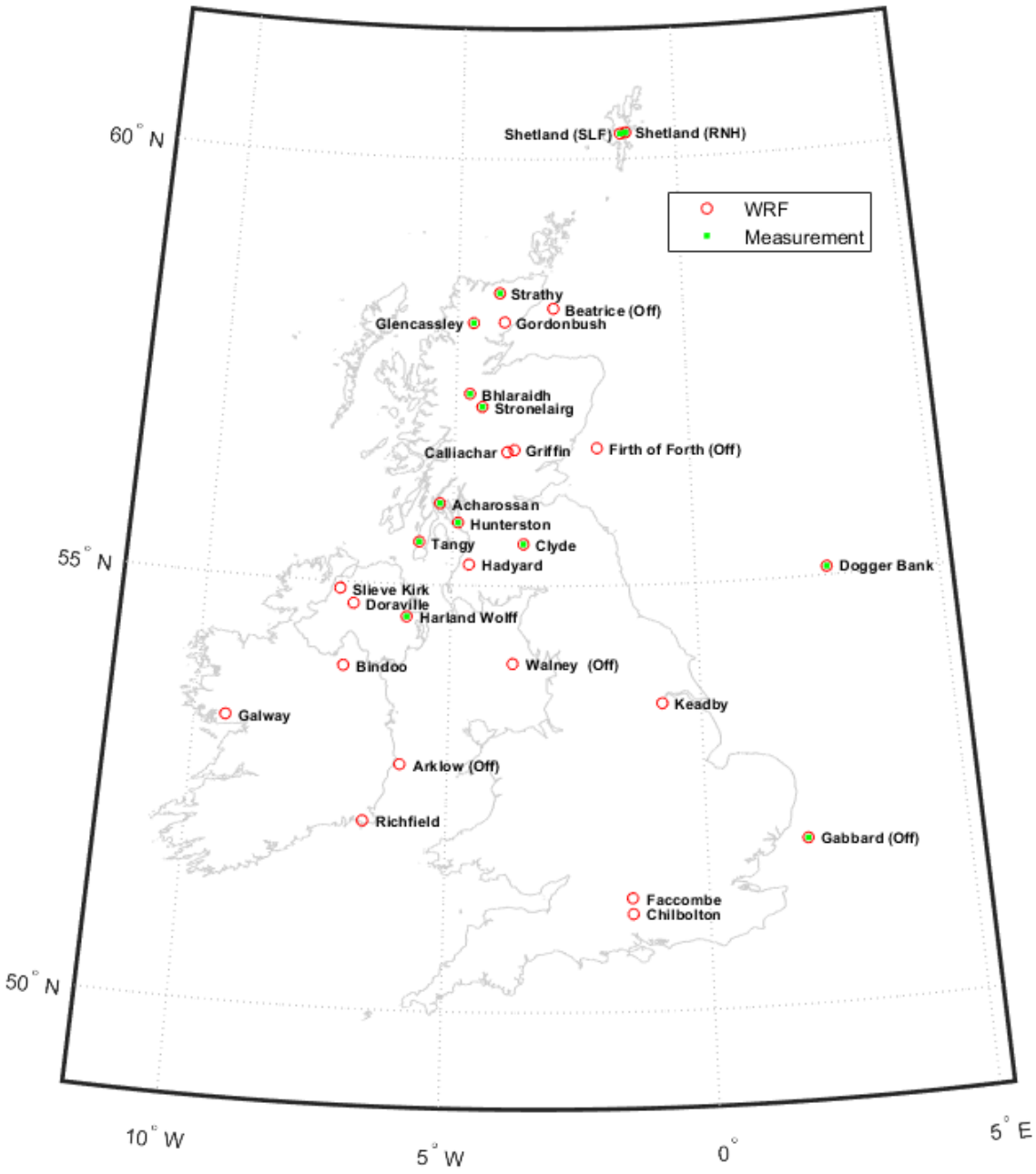


*Figure 4.1: Vortex WRF modelling locations in UK and RoI (red circles) used in this research. Also showing locations of mast-based virtual potential temperature measurements (green dots).*

Figure 4.1 shows the locations of Vortex WRF modelling locations and SSE measurement locations, which are used for validation (see Chapter 5). In addition, seven non-UK/RoI sites were modelled in Vortex in order to set the UK/RoI results in a global context.

### 4.1.2 University of Edinburgh (UoE)

The second source of WRF data – made available by the University of Edinburgh (UoE) – is the result of a 2012 PhD project undertaken by Sam Hawkins [41]. The resultant data set comprises time series data for every point on a 3km resolution grid covering much of the UK and Ireland for the period 01/01/2000 – 31/12/2010.

The model used three nested domains that progressively increase the spatial resolution from 27km to 3km, with the highest resolution domain centred over the UK. A Lambert conformal conic projection was used to give model cells of approximately equal area. The number of vertical levels was set at 28, with the default spacing varied to position more levels close to the surface to improve predictions of the near-ground wind profile and limit errors interpolating from model to physical height.

WRF employs a terrain-following height level system which varies with atmospheric conditions. Hawkins found this to vary little in the lowest levels of the atmosphere, with minor effects only visible above 200m AGL. These are sufficiently stable at typical turbine hub heights to be treated robustly as ‘metre’ height AGL levels.

The boundary conditions (input data) for this work were taken from the NCEP Final Analysis (FNL) dataset. These are archived 6-hourly operational analyses from the NCEP Global Forecast System (GFS), similar to the NCEP reanalysis [11] but at higher resolution, with more recent model configurations and greater use of assimilated data. The GFS assimilates data from a range of validated sources including weather stations, offshore buoys and other sources; some of which are used in validating the model output. The WRF output was captured at an hourly resolution.

Many more output parameters have been retained from the ‘raw’ WRF outputs than in the case of the Vortex data, all of which are available at five heights: 10, 50, 100, 200 and 1000m AGL. This results in an unwieldy 3.2TB data set, made up of zipped files in NETCDF format,

each containing one day of data. Table 4.1 and Table 4.2 summarise the UoE data set alongside the Vortex data set, to allow for comparison between the two.

### 4.1.3 Summary

Both data sets have been used because they offer different research perspectives: Vortex data is concurrent with measured data, allowing for validation against real temperature differential measurements. UoE data has the coverage necessary to analyse spatial trends across a very large area but cannot be directly validated against measurements available to SSE as it extends only until 2010, before measurements began.

In the remainder of this chapter, first the Vortex time series data sets are investigated to show the link between heat flux and temperature differential. Then the same data sets are used to evaluate site level distributions of temperature differential binned by wind direction, wind speed, time of day and month of year. Finally, the UoE data is processed in a similar way to reveal variation in mean stability conditions across the UK and Ireland.

## 4.2 Data Processing

### 4.2.1 Vortex Data Processing

The quantity of interest is $\Delta\theta_v$, the virtual potential temperature differential, which is calculated between 10m and 100m AGL ($\theta_v$(10m) - $\theta_v$(100m). The reasons for adopting this proxy parameter to characterise atmospheric stability are discussed in more detail later. Essentially, this is a quantity that can be directly validated and incorporated into CFD modelling easily.

To recap on the physics summarised in Chapter 2, a virtual potential temperature differential of $\Delta\theta_v < 0$ corresponds to $\frac{d\theta}{dz} > 0$: an *increase* in virtual potential temperature between 10m and 100m (stable atmosphere). A virtual potential temperature differential of $\Delta\theta_v > 0$ corresponds to $\frac{d\theta}{dz} < 0$: a *decrease* in virtual potential temperature between 10m and 100m (unstable atmosphere).

Vortex time series data sets (.txt files) were imported into MATLAB. For each hourly record, first the absolute temperature was calculated from the temperature in degrees Celcius at both 10m and 100m AGL:

$$T(K) = T(°C) - 273.5 \qquad (85)$$

Next, the potential temperature is calculated at both heights as per the method set out in section 2.2.3:

$$\theta = T\left(\frac{p}{p_0}\right)^{\kappa} \qquad (20)$$

Using the modelled pressure, $p$, from the Vortex data and $p_0$=1000 hPa, potential temperature is converted to virtual potential temperature, according to the formula derived in section 2.2.5:

$$\theta_v = \theta \cdot \left[1 + \frac{RH \cdot p_{sat}}{p} \cdot (1 - \varepsilon)\right] \quad (31)$$

This time, also using the Vortex-modelled relative humidity, $RH$, and temperature, $T$, to calculate the saturation vapour pressure, $p_{sat}$. Finally, the difference between this value at 10m and 100m is calculated:

$$\Delta\theta_v = \theta_{v\,10m} - \theta_{v\,100m} \quad (86)$$

This results in time series data sets of virtual potential temperature difference at each site which are used in this chapter for assessing a range of statistical characteristics for atmospheric conditions. In Chapter 5 these are used for comparison against measured data and then in Chapter 6 they are used as an input to CFD modelling.

### 4.2.2 UoE Data Processing

The UoE data set required a more computationally intense process, due to the size of the master data set. Again, MATLAB was used to import the raw data: each of the 4018 daily NETCDF files was unzipped and a third-party suite of scripts (nctoolbox-1.1.0) was used to query the data. 24 hourly values of potential temperature at 10m and 100m were extracted from each daily file, resulting in 96,408 hourly records in total at each of 128,700 locations (390 x 330 grid).

The virtual potential temperature differential was calculated according to the method set out in section 4.2.1. Spatial grids of $\Delta\theta$ values were aggregated by stepping through the time series and building up gradually, re-calculating the weighted average at each time step. This step-by-step approach was necessary as constructing an 11-year time series for each of the 128,700 locations would be computationally impractical.

The resulting spatial grids including mean, standard deviation, daily range and annual range of $\Delta\theta$ are presented in section 4.6.

## 4.3 Heat Flux and Temperature Differential

This section presents a series of sense-checks on the quality of the Vortex data sets, taking three sites (two onshore and one offshore) as test cases.

Section 2.2.7 introduced the concepts of solar irradiance ($\mathrm{K}\downarrow$), sensible heat flux ($Q_H$) and latent heat flux ($Q_E$). The Vortex WRF data time series for three sites (Glencassley, Hadyard Hill and Greater Gabbard), spanning multiple years, were processed into an average Summer day (Apr - Sep) and an average Winter day (Oct – Mar). The flux quantities above were plotted, alongside three alternative measures of temperature differential: absolute temperature differential, potential temperature differential and virtual potential temperature differential ($\Delta\theta_v$), all defined as the difference between 10m and 100m AGL. The last of these three is the proxy used in the bulk of this research to characterise atmospheric stability. These are plotted in Figure 4.2.

Temperature differential ($\Delta T$), potential temperature differential ($\Delta\theta$) and virtual potential differential ($\Delta\theta_v$) exhibit similar daily trends. At the onshore sites (Glencassley and Hadyard Hill), $\Delta T$, $\Delta\theta$ and $\Delta\theta_v$ share a maximum around noon and a minimum just before dawn.

Comparing flux plots against temperature differentials, some traits can be extracted from these profiles which tie in well with the description of surface heat processes outlined in section 2.2.7. In general, peaks in solar irradiance can be seen to align with peaks in $\Delta\theta_v$ (although there is a slight mis-alignment which can be attributed to the time lag between maximum irradiance and the reaction of the surface in terms of reaching maximum temperature). This is in line with expectations: around the time of peak irradiance, the surface is heated to maximum and the differential between the heated lower atmosphere and un-heated upper atmosphere is greatest. This differential drives an unstable atmosphere.

Just before dawn, irradiance is zero and the ground is fully cooled. At the onshore sites, there is a slight downward (into the surface) sensible heat flux: the lower atmosphere is cooling by conduction to the colder surface, leading to a negative temperature differential (stable atmosphere).

The variation in latitude between the sites is reflected in the peak value of $-K\downarrow$ with more intense solar irradiance further south. For the heat budget to balance, this results in increased sensible and latent heat fluxes and increased temperature differential.

$-\mathrm{K}\downarrow$ is much lower in winter as a result of much less direct solar irradiance during the winter months. Accordingly, sensible and latent heat fluxes are lower and temperature differential is less.

Glencassley and Hadyard Hill are onshore whereas Greater Gabbard is offshore, revealing the significant differences in the thermodynamic processes at these two types of site. Greater Gabbard has a constant upward latent heat flux in both summer and winter, e.g. due to evaporation. There is no appreciable sensible heat flux in summer but a small sensible heat flux in winter – particularly at night, potentially driven by cold air and relatively warm sea on winter nights.

To summarise: overall, the Vortex data displays trends that are in line with the established understanding of daily and seasonal stability variation on- and offshore in summer and winter [9] [19], serving as a sense-check of both the unprocessed Vortex data and the calculation of $\Delta\theta_v$ undertaken as part of this research.

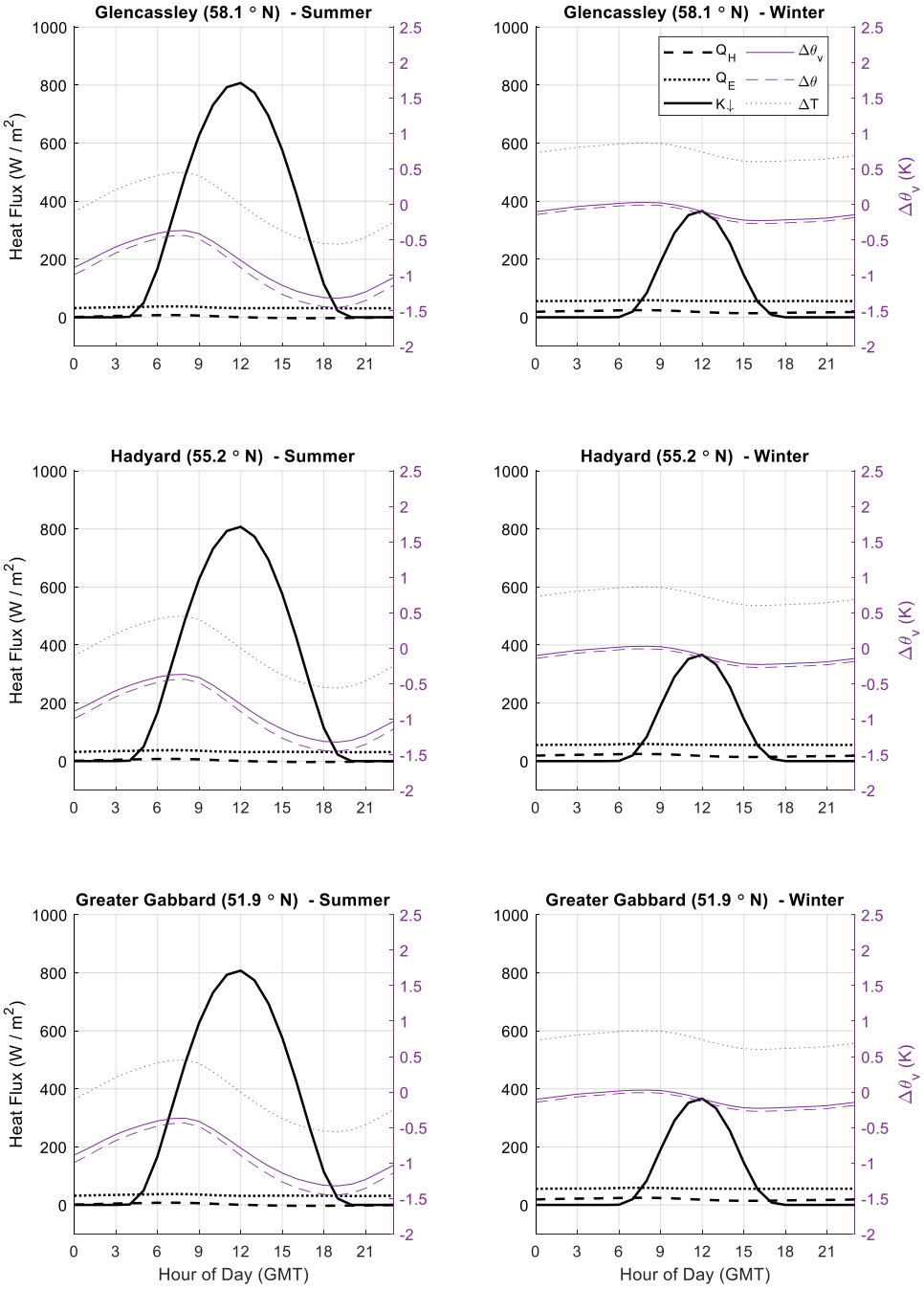


*Figure 4.2: Summer (left) and winter (right) daily average profiles for three sites: solar irradiance ($-\boldsymbol{K}\downarrow$), sensible heat flux ($\boldsymbol{Q_H}$) and latent heat flux ($\boldsymbol{Q_E}$), absolute temperature differential ($\Delta T$), potential temperature ($\Delta\theta$) and virtual potential temperature differential ($\Delta\theta_v$).*

## 4.4 Analysis of temperature and wind speed profiles

This section presents a brief investigation into the average vertical profile of $\theta_v$ over the course of a diurnal cycle according to Vortex data. Figure 4.3 shows average vertical profiles of virtual potential temperature $\theta_v$, where the value plotted is the difference from the value at 10m (i.e. bulk temperature change effects are disregarded). These plots are based on Vortex WRF data for Keadby – a site in the East Midlands with a relatively high degree of variation in stability conditions.

A strong diurnal trend in virtual potential temperature gradient is evident from these plots. Looking at the difference between 10m (lowest height) and 100m (marked with dotted line), the variation can be seen to agree with the first two sets of plots for the onshore sites in Figure 4.2: a positive (unstable atmosphere) and increasing virtual potential temperature differential from late morning onwards, reaching a maximum in late afternoon and then becoming increasingly negative (stable atmosphere) in the evening, reaching a minimum some time before dawn.

The reason for presenting these additional plots (Figure 4.3) is to give insight into the actual shape of the atmospheric profile, beyond a simple monotonic characteristic (i.e. the virtual potential temperature differential between one height and another). If this set of atmospheric profiles were to be characterised in such a monotonic way, different choices of model heights would give significantly different characterisations.

For example, to describe the stability of the lower atmosphere using the virtual potential temperature difference between 10m and 1000m would result in a virtual potential temperature differential ($\Delta\theta_v$) in the range $\Delta\theta_v = -2K$ to $\Delta\theta_v = -7K$. From a quick visual check, it can be seen that this characterisation would be inadequate for describing the variation in $\theta_v$ closer to the surface (i.e. up to 200m) and therefore insufficient for the task of modelling near-surface wind flow. It is on this basis that $\Delta\theta_v$ between 10m and 100m has been selected as a proxy for surface-layer atmospheric stability in this research.

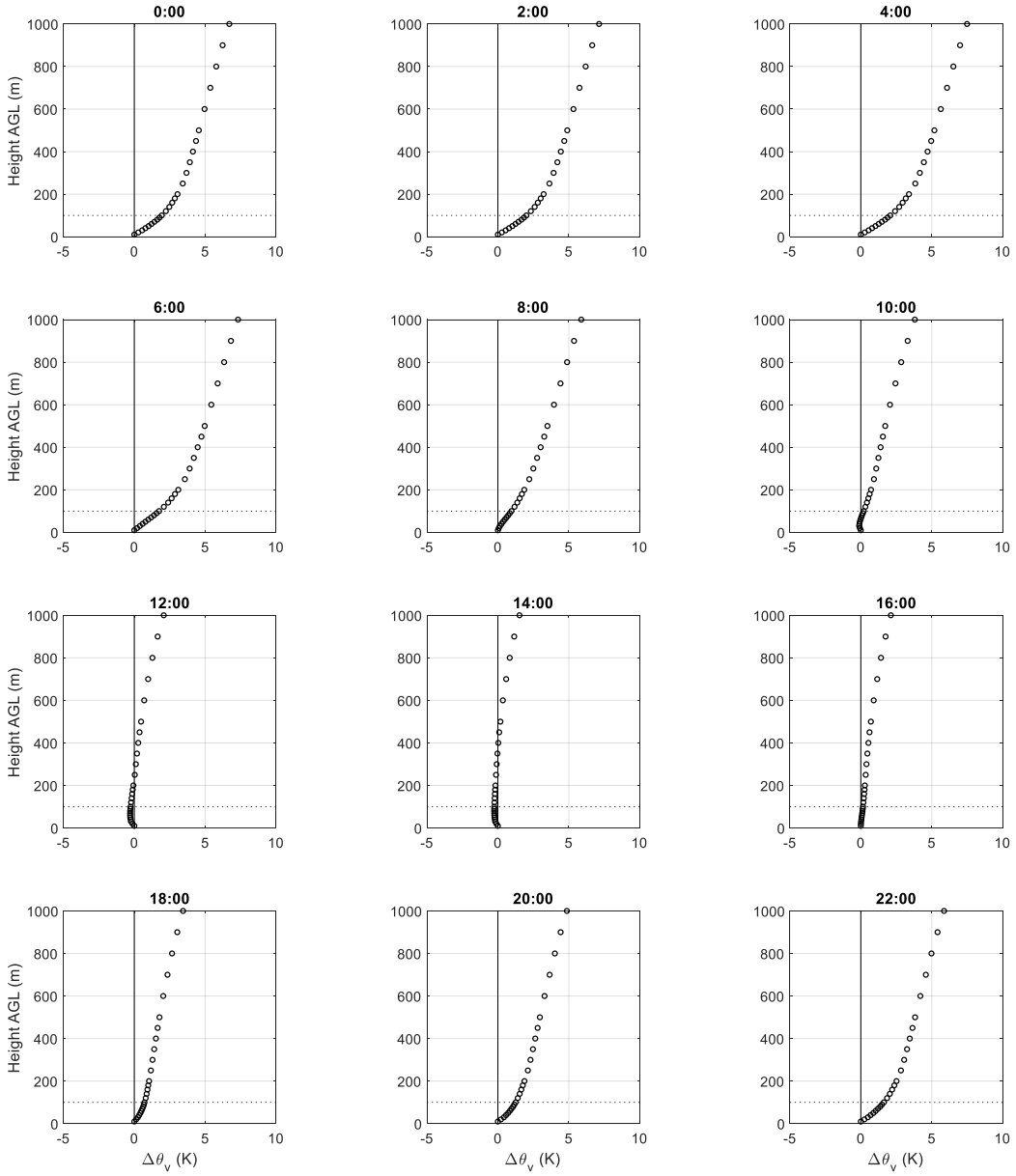


*Figure 4.3: Hourly-average $\theta_v$ profiles, relative to $\theta_v$ at 10m AGL from Vortex WRF data for Keadby in two-hour time steps. 100m AGL marked with dotted line.*

It can be observed that the $\theta_v$ gradient is approximately linear and less variable throughout the day above about 100 to 200m AGL. This indicates the boundary between the surface layer (lowest ~10% of the ABL, which reacts on the scale of minutes to hours to changes in surface heat flux) and the upper ABL which reacts more gradually.

Figure 4.4 gives an alternative visualisation of the same data set, where two ten-day samples of hourly Vortex WRF data (one from February and one from August) have been used to produce time series heat maps of $\Delta\theta_v$ relative to $\theta_v$ at 10m AGL. The blue bands are indicative of slightly unstable/near-neutral conditions in the mid-afternoon. The green-yellow bands indicate stable conditions (increasing $\theta_v$) during the night. In summer, the unstable bands are broader (longer duration of solar irradiation) and the pattern is generally better defined (more intense surface heating/cooling effects). These plots demonstrate that Vortex WRF is capturing inter-seasonal and inter-day variation in atmospheric stability.

Figure 4.5 is a vertically extended plot which is otherwise similar to Figure 4.3. Another inflection point can be observed at around 1000m, above which the tropospheric $\theta_v$ gradient becomes roughly linear and again unchanging from hour to hour. In this case, this is indicative of this being the height of the atmospheric boundary layer.

The magenta line shows a $\theta_v$ gradient of -3.3K per km, which corresponds to the ISO Standard Atmosphere and which we might expect to match the data in the region above the ABL. In fact, the troposphere above the ABL at this site (Keadby) is closer to -3.5K per km, which suggests that this site deviates slightly from the ISO standard, possible because of its relatively high latitude compared to the ISO baseline ('mid-latitudes'). The data does not extend to the tropopause (boundary between troposphere and stratosphere) which is at approximately 10,000m AGL.

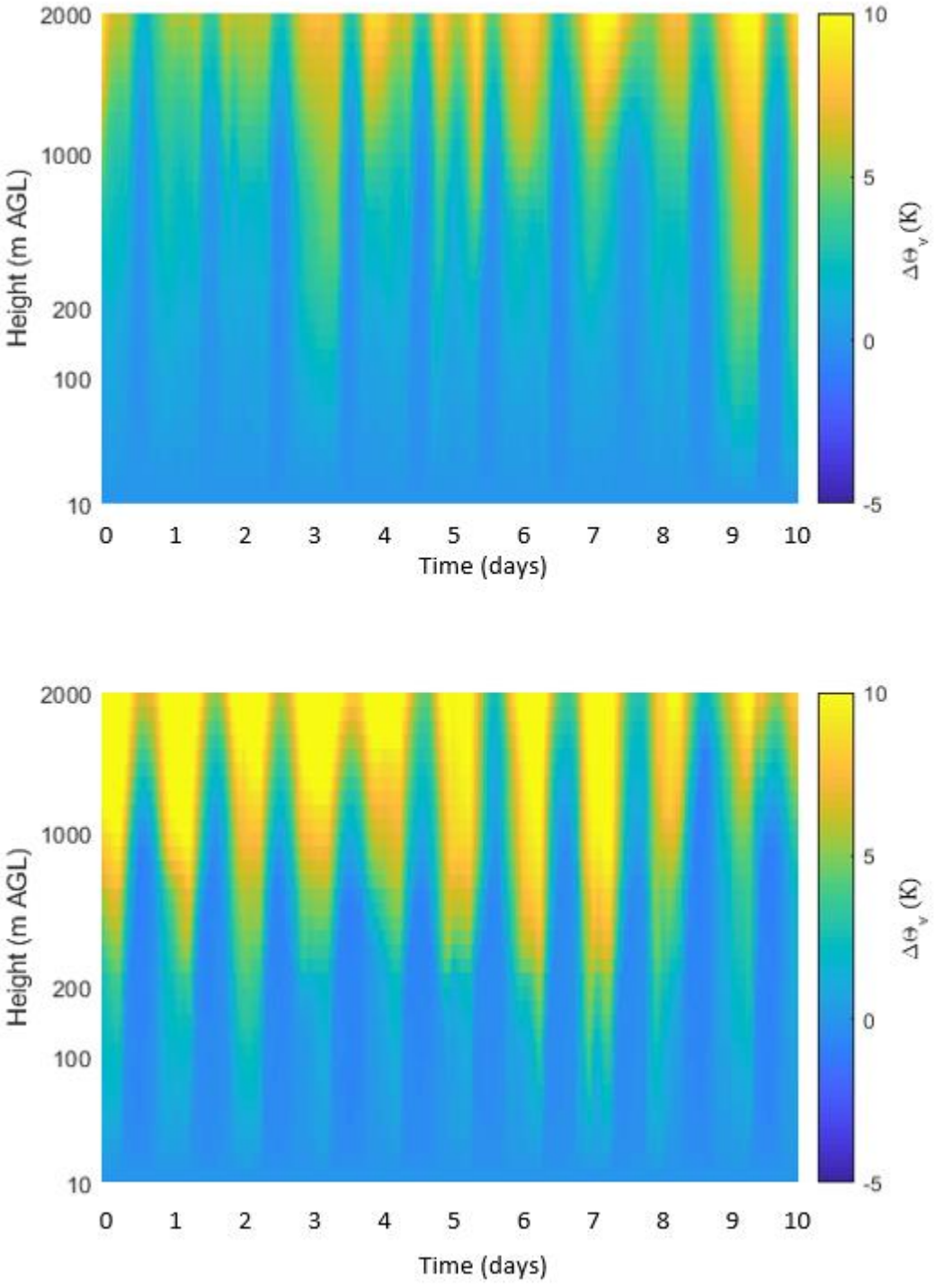


*Figure 4.4: Heat maps showing the diurnal development of stable and unstable atmospheric profiles over two ten-day periods in February (top) and August (bottom) at Keadby, using Vortex WRF data. Note the non-linear y-axis.*

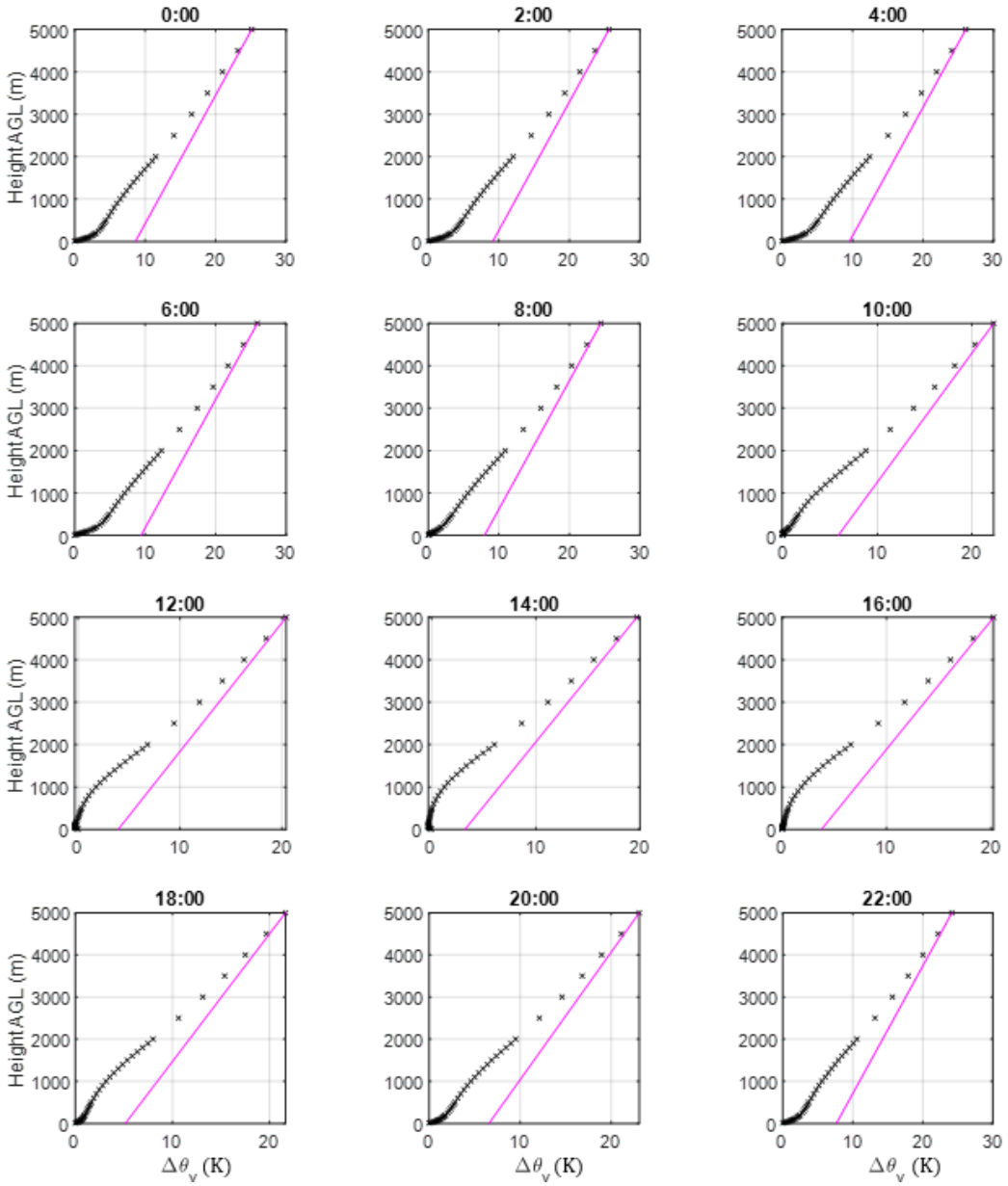


*Figure 4.5: Hourly-average $\theta_v$ (black) profiles, relative to $\theta_v$ at 10m AGL from Vortex WRF data for Keadby in two-hour time steps. Magenta line shows ISO standard atmosphere (3.3K per 1000m), (straight line, fixed to the data at 5000m).*

## 4.5 Analysis of Vortex Virtual Potential Temperature Time Series

In this section, atmospheric stability distributions based on proxy virtual potential temperature ($\Delta\theta_v$) values calculated from WRF data are assessed. Table 4.3 summarises various metrics calculated for each Vortex time series of $\Delta\theta_v$ which were calculated as follows:

- ***Mean*** Straight mean of all records in the time series.
- ***Standard Deviation*** Standard deviation of all records in the time series.
- ***P10*** $\Delta\theta_v$ with 10% chance of exceedance (i.e. threshold of 10% most unstable records)
- ***P90*** $\Delta\theta_v$ with 90% chance of exceedance (i.e. threshold of 10% most stable records)
- ***Annual Range*** Difference in monthly average $\Delta\theta_v$ between most unstable and most stable months (+ve when summer (Apr - Sep) is more unstable; -ve when winter (Oct - Mar) is more unstable)
- ***Daily Range*** Difference in $\Delta\theta_v$ between most unstable and most stable hours of the day (+ve when daytime (4am – 4pm) is more unstable; -ve when nighttime (4pm – 4am) is more unstable)

In Table 4.3, site names with measurement masts are in **bold.** Daily and annual range statistics are omitted for 'Global' sites as these are not directly comparable with near-UK/RoI sites due to time difference and/or seasonal inversion.

These statistical metrics provide an initial indication as to which sites might require particular attention in terms of atmospheric stability treatment (i.e. those with a large deviation of the mean from neutral or large standard deviation). It is often assumed by convention in wind flow modelling that $\Delta\theta_v$ = 0 (neutral) can be taken as a reliable average condition. The data show that mean $\Delta\theta_v$ deviates significantly from zero at numerous sites (e.g. Keadby, Chilbolton and most 'global' sites which have comparatively extreme stability climates).

Also, stability varies at some sites more than others, as demonstrated by looking at the standard deviation of each time series. A hypothetical site with $\Delta\theta_v$ = 0 but exhibiting great variation in $\Delta\theta_v$ would also pose a risk, in terms of applying the 'neutral assumption', as it is

not certain that the physical effects corresponding to $\Delta\theta_v > 0$ (unstable) and $\Delta\theta_v < 0$ (stable) are approximately equal and opposite.

Breaking this down further, the daily and annual components of stability variation can be isolated. The daily range (mean $\Delta\theta_v$ for the most unstable daytime hour minus mean $\Delta\theta_v$ for the most stable night-time hour) reveals the sites which are most diurnally driven (e.g. onshore sites). The annual range (mean $\Delta\theta_v$ for the most unstable summer month minus mean $\Delta\theta_v$ for the most stable winter month) shows that offshore sites are much more seasonally driven. This ties in with the description of land and sea thermodynamics presented in 2.2: the large thermal capacity of the ocean means that surface-atmosphere interactions only take place on the seasonal time scale. On land, which has a much lower thermal capacity and therefore greater tendency to heat up the atmosphere by conduction, the atmosphere responds quickly to diurnal variation in solar heating, on the sub-hour timescale.

| Type | Site | Mean (K) | P10 (K) | P90 (K) | Std. Dev. (K) | Daily Range (K) | Annual Range (K) |
|---|---|---|---|---|---|---|---|
| Onshore | ***Bhlaraidh*** | -0.1 | 0.8 | -0.9 | 0.7 | 1.1 | 0.7 |
| | ***Stronelairg*** | -0.2 | 0.8 | -1.3 | 0.9 | 1.3 | 0.9 |
| | ***Shetland (RNH)*** | -0.2 | 0.7 | -1.2 | 0.7 | 1.1 | 0.7 |
| | ***Glencassley*** | -0.3 | 0.7 | -1.5 | 0.8 | 1.3 | 1.0 |
| | Calliachar | -0.4 | 0.8 | -1.7 | 0.9 | 1.5 | 0.9 |
| | ***Acharossan*** | -0.4 | 0.7 | -1.5 | 0.8 | 1.5 | 0.9 |
| | Griffin | -0.4 | 0.8 | -1.6 | 0.9 | 1.5 | 1.0 |
| | ***Tangy*** | -0.4 | 0.7 | -1.6 | 0.9 | 1.4 | 0.7 |
| | ***Clyde*** | -0.4 | 0.8 | -1.8 | 1.0 | 1.6 | 1.1 |
| | ***Shetland (SLF)*** | -0.5 | 0.8 | -1.9 | 1.0 | 1.5 | 1.1 |
| | Galway | -0.5 | 0.8 | -2.0 | 1.1 | 1.8 | 1.1 |
| | Doraville | -0.6 | 0.8 | -2.1 | 1.1 | 1.8 | 1.1 |
| | ***Strathy*** | -0.6 | 0.7 | -2.1 | 1.1 | 1.6 | 1.2 |
| | Gordonbush | -0.6 | 0.7 | -1.8 | 1.0 | 1.6 | 1.1 |
| | Hadyard | -0.6 | 0.7 | -2.2 | 1.1 | 2.0 | 1.1 |
| | Richfield | -0.7 | 0.6 | -2.3 | 1.2 | 1.8 | 0.9 |
| | Slieve Kirk | -0.7 | 0.7 | -2.4 | 1.2 | 2.0 | 1.2 |
| | Bindoo | -0.8 | 0.7 | -2.7 | 1.3 | 2.1 | 1.3 |
| | Faccombe | -0.8 | 0.7 | -2.8 | 1.3 | 2.3 | 1.3 |
| | Chilbolton | -0.9 | 0.6 | -3.0 | 1.4 | 2.4 | 1.4 |
| | Keadby | -1.0 | 0.6 | -3.1 | 1.4 | 2.4 | 1.5 |
| Coastal | Harland Wolff | -0.3 | 0.8 | -1.7 | 0.9 | 1.7 | 0.9 |
| | ***Hunterston*** | -0.4 | 0.3 | -1.3 | 0.7 | 0.4 | -0.3 |
| Offshore | ***Dogger Bank*** | -0.2 | 0.4 | -1.1 | 0.7 | 0.1 | -0.8 |
| | Horns Rev | -0.3 | 0.4 | -1.4 | 1.0 | 0.3 | -1.2 |
| | Arklow | -0.4 | 0.4 | -1.5 | 0.9 | 0.5 | -1.2 |
| | Beatrice | -0.4 | 0.4 | -1.8 | 1.0 | 0.4 | -1.2 |
| | Walney | -0.4 | 0.4 | -1.8 | 1.1 | 0.6 | -1.3 |
| | Firth of Forth | -0.5 | 0.4 | -2.0 | 1.1 | 0.5 | -1.3 |
| | ***Gabbard*** | -0.5 | 0.4 | -2.1 | 1.2 | 0.6 | -1.4 |
| | Nysted | -0.7 | 0.4 | -2.6 | 1.4 | 0.6 | -1.8 |
| Global | Osorior | -0.4 | 0.4 | -1.8 | 1.0 | - | - |
| | Aapua | -1.0 | 0.5 | -2.9 | 1.3 | - | - |
| | Henderson | -1.4 | 0.5 | -4.2 | 1.9 | - | - |
| | Silverton | -1.8 | 0.7 | -5.3 | 2.4 | - | - |
| | Gansu | -1.9 | 0.9 | -5.5 | 2.5 | - | - |

*Table 4.3: Statistical summary of thirty-six Vortex WRF $\Delta\theta_v$ time series. For mean, P10 and P90: blue = stable and red = unstable. For Std. Dev, Daily Range and Annual Range: more green/yellow = greater range. See Figure 4.1 for map. Site names in **bold** correspond to $\Delta\theta_v$ measurement locations.*

### 4.5.1 Data Binning

The aim of this section is to pick out trends in terms of atmospheric stability and apply some knowledge of atmospheric processes, by way of explanation. Of course, the interactions of atmospheric stability with terrain, local ground coverage (e.g. forestry) and regional ground coverage (e.g. lakes; coastline) are complex and diverse. The aim is not to demonstrate a comprehensive meteorological understanding of the atmospheric processes at each site or the ability of the WRF model to correctly model these processes. Rather, the aim is to assess whether the trends observed in the data for various different site-types are consistent with expectations from the literature.

To aid visualisation, the thirty-six Vortex $\Delta\theta_v$ time series, as calculated according to section 4.2.1, were categorised according to the bin parameters shown in Table 4.4.

| ***Stability Class*** | $\Delta\theta_v$ ***Bin Bottom (K)*** | $\Delta\theta_v$ ***Bin Top (K)*** |
|---|---|---|
| Very Stable (VS) | N/A | -1.25 |
| Stable (S) | -1.25 | -0.75 |
| Slightly Stable (SS) | -0.75 | -0.25 |
| Neutral (N) | -0.25 | 0.25 |
| Slightly Unstable (SU) | 0.25 | 0.75 |
| Unstable (U) | 0.75 | 1.25 |
| Very Unstable (VU) | 1.25 | N/A |

*Table 4.4: $\Delta\theta_v$ ranges corresponding to assumed stability classes, used for visualisation purposes.*

These bin parameters are fairly arbitrary and are chosen to give a good visualisation of stability distributions which works across a range of onshore and offshore sites, rather than to compare directly with other stability metrics from different categorisation methods.

Figure 4.6 to Figure 4.9 are charts showing the $\Delta\theta_v$ distributions at each site, colour-coded according to their atmospheric stability classification (VS, S, SS, N, SU, U or VU) and binned

by each of four key variables: wind direction, wind speed, hour of day and, month of year. The sites have been categorised by Onshore; Coastal; Offshore; non-UK/Ireland; and from least to most stable within each category.

### 4.5.2 Wind Direction

Figure 4.6 shows the pattern of stability states by wind direction with the white line in each of these charts showing the frequency of occurrence in each of the thirty-six direction sector bins. It is evident that there are site-specific patterns, but no over-riding trend appears to apply across all sites.

Considering only the onshore sites, it can be observed that there is significant variation in the frequency of the various stability categories: Bhlaraidh and Keadby, both locations of operational SSE wind farms, experience ~30% and ~10% neutral conditions respectively.

Only two coastal sites (e.g. within a few tens of metres of the shoreline) have been analysed: Harland and Wolff (a shipyard in Belfast) and Hunterston (an SSE wind turbine test site near Hunterston B Nuclear Power Station, west of Glasgow). In these cases, there is very clear directional variation in stability conditions: a tendency towards stable conditions when the wind direction is over the land and neutral when the wind direction is over sea.

The offshore sites are markedly different from onshore with a much greater frequency of neutral events. The UK North Sea and Irish Sea sites (Dogger Bank, Arklow, Beatrice, Walney, Firth of Forth) show similarities in terms of a tendency towards stable conditions when the wind direction is from the south. Even without having to investigate the physical causes for this observation, it is evidence that stability modelling must be undertaken on a directional sector-wise basis to maintain accuracy (e.g. to correctly capture the interaction of stability and wake effects, when designing an offshore wind farm).

The non-UK/RoI onshore sites (all of which are operational or proposed wind farm sites) are included in order to provide a frame of reference for the level of variation observed across the UK/RoI.

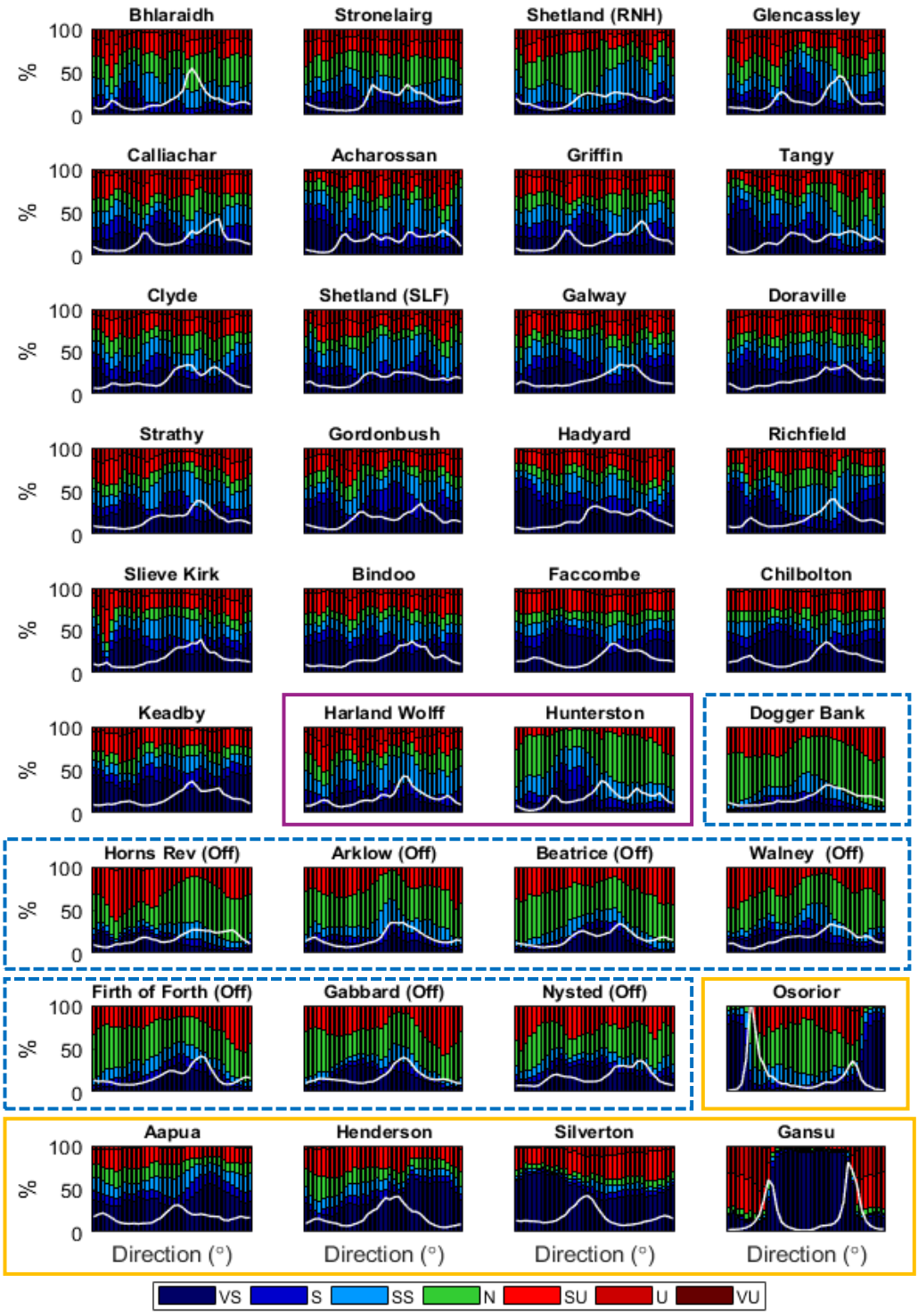


*Figure 4.6: Distributions of $\Delta\theta_v$, binned by concurrent wind direction sector for 36 sites from very stable (VS; bottom) to very unstable (VU; top). UK/RoI onshore except: purple (coastal), blue-dashed (offshore) and yellow (non-UK/RoI onshore). White line indicates frequency of wind speed bin (hidden secondary y-axis scale).*

Osorior (Brazil) has a very consistent bi-modal wind rose and extremely stable conditions on the rare occasions that wind direction is from the northern quadrants. Aapua (northern Sweden) is similar to a very stable UK site. Henderson (Texas, USA) and Silverton (New South Wales, Australia) show very high frequency of both unstable and stable conditions. Gansu again shows a wind rose with consistent bi-modality and a high frequency of stable conditions around the most frequent direction sectors.

### 4.5.3 Wind Speed

Figure 4.7 shows the same $\Delta\theta_v$ time series data, this time binned by concurrent wind speed on the x-axis. The white line shows the frequency of occurrence of each 1m/s wind speed bin: the region of interest is close to peak frequency, as the stability conditions in that region will have most impact on wind farm energy production (i.e. this wind speed region will generally contribute the majority of energy output, depending on the wind turbine power curve in question).

It is clear that in all cases stability tends towards neutral as wind speed increases, as turbulent mixing effects overshadow buoyancy effects (see 2.3.2). However, it is worth comparing the least stable onshore UK/RoI site (Bhlariadh) against the most stable (Keadby), particularly in terms of the frequency of very stable conditions in the region of the most frequent wind speed bins at Keadby.

The offshore sites do not exhibit a similar trend, in terms of tendency towards neutral conditions at high wind speed. Offshore wind flow is much more laminar and less influenced by turbulent mixing processes. The WRF model takes this into account by considering surface roughness, which is taken from various sources, including publicly available surface categorisation data.

Of the overseas sites, Osorior, Silverton and Gansu all show some abnormal trends at high wind speed, specifically a mixture of extremely stable and extremely unstable conditions; however, the low frequency of occurrence of wind speeds in this range means that this could be spurious or at least have relatively little effect.

### 4.5.4 Diurnal

Figure 4.8 shows stability data binned by hour of day. For the UK/RoI onshore sites, this shows a gradual progression throughout the diurnal cycle: the onset of unstable conditions from around dawn onwards (no correction is made to the data for seasonal changes in the timing of sunrise and sunset), reaching peak instability in mid-afternoon. Stable conditions generally dominate by late evening and grow in frequency until dawn. The only differentiating feature between these sites is the depth of the daytime-unstable/night time-stable frequency, which is more pronounced at those sites with greater overall stability variation.

The diurnal trend at the coastal sites is quite revealing: Harland and Wolff clearly behaves much like an onshore site, perhaps unsurprising, given that it has a land fetch in its predominant wind direction, whereas Hunterston shows a similar, but much less defined, shape to offshore sites. The latter site, which has a very frequent offshore fetch, is clearly experiencing different stability conditions when the wind is coming from on- or offshore.

Offshore, the diurnal trend is fairly consistent: there is a slight tendency towards stable conditions in the mid-afternoon (i.e. inverse trend to onshore). This could be explained by air masses warmed over nearby land masses being advected over the site in question and cooled close to the surface by the relatively cold sea, while remaining relatively warm at higher altitude. This explanation is bolstered by the observation that Dogger Bank, which is very far (~100km) offshore, shows almost no diurnal trend because it has sufficient offshore fetch in any direction, so as to not be affected by land-warmed air masses.

The Global onshore sites show day/night trends which are consistent with the UK/RoI onshore sites, albeit generally more extreme. Note that no adjustments have been made to the timestamps, so the mid-afternoon instability peak is offset according to the time difference between the site in question and GMT.

### 4.5.5 Seasonal

Finally, Figure 4.9 shows stability distributions binned by month of year. The onshore UK/RoI sites show a consistent trend: greater prevalence of stable conditions in winter, when there

is essentially less solar irradiance to drive the onset of instability and disrupt the stable boundary layer. In the summer months, the converse is true: greater solar irradiation leads to an increased frequency of unstable conditions. Harland and Wolff again shows its similarity with a typical onshore site, whereas Hunterston demonstrates traits of both onshore and offshore.

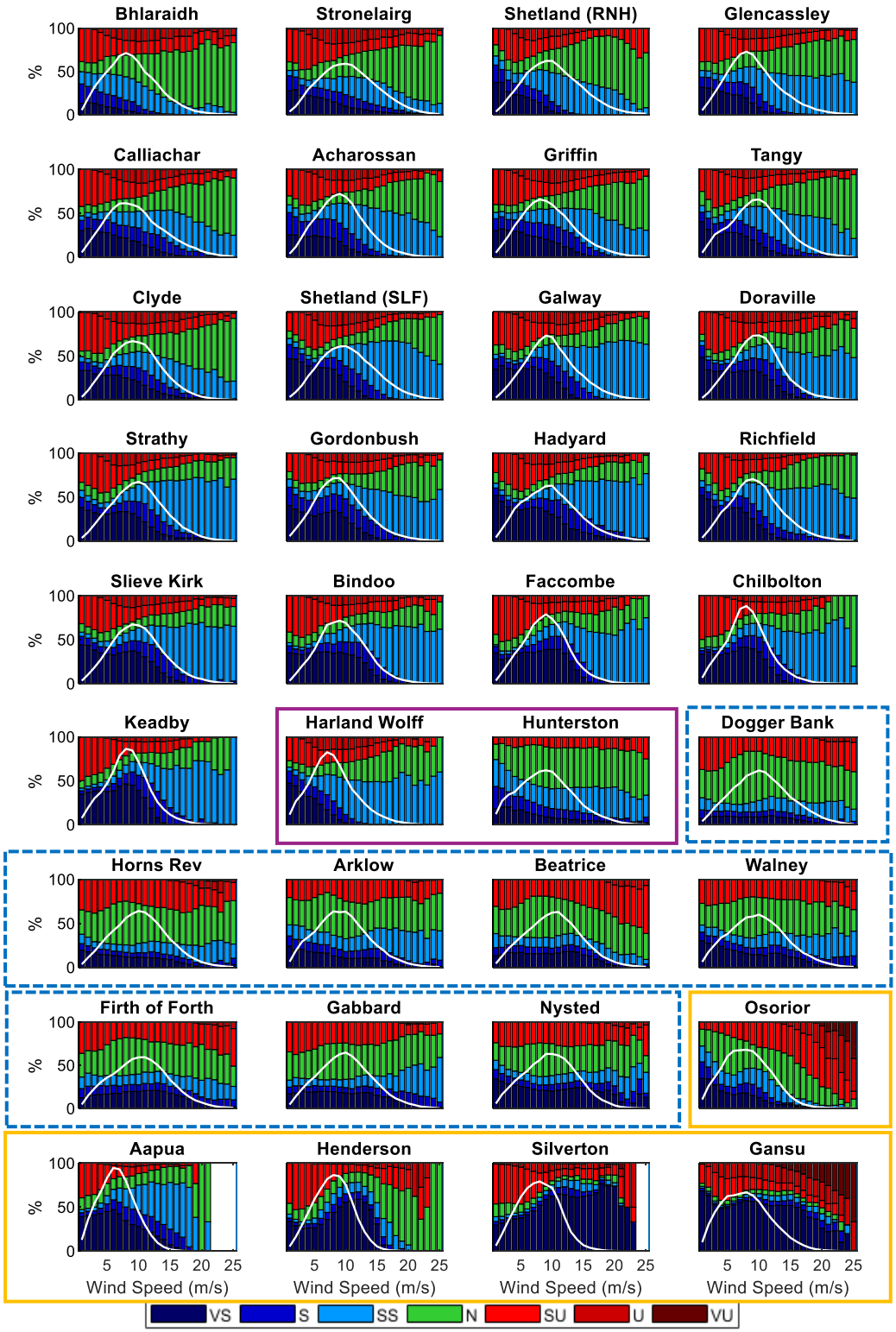


*Figure 4.7: Distributions of $\Delta\theta_v$, binned by concurrent wind speed for 36 from very stable (VS; bottom) to very unstable (VU; top). UK/RoI onshore except: purple (coastal), blue-dashed (offshore) and yellow (non-UK/RoI onshore). White line indicates direction sector frequency (hidden secondary y-axis scale).*

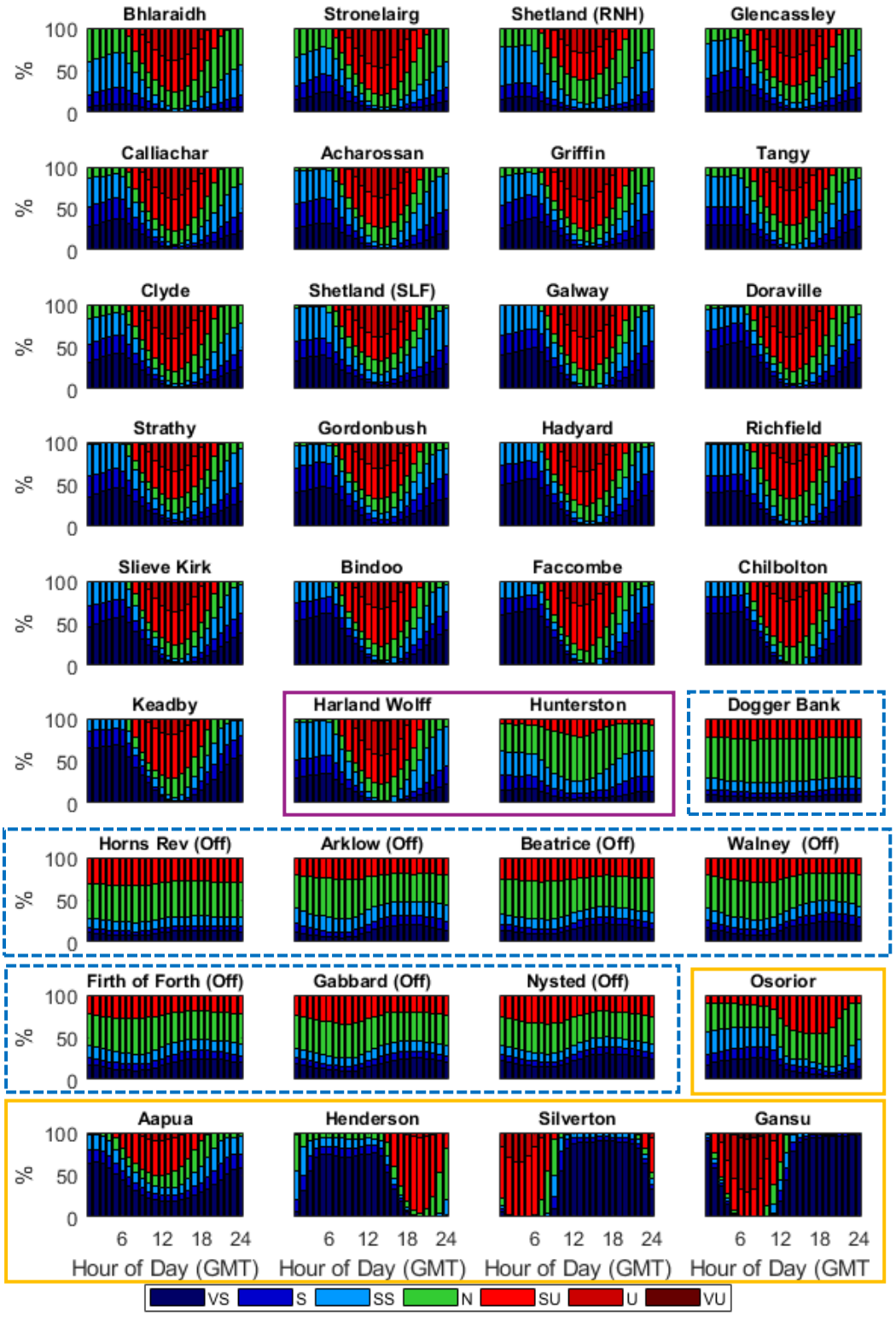


*Figure 4.8: Distributions of $\Delta\theta_v$, binned by hour of day (GMT) for 36 sites from very stable (VS; bottom) to very unstable (VU; top). UK/RoI onshore except: purple (coastal), blue-dashed (offshore) and yellow (non-UK/RoI onshore).*

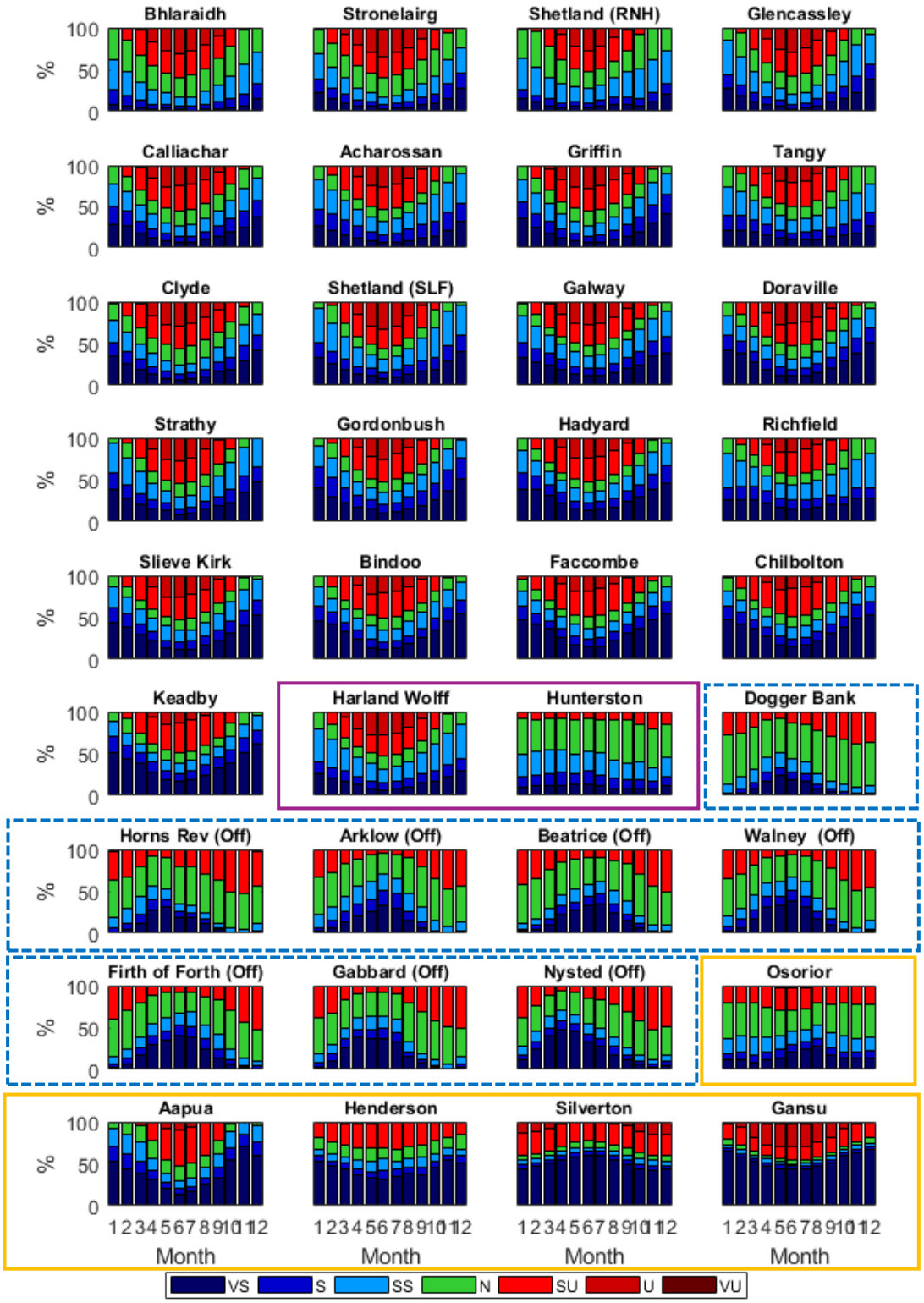


*Figure 4.9: Distributions of $\Delta\theta_v$ , binned by month of year for 36 sites from very stable (VS; bottom) to very unstable (VU; top). UK/RoI onshore except: purple (coastal), blue-dashed (offshore) and yellow (non-UK/RoI onshore).*

Offshore, annual variation in stability is significant (and opposite to that observed onshore). Stability offshore is driven by the difference in temperature between the sea and atmosphere: in summer, air temperature will more regularly exceed sea temperature and the lower layer of the atmosphere will be cooled, giving rise to a positive potential temperature gradient (stable conditions). In winter, sea temperature is more often greater and the lower layer of the atmosphere will be heated, giving rise to a negative potential temperature gradient (unstable conditions).

In terms of the global onshore sites, Osorior stands out as not conforming with the UK/RoI onshore trend; presumably due to near-equatorial location and the effect of that on the annual profile of solar irradiance. Silverton, of course, shows a flipped annual trend compared to the other onshore sites presented, due to it lying in the southern hemisphere.

## 4.6 Analysis of Spatial Virtual Potential Temperature Data

In this section, the UoE data set is used to analyse stability trends over a geographic area covering the UK and Ireland. The data were processed as described in section 4.2.2 and then various heat-maps were produced, corresponding to the trends assessed in the previous section.

Figure 4.10 shows the mean $\Delta\theta_v$ for the entire region covered by the WRF data. In general, there is a clear distinction between the land, which is predominantly slightly stable on average, and the sea, which is largely neutral. Some notable exceptions are the locations of major conurbations which are approximately neutral on average due to the 'heat island' effect. As a consequence of human activity near the surface, there is a difference in temperature between urban areas and surrounding countryside which is greatest at night. In terms of atmospheric stability, this acts as additional heating of the near-surface atmosphere, which suppresses the formation of stable conditions, resulting in mean conditions close to neutral.

Regions of higher elevation (e.g. Scottish highlands) also exhibit more neutral conditions, which could be explained by generally higher wind speeds at higher elevation disrupting the development of stable boundary layers.

### 4.6.1 Mean and Standard Deviation

Some variation in average stability is seen offshore, with stable conditions more likely closer to shore, particularly downwind of the landmass in the prevailing south-westerly wind direction. This could be explained by advection of a stable boundary layer from land out to sea at night and/or by advection of warm air from land out to sea (i.e. a positive potential temperature gradient which is imposed by upstream conditions rather than developing thermodynamically at the site of interest).

Figure 4.11 shows the standard deviation of stability across all hourly records in the 11-year data set. The regions with the greatest variation in stability can be seen to closely match the regions with greatest occurrence of stable conditions (also corresponding to low mean wind speed regions).

### 4.6.2 Diurnal and Seasonal (Spatial)

Figure 4.12 (top) shows the daily variation in atmospheric stability, calculated as the difference between $\Delta\theta_v$ for the most unstable and most stable average hours at each grid node. The calculation method is such that the result is positive when the most stable hour is at night (4pm to 4am) and negative when the most stable hour is during the day (4am – 4pm).

Again, the greatest daily range corresponds with regions which experience the most stable conditions on average: typically low-lying, inland regions. These are often also areas with low mean wind speed, where stable boundary layers are more likely to develop.

Offshore, daily variation in $\Delta\theta_v$ is close to zero for the most part, due to the difference in thermodynamic processes over land and water as detailed in section 2.2.7 (e.g. sea surface temperature does not respond to solar heating on the diurnal timescale).

Figure 4.12 (bottom) similarly shows annual variation in atmospheric stability, calculated as the difference between $\Delta\theta_v$ for the most unstable and most stable average months at each grid node. In this case, the calculation method is such that the result is positive when the most stable month is in winter (Oct – Mar) and negative when the most stable month is in summer (Apr – Sep). This rule of thumb is slightly complicated by the fact that sea

temperature lags significantly behind solar irradiance: more so in deeper waters, where heat capacity is greatest.

Figure 4.13 breaks down the diurnal/seasonal relationship further, revealing the intensely contrasting atmospheric conditions above land and sea during summer daytime. In this case, the stable conditions in near-shore waters are amplified, likely due to offshore advection of land-heated air masses and subsequent cooling over the sea.

In summer at night, onshore stable conditions are intensified by the rapidly cooling surface temperature after sunset. Inland waters (e.g. Severn estuary) exhibit neutral conditions on average rather than stable, potentially due to the propensity of shallower waters to respond to solar heating more rapidly, thereby reducing the air-sea temperature difference. The major conurbations stand out clearly during the summer night times.

### 4.6.3 Wind Speed and Direction

The influence of wind speed and direction was examined by filtering the data by direction and wind speed range. Figure 4.14 shows the relationship between stability and wind speed. Onshore, slightly stable conditions dominate at lower wind speed, giving way to neutral conditions at higher wind speeds. This trend is mirrored offshore, only with lesser magnitude. This is in agreement with Figure 4.7 for the analysis of Vortex time series by wind speed range.

Figure 4.15 shows variation in atmospheric stability with wind direction, where wind direction is simply binned by four quadrants. Clearly there is a trend, in terms of greater prevalence of neutral conditions when wind is coming from the two south quadrants but this would have to be further broken down diurnally and/or seasonally to understand any possible explanation for this. Unfortunately, this filtering combination was not considered during data processing.

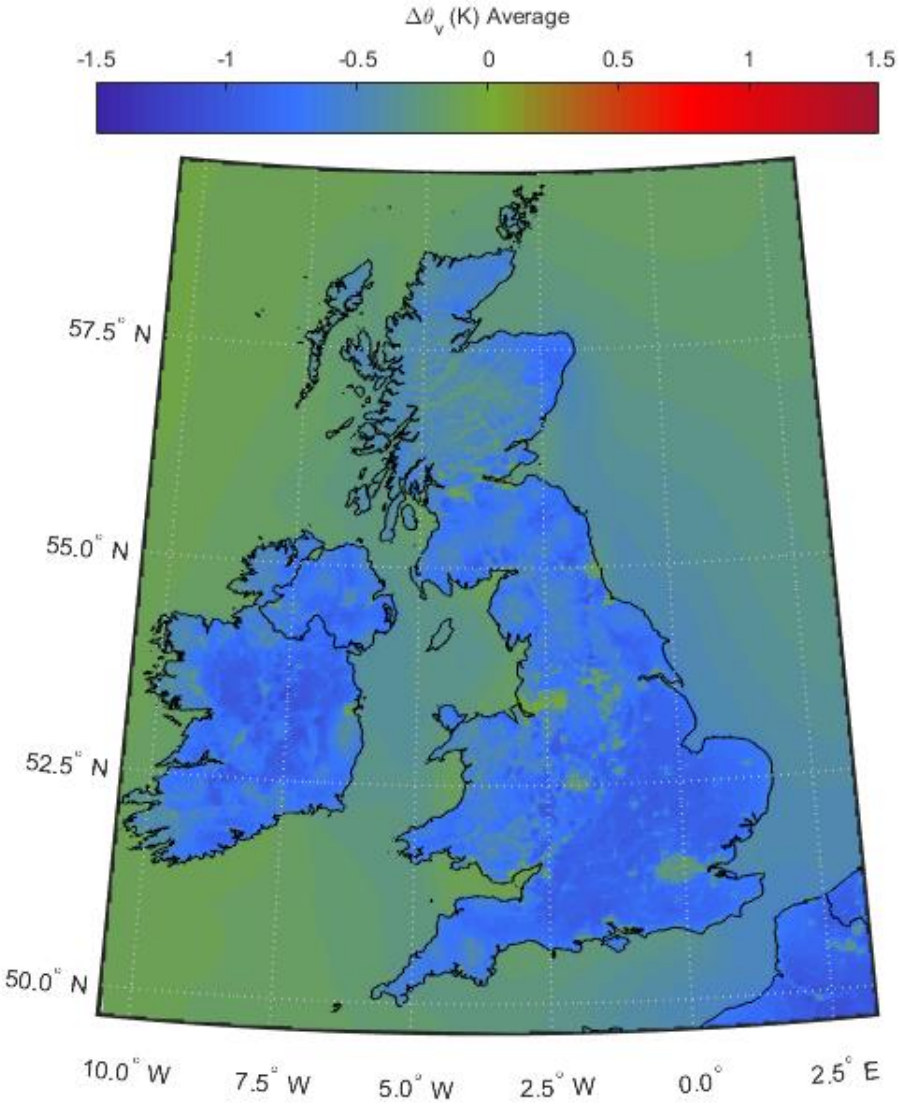


*Figure 4.10: Average atmospheric stability ($\Delta\theta_v$ between 10m and 100m) across UK and RoI, derived from 11 years hourly UoE WRF data with 3km spatial resolution. (In greyscale, darker-shaded areas over land are more stable ($\Delta\theta_v$<0) on average).*

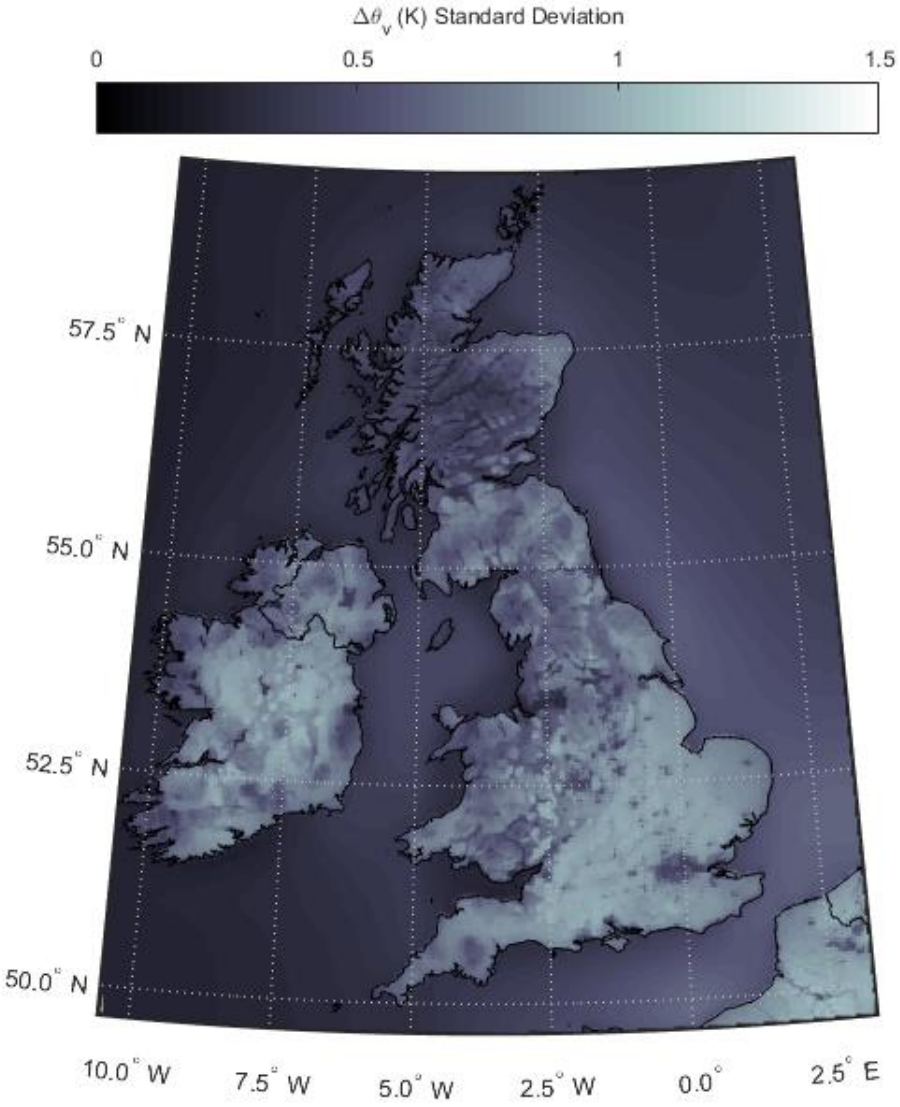


*Figure 4.11: Standard deviation of atmospheric stability ($\Delta\theta_v$ between 10m and 100m) across UK and RoI, derived from 11 years hourly UoE WRF data with 3km spatial resolution.*

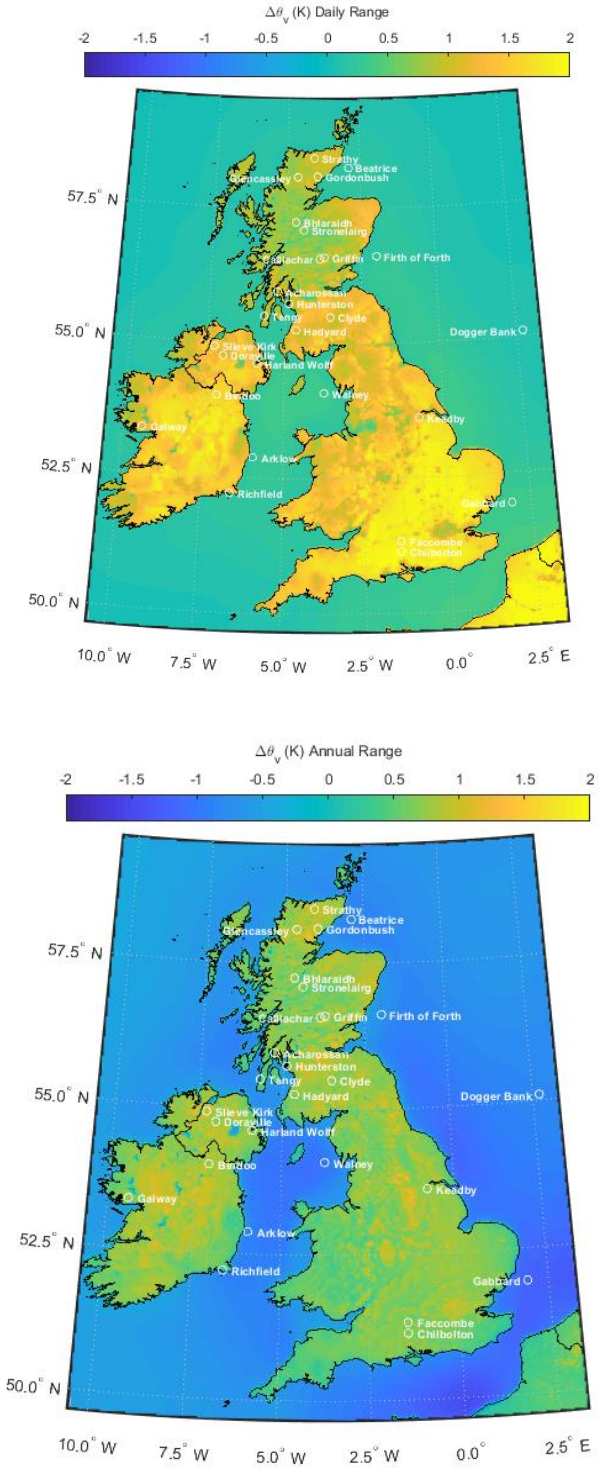


*Figure 4.12: Daily range (top) and annual range (bottom) of atmospheric stability ($\Delta\theta_v$ between 10m and 100m) across UK and RoI, derived from 11 years hourly UoE WRF data with 3km spatial resolution.*

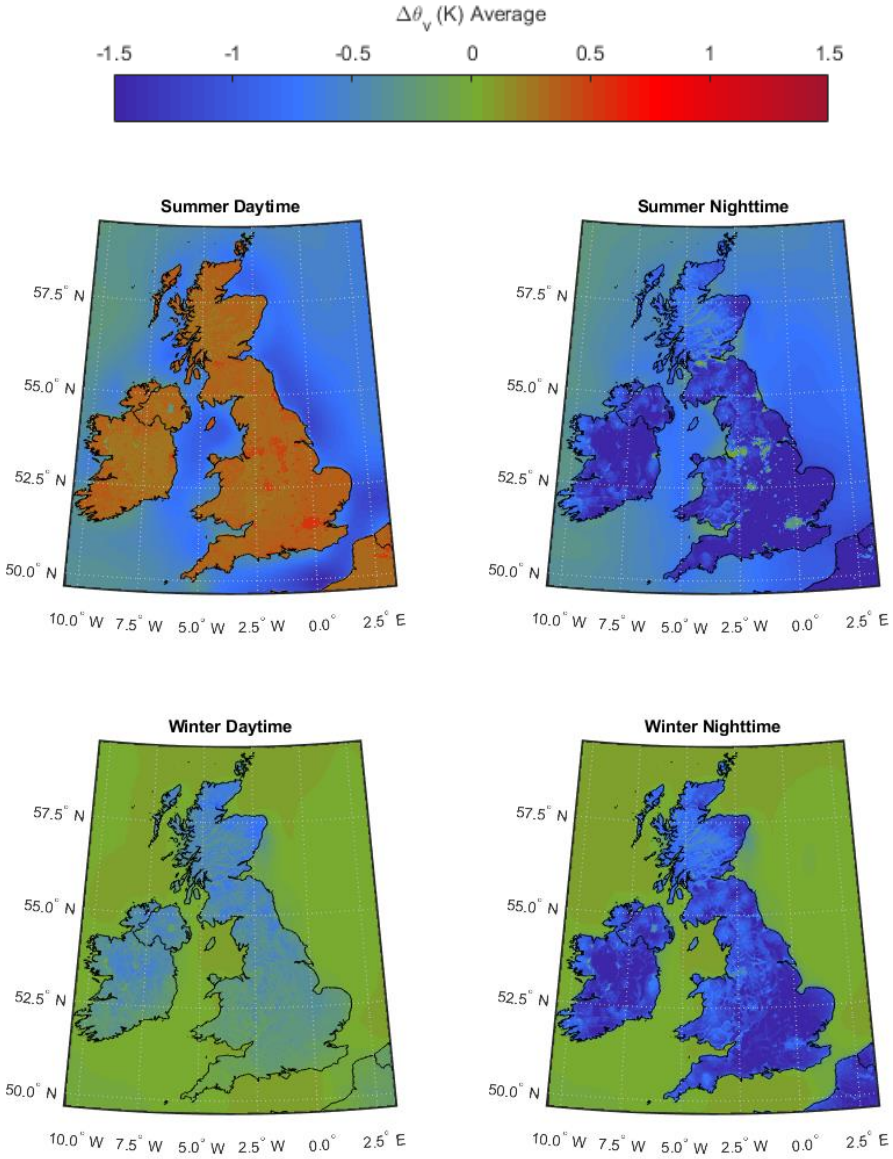


*Figure 4.13: Average atmospheric stability ($\Delta\theta_v$ between 10m and 100m) across UK and RoI, derived from 11 years hourly UoE WRF data with 3km spatial resolution. Filtered by timestamp: summer daytime, summer nighttime, winter daytime, winter nighttime. (In greyscale, darker-shaded regions indicate the least neutral (i.e. more stable or unstable) mean conditions).*

## 4.7 Comparison of Data Sets

This chapter has detailed analyses of both the UoE and Vortex data sets – although direct analytical comparison of one data set against the other was not undertaken.

The UoE data offers an extremely quick and useful reference source, in terms of geographically identifying areas of divergent mean stability or high standard deviation. This data set can therefore come into use when un-validated meteorological parameters for a specific site or region are required quickly (i.e. for a high-level site assessment). On the other hand, Vortex data is calculated on-demand for a site of interest, typically taking 4-5 days processing time (or more if the job is queued) and so is less applicable to this purpose.

However, the Vortex data has the advantage of being concurrent with meteorological measurements, captured in the period 2014-18. This makes the Vortex data set the only one out of the two which can be validated against SSE's measured data set which is the focus of the following chapter.

Further, the Vortex data set was generated more recently (2015-18, compared to 2010 for UoE data) and therefore benefits from more up to date WRF model (version 3.0) and also more up to date initiation data (CFSR, rather than NCEP).

Vortex data is therefore selected for the validation step in Chapter 5 and subsequently, Vortex data is used as an input to CFD modelling in Chapter 6, as a proxy for atmospheric stability.

## 4.8 Chapter Summary

In this chapter, it has been qualitatively demonstrated that the trends observed in both the Vortex and UoE mesoscale data sets compare well with understood atmospheric processes outlined in section 2.2 and also compare well with each other, particularly in terms of the differences between land and sea and their respective diurnal and seasonal interactions.

Onshore UK/RoI sites can be seen to deviate significantly from neutral, in terms of long-term average conditions (although less dramatically so when put in the context of other non-UK/RoI sites) and some sites exhibit much greater diurnal and seasonal variation than others. This calls into question whether the 'neutral assumption' (i.e. simulating wind flow under neutral conditions only, taking this to be adequately representative of all atmospheric states) in wind flow modelling can ever be considered appropriate.

Two data sets are available: UoE and Vortex. Vortex has been selected for the subsequent analysis for the reasons outlined in section 4.7.

At this stage, the relevant questions are: do the mesoscale-modelled values truly reflect actual measured site conditions and; are the site-specific deviations from neutral large enough to have a significant effect on wind flow modelling and wind farm performance? These questions are addressed in Chapters 0 and 6, respectively.

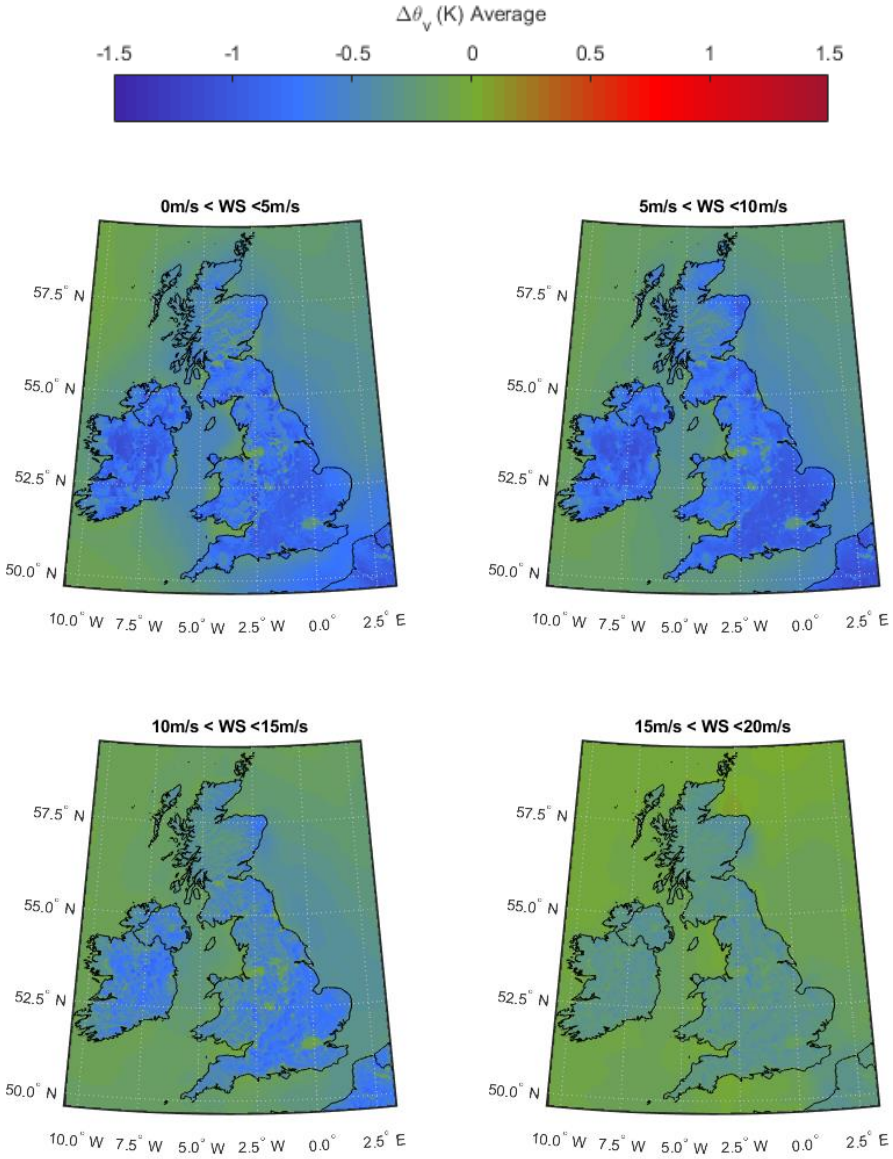


*Figure 4.14: Average atmospheric stability ($\Delta\theta_v$ between 10m and 100m) across UK and RoI, derived from 11 years hourly UoE WRF data with 3km spatial resolution. Filtered by local wind speed: 0 – 5 m/s, 5 – 10 m/s, 10 – 15 m/s and 15 – 20 m/s. (In greyscale, darker-shaded regions indicate the least neutral (i.e. more stable or unstable) mean conditions).*

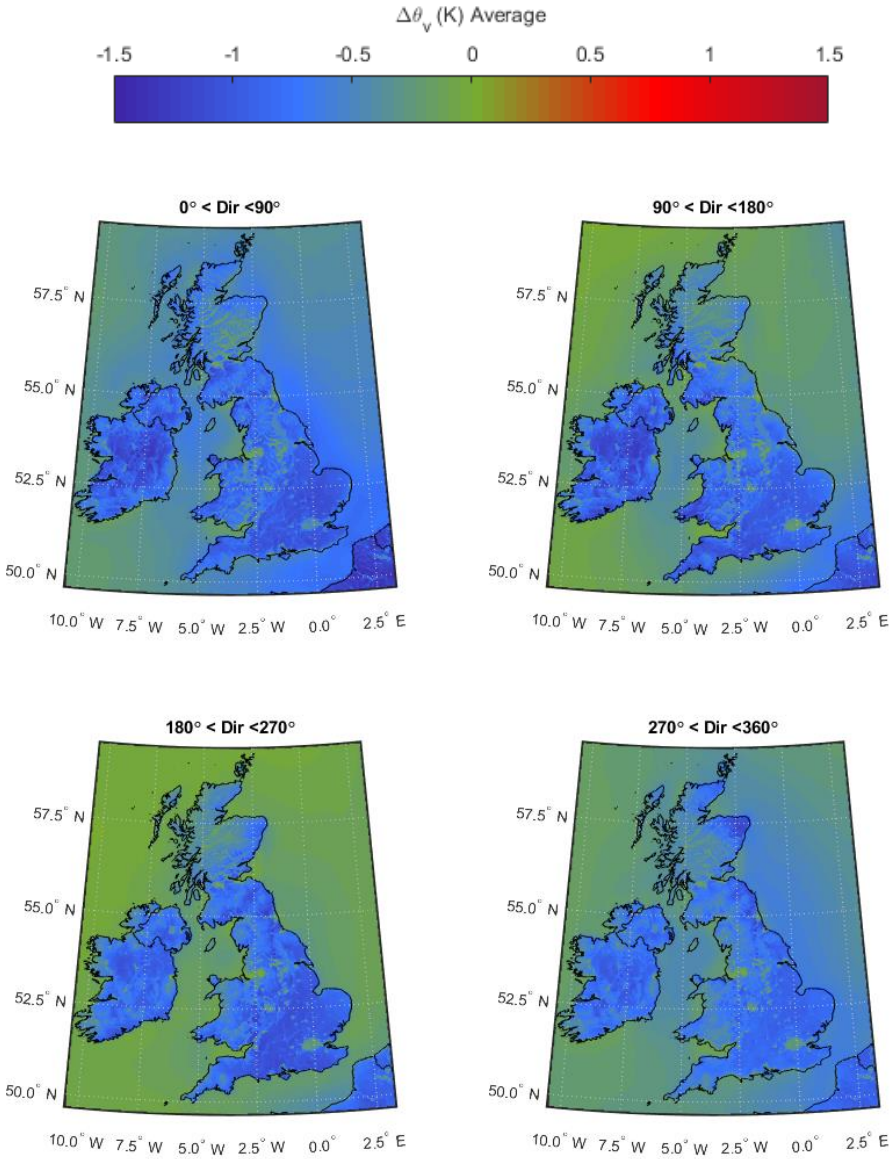


*Figure 4.15: Average atmospheric stability ($\Delta\theta_v$ between 10m and 100m) across UK and RoI, derived from 11 years hourly UoE WRF data with 3km spatial resolution. Filtered by local wind direction: 0-90°, 90-180°, 180-270° and 270-360°. (In greyscale, darker-shaded regions indicate the least neutral (i.e. more stable or unstable) mean conditions).*

# 5 Measurement Analysis

## 5.1 Introduction

SSE has exclusive access to measured meteorological data sets from over a hundred locations from the early 2000s onwards – mostly onshore UK and Ireland but also offshore and overseas. Starting in 2012, a bespoke new campaign of high specification measurements was begun in preparation for this research project, involving the installation of additional instrumentation designed to measure atmospheric stability (via the $\Delta\theta_v$ proxy) across thirteen measurement locations (ten onshore and three offshore).

The aim of this measurement campaign was to construct a suitably large measured database, to inform some of the key questions in this research: what is the optimal atmospheric stability measurement technique and; can modelled (Vortex) data be used as a suitable substitute for measured data?

The primary focus of the campaign was to approximate atmospheric stability via virtual potential temperature differential rather than measuring heat flux. This allows for a straight-forward comparison with mesoscale data and has also been identified as the most straight-forward input to CFD flow modelling.

It was also important that measurements should span a broad range of different sites – both in terms of atmospheric stability distribution, geographic spread and surface conditions (e.g. forestry, sea, open land). Finally, measurement accuracy should be sufficient so as not to introduce significant uncertainty into the evaluation of stability distributions.

A summary of the configurations of the $\Delta\theta_v$ measurement masts is given in Table 5.1. This table summarises the mast identifiers (e.g. “CSD” for “Cat Shoulder”) which are used in the remainder of this report to refer to measurement locations.

In addition to these high-specification masts, most sites have additional ‘secondary’ masts within a few kilometres with conventional instrument configurations. These are used for wind flow model checks.

In this chapter, first a detailed description of the measurement methodology is provided, including descriptions of instruments used and measurement site, how the data were cleaned and calibrated and how the measurement error was assessed. Then, virtual potential temperature differential measurements are validated against one another, where two temperature differential measurements systems are co-located. Next, concurrent measurements of wind shear, turbulence intensity, inflow angle, and wind speed ratio were used to confirm the expected relationships between these quantities and $\Delta\theta_v$. Finally, measured data are compared with mesoscale-modelled WRF (Vortex) data.

## 5.2 Technical Description

### 5.2.1 General Configuration

The $\Delta\theta_v$ measurement approach consists of two boom-mounted sensors making up the primary temperature differential system; one mounted at close to ground level (typically 10m) and one close to the top of each mast, typically 2m below the top anemometers (see Figure 5.1).

In most cases, a secondary temperature differential measurement system, with two more sensors of different types mounted at the same heights is installed, to provide redundancy and an independent check on the primary system.

At least one pressure sensor is used to convert absolute temperature measurements to potential temperature. Where possible, multiple pressure sensors are used to allow greater accuracy in this respect (to avoid having to assume a uniform pressure lapse rate). Relative humidity ($\mathrm{RH}$) sensors (integrated with temperature sensors in most cases) are used in order to convert potential temperature into virtual potential temperature.

A photograph showing the mounting of two temperature gradient systems (upper sensors only) is in Figure 5.2.

| Site Name | Mast ID | Temperature & Relative Humidity | | | | | Ultrasonic Anemometer | | Pressure | | | Anemometer | Wind Vane |
|---|---|---|---|---|---|---|---|---|---|---|---|---|---|
| | | CS215 | PT100 | HMP155 | TG01 | Other RH | THIES 3D | Gill 3D | PTB110B/ CS106 | PTB 210 | Other | | |
| **Acharossan** | DDH | - | - | 76N,6N | 76N,6N | - | 65S | - | 76,6 | - | - | 80S, 80N, 65N, 50S, 50N, 35S | 76N,61N |
| **Bhlaraidh** | CLB | - | - | 8N, 58N | 8N, 58N | - | 50N | - | 2 | - | - | 60S, 60N, 43S, 21S | 58S, 41S |
| **Clyde Ext** | CSD | - | - | 8N,68N | 8N,68N | - | 50N | - | 68 | - | - | 70S, 70S, 50S, 30S | 68S, 48S |
| **Dogger Bank** | DBE | - | 104, 24.5 | 104, 24.5 | - | - | - | 98, 68 | 104, 24.5 | - | - | 110, 110, 104, 98, 83, 83, 68, 53, 53 ,38, 38, | 104, 78, 63 |
| | DBW | - | 104, 24.5 | 104, 24.5 | - | - | - | 98, 68 | 104, 24.5 | - | - | 110, 110, 104, 98, 83, 83, 68, 53, 53 ,38, 38, | 104, 78, 63 |
| **Hunterston** | PMM | - | - | 108, 5 | 108, 5 | - | - | 100 | 108, 2 | - | - | 110, 108, 95, 75, 60, 32 | 104,70 |
| **Greater Gabbard** | IGMMX | - | 18, 77.5 | - | - | 77.5 | - | - | | - | 77.5 | 40, 40, 60, 60, 77.5, 79.5 | 38, 58, 77.5 |
| **Glencassley** | DLM | - | - | 8N, 68N | - | - | 50N | - | 68 | - | - | 70S, 70N, 50S, 30S | 68S, 48S |
| **Strathy** | S8 | - | - | 18N, 68N | 18N, 68N | - | 50N | - | 68 | - | - | 70S, 70N, 50S, 30S | 68S,48S |
| **Stronelairg** | SDB | - | - | 10N, 68N | 10N, 68N | - | 65S | - | 2 | - | - | 70S, 70N, 50S, 50N, 30S, 30N | 68S,48S |
| **Shetland** | RNH | - | - | 66, 38, 10 | 66, 10 | - | 66S | - | - | 66, 10 | - | 70, 50, 30N, 70, 50, 30S | 62, 46, 26S |
| | SLF | - | - | 66, 38, 10N | 66, 10 | - | 66S | - | 2 | - | - | 70, 50, 30N, 70, 50, 30S | 62, 46, 26S |
| **Tangy** | KLRI | 8N, 78N | - | - | 8N, 78N | - | 63N | - | 2 | - | - | 80S, 80N, 60S, 40S | 77S, 60S |
| | KLRII | - | - | 8N, 78N | 8N, 78N | - | 63N | - | - | 78, 8 | - | 80N, 80, 62, 40S | 78S, 61S, 38S |

*Table 5.1: Summary of SSE's atmospheric stability measurement mast configuration showing the height above ground level (m) and, in some cases, the orientation of the instrument relative to the mast structure ('N' = North, 'S' = South).*

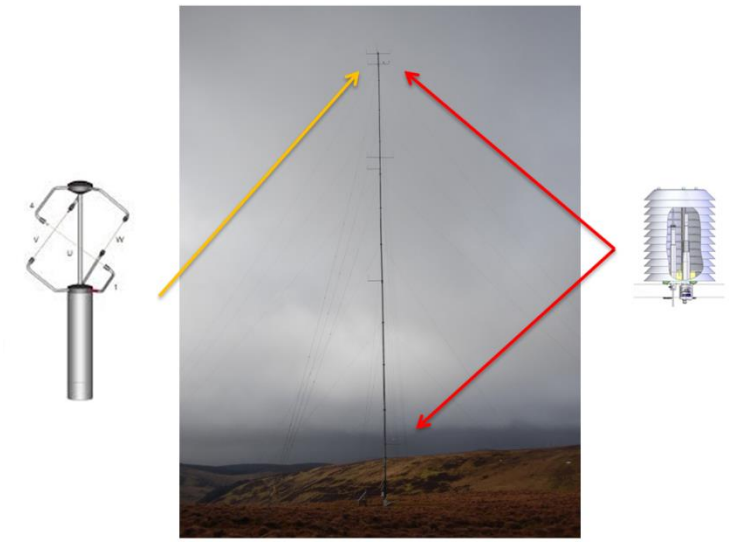

*Figure 5.1: Clyde Extension BWR met mast indicating the locations of the ultrasonic anemometer (left) and temperature sensors (right).*

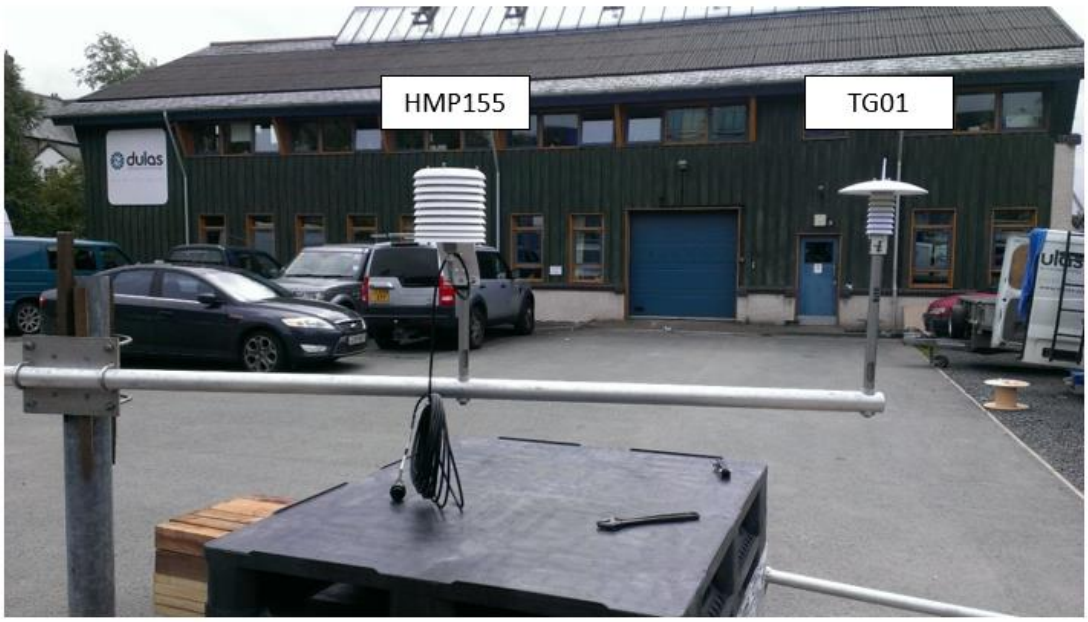


*Figure 5.2: Photograph showing a boom-mounted HMP155 temperature sensor with DT13 radiation shield (left) and TG01 temperature gradient sensor (right).*

### 5.2.2 HMP 155 Temperature Sensor

Two or more Väisälä HMP155 temperature sensors displaced vertically across a tall mast can be used to measure the temperature gradient. HMP155 sensors also incorporate a relative humidity sensor, which is used in the conversion of temperature to virtual temperature. For deployment in the natural environment, radiation screens can be fitted in order to ensure that the quantity measured is the ambient air temperature and mitigate against the effect of varying solar heating. A mixture of DT13 (as photographed in Figure 5.2 (left)) and DT503 radiation screens were deployed as part of this project.

Like most electronic temperature sensors, the HMP155 uses a material which increases in electrical resistance with increasing temperature. When a voltage is applied across the material, the resistance can be inferred from the resulting current flow. The temperature measurement is then derived using a known transfer function (a relationship between temperature and resistance which is specific to the device type). A potential source of uncertainty is the excitation voltage which is applied by the data logger. In this project all HMP155 sensors were 'mutually excited' by wiring them into a single power output at the logger, to ensure no discrepancy in the voltage applied and to minimise this uncertainty.

### 5.2.3 WindSensor TG01 Temperature Gradient Sensor

The WindSensor TG01, which is designed specifically for temperature gradient applications, is a measurement system comprising two separate sensors which are manufactured and calibrated as a single system. Instead of each sensor giving an individual temperature reading, only the temperature difference can be derived from the raw measurements of electrical resistance.

The principle behind this design is to reduce or eliminate the errors that come along with the process of measuring temperature at two points and subtracting one reading from the other.

Such errors could be related to small differences that are introduced in the sensor manufacturing process, errors caused by the sensor to logger cabling or due to inaccuracy in the excitation voltage applied by the data logger. A TG01 sensor is displayed in Figure 5.2 (right).

### 5.2.4 Campbell Scientific CS215 Temperature Sensor

The Campbell Scientific CS215 is a commonly used sensor for simple temperature measurement applications where high precision is not a concern. It also incorporates relative humidity measurement. These sensors are not calibrated in-house as standard.

### 5.2.5 Pressure Sensors

The Väisälä PTB101 is a standard pressure measurement device for general meteorological applications and well suited to atmospheric stability ($\Delta\theta_v$) measurement. Pressure sensors must be contained in a weather-proof housing (to protect the electronics) with a valve to allow for pressure equalisation.

The PTB210, also manufactured by Väisälä, is a higher precision instrument. This was trialled on two SSE sites in order to assess any benefit associated with improved accuracy. Figure 5.3 shows both pressure sensors used in the measurement campaign.

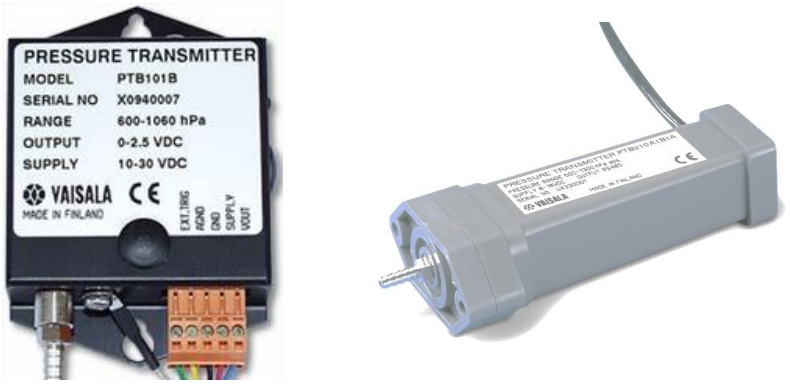


*Figure 5.3: PTB101 (left) and PTB210 (right) pressure sensors.*

### 5.2.6 Thies 3-D Ultrasonic Anemometer

Thies 3D ultrasonic anemometers (pictured in Figure 5.4 (left)) were deployed at ten onshore sites. These sensors work by measuring the time of flight of ultrasonic acoustic pulses between three pairs of emitters/receptors. Data from these sensors was used to measure inflow angle ('wind direction elevation'). The sensor has an on-board computer, meaning that very little data post-processing at the onsite logger is required.

The full list of default signals is provided in Table 5.2.Note, only wind direction elevation was used in this research (see 8.4.4 for proposed future work related to the use of ultrasonic anemometry).

| Signal ID | Description |
|---|---|
| UA1_65N_wvx | X wind velocity |
| UA1_65N_wvy | Y wind velocity |
| UA1_65N_wvz | Z wind velocity |
| UA1_65N_wvt | Total wind velocity |
| UA1_65N_wva | Wind velocity azimuth |
| UA1_65N_wda | Wind direction azimuth |
| UA1_65N_wde | Wind direction elevation |
| UA1_65N_avt | Acoustic virtual temperature |
| UA1_65N_shstsp | Shearing stress speed |
| UA1_65N_shst | Shearing stress |
| UA1_65N_gfc | Ground friction coefficient |
| UA1_65N_shf | Sensible heat flux |
| UA1_65N_obl | Obukhov length |
| UA1_65N_dyn | Dynamic Temperature |
| UA1_65N_vpc | Vertical pulse current |

*Table 5.2: Typical signal list for Thies 3D ultrasonic anemometer.*

### 5.2.7 Cup Anemometers

This project utilised a mixture of Thies Clima First Class, Vector A100LK and Risoe P2546A cup anemometers; all certified first class anemometers according to IEC-61400-1 [34], designed for high precision wind resource assessment. Figure 5.4 shows the types of anemometer used for wind speed measurement.

*Figure 5.4: Types of cup anemometer used for wind speed measurement: Thies Clima 3DUS (left), Thies Clima First Class (second from left), WindSpeed A100LK (second from right) and WindSensor P2546A (right).*

## 5.3 Data Cleaning

Before conducting analysis, it was necessary to clean each measured data set in order to ensure that instrument readings are appropriately calibrated and spurious measurements have been removed from the final data set. Data cleaning was carried out in the Windographer software package [71] according to the following summary.

***All Instruments***

- Remove invalid data from periods during which the sensors and/or data logger were undergoing installation, maintenance or decommissioning.
- Remove periods of apparent sensor failure (e.g. due to failure of the power supply which can in turn be caused by degrading batteries or insufficient PV charge during winter months). These can generally be identified by checking for unphysically high or low values or cross-referencing against battery voltage measurement.

***Anemometers***

- Remove specific incidences of sensor malfunction or icing, identified by a persistent zero or inconsistent reading compared to other anemometers.
- Disregard any anemometers which are experiencing long-term degradation. One way to identify degradation is to examine the ratio of wind speeds recorded by two anemometers (preferably of different types) over a long-term period (at least one year) and look out for any gradual change.

***Wind Vanes***

- Remove specific incidences of sensor malfunction or icing, identified by a persistent un-changing or inconsistent reading compared to other wind vanes.

## 5.4 Calibration and Sensor Error

All sensors used in this study were calibrated at ISO-accredited test facilities [72]. The specific approach followed for each instrument type is detailed in the following sections.

### 5.4.1 Anemometers

All anemometers used in this project were calibrated at an independent wind tunnel test facility – generally either at Svend Ole Hansen in Denmark [73] or Deutsche WindGuard in Germany [74]. The wind tunnel provides a calibration certificate which states the measured transfer function (slope and offset) to be applied to the rotational speed of the anemometer to convert to wind speed in m/s.

This transfer function is sometimes programmed into the on-site data logger and applied 'on-line' to the raw measurements before the data is stored. Otherwise, the data logger is programmed with a generic slope and offset, meaning that the data needs to be post-processed later. It is therefore necessary to compare the data logger programme and calibration certificate for each instrument and make any adjustments necessary to the wind speed data. Where an adjustment is necessary, Windographer is used to remove the generic transfer function and re-calibrate using the correct function.

### 5.4.2 HMP155 Temperature Sensors

Calibration was conducted in-house by the manufacturer, Vasiala, [75] at a range of up to nine temperature points spanning the typical temperature range anticipated in the measurement environment. An extract from the calibration results for the 8m and 68m HMP155 sensors at one site is presented in Table 5.3.

As a following step, the net correction factor was calculated, this being the required adjustment to the measurement of the difference between one sensor and the other. For example, if a +0.1°C adjustment was required to both sensors, the net correction factor would be zero. In each case, the net correction was calculated at the temperature set point closest to the anticipated environmental temperature during deployment (e.g. approximately 10°C). The results of these calibrations are presented in Table 5.4.

| *Reference Temp (°C)* | *68m Sensor Temp (°C)* | *68m Correction Factor (°C)* | *8m Sensor Temperature (°C)* | *8m Correction Factor (°C)* | *Test Uncertainty (°C)* |
|---|---|---|---|---|---|
| -40.08 | -40.07 | -0.01 | -40.11 | +0.03 | ± 0.03 |
| -30.06 | -30.02 | -0.04 | -30.06 | +0.00 | ± 0.03 |
| -20.05 | -19.98 | -0.07 | -20.02 | -0.03 | ± 0.03 |
| -10.02 | -9.92 | -0.10 | -9.96 | -0.06 | ± 0.03 |
| 0.01 | 0.13 | -0.12 | 0.09 | -0.08 | ± 0.03 |
| 10.00 | 10.14 | -0.14 | 10.1 | -0.10 | ± 0.03 |
| 19.99 | 20.15 | -0.16 | 20.11 | -0.12 | ± 0.03 |
| 30.00 | 30.17 | -0.17 | 30.13 | -0.13 | ± 0.03 |
| 40.00 | 40.18 | -0.18 | 40.14 | -0.14 | ± 0.03 |

*Table 5.3: Calibration results for 8m and 68m HMP155 sensors from tests conducted before deployment at Strathy (S8) mast.*

| *Site* | *Mast* | *Temperature Set Points* | *Top Sensor Correction* | *Bottom Sensor Correction* | *Net Correction* |
|---|---|---|---|---|---|
| Acharossan | DDH | 9 | -0.02 | -0.14 | -0.12 |
| Bhlaraidh | CLB | 9 | -0.14 | -0.17 | -0.03 |
| Clyde Ext | CSD | 9 | -0.07 | -0.10 | -0.03 |
| Dogger Bank | DBE | 1 | -0.04 | -0.04 | 0.00 |
| Dogger Bank | DBW | 1 | 0.03 | -0.04 | -0.07 |
| Glencassley | DLM | 9 | -0.12 | 0.00 | 0.12 |
| Hunterston | PMM | 6 | -0.09 | -0.08 | +0.01 |
| Shetland | RNH | 7 | 0.00 | 0.00 | 0.00 |
| Shetland | SLF | 7 | 0.00 | 0.00 | 0.00 |
| Strathy | S8 | 9 | -0.14 | -0.10 | +0.04 |
| Stronelairg | SDB | 1 | -0.04 | -0.10 | -0.06 |
| Tangy | KLRI | 1 | 0.00 | 0.00 | 0.00 |

Table 5.4: *Calibration results for HMP155 sensors on all masts, showing the required correction to the top and bottom sensors and also the resulting net correction to the differential (bottom – top) measurement.*

### 5.4.3 WindSensor TG01 System

TG01 systems were calibrated at the DTU calibration facility in Denmark [76]. In this case, the calibration was reported as the measured electrical resistance of each sensor at three temperatures (-20, 0 and 30 °C). In all cases, the difference in resistance was in the range ± 0.1% (i.e. ± 0.01 °C at 10°C) and no further corrective steps were taken.

### 5.4.4 Pressure and RH Sensors

Pressure and relative humidity (RH) sensors were calibrated in-house by the manufacturer (in most cases, Väisälä) at a range of 5 – 7 reference values. The calibration conducted at the reference value closest to the operational environment was selected to define the measurement error, typically ~1000hPa and 95% RH.

In all cases, the calibration results showed that the measurement error was within the stated calibration error (the error introduced by uncertainty in the calibration process, including the measurement error associated with the instruments used to establish the 'true' reference value). No systematic corrections were therefore made to either the pressure or RH measurements and the measurement error was taken to be equal to the stated calibration error in each case. A summary of the pressure and RH sensor calibration results is given in Table 5.5 for both the upper and lower instruments, where applicable.

| **Site** | **Mast** | **Pressure Measurement Error (hPa)** | | **RH Measurement Error (%)** | |
|---|---|---|---|---|---|
| | | **Upper** | **Lower** | **Upper** | **Lower** |
| Acharossan | DDH | 0.10 | 0.10 | 1.0 | 1.0 |
| Bhlaraidh | CLB | - | 0.15 | 1.0 | 1.0 |
| Clyde Ext | CSD | 0.15 | - | 1.0 | 1.0 |
| Dogger Bank | DBE | 0.15 | 0.15 | 1.0 | 1.0 |
| Dogger Bank | DBW | 0.15 | 0.15 | 1.0 | 1.0 |
| Glencassley | DLM | 0.15 | - | 1.0 | 1.0 |
| Greater Gabbard | IGMMX | 0.50 | - | 1.0 | - |
| Hunterston | PMM | 0.06 | 0.06 | 0.5 | 0.5 |
| Shetland | RNH | - | 0.15 | 1.0 | 1.0 |
| Shetland | SLF | - | 0.15 | 1.0 | 1.0 |
| Strathy | S8 | 0.15 | - | 1.0 | 1.0 |
| Stronelairg | SDB | - | 0.10 | 1.0 | 1.0 |
| Tangy | KLR I | - | 0.15 | 1.0 | - |
| | KLR II | 0.07 | 0.07 | - | - |

*Table 5.5: Summary of pressure sensor calibration results.*

## 5.5 Data Synthesis

At each site, pressure and relative humidity measurements at both temperature measurement heights are required in order to calculate $\Delta\theta_v$ accurately. Where this is not the case, due to sub-optimal instrument configuration or failed instruments, data synthesis has been utilised to backfill the missing measurements in the relevant periods.

The following data synthesis processes were implemented:

- Where pressure measurements were only available at a single temperature measurement height, pressure at the second temperature measurement height was extrapolated from the available measurements, according to the hydrostatic equation (5) with ρ = 1.225 kg/m$^3$.
- Where relative humidity (RH) measurements were only available at a single temperature measurement height, RH at the second temperature measurement height was assumed to be equal (i.e. assuming uniform RH with height).
- Where no pressure measurements were available, pressure at 10m AGL was taken from reference (Vortex) data and extrapolated to additional heights according to the hydrostatic equation with ρ = 1.225 kg/m$^3$.
- Where no RH sensors were available, it was assumed that RH is constant RH = 90%, assuming uniform RH with height.

Out of the 14 mast configurations analysed, 13 had RH sensors at multiple heights and 6 had pressure sensors at multiple heights. Measurements from these masts were used to assess the uncertainty associated with the data synthesis approach described above. For example, for each of the six masts with dual pressure sensors, the measured data at each instrument was compared to the equivalent synthesised data and the average deviation calculated. By this method, a set of errors were calculated for these synthesised time series, as shown in Table 5.6.

| Synthesis Process | Synthesis Error |
|---|---|
| Extrapolation of Pressure | ± 0.8 hPa / 100m |
| Extrapolation of RH | ± 4 % / 100m |

*Table 5.6: Errors introduced by implementing data synthesis for missing instruments.*

## 5.6 Data Rounding

Each measurement time series (temperature, pressure and relative humidity) was checked in order to assess the impact of output precision on $\Delta\theta_v$ calculation. Temperature and RH measurements were found to be sufficiently precise in all cases, so as to have a negligible impact on overall $\Delta\theta_v$ measurement uncertainty.

However, due to an error in logger programming, the output precision of pressure measurements was generally to the nearest 1 hPa (except in the case of the Hunterston PMM measurement location, where the logger was programmed differently).

This led to a small but significant error in the measurement of pressure gradient and therefore the process of converting from temperature to potential temperature. Equation (20) can be applied to show that, at $T = 283K$, a $0.5hPa$ error in pressure measurement corresponds to a significant $0.04\mathrm{K}$ error in potential temperature measurement.

## 5.7 Data Coverage

For each mast, data coverage was checked to ensure that there was at least one year of measured data, in order that the data sets are representative of an annual cycle. Data was also checked to ensure that there was good data coverage in each calendar month, so as to avoid introducing seasonal bias.

In order to flag a 10-minute data period as valid, a calculation of virtual potential temperature gradient ($\Delta\theta_v$) must be possible so that at least two temperature sensors must be recording valid measurements (pressure and RH measurements were synthesised when not available).

If this minimum requirement is not met, $\Delta\theta_v$ cannot be calculated and the record for that period is invalid.

Notable periods of data loss occurred at Dogger Bank (masts had to be removed for structural repairs), Acharossan (faulty logger programme) and Strathy (faulty power supply). These resulted in many months lost data but did not affect the annual representation, as the data sets each spanned multiple years, including at least one of each calendar month.

In summary, the measurement campaign has resulted in satisfactory data sets being recorded at all measurement locations.

## 5.8 Uncertainty Assessment

### 5.8.1 Model Set-Up

In order for measured distributions of $\Delta\theta_v$ be used to validate WRF data, it is necessary to understand the level of confidence that we can have in the measured values (i.e. the total measurement uncertainty). To this end, a Monte-Carlo model was developed to statistically evaluate the standard error on $\Delta\theta_v$ for each mast configuration under consideration.

Monte-Carlo modelling is a method for assessing the likelihood of various outcomes (in this case, a range of values of $\Delta\theta_v$) from multiple input variables (in this case, individual measured quantities, each affected by measurement and other errors). In principle, the desired value ($\Delta\theta_v$) is calculated N times, each time randomly adjusting the input variables within their defined ranges. The resulting distribution of N output values can then tell us a lot about the measurement process. For example, the standard deviation of this distribution can be taken to be the net measurement error.

First, the domain of possible inputs was defined: for measurement of $\Delta\theta_v$, there are three 'raw' quantities being measured (temperature, pressure and relative humidity) and up to three error types for each measurement (measurement/calibration error, synthesis error and rounding error). In order to facilitate the calculation of $\Delta\theta_v$, some typical reference values of temperature, pressure and RH were calculated from the available measured data sets. The measurement types, error types, error ranges, typical reference values and probability distributions are summarised in Table 5.7.

For each scenario, the calculation of $\Delta\theta_v$ was iterated 100,000 times, where values of temperature, pressure and RH were permutated by random values from within ranges defined by the various sources of uncertainty under consideration. For measurement/calibration and data synthesis errors, the magnitude of the permutation was calculated according to a normal distribution with a mean value of zero and a standard deviation equal to the stated error. For data output precision errors, the permutation was calculated assuming an equal probability of values within the stated uncertainty range (i.e. uniform distribution).

The standard error on $\Delta\theta_v$ was then calculated as the standard deviation of all iterations with respect to the reference value of $\Delta\theta_v$.

| Error Type | Sensor | Units | Reference Value | | Error Range | Probability Distribution |
|---|---|---|---|---|---|---|
| | | | Lower | Upper | | |
| **Sensor Calibration Error** | Temperature | K | 282.5 | 283.0 | ±0.01 (TG01) ±0.03 (HMP155) | Normal |
| | Pressure | hPa | 990 | 1000 | (as per Table 5.5) | |
| | Relative Humidity | % | 90 | 90 | (as per Table 5.5) | |
| **Synthesis Error** | Pressure | hPa | 990 | 1000 | (as per Table 5.6) | |
| | Relative Humidity | % | 90 | 90 | (as per Table 5.6) | |
| **Rounding Error** | Pressure | hPa | 990 | 1000 | ±0.5 (Hunterston: ±0.005) | Uniform |

*Table 5.7: Monte-Carlo input values.*

Table 5.8 summarises the results of the site-specific uncertainty calculations for $\Delta\theta_v$, showing the evaluated standard error, $\sigma(\Delta\theta_v)$, for each measurement location, according to each location's specific measurement configuration and also the relative error, calculated as the standard error divided by the standard deviation of all *measured (i.e.* rather than simulated) $\Delta\theta_v$ values, $SD(\Delta\theta_v)$. While not a conventional approach to calculating the relative error, this gives a more useful view of the measurement error relative to the measured range of $\Delta\theta_v$ values than would be the case if dividing by the mean temperature differential, $\overline{\Delta\theta_v}$, since the mean is close to zero in all cases.

| *Site* | *Mast* | *Measurement Error (K)* $\sigma(\Delta\theta_v)$ | *Relative Error (%)* $\sigma(\Delta\theta_v)/$ $SD(\Delta\theta_v)$ |
|---|---|---|---|
| Acharossan | DDH | 0.04 | 5% |
| Bhlaraidh | CLB | 0.08 | 11% |
| Clyde | CSD | 0.08 | 8% |
| Dogger Bank | DBE | 0.06 | 9% |
| Dogger Bank | DBW | 0.06 | 9% |
| Glencassley | DLM | 0.08 | 10% |
| Greater Gabbard | IGMMX | 0.11 | 9% |
| Hunterston | PMM | 0.02 | 3% |
| Shetland | RNH | 0.07 | 10% |
| Shetland | SLF | 0.08 | 8% |
| Strathy | S8 | 0.08 | 7% |
| Stronelairg | SDB | 0.07 | 8% |
| Tangy | KLRI | 0.10 | 11% |
| Tangy | KLRII | 0.09 | 10% |

*Table 5.8: Measurement uncertainty for each measurement location, as calculated using each measurement configuration in a Monte-Carlo approach.*

### 5.8.2 Discussion

Table 5.8 highlights a significant spread in the total measurement errors for each of the fourteen configurations assessed; the best being Hunterston (± 0.02K) and the worst Greater Gabbard (± 0.11K). Table 5.1 is a good reference for explaining the main reason for this difference: Hunterston has co-located pressure, RH and temperature sensors whereas Greater Gabbard only has a single pressure sensor (so that the pressure at the second height must be synthesised). Also, the Greater Gabbard temperature and pressure sensors were calibrated less precisely and the pressure data rounded to nearest 1 hPa.

The main thing to note is that these error values are relatively small in relation to the daily and annual variation in $\Delta\theta_v$ that is being measured (typically of the order of 1K). However, there is an obvious preference to achieve a total error which is as low as practically possible. In summary, the key requirements, in terms of reducing total $\Delta\theta_v$ measurement uncertainty are:

- Purpose-designed temperature differential measurement systems, calibrated to ensure measurement error <0.01K, such as the WindSensor TG01 system.
- Pressure sensors at the height of each temperature sensor, with precision <=0.1 hPa.
- RH sensors at the height of each temperature sensor.

## 5.9 Site Descriptions

This section presents some key information on each of the eleven atmospheric stability measurement sites. Maps of these sites are provided in Figure 5.5 and Figure 5.6.

***Acharossan*** was a proposed SSE development site on the Cowal peninsula in Argyll, western Scotland. Complex terrain – prominent summit to the SE of measurement location. Otherwise, generally sloping down to coastline to the SW (sea loch). Almost completely enclosed by managed forestry but mostly at least 500m distant.

***Bhlaraidh*** is an operational wind farm site in the Scottish Highlands sited to the north of Loch Ness (32 x Vestas V112/117-3.45MW). Slightly complex with multiple lochans in immediate vicinity.

***Clyde Ext*ension** (Clyde Ext) is an operational SSE site made up of 54 x Siemens 3.2MW-101 turbines, energised in 2018. It is an extension to Clyde Wind Farm to the South-West (152 x Siemens 2.3MW-93 turbines). Measurements are from the pre-operational phase. The site is a network of steep-sided ridges. Some large nearby forestry blocks but generally at much lower elevation than mast.

***Hunterston*** is home to SSE's offshore wind turbine test facility (1 x Siemens 6.0MW & 1 x MHI-7.0MW), constructed on a former dry dock in the Firth of Clyde. The permanent met

mast (PMM) was used for power-performance measurement of test turbines. Flat semi-industrial landscape. Significant offshore fetch in the SW and W direction sectors.

***Glencassley*** is a proposed wind farm site in the Scottish Highlands. Slightly complex – general SW-NE slope.

***Strathy*** is a proposed wind farm site in the Scottish Highlands. Measurement location is surrounded by 10-15m coniferous commercial forestry.

***Stronelairg*** is an operational SSE wind farm site (67 x Vestas V112/117-3.6MW). Measurements from pre-operational phase. Slightly complex.

***Viking*** is a proposed SSE wind farm site (103 x turbines) on the Shetland mainland. Complex around both primary masts. Coastline within 1-2km of both.

***Tangy*** is a SSE wind farm site (22 x Vestas V52) on the Kintyre peninsula. Complex, with coastline 1.5km west of primary measurement location. CNG mast (secondary mast) is within forestry block.

***Greater Gabbard*** is an operational SSE offshore wind farm located off the coast of East Anglia (140 x Siemens 3.6MW-107m).

***Dogger Bank*** is an offshore wind farm development site, in which SSE shares a commercial interest.

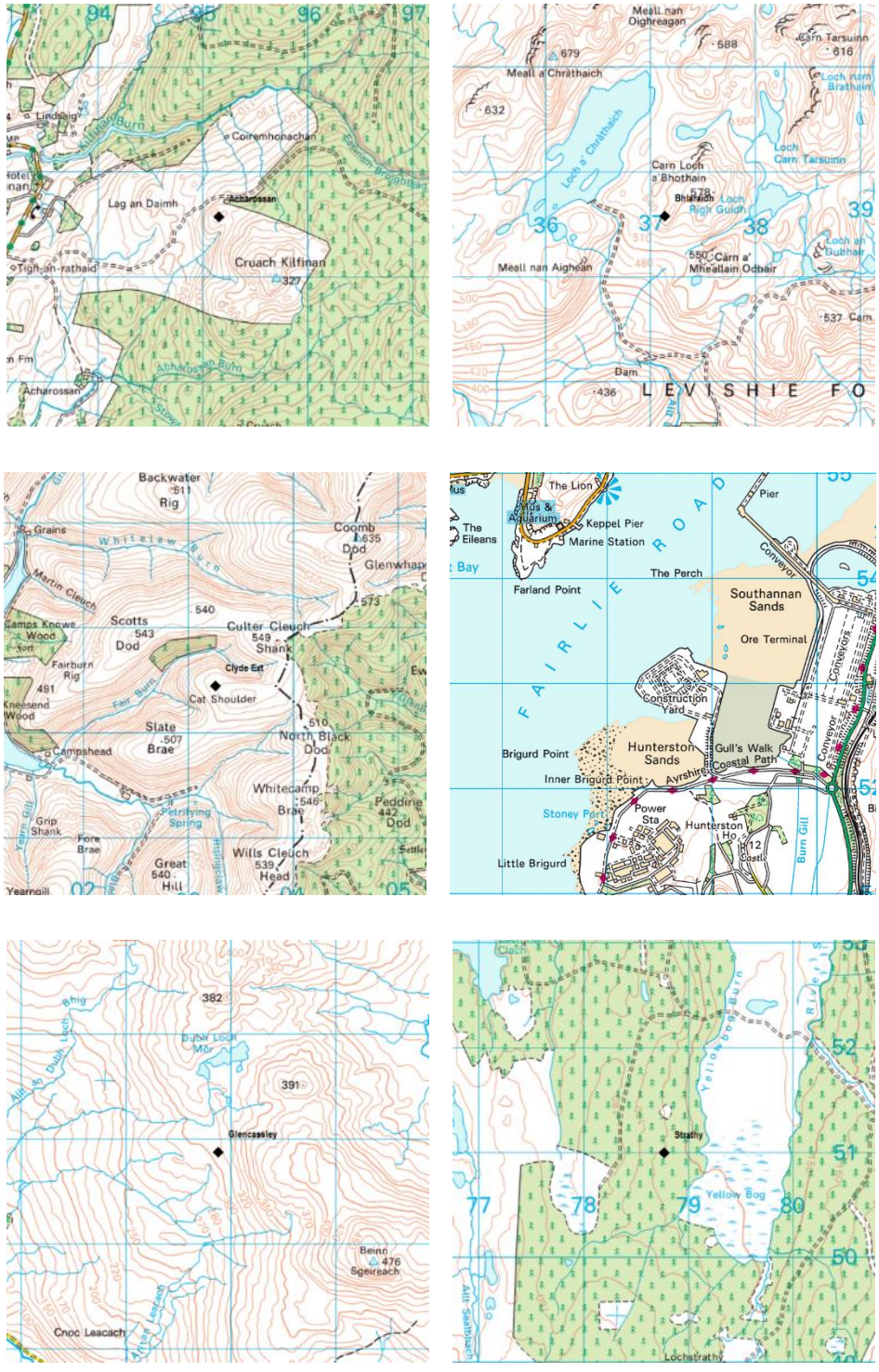


*Figure 5.5: Site maps of atmospheric stability measurement locations: Acharossan, Bhlaraidh, Clyde Ext, Hunterston, Glencassley and Strathy* [77].

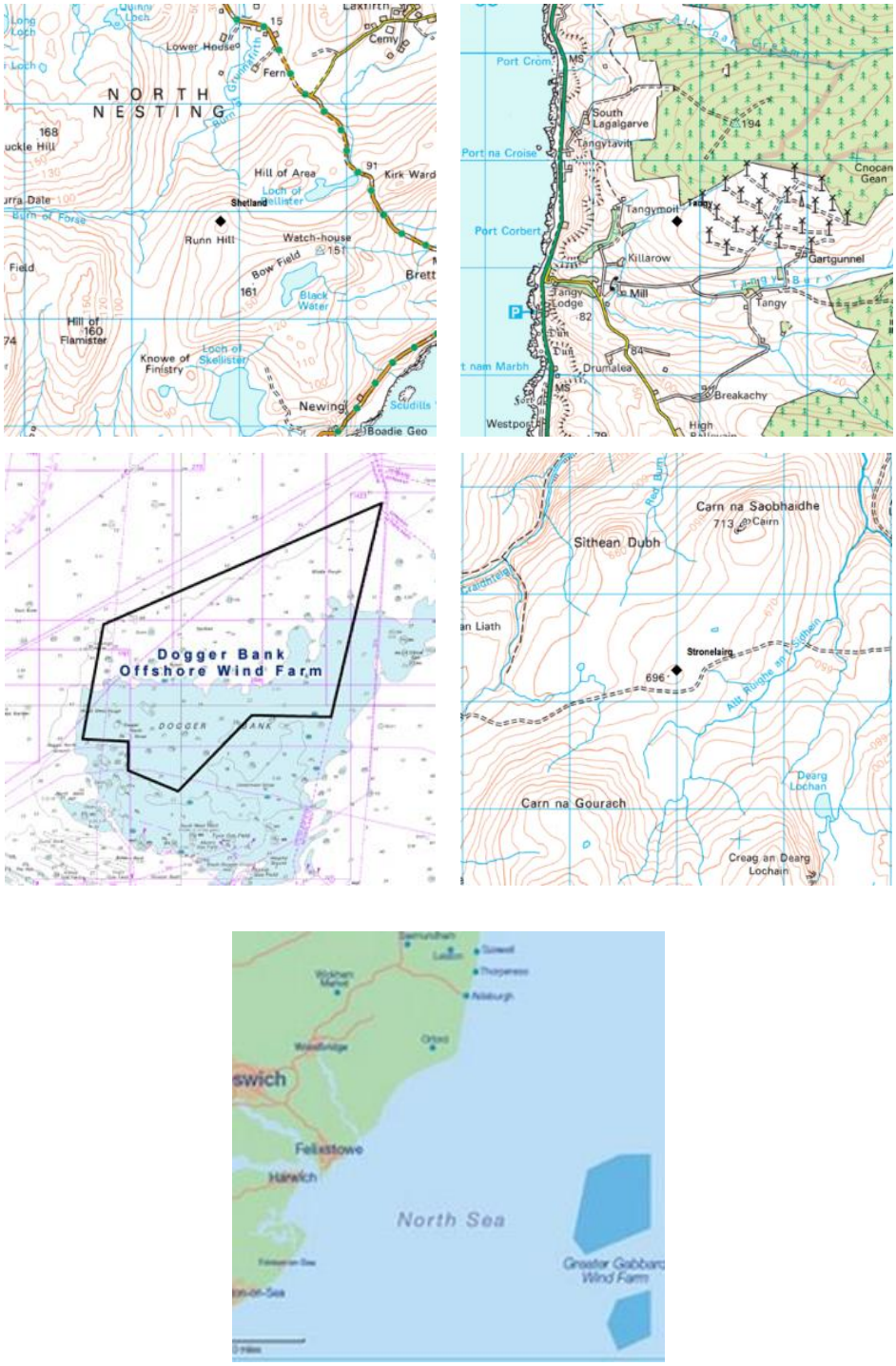


*Figure 5.6: Site maps of atmospheric stability measurement locations: Shetland (RNH), Tangy, Dogger Bank (DBE & DBW), Stronelairg and Greater Gabbard* [77].

## 5.10 Comparison of measurement techniques: TG01 vs HMP

### 5.10.1 Introduction

At nine measurement locations, both a primary and secondary temperature differential measurement system were installed.

At eight measurement locations, one WindSensor TG01 system and one pair of HMP155 sensors were installed. The TG01 is a purpose-designed system which, through its design and calibration process achieves a lower stated measurement error than the HMP155 (combined error of 0.01K for the TG01 sensor pair, compared to 0.03K for each HMP155 sensor). The drawback of the TG01 system is (i) greater cost and (ii) it is unable to give an absolute temperature measurement, in addition to the temperature differential measurement (it must be combined with at least one other type of temperature sensor so that both temperature differential and absolute temperature can be measured).

Additionally, at one measurement location (Tangy) there was, for an initial period before the measurement mast was refurbished, a TG01 system co-located with a pair of uncalibrated Campbell Scientific CS215 temperature sensors.

This section presents a thorough comparison of the TG01 (primary) against secondary virtual potential temperature differential ($\Delta\theta_v$) measurements. The main aim of this exercise is to demonstrate mutual validation of measurements from two partly independent measurement systems. It is desirable to understand whether either the HMP155 or CS215 system can be used as a cheaper, more useful alternative at future measurement sites.

In terms of pre-processing; temperature, pressure and RH measurements were used to calculate a value of $\Delta\theta_v$ for each time step employing a calculation method which has already been well established. It is worth noting that for the TG01 measurement, $\Delta\theta_v$(TG01), the conversion from potential temperature to virtual potential temperature necessarily used the measurement of absolute temperature from the secondary system (HMP155 or CS215). This means that the two measurements of $\Delta\theta_v$ are not strictly independent of one another.

### 5.10.2 All data

Figure 5.7 shows the results of a simple correlation between $\Delta\theta_v$ measured using the WindSensor TG01 system ($\Delta\theta_v$ (TG01)) and $\Delta\theta_v$ measured using the secondary system (2 x Väisälä HMP155 (all except Tangy) or 2 x Campbell Scientific CS215 (Tangy)). Due to the length of the data sets, it is not practical to visualise all the data so the correlation has been plotted as a series of 0.25K bin averages with error bars showing the standard deviation within each bin. Parity (y=x) is shown by a blue line through the origin.

Generally, the correlations are good with $R^2$ values in the range 0.94 (Clyde Ext - CSD) to 1.00 Strathy - S8). Hunterston (PMM) and Stronelairg (SDB) exhibit some divergence in the extremely unstable ($1 < \Delta\theta_v < 2$) region but this stability range is highly infrequent (i.e. possibly spurious data).

Immediately, Tangy (KLR I) presents itself as potentially problematic. The correlation between the primary and secondary systems is good ($R^2$=0.97) but there is a very significant offset: the secondary system (2 x CS215) is under-estimating $\Delta\theta_v$ by around 0.4K compared to the primary system (TG01). This issue is investigated further in the following sections.

### 5.10.3 Wind Speed Dependency

The effects of wind speed on temperature measurement pose a problem for high-precision applications: higher wind speed can lead to greater localised temperature variation (i.e. warm and cold spots) in the vicinity of temperature sensors.

The technological solution to this problem is to use aspirated temperature sensors, which use a powered fan to maintain a consistent flow of air through the measurement chamber. However, the power requirements and likelihood of failure prohibit this being a viable solution for remote measurements such as presented here.

The next best solutions are to utilise radiation shields which constrain wind flow across the sensor and also to ensure that upper and lower sensors are mounted identically so that any wind speed effects are at least as consistent as possible across both instruments (so that the

temperature differential measurement is not significantly affected, even if both the upper and lower temperature measurements are affected).

Figure 5.8 shows the dependence of absolute measurement discrepancy ($\Delta\theta_v$ (TG01) - $\Delta\theta_v$ (Secondary)) on wind speed, as measured using the top-most anemometer on each measurement mast. Average measurement discrepancy has been calculated for 1m/s width wind speed bins in the range 0 to 25m/s, with error bars showing the standard deviation within each bin.

At five out of nine sites, there is no noticeable trend in average discrepancy or standard deviation of discrepancy with wind speed, which is desirable. At Acharossan (DDH), average discrepancy is fairly consistent but the discrepancy becomes much more variable in the wind speed region above around 15m/s. At Strathy (S8), the same is true, as well as there being a significant (up to 0.25K) mean measurement discrepancy in the same wind speed range. One possible explanation for this is that the Strathy (S8) measurement location is surrounded by forestry, resulting in very high wind shear. This means that the upper sensors might experience significantly greater localised temperature variation than the lower sensors and, if one sensor type was more vulnerable to this effect than the other, this would show up as a measurement discrepancy between the two systems. At Hunterston (PPM), the converse can be observed: a tendency for the TG01 system to under-predict $\Delta\theta_v$ relative to the HMP155 system in the wind speed range below about 5m/s. This is less readily explained by localised temperature variation. At Tangy (KLR I), as well as the 0.4K offset which has already been established, there does seem to be slight convergence of measured $\Delta\theta_v$ as wind speed increases.

### 5.10.4 Wind Direction Dependency

Figure 5.9 shows the dependence of absolute measurement discrepancy ($\Delta\theta_v$ (TG01) - $\Delta\theta_v$ (Secondary)) on wind direction sector, as measured using the top-most wind vane on each measurement mast. Average measurement discrepancy has been calculated for 10° width wind direction sector bins, with error bars showing the standard deviation within each bin.

This check was conducted mainly to investigate the possibility that wind-induced localised temperature variation effects on temperature measurements might be more prevalent from some directions than others due to, for example, flow distortion effects around the measurement mast structure or horizontally mis-aligned instrument shields. However, this does not appear to be the case to any noticeable degree at most measurement masts.

Some directional dependence is evident at Bhlaraidh: a much greater variation in discrepancy around 270° (which is a highly frequent direction sector). However, no technical explanation could be identified for this discrepancy in terms of the instrumentation set-up.

### 5.10.5 Temperature Dependency

Figure 5.10 shows the dependence of absolute measurement discrepancy ($\Delta\theta_v$ (TG01) - $\Delta\theta_v$ (Secondary)) on ambient temperature, as measured using the primary temperature sensor on each measurement mast. Average measurement discrepancy has been calculated for 1˚C width temperature bins in the range -5 to 10 ˚C, with error bars showing the standard deviation within each bin.

The purpose of this check was to highlight any measurement discrepancy due to divergent response rates of the temperature sensors systems in different temperature ranges. Tangy (KLR I) can be seen to have a strong dependence on temperature, with measurement discrepancy decreasingly steadily from 0.5K at $T$≒- 5°C to 0.3K at $T$≒10°C. Possible reasons for this trend are (i) instrument quality (e.g. non-linear response rate) (ii) inadequate shielding or mounting (e.g. one CS215 sensor receiving more direct solar heating than the other).

### 5.10.6 Time Dependency

Figure 5.11 shows the variation in absolute measurement discrepancy ($\Delta\theta_v$ (TG01) - $\Delta\theta_v$ (Secondary)) on wind speed over the measurement period (omitting any data gaps). The time series has been broken into 20 subsets and the average measurement discrepancy has been calculated within each, with error bars showing the standard deviation within each subset.

Notably, the measurement discrepancy at Tangy (KLR I) seems to show a regular annual variation. This bolsters the findings of the previous section (Figure 5.10): the measurement discrepancy is lowest in Summer (higher ambient temperature) and greatest in Winter (lower ambient temperature).

Bhlaraidh and Clyde Ext both show divergences in time periods corresponding to winter. This ties in with observations of increases in standard deviation at low temperature and might suggest the influence of snow/ice formation on one or more temperature sensors. However, the influence of ice formation in these specific periods could not be corroborated by analysis of concurrent wind speed/direction data.

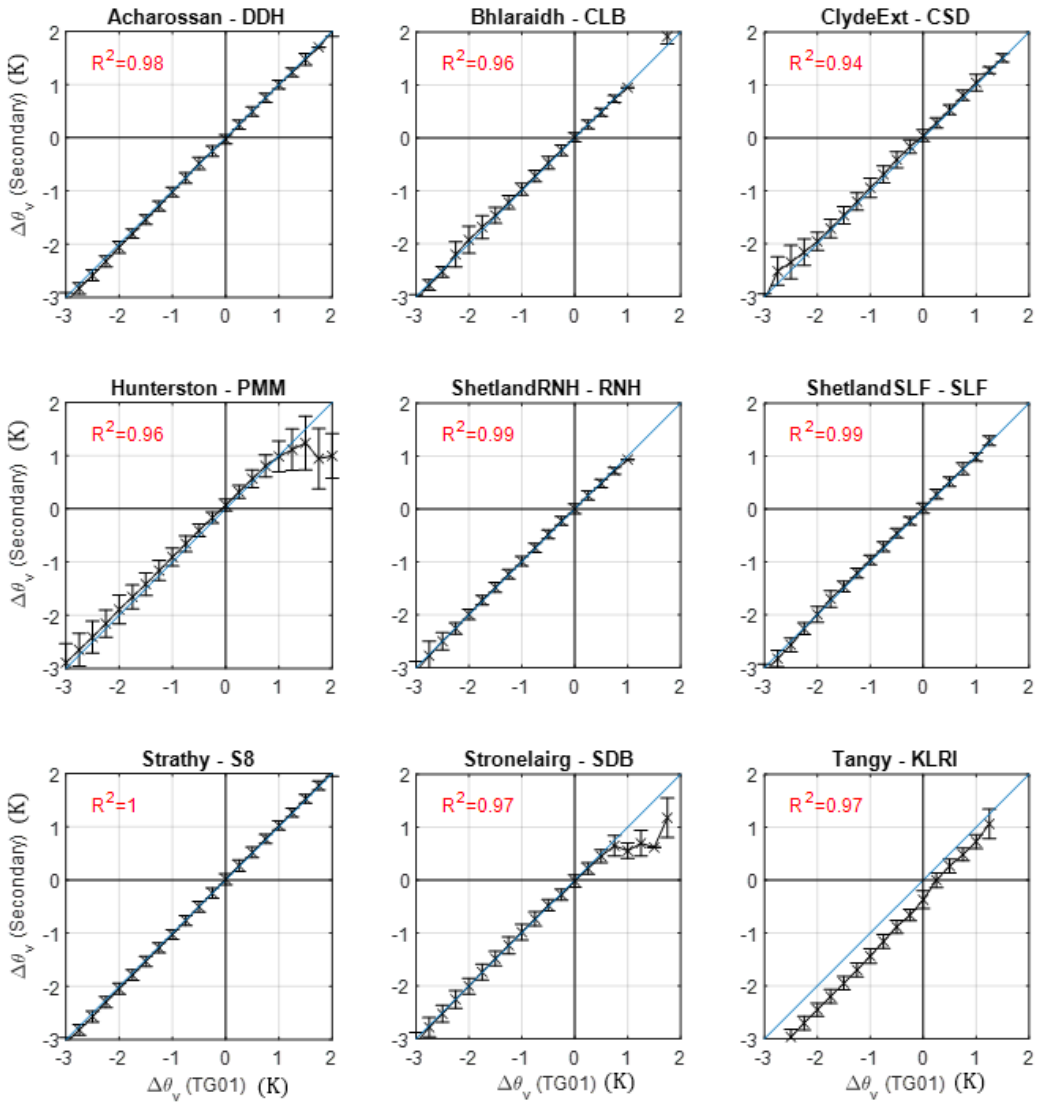


*Figure 5.7: Correlation of temperature offset using both primary (TG01) and secondary (HMP155 or CS215) temperature sensors. Blue line is parity (y=x).*

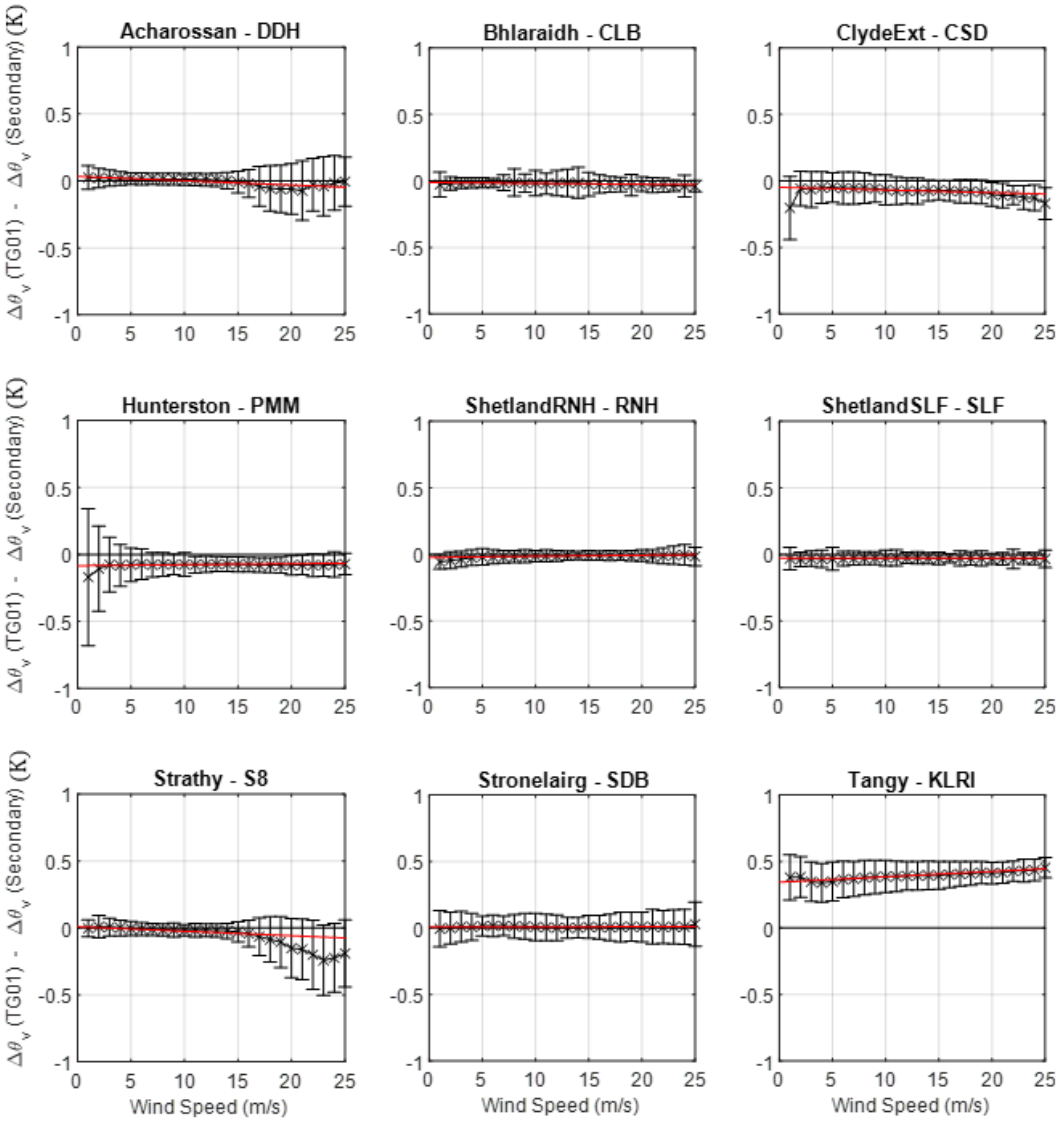


*Figure 5.8: Measurement discrepancy ($\Delta\theta_v$ (TG01) - $\Delta\theta_v$ (Secondary)) binned by **wind speed** for each of nine measurement locations. Average measurement discrepancy has been calculated for 1m/s width wind speed bins in the range 0 to 25m/s, with error bars showing the standard deviation within each bin. Red line shows line of best fit through the measurement discrepancy data.*

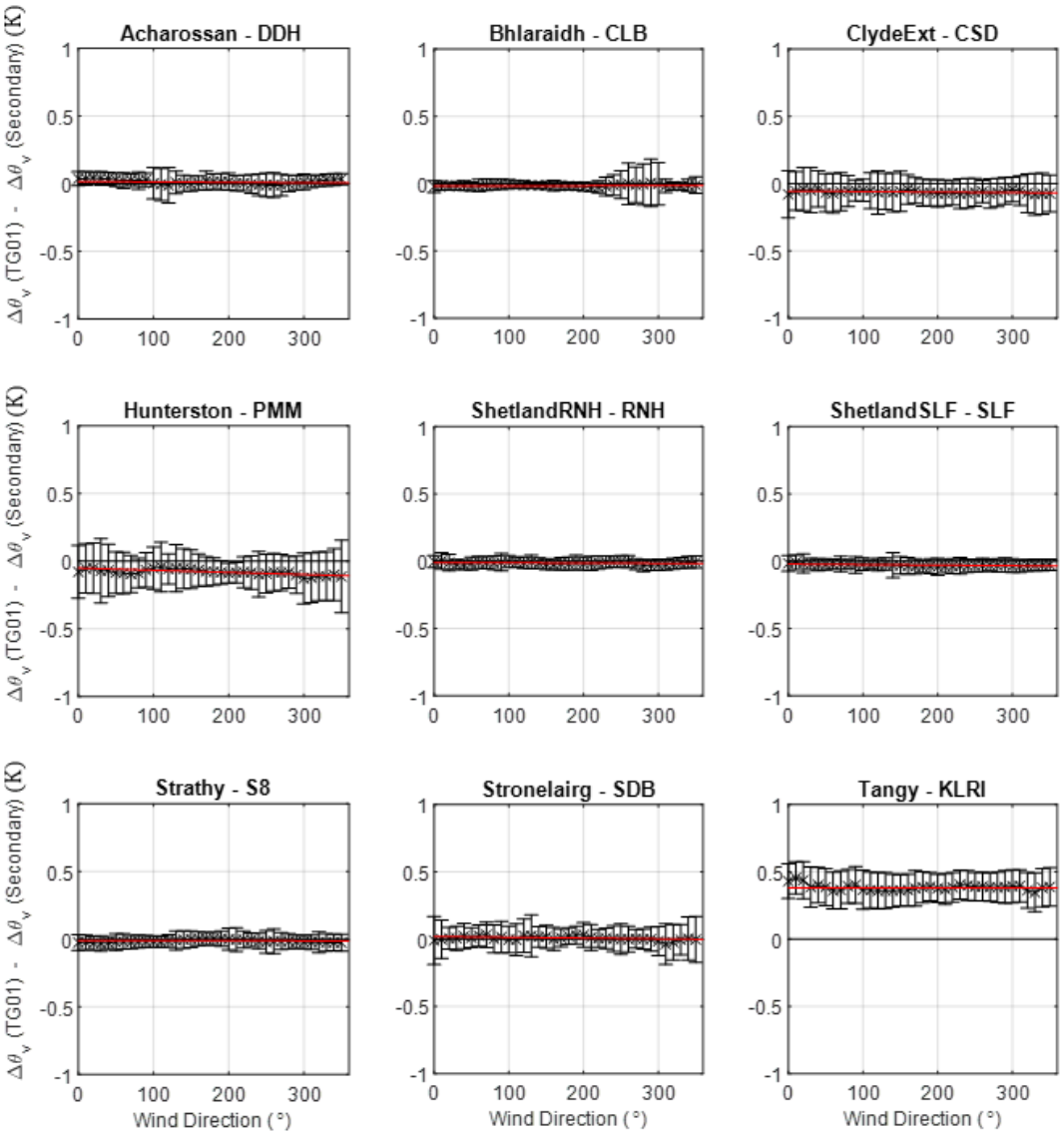


*Figure 5.9: Measurement discrepancy ($\Delta\theta_v$ (TG01) - $\Delta\theta_v$ (Secondary)) binned by **wind direction sector** for each of nine measurement locations. Average measurement discrepancy has been calculated for 10˚ wind direction bins, with error bars showing the standard deviation within each bin. Red line shows line of best fit through the measurement discrepancy data.*

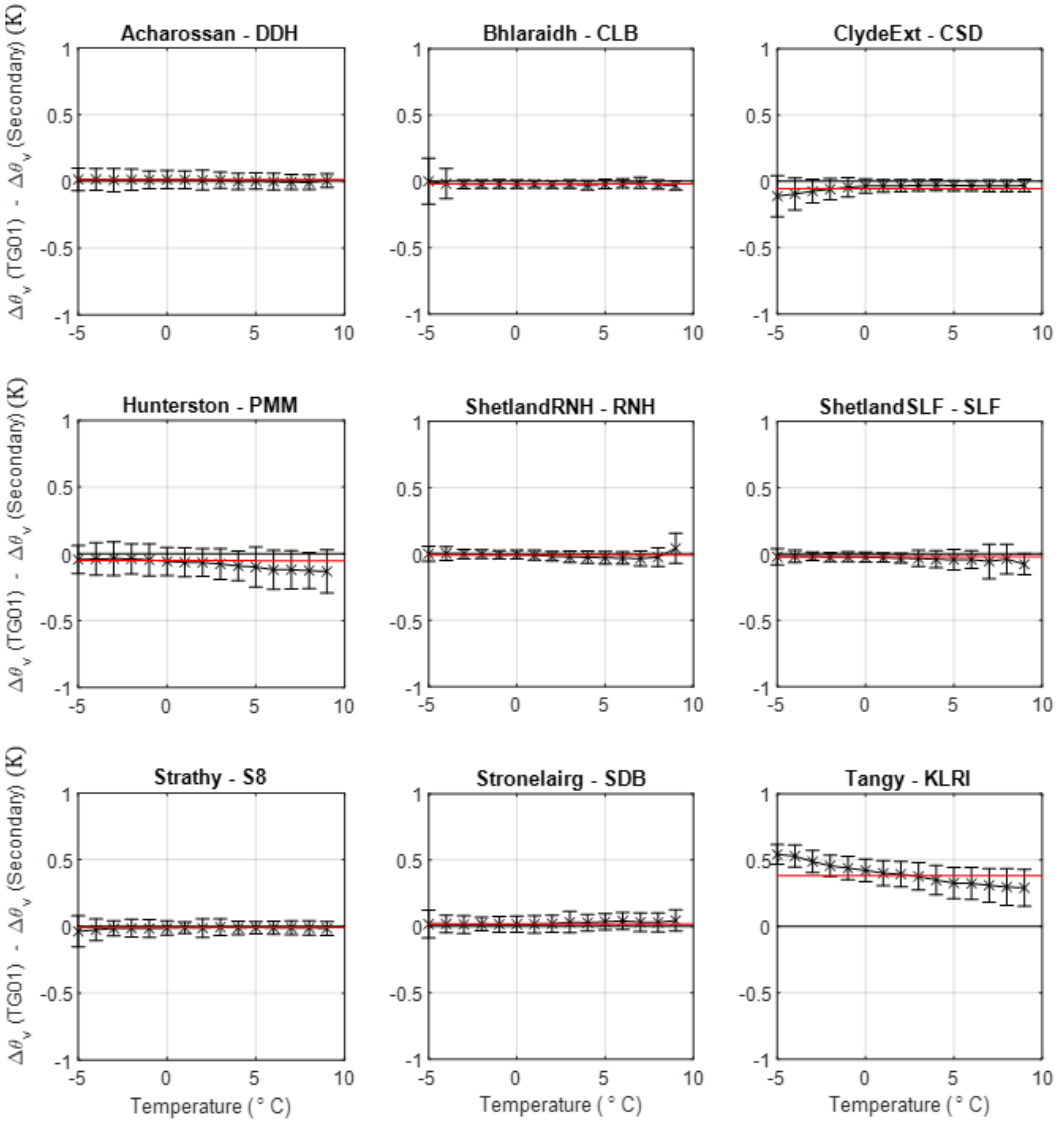


*Figure 5.10: Measurement discrepancy ($\Delta\theta_v$ (TG01) - $\Delta\theta_v$ (Secondary)) binned by **ambient temperature** for each of nine measurement locations. Average measurement discrepancy has been calculated for 1˚C ambient temperature bins for the range -5 to 10 ˚C, with error bars showing the standard deviation within each bin. Red line shows line of best fit through the measurement discrepancy data.*

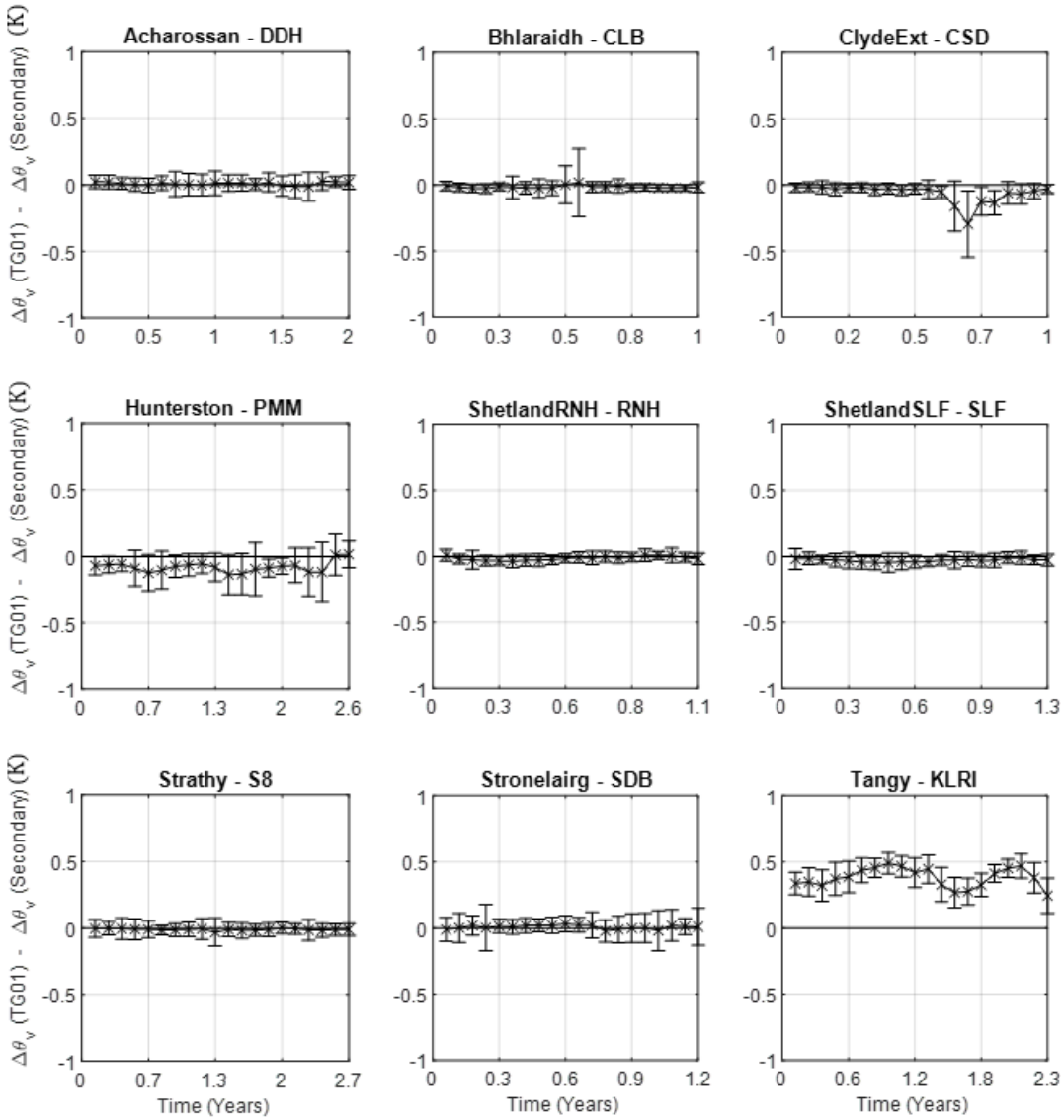


*Figure 5.11: Measurement discrepancy ($\Delta\theta_v$ (TG01) - $\Delta\theta_v$ (Secondary)) plotted as **time series** for each of nine measurement locations. To aid visualisation, each time series has been down-sampled into 20 sub-sets, with error bars showing the standard deviation within each sub-set.*

### 5.10.7 Section Summary

This section has demonstrated good agreement between two methods of measuring virtual potential temperature differential, using independent sensor systems. This demonstration is significant in terms of giving confidence in the measured values of virtual potential temperature differential.

Calibrating and bias-correcting the HMP155 sensors was a significant step in terms of achieving this alignment. The CS215 sensors at Tangy can be seen to compare very poorly to the TG01 system – possibly due to a combination of not having been calibrated/bias-corrected and potentially an additional issue around instrument quality, mounting and/or insufficient shielding.

## 5.11 Dependence of wind characteristics on stability

In Chapter 2, the various expected relationships between atmospheric stability and various wind flow parameters were introduced. Later, in Chapter 6, the ability of CFD modelling to predict such relationships will be investigated. Now, as an interim step, analysis is presented to show that these relationships are indeed evident in the measured data.

This series of checks was conducted for 12 masts equipped with temperature differential measurement systems. The measurement location at Dogger Bank West (DBW) was omitted as the conditions do not deviate appreciably from Dogger Bank East (DBE), to avoid effective duplication.

### 5.11.1 Shear

Shear exponent (α) was calculated for every timestep in each measured data set using a combination of at least three anemometers at different heights on each mast, according to equation (61). α was evaluated as the straight-line gradient through measured mean wind speeds plotted against measurement heights on log-log axes. Then, the data sets were filtered into stable ($\Delta\theta_v < -0.125\mathrm{K}$), neutral ($-0.125\mathrm{K} < \Delta\theta_v < 0.125\mathrm{K}$) and unstable ($\Delta\theta_v > 0.125\mathrm{K}$) sub-sets (note this is a different categorisation to that used for visualisation in Chapter 4) . Only three stability classes were considered in order to avoid having spurious

data in infrequent stability classes. Finally, the stability-filtered sub-sets were binned into 12 direction sectors, in order to isolate stability effects from other effects, such as topography and forestry.

Figure 5.12 shows mean wind shear exponent binned into twelve direction sectors and filtered by stability class (stable (blue), neutral (green) or unstable (red)). Sectors where mast shading might have affected the shear exponent measurement were not removed from the check but have been highlighted in yellow and can be disregarded.

In all cases, the expected trend is observed: greatest shear in all direction sectors during stable conditions and lowest shear during unstable conditions, with neutral conditions lying between. The unfiltered average generally lies close to the most frequently occurring stability class at each measurement location.

### 5.11.2 Turbulence Intensity

Turbulence intensity was calculated using equation (73) for each time step, and similarly binned by direction sector and filtered for $\Delta\theta_v$. Figure 5.13 shows TI for stable, neutral and unstable conditions. Again, the expected trend is observed: higher TI in unstable conditions (due to convective vertical mixing of horizontal momentum), lower TI in stable conditions (due to the absence of the same) and neutral as an intermediate state.

### 5.11.3 Inflow Angle

Inflow angle was extracted directly from 3D ultrasonic (US) measurements, for those nine sites with sufficient overlapping $\Delta\theta_v$ and US measurements. A working theory had been that inflow angle might increase in unstable conditions due to the combination of horizontal advection with increased convective vertical air movement.

Figure 5.14 shows inflow angle for stable, neutral and unstable conditions. Although there is significant variation in inflow angle by direction (which may or may not be due to non-horizontal instrument alignment), there is no discernible relationship between inflow angle and $\Delta\theta_v$. These plots exhibit some outliers in unstable conditions (e.g. Shetland SLF at 180˚ and Stronelairg at 240˚) but this was inconclusive due to low data count in these bins.

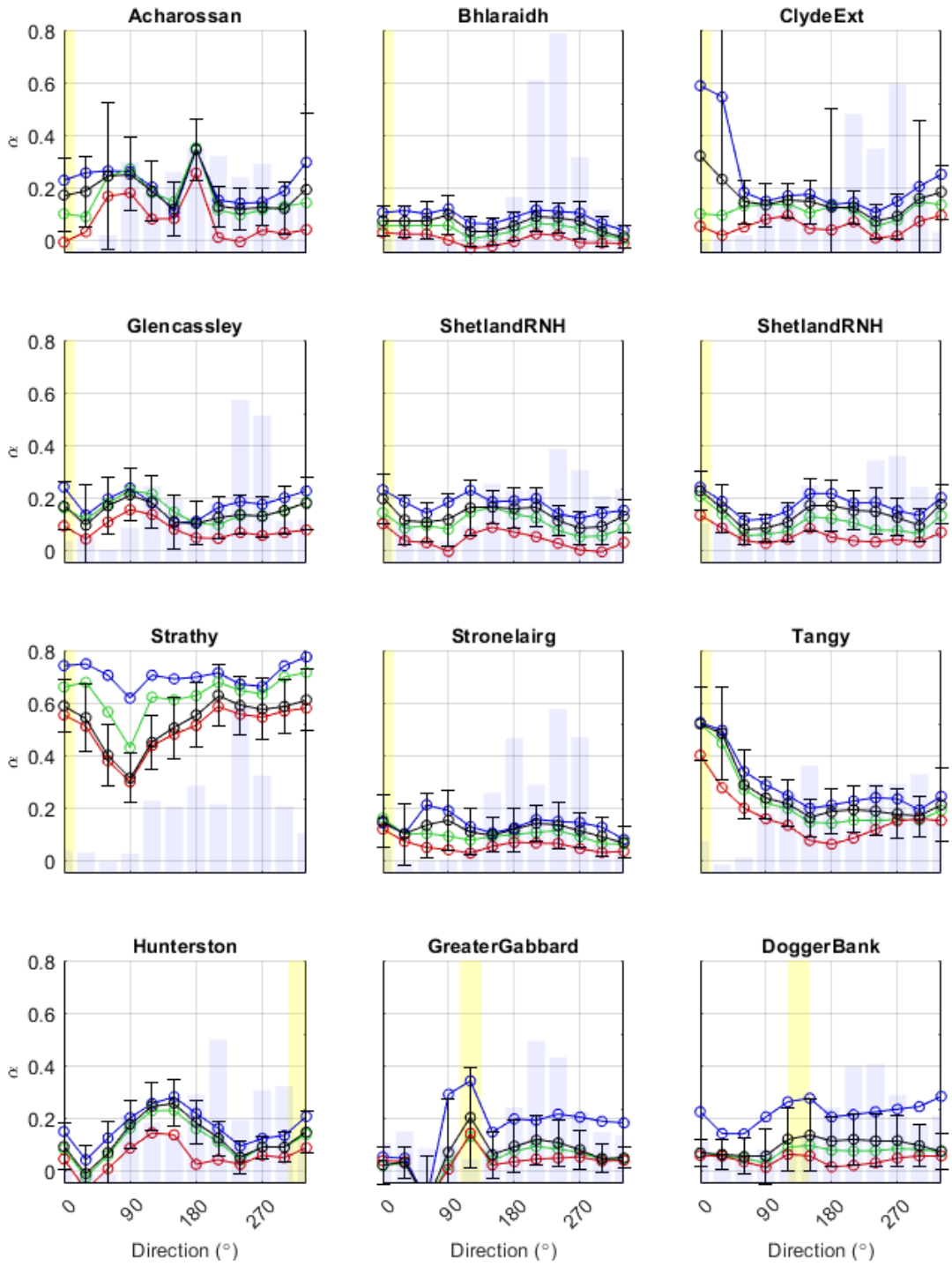


*Figure 5.12: Wind shear exponent by direction for stable (blue), neutral (green), unstable (red) and all (black) conditions at twelve measurement locations. Errors bars indicate standard deviation for all records (black). Blue histogram shows frequency of occurrence of each direction sector. Sectors with mast interference highlighted yellow.*

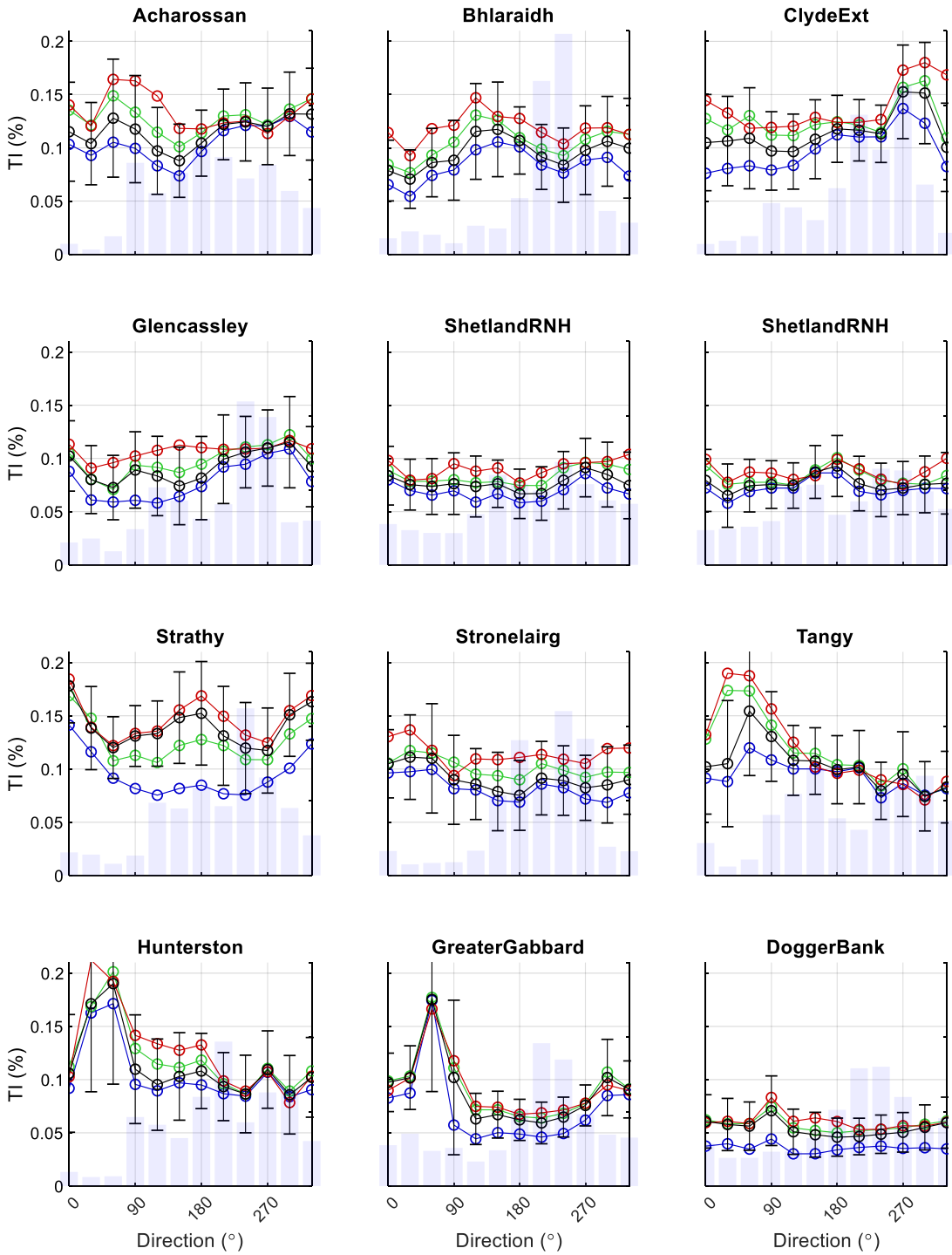


*Figure 5.13: Turbulence intensity by direction for stable (blue), neutral (green), unstable (red) and all (black) conditions at twelve measurement locations. Errors bars indicate standard deviation for all records (black). Blue histogram shows frequency of occurrence of each direction sector.*

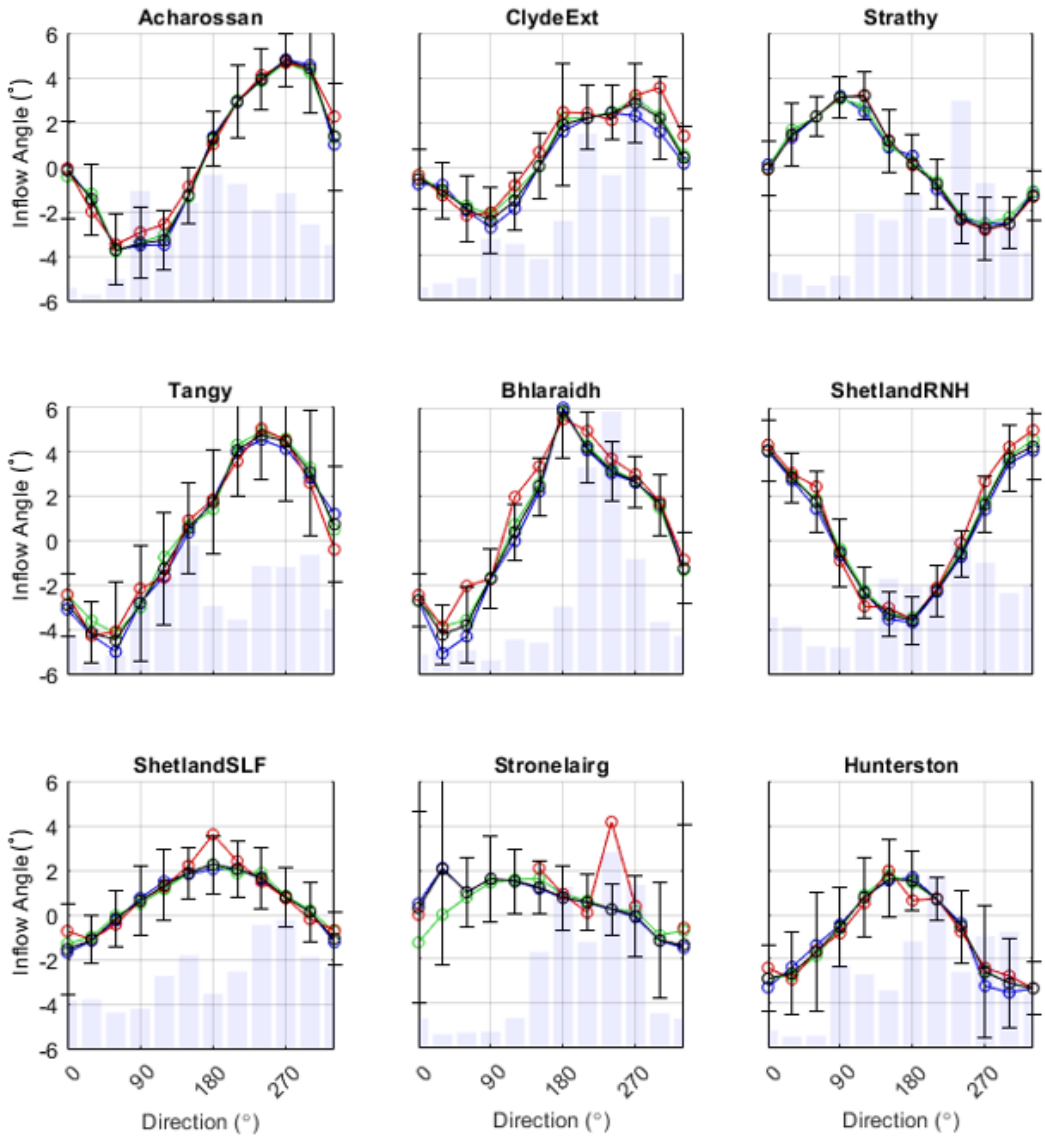


*Figure 5.14: Inflow angle by direction for stable (blue), neutral (green), unstable (red) and all (black) conditions at twelve measurement locations. Errors bars indicate standard deviation for all records (black). Blue histogram shows frequency of occurrence of each direction sector.*

### 5.11.4 Wind Speed Ratio

Figure 5.16 shows the wind speed ratio (WSR, the ratio of concurrent wind speed at one measurement location to another on the same site) for twelve sites. This is an important value in terms of wind flow modelling, as it tests the sensitivity of extrapolating wind distributions between the measurement location and proposed turbine locations to atmospheric stability.

Looking first at the unfiltered mean values for each sector (black), significant variation can be seen depending on wind direction for all mast pairs. Considering two masts at Bhlaraidh named 'CLB' and 'LRD' (3rd row; 1st column), the wind speed ratio (CLB/LRD) is greater than one in all direction sectors. This is due to the greater elevation of the CLB mast, which will result in higher wind speed in all atmospheric conditions.

Unstable (red) and stable (blue) conditions can be seen to result in a significant (~10%) difference in WSR between these two measurement points across all direction sectors. More importantly, there is some subtle but significant variation between wind speed ratio in neutral conditions (green) and unfiltered conditions (black). The weighted-average neutral WSR is 0.5% lower than the unfiltered equivalent across all direction sectors; up to 6.7% lower in the 105 - 135˚ direction sector.

This is an important finding: wind flow at this site can be seen to vary significantly with atmospheric stability and the average flow deviates significantly from flow in neutral conditions. If a CFD simulation assuming neutral conditions, which is otherwise perfectly accurate, were to be used to model this site, it would result in a 0.5% (or, in the worst-case direction sector, 6.7%) underprediction of wind speed for a turbine at the location of LRD, predicted from CLB. This translates to approximately to a 0.5% underprediction in that turbine's energy yield and therefore revenue. In the case of a turbine at the location of CLB, predicted from LRD, it would be an equivalent over-prediction.

Similar and even greater levels of variation between neutral and unfiltered observations can be observed in all mast-pairs presented. This variation will have greater impact in terms of under- or over-estimate in those direction sectors with greater frequency of occurrence.

### 5.11.5 Section Summary

This section has demonstrated a dependency of key wind flow metrics (shear, TI and wind speed ratio) on atmospheric stability as categorised according to virtual potential temperature differential, $\Delta\theta_v$. Further this dependence aligns with expectations from the literature (e.g. high shear and low turbulence in stable conditions). Importantly, this lends confidence to the use of $\Delta\theta_v$ as a proxy for defining and modelling atmospheric stability.

The magnitude of variation in wind shear, TI and, in particular, wind speed ratio is significant enough, such that predictions of wind turbine energy yield would be expected to diverge under different atmospheric stability conditions.

This set of observations serves as a prelude to Chapters 6 and 7; the aim of which, in certain terms, is to find a way to model the true spread of atmospheric stability states, instead of only neutral conditions and then to quantify the impact of doing so.

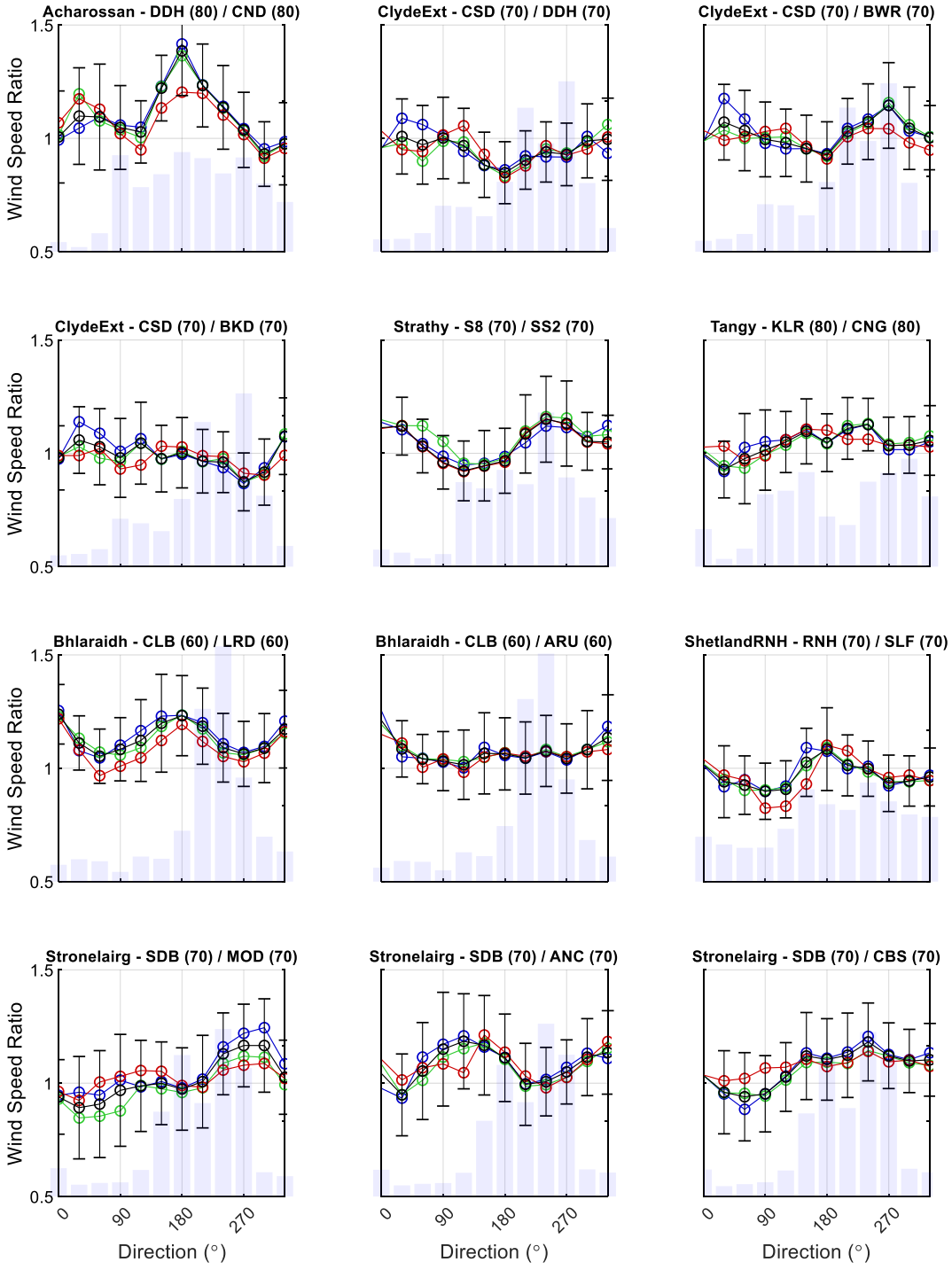


*Figure 5.15: Ratio of wind speed between nine mast pairs by direction for stable (blue), neutral (green), unstable (red) and all (black) conditions at twelve measurement locations. Errors bars indicate standard deviation for all records (black). Blue histogram shows frequency of occurrence of each direction sector.*

## 5.12 Comparison with modelled (Vortex) data

In this final section, distributions of $\Delta\theta_v$ evaluated from Vortex WRF mesoscale data (the processing and analysis of which was covered in Chapter 4) are correlated and compared with measured data for multiple sites.

The key aim is to ascertain whether Vortex WRF data (which are cheaper, quicker and easier to acquire) are a suitably accurate substitute for measured data.

### 5.12.1 Pre-processing

For each site, first the Vortex data for the model heights most closely matching the measurement heights were imported into MATLAB and a linear interpolation algorithm was run to convert the hourly time series to 10-min values. Then the measured data were imported and an inner-join function was used to create a single data set, aligned by time-stamp, with non-concurrent periods discarded. A query was run to identify and remove any null $\theta_v$ values in the Vortex or measured data sets from the combined set.

### 5.12.2 Synchronicity Checks

Although the data sets are now ostensibly synchronised according to their timestamps, it is necessary to check for potential time offsets between one data set and the other. These could be due to (i) incorrect or inconsistent time-stamping of either the measured (e.g. time stamp represents end, rather than start or centre of the averaging window or; (ii) physical distance between the measurement location and the nearest WRF grid node, creating a small time lag between the two. The timestamp of the Vortex data corresponds to the instantaneous sample time.

To check the synchronicity, the $\Delta\theta_v$(Mast) and $\Delta\theta_v$(Vortex) were correlated and the $R^2$ value of a linear regression was calculated. Then $\Delta\theta_v$(Vortex) was offset in the time domain by one time stamp (10 mins) and the correlation repeated. This was repeated for offsets of -125 timestamps (20.8 hours) to +125 timestamps.

Figure 5.16 shows the results of this check. In all cases, a distinct peak $R^2$ is identifiable. The width of the peak is an indication of the shorter-term temporal variability of the stability

climate: onshore sites have narrow peaks (high variability) whereas offshore sites have wider peaks (low variability). The most significant difference was at Greater Gabbard where an offset of one hour was apparent.

A decision was taken to select the offset value corresponding to the peak $R^2$ and apply this to the $\Delta\theta_v$(Vortex) time series for the purposes of subsequent correlations.

### 5.12.3 Correlation

Figure 5.17 shows the final correlation between $\Delta\theta_v$(Mast) and $\Delta\theta_v$(Vortex), including time offset, where the plotted values are the mean $\Delta\theta_v$ (Vortex) values corresponding to $\Delta\theta_v$ (Mast) bins of 0.25K width. The vertical error bars show the standard deviation of $\Delta\theta_v$ (Vortex) values within each bin and the horizontal error bars correspond to the standard measurement error as calculated in section 5.8. The latter can be seen to be much less significant.

The plotted data shows a tendency for Vortex to over-predict the magnitude of $\Delta\theta_v$ in the stable region (-4K < $\Delta\theta_v$ < 0K) by approximately 0.1 – 0.5K. Also, there is a very distinct under-prediction of the magnitude of $\Delta\theta_v$ in the unstable region (0K < $\Delta\theta_v$ < +2K) which suggests a fundamental inability of either WRF or the underlying reanalysis data to simulate all but the most subtle unstable conditions. However, the latter range occurs far less frequently, meaning that the former effect is greater and the overall bias in the Vortex data is towards stable conditions.

Table 5.9 summarises the Mean Absolute Error (MAE) and Mean Bias (MB) observed in each correlation. The MAE is useful for judging the ability of Vortex data to match measured data over a short time period. The MB is more useful for judging the similarity between overall long-term distributions. On the basis that the mean bias values are small compared to the full range of $\Delta\theta_v$ in the modelled distribution (typically a range spanning >3K), the Vortex data are considered to be suitable for use in defining long-term $\Delta\theta_v$ distributions, with no systematic corrections necessary. The larger MAE values suggest that Vortex data might not be as suitable for short-term prediction applications such as $\Delta\theta_v$ forecasting of individual hourly periods.

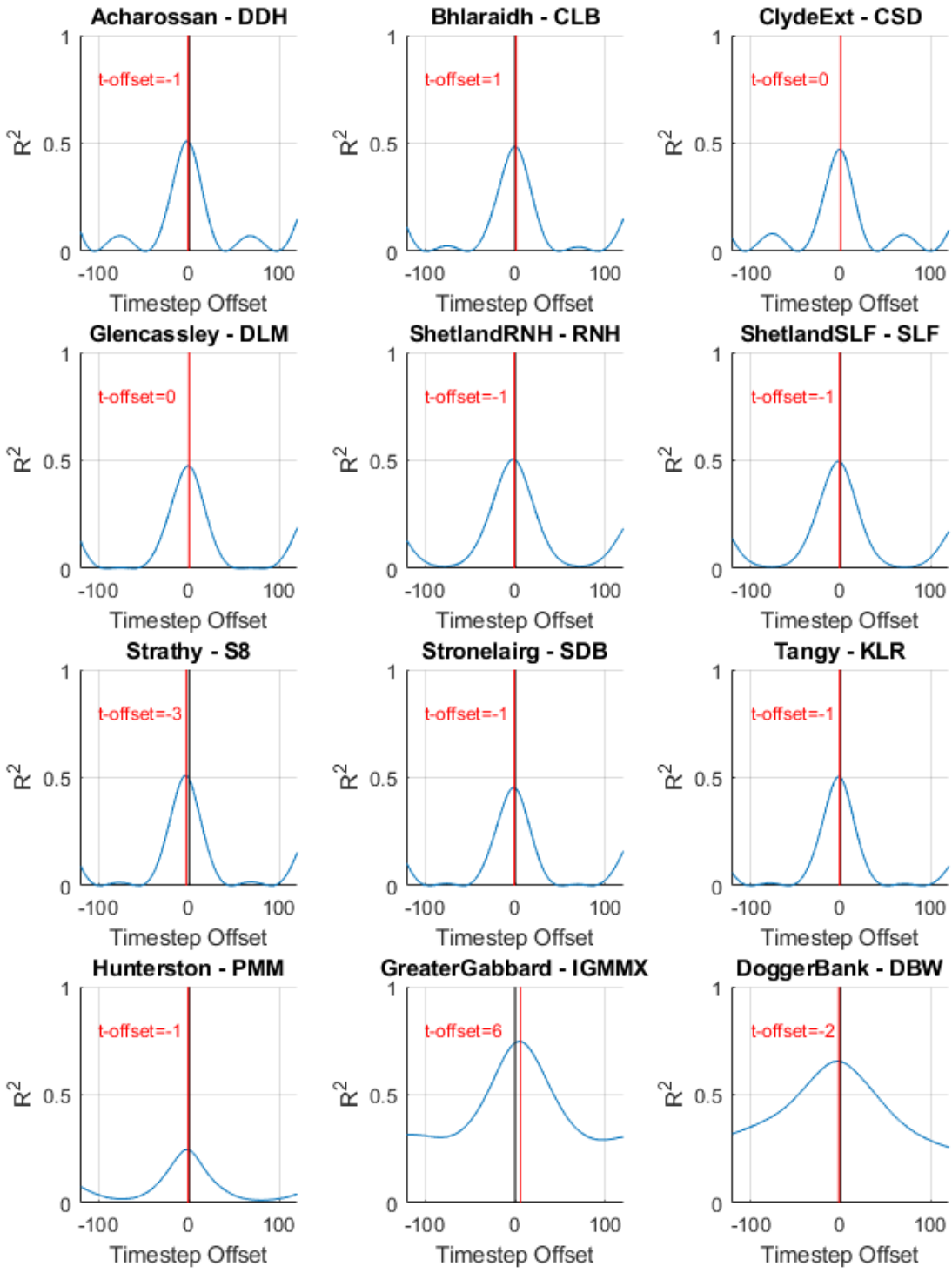


*Figure 5.16: Showing the variation in $R^2$ with varying time-shift between measured and Vortex data sets. The vertical red line shows the location of the peak $R^2$ (i.e. the most likely time-shift).*

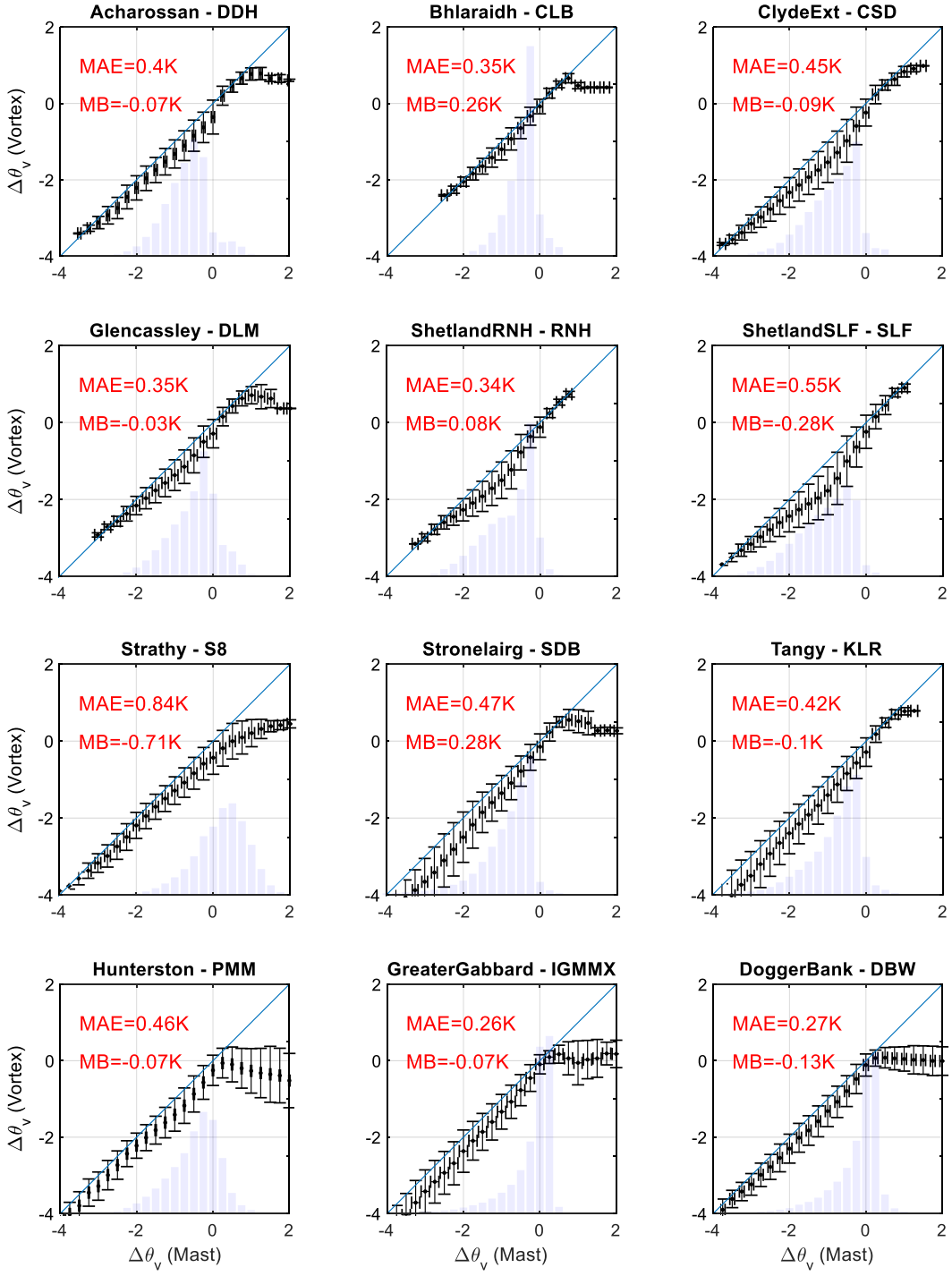


*Figure 5.17: Correlation of measured virtual potential temperature ($\Delta\theta_v\ (Mast)$) against same from Vortex (WRF) mesoscale data ($\Delta\theta_v(Vortex)$). Binned into 0.25K $\Delta\theta_v$ bins with vertical error bars showing standard deviation in each bin and horizontal error bars showing measurement error. Blue bars show frequency of occurrence of each 0.25K $\Delta\theta_v$ (Mast) bin.*

| ***Site*** | ***Mean Absolute Error (K)*** | ***Mean Bias (K)*** |
|---|---|---|
| *Acharossan – DDH* | *0.40* | *-0.07* |
| *Bhlaraidh – CLB* | *0.35* | *0.26* |
| *Clyde Ext – CSD* | *0.45* | *-0.09* |
| *Glencassley – DLM* | *0.35* | *-0.03* |
| *Shetland – RNH* | *0.34* | *0.08* |
| *Shetland - SLF* | *0.55* | *-0.28* |
| *Strathy – S8* | *0.84* | *-0.71* |
| *Stronelairg – SDB* | *0.47* | *0.28* |
| *Tangy – KLR* | *0.42* | *-0.10* |
| *Hunterston – PMM* | *0.46* | *-0.07* |
| *Greater Gabbard – IGMMX* | *0.26* | *-0.07* |
| *Dogger Bank - DBW* | *0.27* | *-0.13* |
| ***Abs Avg.*** | *0.43* | *0.18* |
| ***Abs Max*** | *0.84* | *0.71* |
| ***Abs Min*** | *0.26* | *0.03* |

*Table 5.9: Summary of Mean Absolute Error (MAE) and Mean Bias (MB) from correlations of $\Delta\theta_v$ (Mast) and $\Delta\theta_v$ (Vortex).*

## 5.13 Chapter Summary

In this chapter, the accuracy of $\Delta\theta_v$ measurements from various measurement configurations has been demonstrated, first through an uncertainty assessment and then through inter-comparison of measurements from primary and secondary systems.

Then, distributions of $\Delta\theta_v$ values from Vortex WRF were shown to be comparable with measured distributions, giving confidence that the Vortex data can be used as a viable alternative to measurements. In Chapter 6, distributions of $\Delta\theta_v$ from Vortex are used in an improved CFD wind flow simulation approach.

# 6 CFD Simulation

## 6.1 Introduction

In previous chapters, it has been established that wind flow (specifically, wind speed ratio between two measurement points, wind shear and turbulence intensity) has a strong dependence on atmospheric stability (approximated, using virtual potential temperature differential between 10m and 100m as a proxy). It has also been shown, via comparison with measured data, that Vortex WRF can be used as a reliable data source to describe site-specific distributions of virtual potential temperature differential.

However, this knowledge alone does not help to improve wind farm energy yield assessment and layout design: the next step is to incorporate Vortex-derived virtual potential temperature differential distributions into CFD wind flow modelling and demonstrate that this results in more accurate modelling of wind flow over a prospective wind farm site. Specifically, the results of 'diabatic' CFD simulations, which include the implantation of site-specific virtual potential temperature differential distributions in the modelling, will be compared against 'neutral' simulations which assume zero virtual potential temperature differential in the surface layer.

Background information on CFD was laid out in Chapter 2. In this chapter, first some additional information is provided, which is specific to the CFD modelling approach taken in this research. Then, various options for parameterising stability for input to the CFD model are discussed and the selected method, which has been developed as part of this project, is described. Finally, a validation exercise is summarised, showing an improvement in wind flow modelling accuracy when comparing neutral flow modelling (no consideration of boundary layer atmospheric stability) with diabatic CFD at six sites.

### 6.1.1 Computational Resources

All simulations were carried out on SSE's dedicated 64-core CFD cluster, commissioned in 2014. The cluster is engaged at near-100% utilisation for all of SSE's development and operational wind farm sites for both ambient wind flow modelling and wake simulation. It is

therefore necessary to be fairly targeted in terms of dedicating computational resource to research projects.

### 6.1.2 General Approach

SSE's pre-existing approach to (neutral) ambient wind flow modelling is to model each site with individual simulations for each of thirty-six direction sectors. The input wind speed for each simulation is derived from site-specific measurements and is kept the same for each direction sector. For each simulation, Windmodeller (a bolt-on software package to ANSYS CFX) handles steps such as mesh generation, topography and forestry definition (.XYZ files) and implementation of user-definable variables. It then passes an instruction set (in the form of a .DEF file) to the main CFD solver for processing. The simulation solution is transiently-averaged from the end of a defined warm-up period (during which the simulation begins to converge) until the user-defined end time.

The mesh used is an elongated elliptical mesh with horizontal resolution of 25m in an inner region, increasing towards the outer edges with expansion factor of 1.1. The vertical expansion factor is also 1.1 with a baseline cell size of 0.5m at the ground.

When the simulation completes, Windmodeller then handles the processing of raw results (.RES files) for all simulations into a combined set of results covering all direction sectors, down-sampled to only the locations and heights of interest.

These combined results files can then be picked up by non-CFD software (MATLAB or DNV-GL WindFarmer) for energy yield and optimisation studies.

The objective here is to make a subtle change to this general approach: introduce boundary layer stability in the CFD solving stage by defining it via Windmodeller at the pre-processing stage.

The issue of optimising the allocation of computational resource is central to this project, in terms of fulfilling the need for an efficient CFD process. Incorporating atmospheric stability into CFD can be achieved in many different ways which will be explored in more detail in

section 6.2. Some involve extending solution time to model a greater range of conditions within a single simulation whereas some involve adding additional simulations.

### 6.1.3 Model Configuration

A summary of the CFD configuration used for both neutral (status quo) and diabatic flow modelling is given in Table 6.1. An exhaustive investigation into how CFX works is out of scope but some key features of this CFD configuration should be highlighted in particular in terms of their relevance to modelling diabatic conditions.

First, the height of the ABL is calculated depending primarily on the inlet wind speed and therefore has a fixed value (i.e. typically 850-1050m) and does not vary across simulations of different atmospheric stability states. In reality, it would be expected that the ABL height would increase during unstable conditions (e.g. up to 2000m) and decrease during stable conditions (down to close to 100-200m) and that this in itself would impact on wind flow characteristics – an effect which is neglected here.

Specifically, the height of the ABL is calculated by CFX as:

$$h_{ABL} = \frac{1}{4\, f_c}\left[\frac{\kappa\, U_{ref}}{\ln\left(\frac{z\left(U_{ref}\right)}{z_0}\right)}\right] \qquad (87)$$

where $f_c$= $0.00012\text{s}^{-1}$ is the Coriolis parameter, $z_0$ is the 'background' roughness (i.e. the roughness of the majority of the surface), $\kappa \cong 0.42$ is the Von Karman constant and $U_{ref}$ is the user-defined input wind speed at the inlet at height $z\left(U_{ref}\right)$ AGL.

For a site with typical background roughness $z_0$=0.03, this equation yields: $h_{ABL} \cong 850m$ (for $U_{ref} = 8$ m/s at 90m AGL) and $h_{ABL} \cong 1050m$ (for $U_{ref} = 10$ m/s at 90m AGL).

The discrepancy between the modelled ABL height (850-1050m) and the actual ABL height is likely to introduce some uncertainty to the simulations due to the effect of ABL height on wind flow that is not being captured.

Second, Coriolis effects are excluded, meaning that Ekman spiralling (the effect of wind direction rotating clockwise relative to the geostrophic wind closer to the surface in the northern hemisphere) is not modelled. Wind direction is therefore uniform with height. One effect of which is to exacerbate unwanted flow development (i.e. wind speed-up or slow-down throughout the domain). This is an accepted inaccuracy, due to the fact that although the resulting flow development (especially in stable conditions) might be significant from inlet to outlet, the effect is negligible over distances which are small relative to the size of the CFD domain, such as when extrapolating between measurement points and turbine locations within the inner region of the domain. It should be noted that CFX is capable of modelling Coriolis effects.

Figure 6.1 shows a visualisation of the mesh generated for the Tangy simulation. Figure 6.2 shows the terrain (elevation) map implemented in the same simulation.

### 6.1.4 Forestry Modelling

It is necessary to define the extent and height of forestry on wind flow so that the effect of the forest canopy on wind flow (i.e. increased surface drag, leading to increased shear and lower wind speed downstream) can be captured. Forestry is modelled as a volume with a resistive body force [78] and interacts with wind flow according to the Katul model [79] (alternative models can be specified in CFX).

For the three sites with significant tree cover, LiDAR flyover (airborne laser-reflection measurement) was used to create a 3D map of forestry with 10m horizontal resolution in and around an inner region, near turbines. This map was read into CFX as an XYZ file. For the outer region, forestry was more simply included as blocks of uniform 20m height, defined in a .map (contour) file.

Other than forested areas, the background roughness was set to 0.03 and surface water was assigned roughness 0.001.

The forestry measurement and map creation process was undertaken separately to this research and is therefore not described in further detail here.

Figure 6.3 shows a visualisation of the forestry model implemented in the Tangy simulation.

### 6.1.5 Incorporating $\Delta\theta_v$

The modifications to the Navier-Stokes equations, implemented in CFX to incorporate atmospheric stability (via a virtual potential temperature differential proxy) were set out in section 2.9.2. Virtual potential temperature differential has been chosen as the input to CFX as this is the parameter which has been calculated from mesoscale data and validated against measurements (in Chapters 4 and5).

As an input parameter to define atmospheric stability within the ABL, CFX Windmodeller requires the temperature offset between the ground and the height of the 'surface layer', with the height of the surface layer, $h_{SL}$, defined as approximately one tenth the height of the ABL ($h_{SL}$= $h_{ABL}/10$). CFX then extrapolates between these two heights according to a logarithmic fit, resulting in there being zero temperature difference (neutral stratification) between $h_{SL}$ and $h_{ABL}$ [50]. This approach, developed at SSE in collaboration with ANSYS had already been used to model steady-state diabatic wind flow with satisfactory results [64], as summarised in 3.1.3.

This approach presents two potential issues: first, the assumption made by CFX that virtual potential temperature decreases according to a logarithmic profile in the surface layer and then stays constant up to the top of the ABL is not borne out by measurements (for example, Figure 4.3). Second, the assumption that modelled $\Delta\theta_v$ (being the difference between $\theta_v$ at 10m and $\theta_v$ at 100m) is a good proxy for $\Delta\theta_v$ between 0m and $h_{SL}$ AGL. This implies that $\theta_v$ (10m) $\cong$ $\theta_v$ (0m) and $\theta_v$ (100m) $\cong$ $\theta_v$ ($h_{SL}$), which are not substantiated assumptions.

This is, then, an imperfect link between the available input data and the CFD input requirements and must be considered a key limitation of the research as a whole. However, this approach is favoured in order to preserve the simplicity of the overall process, which is a key objective of this project.

The following sections detail the link between site-specific $\Delta\theta_v$ distributions and CFD inputs.

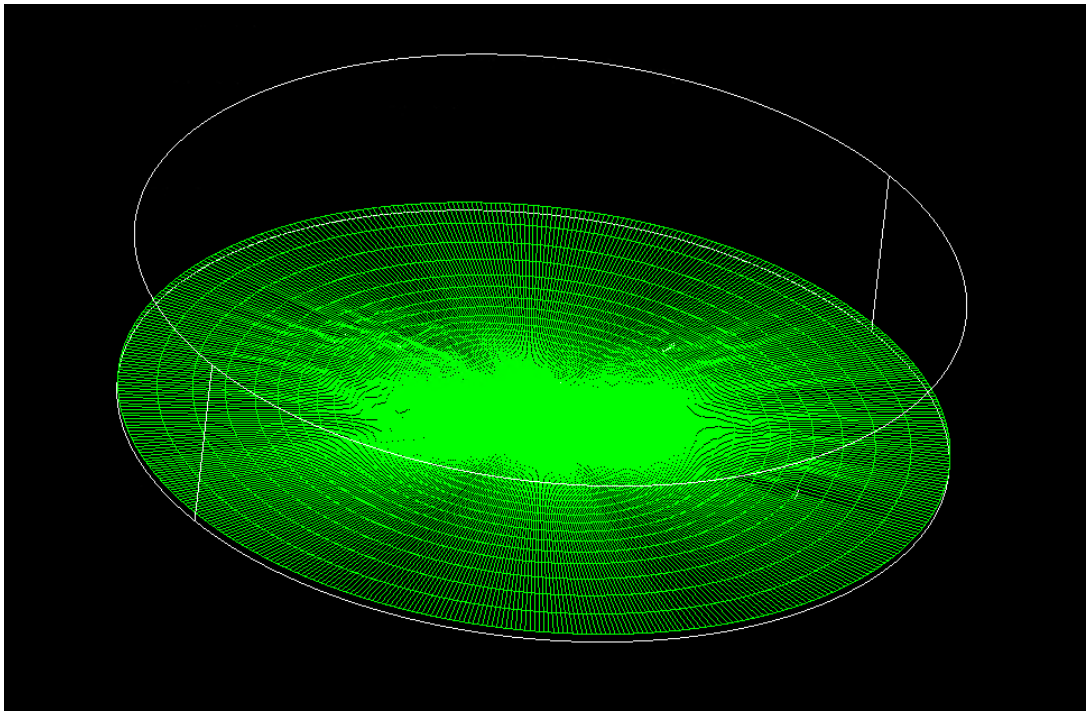

*Figure 6.1: Visualisation of mesh (single horizontal plane) implemented in CFD (for Tangy).*

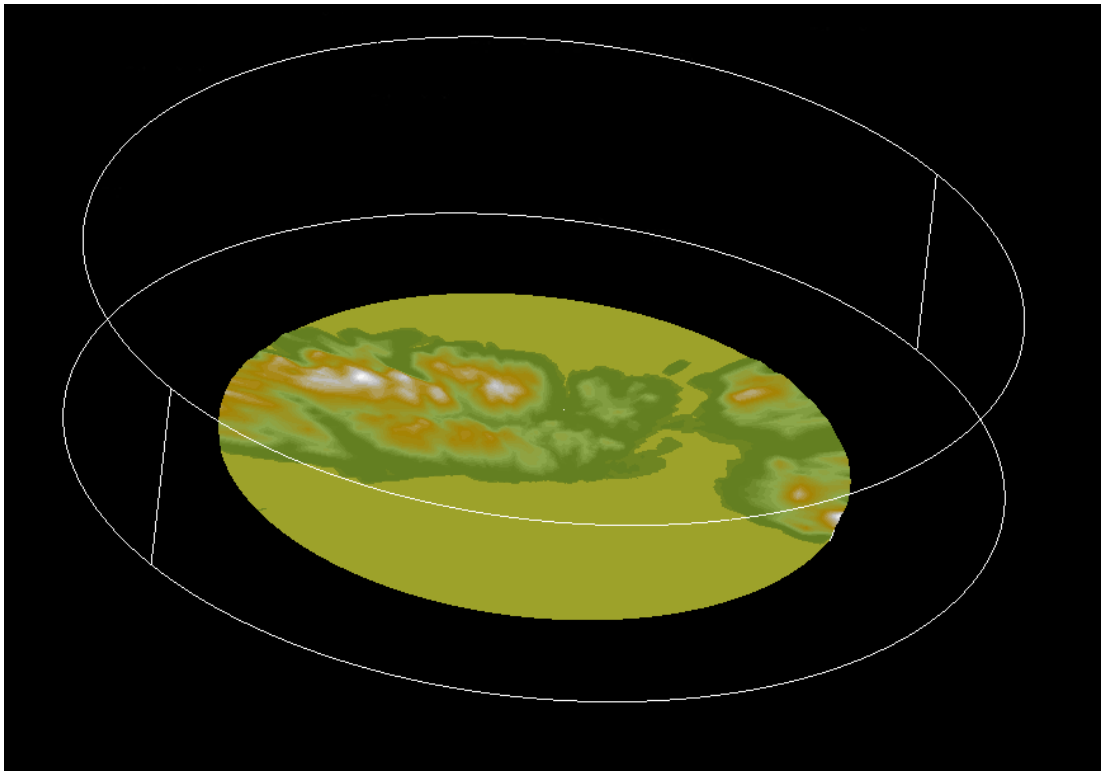

*Figure 6.2: Visualisation of terrain model implemented in CFD (for Tangy).*

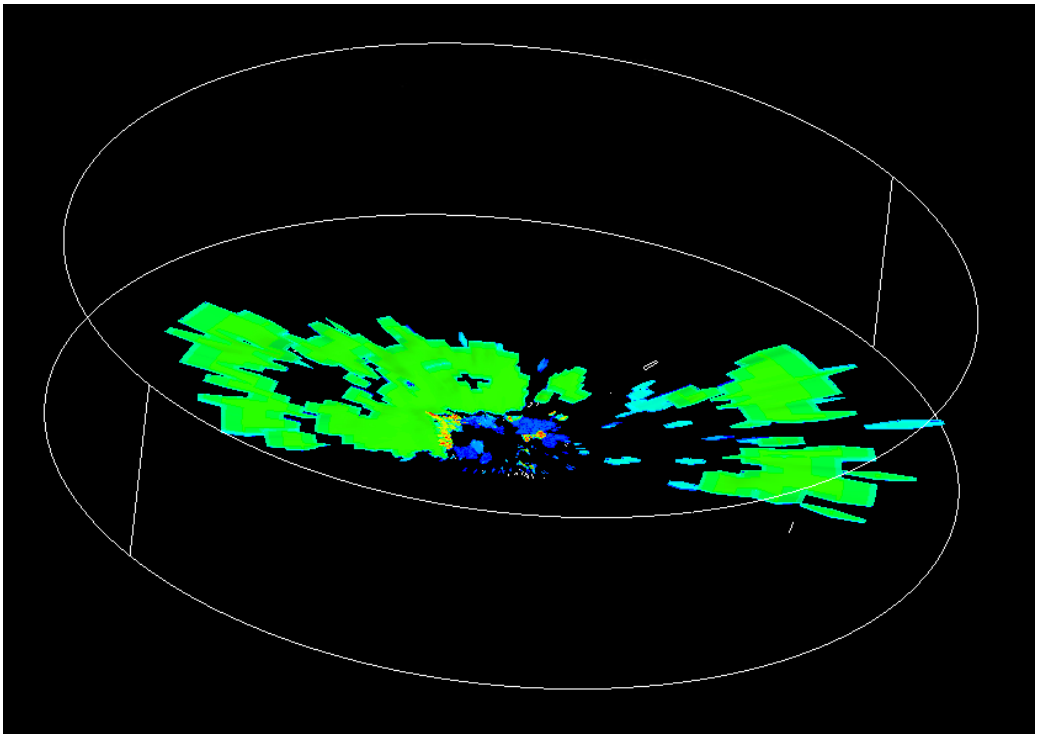

*Figure 6.3: Visualisation of forestry model implemented in CFD (for Tangy simulation).*

| | |
|---|---|
| **CFD Platform** | *ANSYS CFX v18.0* |
| **Bolt-on** | *Windmodeller* |
| **Mesh** | *Elongated radial mesh with expansion factor of 1.1.* |
| **Horizontal mesh resolution** | *25m in inner region with outer region expansion factor of 1.1* |
| **Vertical mesh resolution** | *0.5 (bottom) - 130m (top) with expansion factor of 1.1* |
| **Turbulence Model** | *SST with reattachment modification* |
| **Forestry Model** | *Katul with loss co-efficient = 0.01* |
| **Inlet Wind Speed** | *Fixed in each direction sector according to site-specific measurements* |
| **Tropospheric Stability** | *+3.3K / km above ABL height* |
| **ABL Stability** | *Site specific time-varying ground/surface layer virtual potential temperature offset (diabatic model) or zero offset (neutral model).* |
| **Coriolis Force** | *None* |
| **ABL Height** | *Non-varying function of site-specific friction velocity.* |
| **Domain Height** | *10,000m* |
| **Co-efficient Loops** | *Minimum = 1; Maximum = 5* |
| **Residual Target** | *0.0001* |
| **Nominal Simulation Time** | *7200s (Neutral)*<br>*16400s (Diabatic)* |

*Table 6.1: Summary of CFD configuration.*

## 6.2 Input Parametrisation

Stability input profiles were calculated directly from Vortex WRF time series data, using the process outlined in Chapter 4. The aim of this exercise is to construct a CFD model in which the evaluated transient-average result is reflective of the full range of observed stability states.

### 6.2.1 Time Series Input

Perhaps the most physically correct approach, and a good starting point for discussion, is to run CFD with a time-series stability input with hourly values covering one or more whole years (in order to capture both diurnal and seasonal variation).

Figure 6.4 shows a hypothetical stability input time-series. This time-series approach has attractive qualities: the full range of observed stability states can be modelled as a non-convergent simulation and no re-averaging is necessary. It is also advantageous that the stability time series can be used alongside a concurrent wind speed time series, instead of running at a fixed wind speed.

However, the drawbacks are obvious: it is impractical to model 8760 hourly stability states in a short CFD simulation. There is an upper limit on the ratio of simulation time to real time, which is driven by CPU processing power (i.e. a one year CFD simulation might take multiple months in real time to complete – likely to be considered an unacceptable utilisation of computational resource).

This could potentially be sped-up by reducing the ratio of CFD time to real time (i.e. by purchasing faster, more advanced processors) but only at great cost.

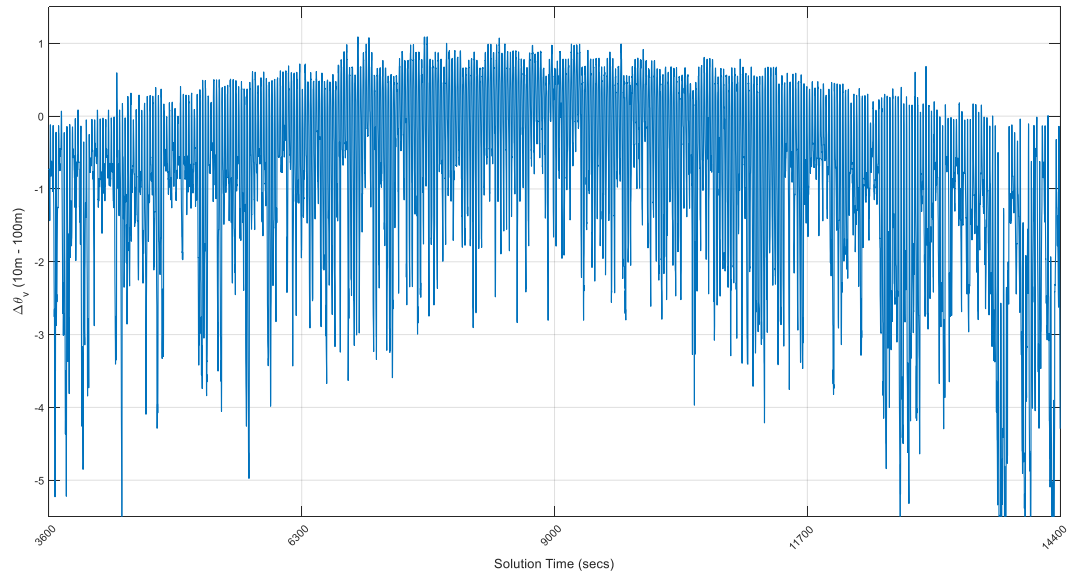


*Figure 6.4: Visualisation of a CFD stability input time series, where the input is a full year of hourly stability values.*

### 6.2.2 Multiple Fixed Inputs

An alternative approach is to run multiple CFD simulations, each with a fixed stability state, and then re-aggregate the CFD outputs according to the observed frequency of each state. Table 6.2 shows a worked example of this approach, where the results of six CFD simulations, each with a fixed temperature offset from -4K (extremely stable) to 1K (unstable), are averaged together to evaluate some quantity (nominally 'Wind Speed'). The bin frequency can be calculated from time-series stability data.

An advantage of this approach is that it has the ability to retain the link between wind speed and stability: the input wind speed for each simulation can be set to the mean wind speed observed during each stability state (i.e. typically, lower wind speed for diabatic and higher wind speed for neutral conditions) which would bring the simulations more closely in line with reality.

However, this approach also has its drawbacks: primarily, a CFD simulation of wind flow with a constant stability state is far removed from reality and could lead to unrealistic results. For example, phenomena such as gravity waves and roll vortices could dominate stable and

unstable simulations respectively, whereas in reality the conditions that lead to their onset are rarely persistent enough for them to form.

| Stability ($\Delta\theta_v$(K)) | Bin Bottom ($\Delta\theta_v$(K)) | Bin Top ($\Delta\theta_v$(K)) | Bin Frequency (%) | Wind Speed (m/s) |
|---|---|---|---|---|
| -4 | -4.5 | -3.5 | 2 | 6.0 |
| -3 | -3.5 | -2.5 | 4 | 7.0 |
| -2 | -2.5 | -1.5 | 15 | 7.5 |
| -1 | -1.5 | -0.5 | 25 | 8.0 |
| 0 | -0.5 | 0.5 | 35 | 8.0 |
| +1 | 0.5 | 1.5 | 19 | 8.1 |
| | | | Weighted Average: | 7.9 |

*Table 6.2: Worked example of using multiple CFD simulations with fixed stability to evaluate wind speed (as an example) by taking an average across all simulation outputs, weighted by the observed frequency of each state.*

In addition, this approach also places a burden on computational resource: even if six discrete-stability simulations (i.e. -4K to 1K at 1K increments) can be considered adequate to represent the full range of stability conditions, it is necessary to replicate this approach for each of 36 direction sectors, leading to 216 simulations per site in total. If eleven simulations per direction sector were required for increased flow resolution, the total would be 396 simulations per site.

With SSE's current CFD cluster, this number of runs per site is unfeasible. Additional and/or higher-specification cores could be utilised to make this manageable but, again, at great cost. It is also worth noting that conducting a high-number of additional runs incurs a great deal of additional pre-processing, spin-up and post-processing, all of which increase complexity, overall time (especially because some sub-processes cannot be carried out on parallel cores) and software license requirements.

Of course, some practical compromises could be made to reduce the total number of simulations, such as reducing the number of stability states in less frequent (i.e. less important) direction sectors. Even so, it is desirable to pursue a solution which only requires one simulation per direction sector.

### 6.2.3 Transient Simulation (hourly/monthly average)

The conclusion of the preceding sections is that it is necessary to collapse down the stability time series data into a manageable input profile which incorporates the whole range of stability conditions experienced at the site (in the direction sector being modelled) and their observed frequencies. This would mean that each direction sector could be modelled with a single, relatively short CFD simulation, in which stability varies throughout the simulation, thereby bringing the required computational resource down to a manageable level.

An approach which has been taken by others, e.g. [63], is to construct a stability profile as a series of 24 values, each representing one hour in an average day derived from a time series of one year or more. Figure 6.5 (top-left) shows a stability input profile constructed in this manner for two sites with very different stability patterns, where the first point on each profile is the average measured stability for 00:00 – 01:00 and so on. Similarly, Figure 6.5 (top-right) shows another potential approach: a stability input profile constructed as a series of 12 monthly averages, where the first point is the average stability in January and so on.

Both of these approaches are adequate for describing the mean stability climate at each location: the mean of the 24 hourly means or 12 monthly means will equal the mean stability for the whole time series (approximately, in the latter case, because of variation in number of days per month). However, these approaches are insufficient in terms of capturing the observed range of stability states, as demonstrated by the large standard deviations associated with each hourly or monthly average. This is primarily because the daily-average approach is failing to capture the effects of monthly (seasonal) variation and vice versa. The next section details the solution to this issue.

### 6.2.4 Transient Simulation (sorted bin-average)

A statistical solution was developed in order to address this issue of input parametrisation. First, the time series of hourly $\Delta\theta_v$ values is sorted from most negative (most stable) to most positive (most unstable). Then, the time series is divided into twenty equally sized sub-sets and the average stability of each subset is taken (i.e. a rolling average). Having twenty sub-sets results in an input file which is easy to understand and handle, while retaining the approximate 'shape' of the input profile. The resulting twenty bin-averages form the stability input profile for the CFD simulation, as represented in Figure 6.5 (bottom).

This approach has the advantages of being computationally non-intensive (one short 2 to 5 hour simulation required per direction sector) while generating an input profile which retains close to the full range of observed stability states and preserves the mean value of the original time series.

One disadvantage of collapsing the time series to this extent is that the relationship between wind speed and stability is lost. It is not practical to transiently vary more than one input parameter (i.e. wind speed as well as $\Delta\theta_v$) so wind speed has to be held constant for each simulation. Specifically, the input wind speed is set to the observed mean for each direction sector.

This issue is introduced in the diabatic simulations: neutral wind flow is invariant with wind speed, whereas stability-related effects are often exaggerated at low wind speed. The risks of running at a fixed mean wind speed with variable stability are that the exaggerating effect of low wind speed and the suppressing effect of high wind speed on stability-induced wind flow are not being captured. This is an important limitation which should be borne in mind when reviewing results.

Input parametrisation was carried out using this approach for the six sites which were selected for CFD modelling: Bhlaraidh, ShetlandRNH, Stronelairg, Tangy, ClydeExt and Hadyard Ext. Figure 6.6 shows the resulting input profiles for all six sites: in each case, the 36 input profiles used in CFD are shown (coloured lines) to give an indication of the

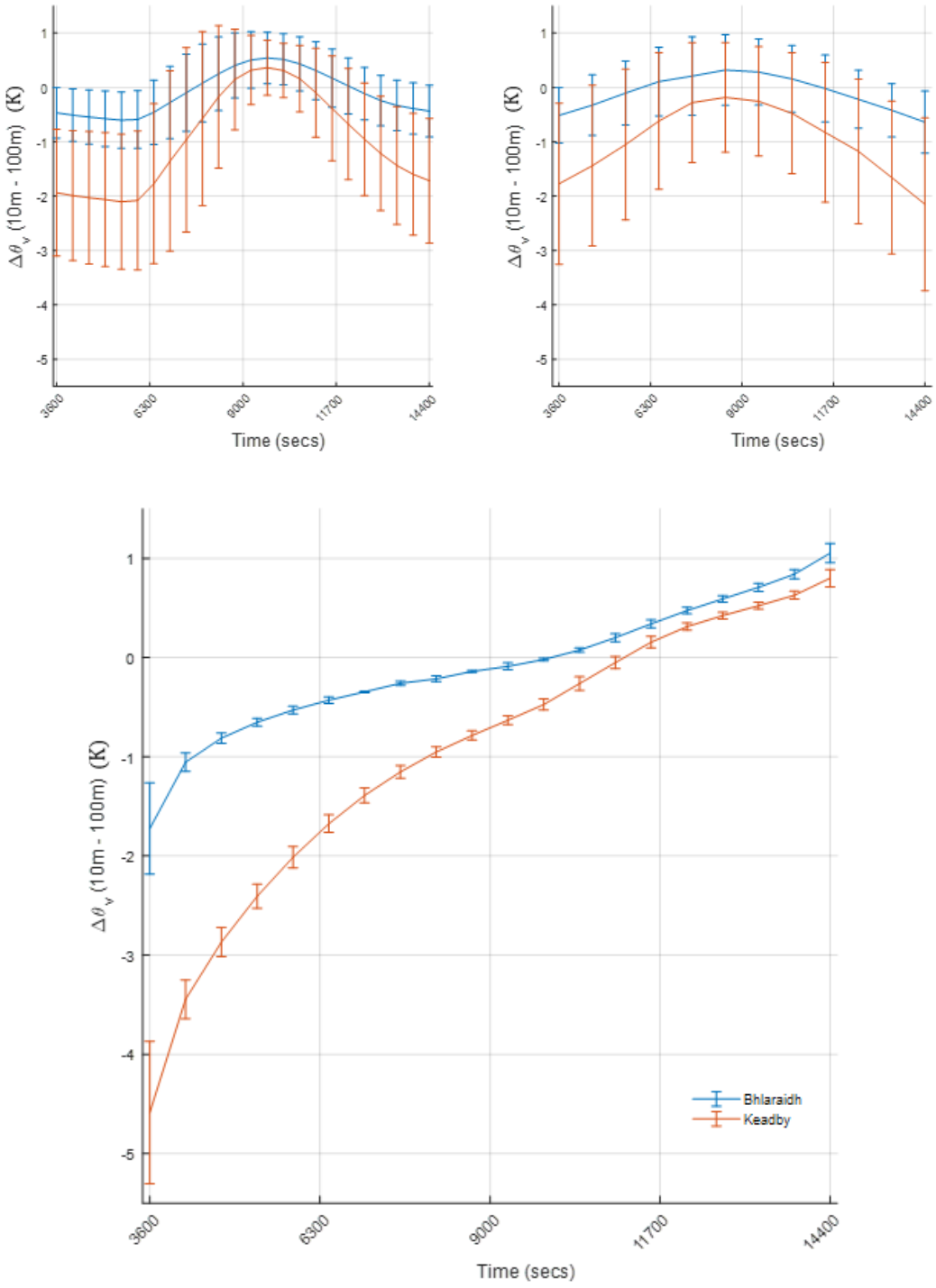


*Figure 6.5: $\Delta\theta_v$ input profiles evaluated as hourly averages (top-left), monthly averages (top-right) and sorted bin-averages (bottom). Error bars show the standard deviation in each bin.*

directional spread in $\Delta\theta_v$ inputs. The weighted mean is also shown (black line) for interest. Figure 6.7 shows a screenshot of the final exported CFD input profile in Excel. The first column is the solution time: an instruction to the solver in terms of when to implement the $\Delta\theta_v$ values in the subsequent columns. There is an initial 3600s timestep (for the simulation to settle), followed by twenty equally spaced timesteps which define the progression of $\Delta\theta_v$ values from most stable to most unstable. The columns are ordered and named according to the direction sectors being modelled: 'dT_30' is virtual potential temperature differential for 30 degrees. (NB: the data precision displayed is far greater than measurement accuracy).

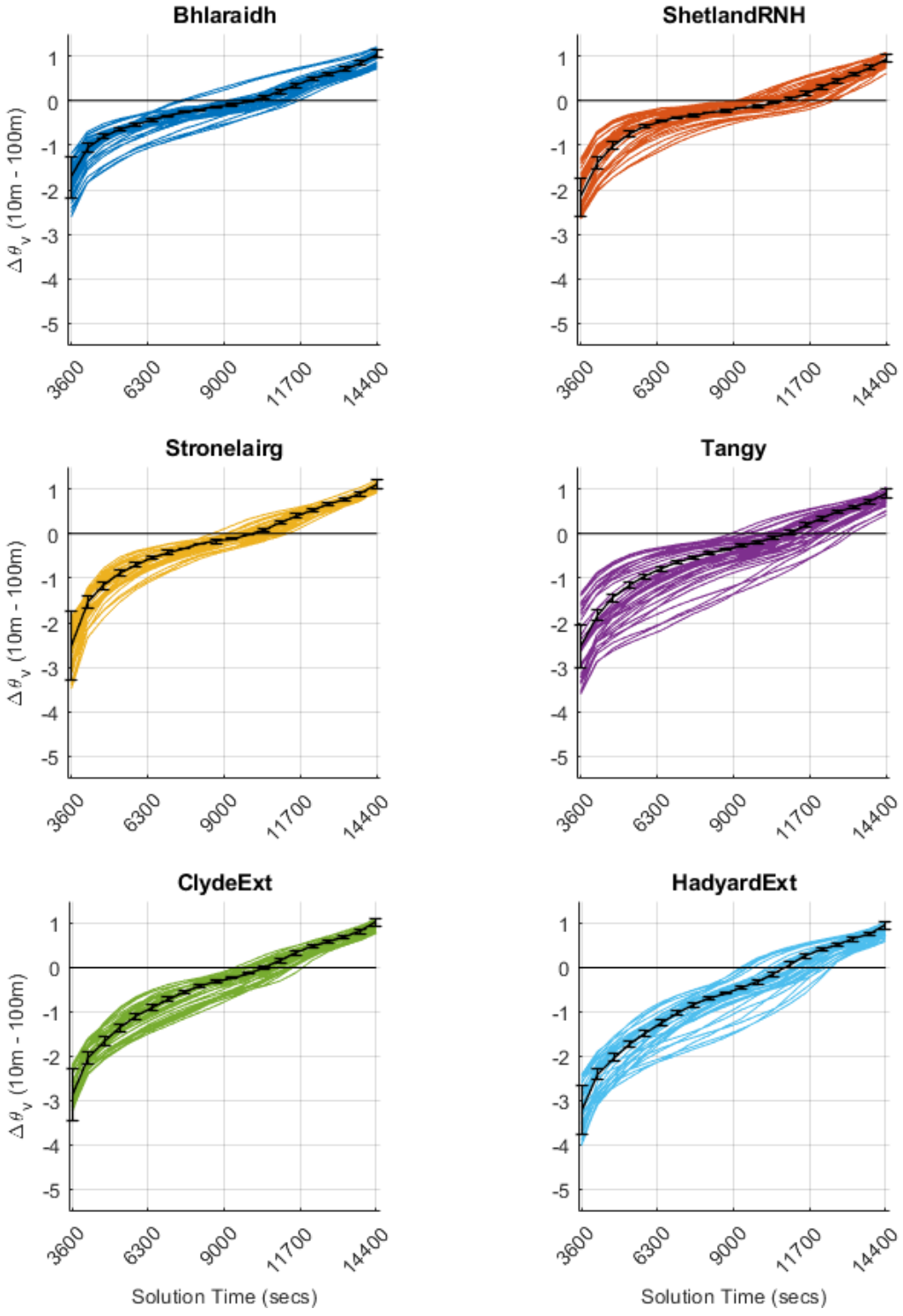


*Figure 6.6: $\Delta\theta_v$ input profiles for six sites showing the average profile (black line with error bars showing standard deviation) and each of 36 directional profiles (coloured line), showing the spread in stability profile by direction.*

| [Name] | | | | | | | | | | |
|---|---|---|---|---|---|---|---|---|---|---|
| diurnaldT | | | | | | | | | | |
| [Spatial Fields] | | | | | | | | | | |
| t | | | | | | | | | | |
| [Data] | | | | | | | | | | |
| t[s] | dT_0 | dT_10 | dT_20 | dT_30 | dT_40 | dT_50 | dT_60 | dT_70 | dT_80 | dT_90 |
| 0 | -3.01362 | -2.73956 | -2.54778 | -2.3088 | -2.20546 | -2.37877 | -2.41419 | -2.28047 | -2.161 | -2.19088 |
| 3600 | -3.01362 | -2.73956 | -2.54778 | -2.3088 | -2.20546 | -2.37877 | -2.41419 | -2.28047 | -2.161 | -2.19088 |
| 4168.4 | -2.22847 | -2.16806 | -1.93322 | -1.74703 | -1.61971 | -1.79224 | -1.74462 | -1.75417 | -1.54725 | -1.59781 |
| 4736.8 | -1.95456 | -1.89307 | -1.66518 | -1.48743 | -1.35889 | -1.51736 | -1.45364 | -1.3824 | -1.22469 | -1.29275 |
| 5305.3 | -1.74013 | -1.65807 | -1.43744 | -1.22661 | -1.1545 | -1.32859 | -1.23733 | -1.11184 | -0.97024 | -1.04256 |
| 5873.7 | -1.50946 | -1.45398 | -1.24806 | -1.01866 | -0.95924 | -1.16697 | -1.06828 | -0.88179 | -0.77282 | -0.81336 |
| 6442.1 | -1.34426 | -1.27098 | -1.06735 | -0.83219 | -0.76498 | -0.98676 | -0.91174 | -0.68529 | -0.62598 | -0.64901 |
| 7010.5 | -1.17017 | -1.10655 | -0.89617 | -0.66991 | -0.57799 | -0.81839 | -0.75231 | -0.51988 | -0.496 | -0.51189 |
| 7578.9 | -1.01958 | -0.95449 | -0.72426 | -0.49459 | -0.4101 | -0.66225 | -0.59663 | -0.38675 | -0.39619 | -0.3975 |
| 8147.4 | -0.85508 | -0.8091 | -0.58157 | -0.34806 | -0.26107 | -0.51005 | -0.44516 | -0.29474 | -0.28547 | -0.30094 |
| 8715.8 | -0.70841 | -0.67667 | -0.4282 | -0.1866 | -0.1277 | -0.37646 | -0.30689 | -0.17947 | -0.17375 | -0.2066 |
| 9284.2 | -0.56158 | -0.52642 | -0.27849 | -0.06008 | 0.013726 | -0.25656 | -0.1802 | -0.06949 | -0.05789 | -0.09386 |
| 9852.6 | -0.40236 | -0.39352 | -0.14363 | 0.081323 | 0.160322 | -0.1325 | -0.06504 | 0.04627 | 0.057452 | 0.017643 |
| 10421 | -0.22936 | -0.26207 | -0.01552 | 0.229304 | 0.311928 | -0.0166 | 0.053739 | 0.185312 | 0.198127 | 0.142365 |
| 10989.5 | -0.06139 | -0.12016 | 0.14933 | 0.364826 | 0.434751 | 0.153856 | 0.20093 | 0.326756 | 0.330568 | 0.29633 |
| 11557.9 | 0.125565 | 0.069803 | 0.315897 | 0.479994 | 0.525004 | 0.319525 | 0.356606 | 0.457756 | 0.448532 | 0.425357 |
| 12126.3 | 0.315588 | 0.26253 | 0.450616 | 0.575831 | 0.610861 | 0.450386 | 0.488594 | 0.568739 | 0.547109 | 0.527916 |
| 12694.7 | 0.487231 | 0.418224 | 0.556855 | 0.673279 | 0.694188 | 0.571923 | 0.598999 | 0.663766 | 0.625332 | 0.613356 |
| 13263.1 | 0.617692 | 0.566151 | 0.671421 | 0.772969 | 0.772949 | 0.689822 | 0.714623 | 0.751176 | 0.713951 | 0.702736 |
| 13831.6 | 0.731234 | 0.714446 | 0.816823 | 0.887164 | 0.879095 | 0.831928 | 0.848216 | 0.851882 | 0.841009 | 0.807224 |
| 14400 | 0.907714 | 0.902486 | 1.028457 | 1.097521 | 1.10584 | 1.044762 | 1.025858 | 1.011819 | 1.012744 | 0.967224 |
| 16400 | 0.907714 | 0.902486 | 1.028457 | 1.097521 | 1.10584 | 1.044762 | 1.025858 | 1.011819 | 1.012744 | 0.967224 |

*Figure 6.7: Screenshot of the final processed .csv temperature differential CFD input file in Excel.*

## 6.3 CFD Modelling

Six sites were selected for CFD modelling from the long-list presented in Chapter 5. This selection was primarily based on targeting those sites which would best reveal the interaction between atmospheric stability and complex terrain.

Two sets of simulations were produced for each site (neutral and diabatic) and each set comprised one simulation for each of 36 direction sectors. In total, 432 CFD simulations were undertaken in order to be able to facilitate a thorough comparison between neutral and diabatic wind flow simulations.

Table 6.3 shows key metrics pertaining to these CFD simulations. Of particular note is that diabatic simulations take up to three times as long as neutral simulations, depending on both

the ambient complexity of the site and the deviation from neutral conditions. This is due to the extended transient averaging period over which stability is varied, compared to the neutral simulations (described in 6.2.4).

| Site | Completion Time per direction sector (mins) | | RES File Size per direction sector (MB) | | Mean $\Delta\theta_v$ | St Dev $\Delta\theta_v$ | Domain Size (km) |
|---|---|---|---|---|---|---|---|
| | Neutral | Diabatic | Neutral | Diabatic | | | |
| **Bhlaraidh** | 50 | 120 | 650 | 650 | -0.1 | 0.7 | 3.2 x 4.7 |
| **Shetland RNH** | 90 | 180 | 1970 | 1970 | -0.2 | 0.7 | 7.5 x 11.9 |
| **Stronelairg** | 120 | 210 | 1100 | 1100 | -0.2 | 0.9 | 4.7 x 9.1 |
| **Tangy** | 100 | 150 | 390 | 390 | -0.4 | 0.9 | 2.7 x 3.4 |
| **Clyde Ext** | 240 | 300 | 1230 | 1230 | -0.4 | 1.0 | 5.2 x 8.1 |
| **Hadyard Ext** | 80 | 240 | 1380 | 1380 | -0.6 | 1.1 | 4.3 x 11.2 |

*Table 6.3: Key metrics pertaining to CFD simulations of six wind farm sites.*

The raw output from each simulation is a RES file which is generally a few GB in size. CFX POST is used to interrogate these RES files and extract useful information. For the purposes of this investigation, two sets of results were extracted:

1. ***Gridded Values*** Wind speed, wind direction, shear exponent and turbulence intensity at every grid node on a horizontal plane through the simulation domain at hub-height AGL.
2. ***Point Values*** Wind speed, wind direction, shear exponent and turbulence intensity at exact measurement mast locations at measurement height(s). (CFX POST interpolates between grid nodes).

Owing to the fact that the CFD domain is an elliptically-bounded mesh with a non-uniform cell size, MATLAB was used to re-sample the gridded values into a regularly spaced (25x25m) rectangular grid, in order to facilitate further analysis.

For wind speed values, CFX reports the ratio of the simulated wind speed at each grid node to the inlet wind speed rather than the absolute wind speed. This means that the neutral and diabatic wind speed grids are not directly comparable, since the inlet wind speed is not consistent between the two simulation types (inlet wind speed varies with direction in the diabatic simulations). In order to address this, both sets of wind grids are re-normalised to the wind speed at a fixed location, that being the location of the primary on-site measurement masts.

Then, the 36 directional simulations are averaged together (weighted by the directional frequency measured by the mast) to generate an omni-directional wind speed grid. This provides a basis to generally compare the wind grids generated by neutral simulations to those created by diabatic simulations.

Figure 6.8 shows wind speed ratio maps for each of the six sites, visualising the ratio of diabatic to neutral simulation wind speed (e.g. one grid divided by the other). In these visualisations, red indicates areas where this ratio is less than 1, and the mast-normalised wind speed in the diabatic simulation is less than in the neutral simulation. Green indicates areas where the ratio exceeds 1, and the mast-normalised wind speed is greater in the diabatic simulation. White indicates areas where the ratio equals 1, and the measurement mast will always be located in a white area due to the fact that this point has been used to normalise both grids.

It can be observed that wind speed varies by up to 10%, comparing diabatic against neutral simulations. The wind speed variation is greater for those sites with very complex terrain (Clyde Ext) or strong stability variation (Hadyard Ext) and less for sites with weak stability variation and/or high mean wind speed (Shetland). However, at all six sites the wind speed variation is highly significant (e.g. broadly greater than 1%) in terms of wind resource assessment.

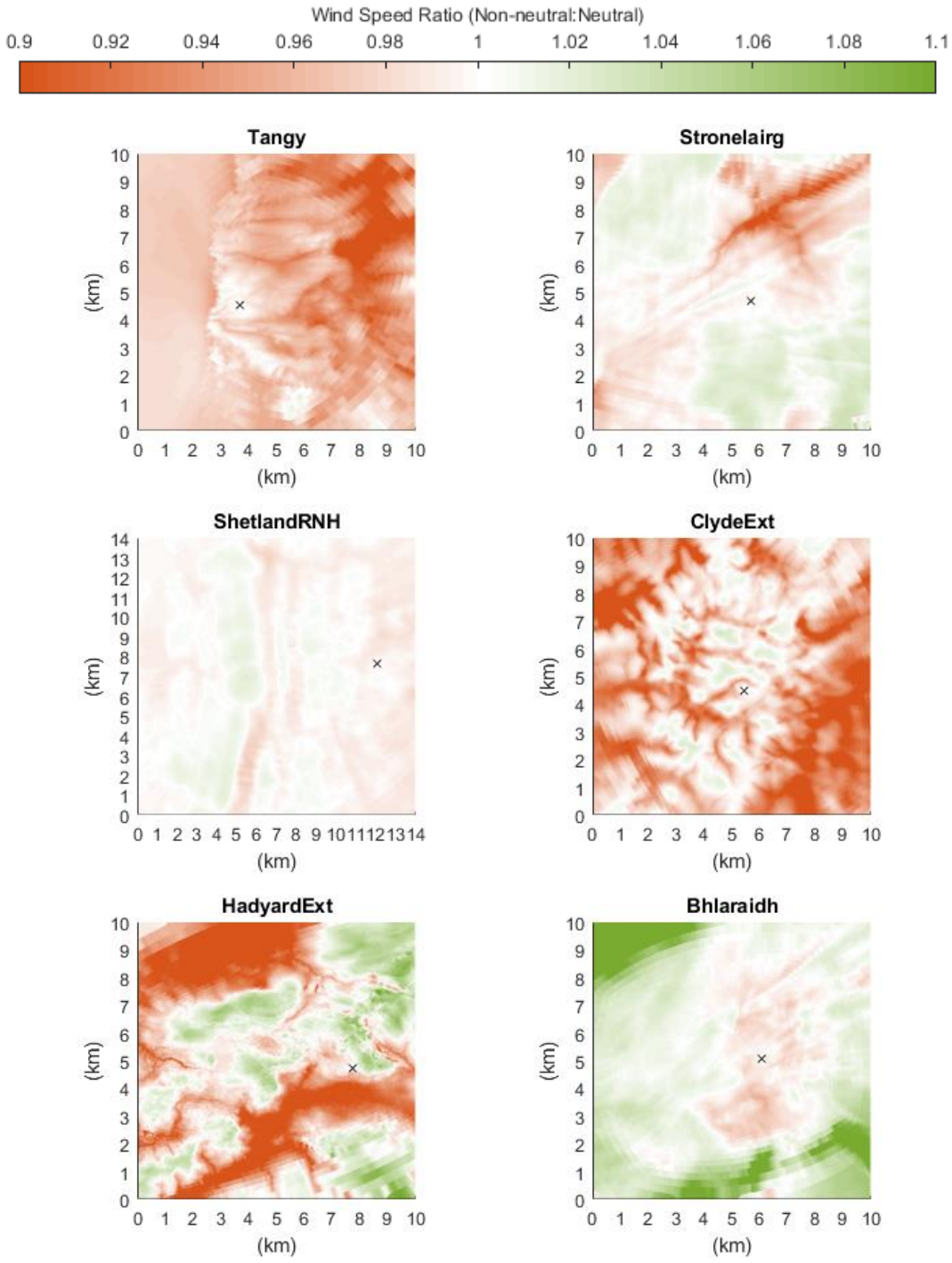


*Figure 6.8: Wind speed ratio maps for six sites, visualising the ratio of diabatic to neutral simulation wind speed. Diabatic simulation results in a greater wind speed when this ratio is greater than 1 (green) and a lower wind speed when lower than 1 (red). The mast used for normalisation is marked by a black cross.*

## 6.4 Validation

In order to gain confidence in the outputs of diabatic CFD simulations, the simulated wind conditions (shear, turbulence intensity (TI) and wind speed ratio) were compared against measured wind conditions at meteorological mast locations. These three wind flow parameters and their sensitivity to atmospheric stability were discussed in Chapter 2.

Validation was carried out at five of the six sites which were modelled in CFD. Hadyard Ext was omitted due to the lack of stability measurements.

### 6.4.1 Pre-Processing

All of the measurement masts and instruments used in this exercise are detailed in Chapter 5. The following process was followed for each of 21 measurement masts.

First, cleaned and calibrated data, including pre-calculated shear exponent and turbulence intensity, are imported into the validation database for the mast under consideration ('TMM I'). Next, concurrent cleaned and calibrated data are imported for a second measurement mast on the same site ('TMM II') and concurrent cleaned/calibrated stability (temperature offset) data are imported from whichever on-site mast is equipped with temperature offset measurement equipment. An inner-join function is used to align and unify these three data sets according to their stated timestamps.

Data sets were checked to see if a time-step adjustment was required, to ensure that the first and second mast data sets are synchronous. As for the WRF/mast validation in Chapter 5, this was done by correlating wind speeds measurements for both masts with each other, offsetting the data sets by ten minutes relative to one another, re-correlating and so on until the strongest correlation is found. In the data sets analysed, no time-step adjustments were necessary.

A directional correction is applied to TMM I and TMM II to facilitate accurate directional validation. Because wind direction can be affected by topography in the vicinity of the masts, this can lead to incorrect directional binning. To correct for this, mast measurements from both masts are adjusted independently (typically only by a few degrees) to match the inlet

wind direction, using wind direction outputs from the CFD model, so that both masts and CFD are being compared on the same directional basis.

In the following sections, CFD simulation results are compared against measured values. Dashes are used to indicate CFD results ($\alpha'$, $TI'$ and $WSR'$) whereas un-dashed variables indicate measured values ($\alpha$, $TI$ and $WSR$). For CFD simulation results, the sub-scripts 'N' and 'D' are used to indicate the results of neutral and diabatic simulations respectively. For measured values, the subscript 'N' indicates the data set has been filtered to only include periods of neutral stability (-0.125K < $\Delta\theta_v$ < 0.125K) and 'D' indicates that the data set is unfiltered.

### 6.4.2 Shear

CFD-modelled shear exponent is extracted by calculating the gradient of a linear fit through a log-log plot of wind speed predictions at various heights (matching those heights of anemometers on the measurement mast). This results in a value which is consistent with how shear exponent is calculated from the measured data. By this method, a value of shear exponent is calculated from the outputs of both neutral CFD simulations ($\alpha'_N$) and diabatic ($\alpha'_D$).

A simple approach to validation would be to compare the simulated values from both neutral and diabatic simulations, $\alpha'_N$ and $\alpha'_D$, against the unfiltered measured value, $\alpha_D$. However, this neglects the fact that the measured value $\alpha_D$, is influenced by a great number of more prominent factors such as terrain, ground cover and roughness – not just stability. It is therefore necessary to isolate the effect of diabatic conditions, compared to neutral, on both the simulated and measured values and conduct a comparison on this basis.

The CFD-modelled difference in shear exponent between neutral and diabatic simulations at the measurement mast locations is calculated as:

$$\Delta\alpha' = \alpha'_N - \alpha'_D \quad (88)$$

Next, the measured data are filtered for wind speed range 5 – 25m/s in order to filter out low wind speed periods (which are more prone to instrument error) and very high wind speed periods (which are not representative of the normal wind climate) and the measured shear exponent is calculated by taking an average of all records ($\alpha_D$). In the case that more than one year of data are available at a measurement location, a seasonal-balancing algorithm is applied to remove the effect of having, for example, two winters and only one summer in the data set which could skew the results. The seasonal balancing algorithm works by first calculating an average for each month of the year and then averaging these together, weighting according to number of days in each month.

Then, the data are filtered again for stability, to exclude all except neutral stability periods (-0.125K < $\Delta\theta_v$ < 0.125K) and an average is again calculated ($\alpha_N$). The percentage of data within this neutral range is typically 15-20% for the sites under consideration. It is important that this filtering is conducted using measured, rather than WRF-derived, stability data to maximise filtering accuracy (as discussed in Chapter 5).

The measured difference in shear exponent is calculated as the difference between the stability-filtered and unfiltered values:

$$\Delta\alpha = \alpha_N - \alpha_D \quad (89)$$

So, we now have a basis on which to assess the agreement of measured and modelled shear exponent: the measured change when comparing neutral (filtered) with diabatic (unfiltered) ($\Delta\alpha$) and the modelled equivalent ($\Delta\alpha'$).

In terms of expectations, it is established that stable conditions lead to greater wind shear (higher $\alpha$). Also, it has been observed that the site-specific stability distributions that have been measured and modelled exhibit a greater frequency of stable conditions than unstable.

Therefore, unless the effects of unstable conditions are opposite to and much greater in magnitude than the effects of stable conditions, it should be expected that $\Delta\alpha$ will be positive in all cases (i.e. because the effects associated with stable conditions will dominate).

Figure 6.9 shows the $\Delta\alpha$ for measured and CFD cases at each mast. In all cases $\Delta\alpha$ is shown to be positive with the measured increase in shear exponent approximately in the range 0.01 to 0.04. It can also be seen that CFD predicts an increase in shear ($\Delta\alpha' > 0$) when switching from neutral to diabatic simulations.

Taking the neutral simulation as a baseline, the diabatic CFD approach is judged to be successfully validated at each mast location if the modelled change matches the measured difference between the neutral-filtered and unfiltered measured values.

There are two circumstances in which the diurnal simulation validation would fail: if the modelled change is in the opposite direction to the measured difference or; if the modelled change is in the same direction but greater than twice the magnitude of the measured difference (i.e. over-shooting). Therefore, if the measured difference between neutral-filtered $\alpha$ and unfiltered $\alpha$ were +0.01, the modelled change must be in the range 0 – 0.02 or else the shift in modelling methodology has reduced, rather than increased, modelling accuracy.

So, the success criterion is more precisely expressed as the simulated difference being (i) in the same direction as and (ii) not more than double the measured change:

$$0 < \Delta\alpha' < 2.\Delta\alpha \qquad (90)$$

In the results, this criterion can be seen to be met for every mast location under consideration, leading to the conclusion that the change to the simulation method (shifting from neutral to diabatic simulation) is validated by consideration of the measured data. In the case of the Shetland masts (RNH, SLF, FMS, SMF, MKN, SCQ), the measured difference between neutral-filtered and unfiltered data sets is much greater than the simulated

difference in CFD. These cases are still considered successful validations, however, since the CFD-modelled change still represents an improvement on the neutral simulation.

Figure 6.10 shows CFD-modelled and measured values of shear exponent for a subset of nine sites and 12 out of total 36 direction sector simulations. These plots show the same information as Figure 6.9 with increased directional resolution. This allows us to see that significant errors remain, in terms of the CFD's ability to correctly predict wind shear (either neutral-filtered or unfiltered) in every direction sector. However, the greatest deviations between CFD and measurement are often in low-frequency direction sectors, limiting the relevance of these comparisons and the impact on the overall weighted average.

In general, CFD modelling tends to over-predict wind shear (i.e. black-solid line above black-dash line) with the exception of Tangy, where significant forestry effects and the interaction of stability and forestry may have been a complicating factor.

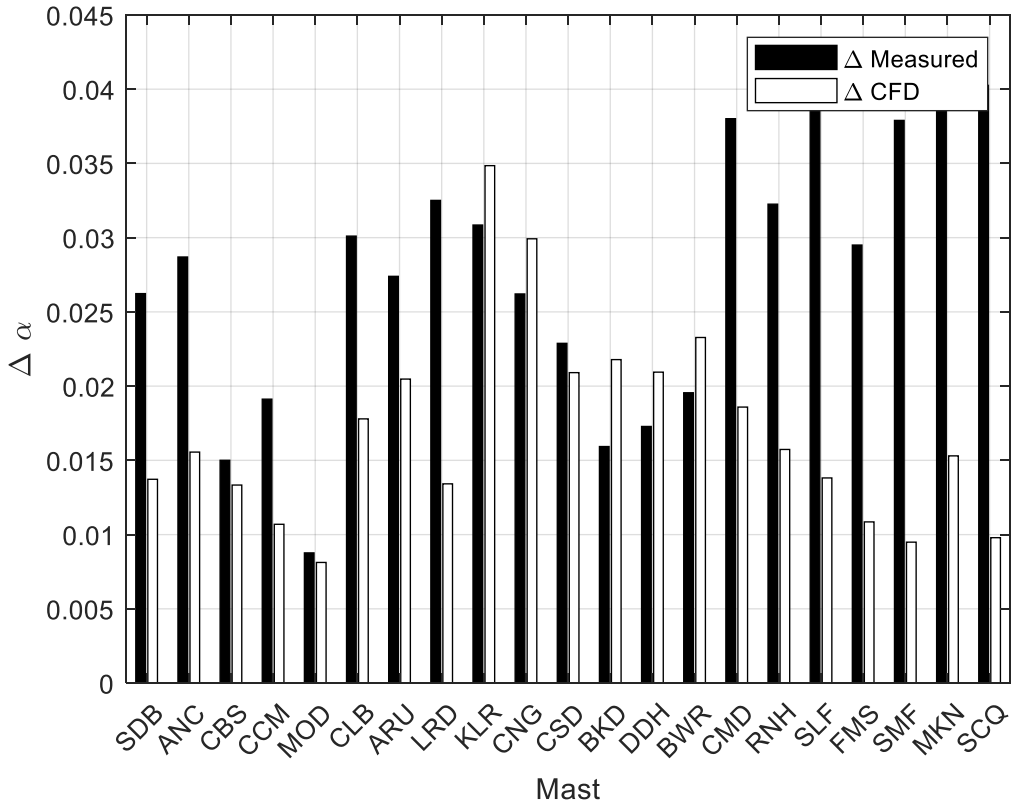


*Figure 6.9: Showing the CFD-modelled change in wind shear exponent between neutral and diabatic modelling alongside the measured equivalent.*

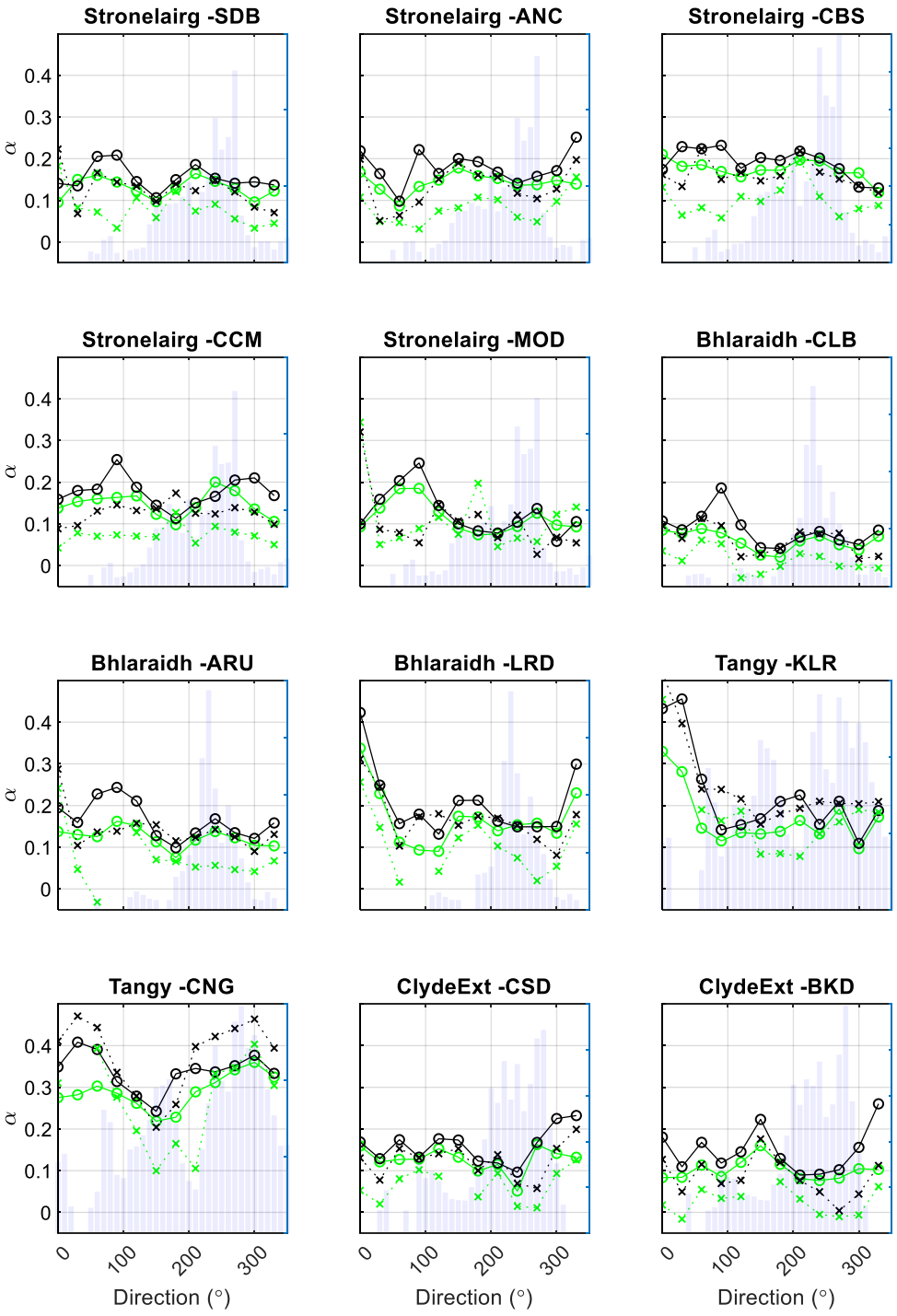


*Figure 6.10: Neutral/diabatic CFD predictions of wind shear for 36 direction sectors (green/black solid lines with circles) and neutral-filtered/unfiltered measurements of wind shear (green/back dashed lines with crosses). Only showing 12 out of 36 direction sectors modelled. Directional frequency shown by blue bars.*

### 6.4.3 Turbulence Intensity

This section can be covered more briefly as the validation process is the same, in principle, as for shear exponent.

Modelled values of turbulence intensity (TI) are extracted from the CFD model for both neutral ($TI'_N$) and diabatic ($TI'_D$) simulations and the change from neutral to diabatic conditions is calculated as:

$$\Delta TI' = TI'_N - TI'_D \quad (91)$$

The measured data are again filtered for wind speed (this time, for 8 – 12m/s to be comparable with the wind speed in the CFD model, since TI is sensitive to wind speed) and the average measured TI is calculated first for all stability conditions ($TI_D$), then for neutral-filtered conditions ($TI_N$). Then the measured difference can be calculated:

$$\Delta TI = TI_N - TI_D \quad (92)$$

TI is expected to be lower in stable conditions and the sites under consideration are slightly stable on average, so we expect $\Delta TI$ to be negative in all cases. Figure 6.11 shows that for the measured data there is a reduction in TI in the range 0.0 – 1.0%.

The success criteria are set the same as before. It is observed that CFD is not able to match this reduction at every validation point: at four mast locations on Stronelairg CFD incorrectly predicts a very small increase in TI. Further modelling is required to trace the source of this error.

Even so, the diabatic approach is judged to more accurately predict TI on the grounds that 17 out of 21 validation points (and 4 out of 5 sets of simulations) are successfully validated.

Figure 6.12 shows modelled versus measured TI for a subset of nine sites for 12 out of 36 direction sectors. Similarly to above, the CFD-modelled change in TI agrees overall with the measured change – although the sector-specific results taken alone show a high amount of variation.

These plots show that TI is generally under-predicted in both the neutral and diabatic model: the modelled results (black and green solid lines) are generally below the unfiltered measured results (dashed black line). However, the extent of over-prediction is less with the diabatic model (solid black line), with the exception of the measurement points at Stronelairg.

Results for all five measurement masts at Stronelairg (SDB, ANC, CBS, CCM and MOD) have been presented sector by sector in this plot. This is to show that the cause of the increase in CFD predictions of TI (rather than expected decrease) cannot be explained by a spurious result from any one sector: small increases in CFD-modelled TI are observed right across the directional range. Therefore, this deviation from the overall trend remains unexplained until additional/repeat modelling can be undertaken.

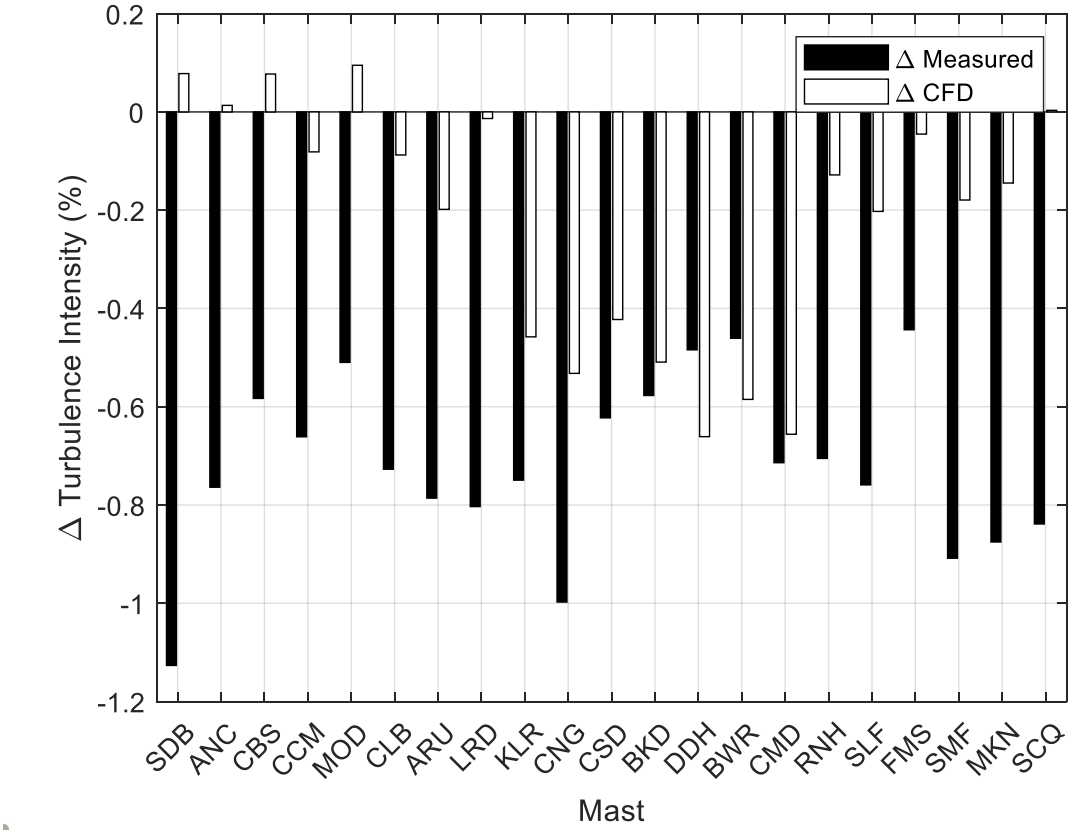


*Figure 6.11: Showing the CFD-modelled change in turbulence intensity between neutral and diabatic modelling alongside the measured equivalent.*

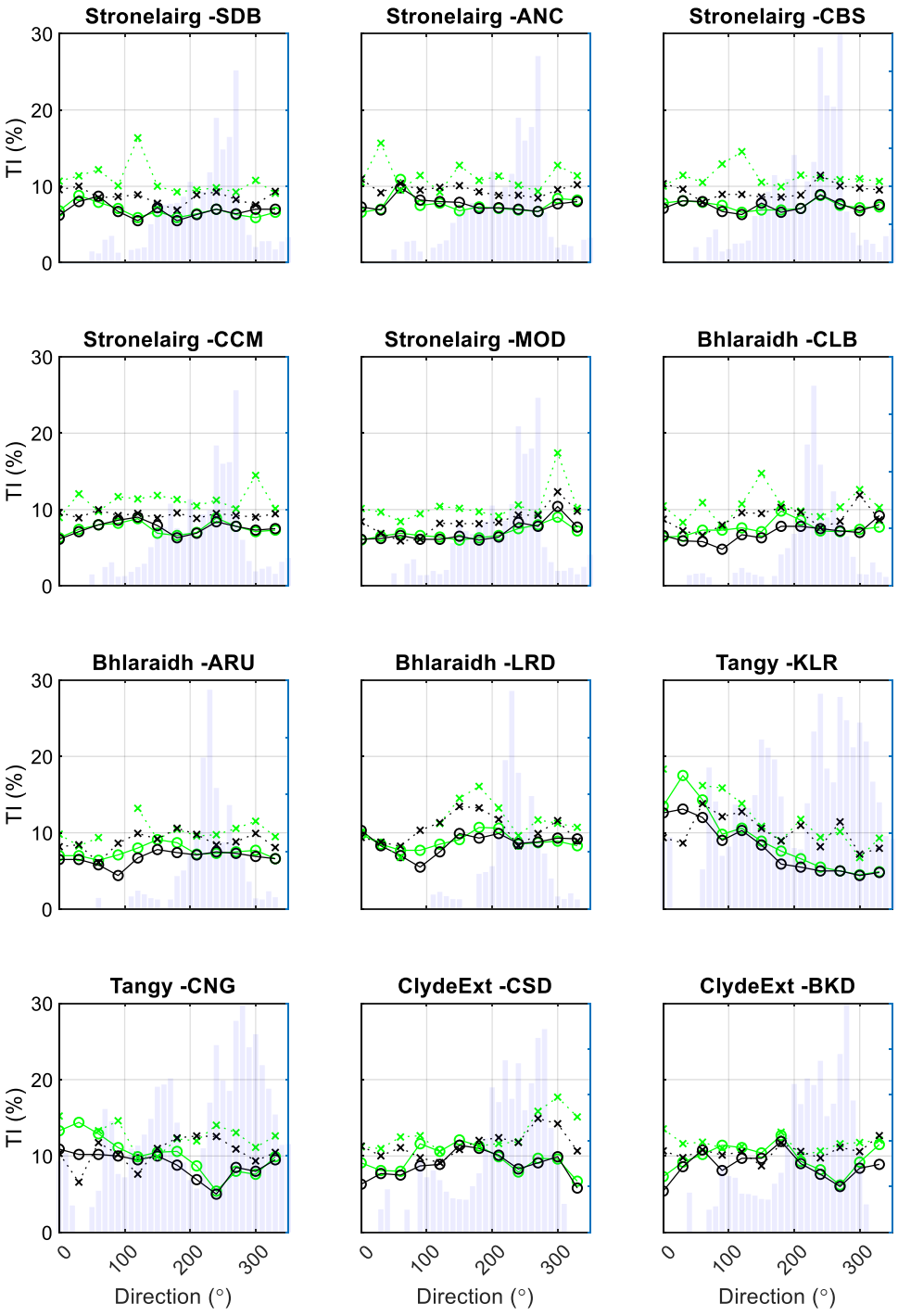


*Figure 6.12: Neutral/diabatic CFD predictions of turbulence intensity for 36 direction sectors (green/black solid lines with circles) and neutral-filtered/unfiltered measurements of turbulence intensity (green/back dashed lines with crosses). Only showing 12 out of 36 direction sectors modelled. Directional frequency shown by blue bars.*

### 6.4.4 Wind Speed Ratio

In this case, wind speed ratio (WSR) first had to be calculated as the ratio of the wind speed at the primary mast to that at the secondary mast. This is calculated using the modelled mean values from CFD and in each 10-minute time-step for the measured data. The measured data is then again wind speed filtered (5 – 25m/s) and an additional filter is applied to omit spurious values of WSR (0.5 < WSR < 2) which might be caused by instrument failure or icing.

ΔWSR' and ΔWSR are calculated similarly to before. This time, it is less clear what should be expected: perhaps an increase in WSR when the primary mast is at greater elevation than the secondary and vice versa, due to large-scale vertical stratification effects. Figure 6.13 shows the ΔWSR' and ΔWSR and the measured difference in WSR can be seen to be positive in some cases and negative in others: both increases and decreases within the range ±2%, when comparing neutral-filtered against unfiltered measurements. However, the diabatic CFD validates at 18 out of 21 measurement mast locations (or 3-4 out of 5 sets of simulations).

There are effectively two cases in which switching to diabatic does not offer an accuracy improvement.

First, KLR/CNG and CNG/KLR at the 'Tangy' site (which are simply the inverse ratio of one another). In this case, measurement mast CNG is at slightly greater elevation and surrounded by dense forestry. The measured data shows ΔWSR>0 for CNG/KLR, which seems plausible because of the elevation difference. It may be that diabatic CFD is incorrectly modelling the interaction between the forestry and stability. In any case, ΔWSR is within ±0.5% and therefore well within the uncertainty of both CFD modelling and wind/stability measurement. Further diabatic CFD runs of forested sites with temperature gradient measurements and multiple measurement points would be required to illuminate this problem.

Second, CSD/CMD at Clyde Ext. In this case, diabatic CFD correctly predicts ΔWSR<0 but overshoots the magnitude. This site is known for its extremely complex terrain and this could

be explained by spurious flow behaviour in the CFD model. CFD validates well at the other four measurement mast locations on the same site.

Figure 6.14 shows modelled versus measured wind speed ratio for a subset of nine sites for 12 out of 36 direction sectors. Again, the neutral and diabatic simulations can bee seen to diverge in some sectors more than others. In some sectors (for example, Clyde Ext – BKD/CMD sector 10) CFD can be seen to predict wind speed ratio very poorly, in both the neutral and diabatic modelling cases. In other cases (for example, Bhlaraidh – ARU/LRD sector 6), only the diabatic prediction shows such a deviation. However, for both of these examples, the overall effect (weighted average) of switching from neutral to diabatic still shows a benefit.

Diabatic CFD can therefore be considered to more accurately capture the effect of atmospheric stability on the wind flow, as measured by comparing concurrent wind speed at two measurement points on the same site.

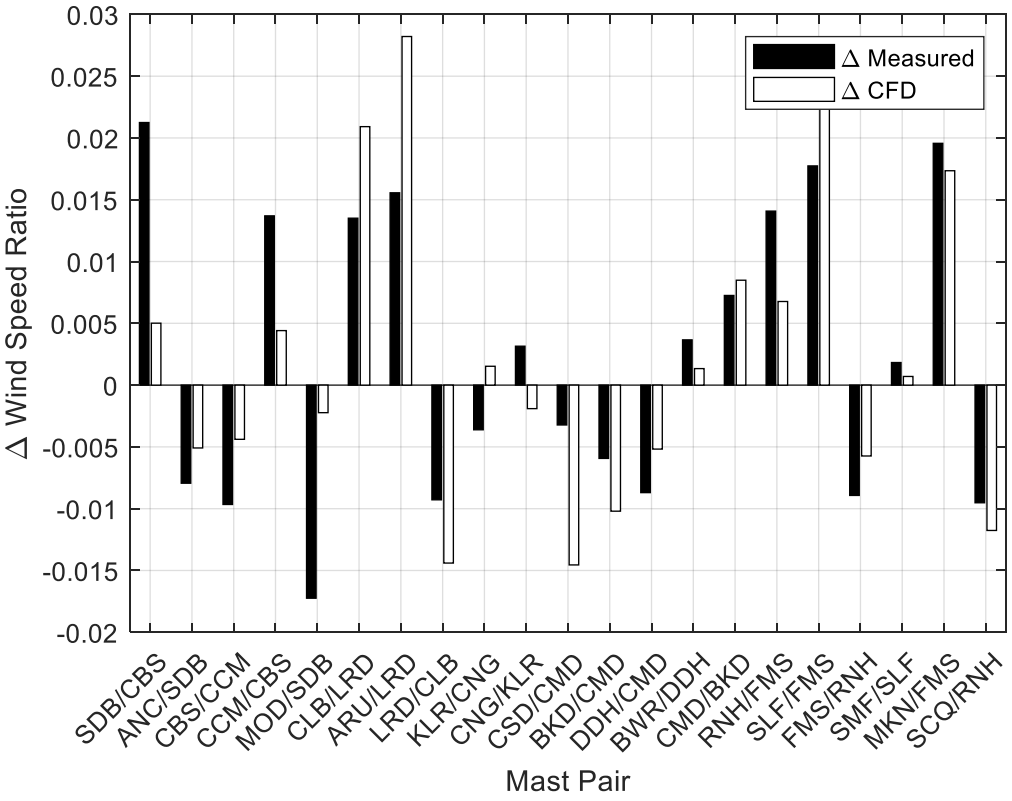


*Figure 6.13: Showing the CFD-modelled change in wind speed ratio between neutral and diabatic modelling alongside the measured equivalent.*

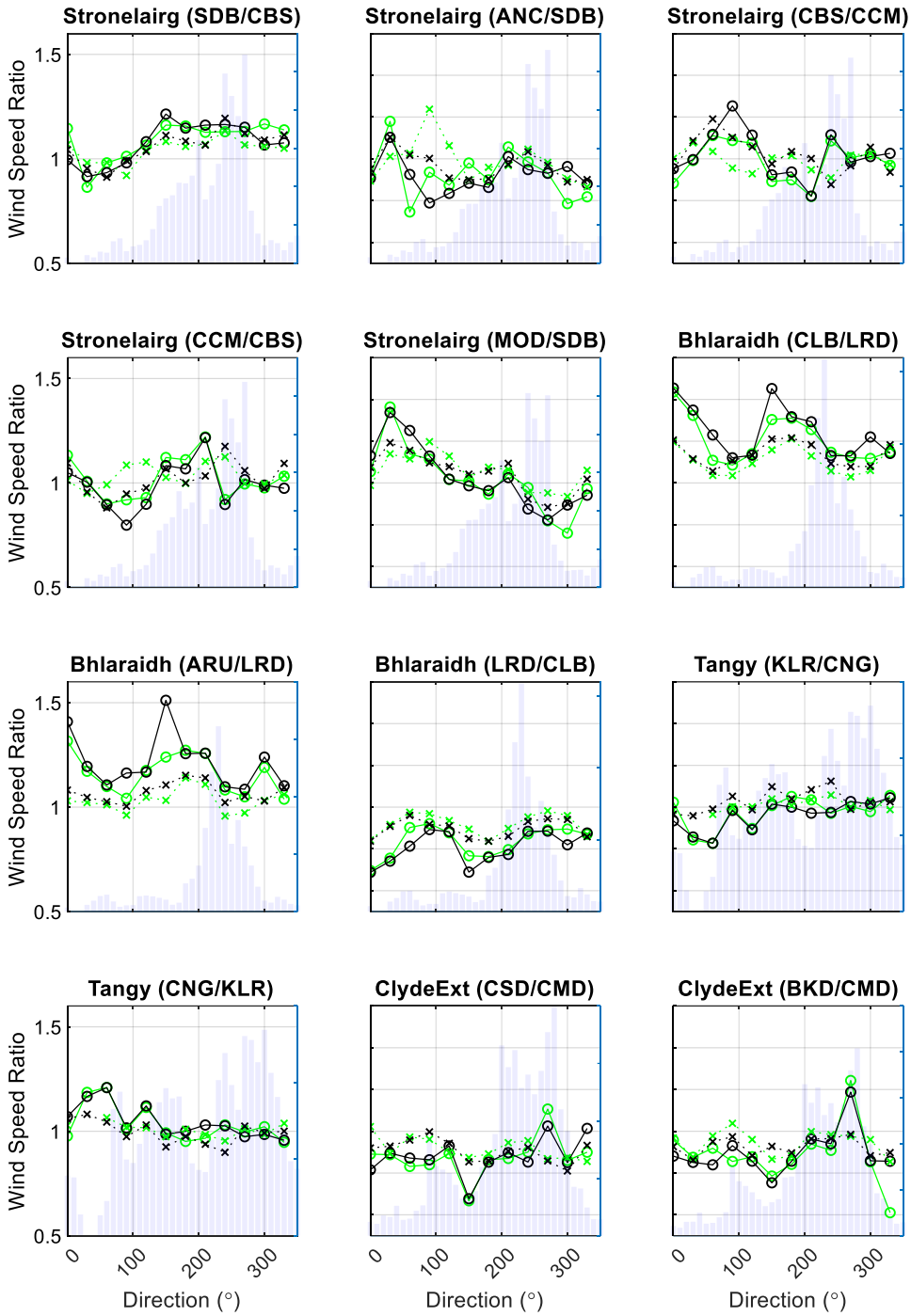


*Figure 6.14: Neutral/diabatic CFD predictions of wind speed ratio for 36 direction sectors (green/black solid lines with circles) and neutral-filtered/unfiltered measurements of wind speed ratio (green/back dashed lines with crosses). Only showing 12 out of 36 direction sectors modelled. Directional frequency shown by blue bars.*

| Site | TMM I | TMM II | Data (yrs) | % Neutral | Δ Wind Speed Ratio | | Δ Turbulence Intensity | | Δ Shear Exponent | |
|---|---|---|---|---|---|---|---|---|---|---|
| | | | | | Mea-sured | CFD | Meas-ured | CFD | Meas-ured | CFD |
| Stronelairg | 'SDB' | 'CBS' | 1.23 | 16% | 0.02 | 0.01 | -1.1% | 0.1% | 0.03 | 0.01 |
| | 'ANC' | 'SDB' | 1.23 | 17% | -0.01 | -0.01 | -0.8% | 0.0% | 0.03 | 0.02 |
| | 'CBS' | 'CCM' | 1.23 | 15% | -0.01 | 0.00 | -0.6% | 0.1% | 0.02 | 0.01 |
| | 'CCM' | 'CBS' | 1.23 | 16% | 0.01 | 0.00 | -0.7% | -0.1% | 0.02 | 0.01 |
| | 'MOD' | 'SDB' | 1.23 | 18% | -0.02 | 0.00 | -0.5% | 0.1% | 0.01 | 0.01 |
| Bhlaraidh | 'CLB' | 'LRD' | 0.95 | 20% | 0.01 | 0.02 | -0.7% | -0.1% | 0.03 | 0.02 |
| | 'ARU' | 'LRD' | 0.91 | 19% | 0.02 | 0.03 | -0.8% | -0.2% | 0.03 | 0.02 |
| | 'LRD' | 'CLB' | 0.95 | 18% | -0.01 | -0.01 | -0.8% | 0.0% | 0.03 | 0.01 |
| Tangy | 'KLR' | 'CNG' | 1.07 | 21% | 0.00 | 0.00 | -0.7% | -0.5% | 0.03 | 0.03 |
| | 'CNG' | 'KLR' | 1.07 | 21% | 0.00 | 0.00 | -1.0% | -0.5% | 0.03 | 0.03 |
| Clyde Ext | 'CSD' | 'CMD' | 0.94 | 21% | 0.00 | -0.01 | -0.6% | -0.4% | 0.02 | 0.02 |
| | 'BKD' | 'CMD' | 0.94 | 20% | -0.01 | -0.01 | -0.6% | -0.5% | 0.02 | 0.02 |
| | 'DDH' | 'CMD' | 0.94 | 20% | -0.01 | -0.01 | -0.5% | -0.7% | 0.02 | 0.02 |
| | 'BWR' | 'DDH' | 0.97 | 22% | 0.00 | 0.00 | -0.5% | -0.6% | 0.02 | 0.02 |
| | 'CMD' | 'BKD' | 0.94 | 20% | 0.01 | 0.01 | -0.7% | -0.7% | 0.04 | 0.02 |
| Viking | 'RNH' | 'FMS' | 0.86 | 16% | 0.01 | 0.01 | -0.7% | -0.1% | 0.03 | 0.02 |
| | 'SLF' | 'FMS' | 1.03 | 16% | 0.02 | 0.02 | -0.8% | -0.2% | 0.04 | 0.01 |
| | 'FMS' | 'RNH' | 0.86 | 16% | -0.01 | -0.01 | -0.4% | 0.0% | 0.03 | 0.01 |
| | 'SMF' | 'SLF' | 1.23 | 13% | 0.00 | 0.00 | -0.9% | -0.2% | 0.04 | 0.01 |
| | 'MKN' | 'FMS' | 1.02 | 16% | 0.02 | 0.02 | -0.9% | -0.1% | 0.04 | 0.02 |
| | 'SCQ' | 'RNH' | 0.89 | 14% | -0.01 | -0.01 | -0.8% | 0.0% | 0.04 | 0.01 |

*Table 6.4: Full results of diabatic CFD validation study. Light green-coloured cells indicate successful validation (i.e. cases where moving from neutral to diabatic CFD results in a change which is reflective of the measured equivalent) and red indicates unsuccessful.*

## 6.5 Chapter Summary

In this chapter, first the CFD modelling process was set out and a novel approach to modelling site-specific stability distributions in CFD was described.

The process of validating the new diabatic CFD model, by observing the modelled changes in key wind flow parameters (shear, TI and WSR) when switching from neutral to diabatic simulation was summarised. The modelled changes were compared against the equivalent measured changes, using a technique of filtering the measured data for neutral periods only, using on-site concurrent measurements.

Table 23 summarises the validation across the six sites showing green where the validation is successful and red where it was not. For all three key wind flow parameters, diabatic CFD simulation results in greater flow modelling accuracy than neutral CFD, with only a few exceptions, and can therefore be considered to be validated for continued use.

# 7 Implementation

In the previous chapter, it was demonstrated that the incorporation of site-specific stability profiles derived from Vortex WRF time series data can lead to an improvement in wind flow modelling accuracy at most sites.

This chapter details the implementation of this new methodology in wind farm energy yield assessment and layout design. First, energy yield calculations are carried out using separate neutral and diabatic flow modelling inputs in order to demonstrate the impact of switching from one to the other. Next, wind farm layouts are designed using first neutral then diabatic simulations as a basis and it is shown that wind farms can be designed for significantly increased energy yield using these more accurate inputs.

The sites under consideration in this chapter are the same six for which CFD was run in the previous chapter. 'Tangy' is included, despite the fact that the diabatic CFD validation was not entirely successful, on the basis that the validation probably failed due to complications presented by the dense forestry on one of the measurement masts used, rather than due to the diabatic simulation being less accurate at modelling the site in general.

## 7.1 Inputs

MATLAB was used to prepare inputs for energy yield calculations and the DNV-GL WindFarmer package was used to carry out the energy yield calculations themselves, including evaluating wake effects.

In the previous chapter, MATLAB was used to re-sample CFD wind speed maps into regularly-spaced (25 x 25m) rectangular grids. Now, MATLAB is again used to convert these grids into wind resource grids (WRGs): a different format of wind speed map which can be interpreted by WindFarmer. The WindFarmer WRG format combines the directional frequency and wind speed frequency distributions, rather than just the omni-directional mean wind speed. As is common in wind energy yield assessment, the wind speed distribution is defined as a Weibull distribution, $P(A, k)$, with scale and shape parameters, $A$ and $k$. Specifically, the frequency $P$ of wind speed $u$ is given by:

$$P(A,k) = \frac{k}{A} \cdot \left(\frac{u}{A}\right)^{k-1} e^{-(u/A)^k} \quad (93)$$

The measured wind speed distribution at the mast location is used as a starting point. Then, the wind speed grid from CFD is used to scale the measured distribution by the CFD-predicted ratio of the mean wind speed at each grid point $\overline{U}_{(x,y)}$ to the mean wind speed at the mast location $\overline{U}_{(mast)}$, as per:

$$P(A,k)_{(x,y)} = P\left(A \cdot \left(\frac{\overline{U}_{(x,y)}}{\overline{U}_{(mast)}}\right), k\right)_{(mast)} \quad (94)$$

For practical purposes, the shape factor ($k$) at every point on the site is assumed to equal that at the measurement mast location. This is common practice in wind analysis, for scaling measured wind distributions to other locations. The errors associated with this simplification, in terms of wind speed values, are not of a scale that would affect the wind farm layout optimisation or energy yield assessment.

To allow comparison, this process is repeated for both neutral and diabatic simulations for each site, so that a neutral and diabatic WRGs are created and imported into WindFarmer.

## 7.2 Wind Farm Layout Optimisation

The optimiser function in WindFarmer was used to design layouts for both the neutral and diabatic cases. First, a baseline layout is required, as an initiation point which is kept constant for all sites. MATLAB was used to generate a baseline layout of 16 turbines in a 4 x 4 square layout spaced by 500m in the N-S and E-W directions (Figure 7.1).

The principles of layout design were introduced in section 2.6.1. In this assessment, to preserve a simple and consistent approach from site to site, only ambient wind conditions and wake effects are being taken into consideration. No interaction between stability and wakes is being modelled but wake effects must be included in order to create practical layouts and evaluate meaningful results. (However, there are known to be significant

interactions between atmospheric stability and wake effects. This was mentioned in 3.1.1 and will be presented as further work in 8.5.3).

Then the optimiser was run (with settings noted in Table 7.1), with turbines constrained to a circular site boundary of radius 2.5km, centred on the mid-point of the wind speed map. Additionally, WTGs are constrained by a minimum spacing requirement, specified as an elliptical buffer around each turbine measuring 5 x rotor diameters (RD) in the prevailing wind direction and 3 x RD in the perpendicular (585 x 351m; typical for a UK onshore wind farm).

The optimiser works by moving turbines toward the most energy-dense areas of the site, without compromising the minimum spacing constraint, calculating the wake effects and energy yield for each iteration of the layout and re-iterating until either the energy yield converges on the optimum value (e.g. after the maximum number of fruitless iterations) or the maximum number of iterations is reached. The optimum layout will be that which strikes a balance between clustering turbines in the windiest areas of the site and avoiding turbine proximity in the prevailing wind direction so as to minimise wake effects.

This optimisation was carried out twice for each site: once using the neutral wind map as an input ('neutral-optimised layout') and once using the diabatic wind map ('diabatic-optimised layout'). The number of iterations required is summarised in Table 7.3. In all cases, the optimum layout was identified within the maximum number of allowed iterations. The variation in the number of iterations taken to solve the optimisation is likely mostly random – although the greater number of iterations when using the diabatic wind map could be a reflection of the more diverse wind conditions. The next two sections detail how these layouts were compared in order to assess the impact of switching from neutral to diabatic wind modelling.

| | |
|---|---|
| **Wake model** | 'Modified PARK' |
| **Maximum number of iterations** | 1000 |
| **Maximum number of fruitless iterations** | 100 |
| **Minimum turbine spacing** | 5 x 3 D |

*Table 7.1: Optimisation settings used in DNV-GL WindFarmer.*

## 7.3 Energy Yield Assessment

In this section, the error associated with using neutral instead of diabatic wind modelling for a fixed turbine layout is assessed. The energy yield is calculated for the neutral-optimised layout, first using the neutral wind map and then using the diabatic wind map and the two are compared.

The turbines were all modelled as Vestas V117-4.2MW but the modelled hub-height varied from site to site (70 – 90m).

WindFarmer was again run to calculate the inter-turbine wakes and energy yield. Whereas the PARK wake model was used for layout optimisation, the Eddy Viscosity wake model was used for energy yield assessment so as to be closer in line with standard SSE practice. This is unlikely to have a significant bearing on the calculated energy yield differences, given the relatively small number of turbines being modelled. A detailed description of the WindFarmer Eddy Viscosity wake model is outside of the scope of this thesis but, for information, the settings applied in the wake calculation are detailed in Table 7.2.

The results are presented in Table 7.3. It is evident from looking at the evaluated energy yield values that mean wind speed varies significantly between the six sites, with Shetland having the highest hub-height mean wind speed at turbine locations and Bhlaraidh the lowest.

As described in Chapter 6 the mean wind speeds deviate by generally a few percent and up to around 10% between the neutral and diabatic wind maps, so the two calculations should be expected to result in different answers.

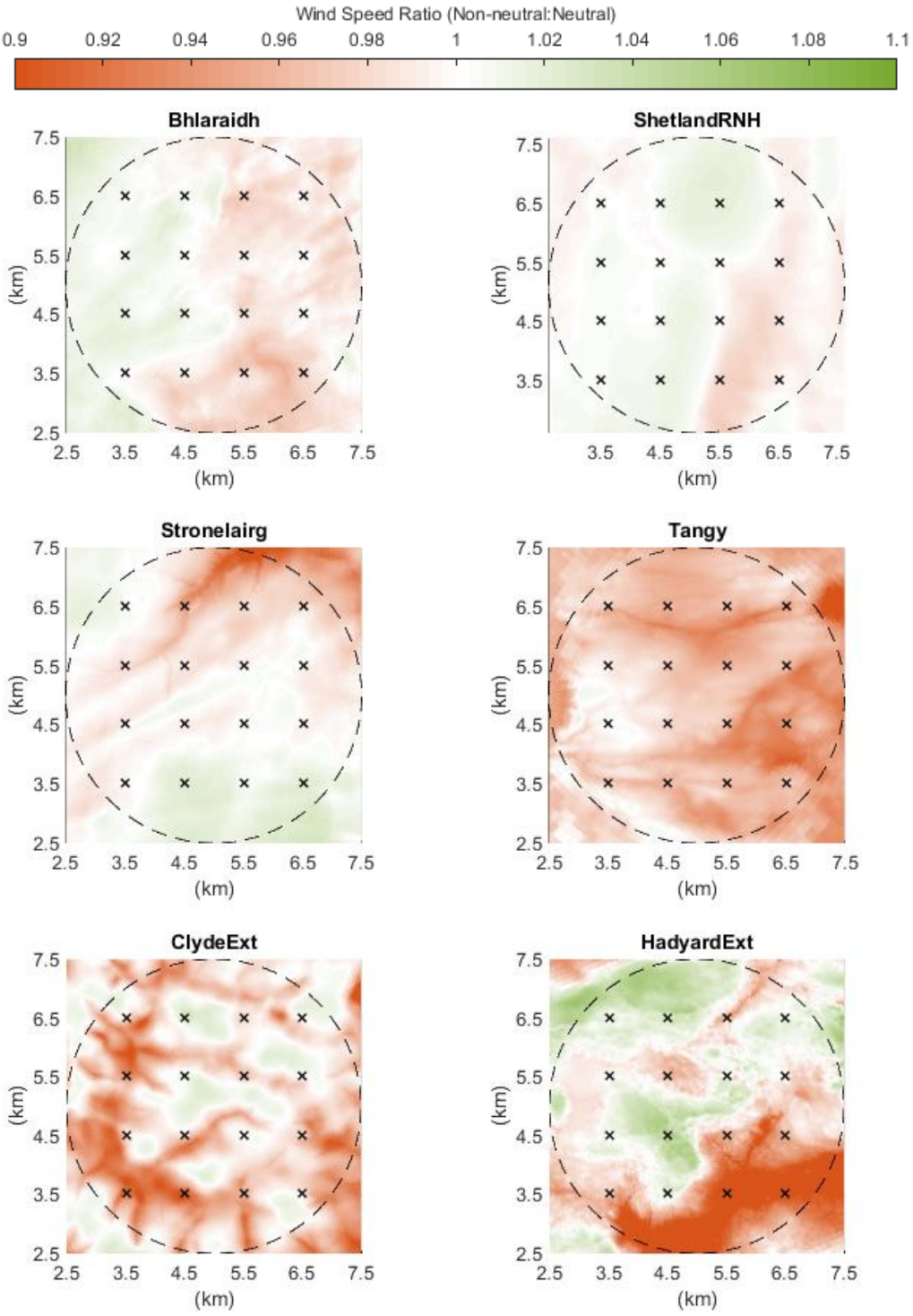


*Figure 7.1: Baseline layouts for 6 sites (4x4 square grid with 500m spacing), used as initiation layouts for the WindFarmer optimisation model. Background shows ratio of diabatic to neutral wind speed. Green >1; red <1.*

| | |
|---|---|
| ***Wake Model*** | Eddy Viscosity |
| ***Large Wind Farm Correction*** | 'On' |
| ***Base roughness*** | 0.03m |
| ***Increased roughness*** | 0.06m |
| ***Geometric width*** | 1 diameters |
| ***Maximum row spacing*** | 5 diameters |
| ***Recovery starts*** | 60 diameters |
| ***50% recovery at*** | 80 diameters |
| ***Maximum Wind Speed*** | 50m/s |
| **Number of direction steps** | 180 |
| **Maximum length of wake** | 50 diameters |

*Table 7.2: Settings used in WindFarmer for energy yield calculations.*

| *Site* | *Mast Height (m)* | *Hub Height (m)* | *Energy Yield (GWh/yr) (neutral)* | *Energy Yield (GWh/yr) (diabatic)* | *Δ Energy Yield* |
|---|---|---|---|---|---|
| *Bhlaraidh* | *60.0* | *76.0* | *244.9* | *244.7* | *-0.1%* |
| *Shetland RNH* | *70.0* | *93.0* | *354.0* | *357.9* | *1.1%* |
| *Stronelairg* | *70.0* | *76.5* | *294.9* | *296.9* | *0.7%* |
| *Tangy* | *80.0* | *72.0* | *281.5* | *279.1* | *-0.8%* |
| *ClydeExt* | *70.0* | *89.5* | *248.6* | *251.7* | *1.2%* |
| *HadyardExt* | *80.0* | *58.0* | *253.3* | *265.4* | *4.8%* |
| | | | | *ABS AVG* | *1.4%* |

*Table 7.3: Inputs and results to neutral and diabatic energy yield calculations for fixed wind farm layout.*

Table 7.3 can be considered alongside Figure 6.8 to make sense of the results. For example, at Tangy the measurement mast is located on a high-elevation, prominent part of the site. The diabatic CFD simulation predicts a greater wind speed drop than the neutral simulation between this location and most of the rest of the site.

Also, modelled wind shear in the diabatic simulation will be greater, meaning that the reduction in wind speed when extrapolating from mast height (80m) to hub height (72m) will be greater than in the neutral simulation. Both of these factors combined lead to an overall reduction in energy yield which is significant in magnitude.

## 7.4 Layout Design

In the previous section, energy yield was assessed using both neutral and diabatic wind map inputs based on a fixed turbine layout. Now, the impact of re-designing a wind farm based on a more accurate diabatic wind map is assessed.

First, the layout was optimised using the neutral wind map, to give a benchmark against which to compare the new method. Then the layout was optimised using the diabatic wind map, using the same input parameters. Both optimised layouts are visualised in Figure 7.2.

Finally, the energy yield was calculated for each layout, using the diabatic wind map as the input in both cases. The settings used to calculate the energy yield (Eddy Viscosity wake model), in both cases, are the same as in the previous section (as this method is held to be more accurate but too computationally intensive for iterative optimisation).

The uplift in energy yield was calculated as the ratio of the energy yield from the diabatic approach to the neutral approach. The results are presented in Table 7.4, showing that in all six cases the layout optimised using the diabatic wind map had a greater energy yield than the neutral-optimised layout, as would be expected. The average uplift in energy yield was 0.5% (ranging from 0.1% to 1.1%).

| Site | Layout optimised for neutral wind map | | Layout optimised for diabatic wind map | | Δ Energy Yield |
|---|---|---|---|---|---|
| | # Iterations | Energy Yield (GWh/a) | # Iterations | Energy Yield (GWh/a) | |
| **Bhlaraidh** | 446 | 244.7 | 319 | 245.3 | 0.2% |
| **Shetland RNH** | 293 | 357.9 | 510 | 358.5 | 0.1% |
| **Stronelairg** | 404 | 296.9 | 810 | 298.9 | 0.6% |
| **Tangy** | 384 | 279.1 | 371 | 280.4 | 0.4% |
| **ClydeExt** | 217 | 251.7 | 357 | 252.8 | 0.4% |
| **HadyardExt** | 280 | 265.4 | 353 | 268.4 | 1.1% |

| AVG | 0.5% |
|---|---|

*Table 7.4: Inputs and results to neutral and diabatic energy yield calculations for optimised wind farm layouts.*

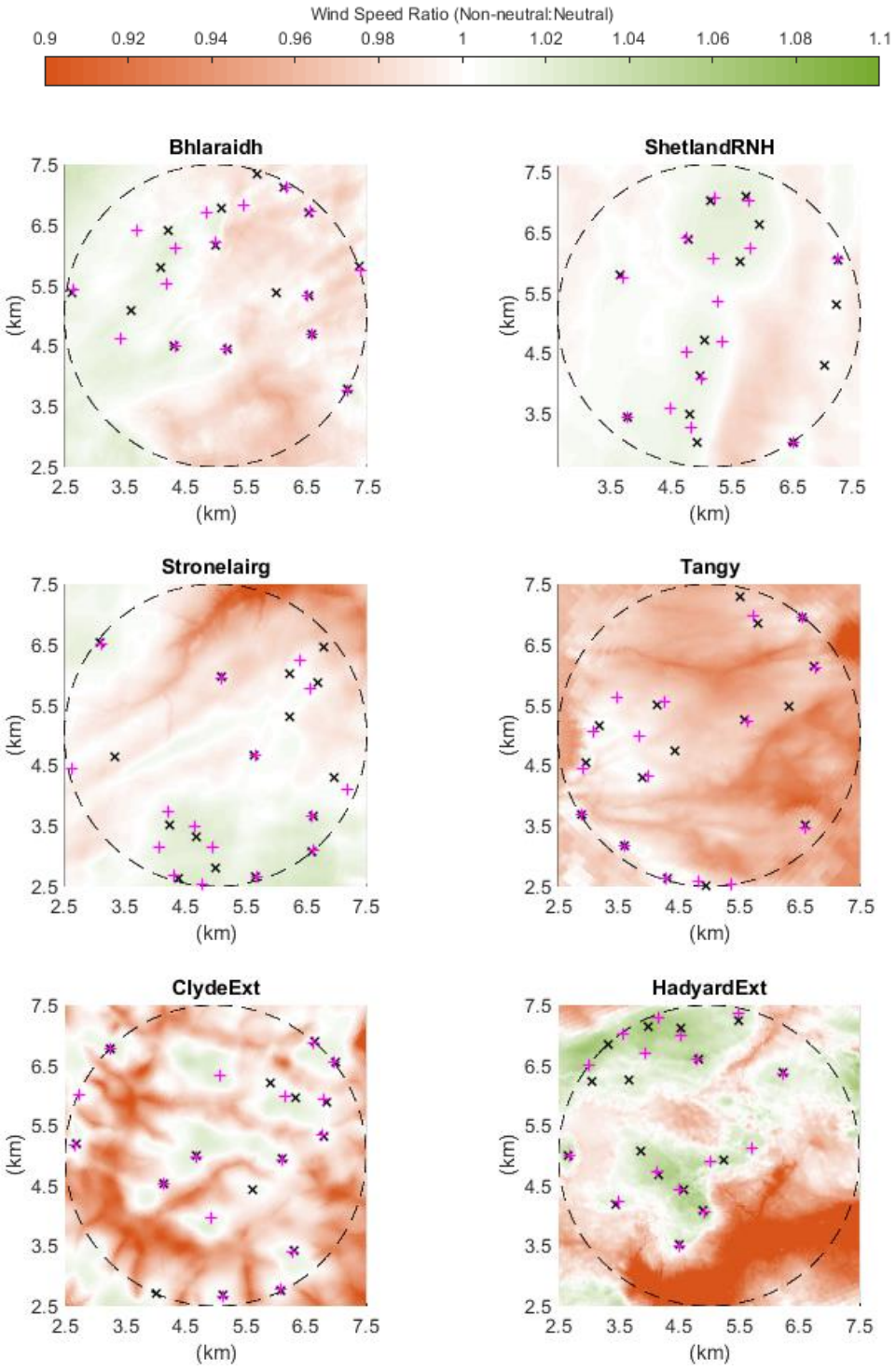


*Figure 7.2: Neutral-optimised (black diagonal crosses) and diabatic-optimised (magenta crosses) layouts for six sites. Background shows ratio of diabatic to neutral wind speed. Green >1; red <1.*

The optimised layouts for both the neutral and diabatic wind maps are visualised in Figure 5.2 for all six sites. As expected, the layouts differ from one another significantly. The uplift in energy yield was least at windy sites with subtle variation in stability (e.g. Bhlaraidh, ShetlandRNH) and greatest at less windy sites with large stability variation and complex terrain (Hadyard Ext).

Figure 7.3 shows the resulting energy yield at turbine level: turbines in the diabatic optimised layout achieve greater wind speeds on average than turbines in the neutral-optimised layout, giving rise to the overall energy yield discrepancy.

In these plots, the turbines have been ordered from most to least productive (left to right) to give a useful visualisation. The largest per-turbine energy yield discrepancies (up to 1 - 2% at Stronelairg #10 and Hadyard Ext #11) can be observed at those sites with the greatest bulk increase.

## 7.5 Chapter Summary

The intention of this chapter was to demonstrate how diabatic flow modelling, which was shown to be more accurate in Chapter 6, impacts on wind farm design and assessment. The impact of switching from neutral to diabatic modelling is checked in two ways: first by considering how the energy yield assessment of a wind farm with fixed layout changes when applying diabatic modelling. Then by considering how wind farm layouts might be designed differently with more accurate diabatic wind inputs and how this impacts on energy yield.

Energy yield was found to deviate by 1.4% on average (up to 4.8%) when assessing wind farms with fixed layout based on diabatic wind inputs, compared to neutral inputs. Wind farm layouts designed using diabatic flow modelling were found to result in 0.5% greater energy yield on average (up to 1.1% greater) than layouts designed using neutral flow modelling (taking the diabatic wind map as the ‘true’ wind map).

Both of these tests result in energy variances which are highly significant in terms of a wind farm business case. It is important to re-iterate that this assessment does not consider the effect of atmospheric stability on the prevalence of wake effects – the aim is to show the significance of stability/terrain interactions on ambient (non-wake) wind speed in isolation.

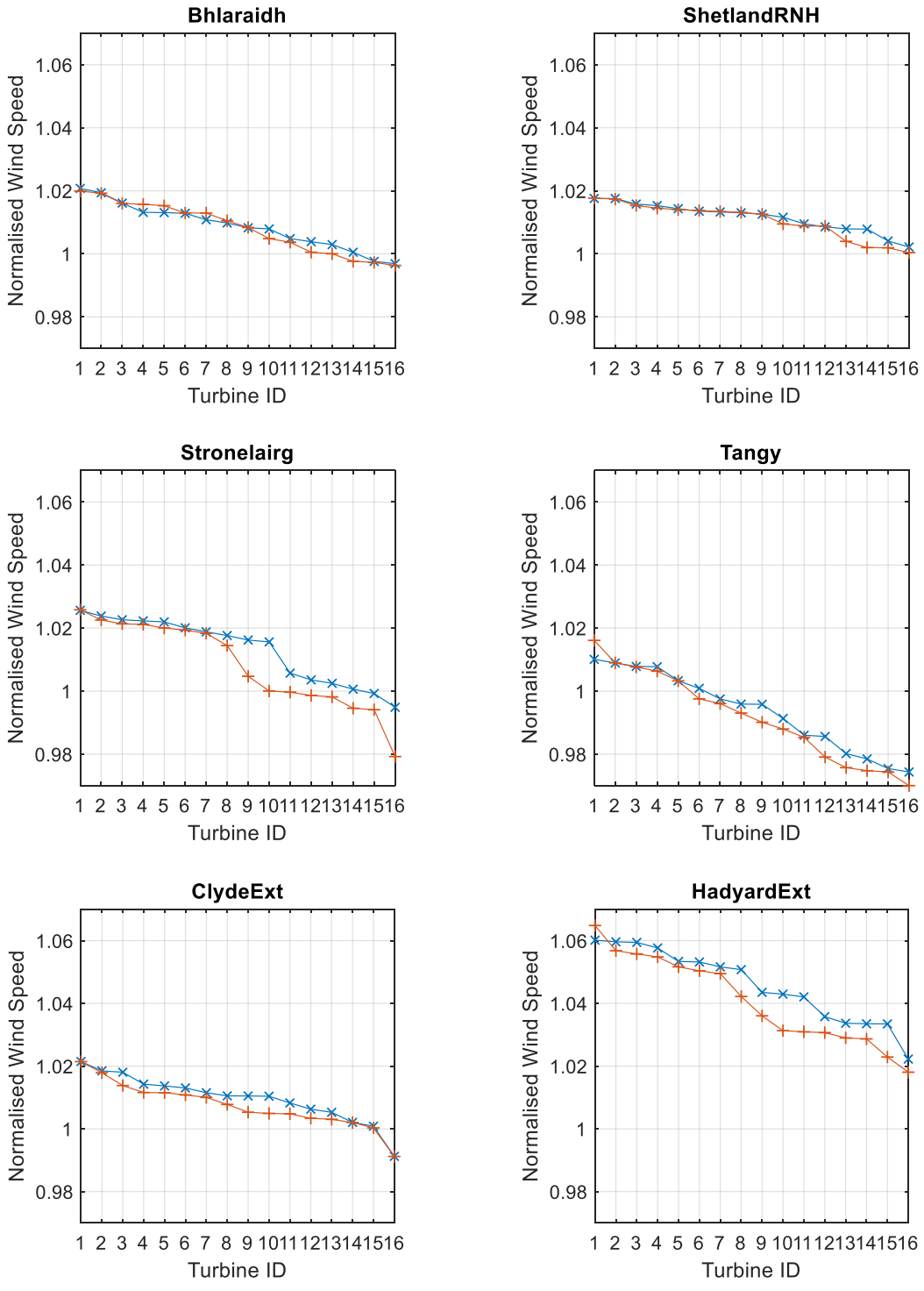


*Figure 7.3: Mast-normalised wind speed plots for six test sites for diabatic-optimised layouts (blue with diagonal crosses) and neutral optimised layouts (orange with horizontal crosses). Using diabatic wind map as input in both cases.*

# 8 Conclusions

## 8.1 Thesis Summary

In **Chapter 1**, the importance of wind energy research was placed in the context of wider political and commercial. **Chapter 2** set out some background physics and introduced some key concepts in the field of wind energy modelling, particularly in relation to the impact of atmospheric stability.

**Chapter 3** summarised some key papers in the field of atmospheric stability and wind energy. Then, the aims and objectives of this research were presented: to address questions around the sensitivity of wind flow modelling to atmospheric stability, to determine the best way to acquire input data and to evaluate the impact of considering atmospheric stability on wind farm layout design and energy yield.

The objectives were aligned with the development of an efficient, reliable and straight-forward methodology for incorporating site-specific atmospheric stability data into wind farm layout design and energy yield assessment practice which is of practical use to wind energy developers.

In **Chapter 4** , two different sets of mesoscale data from the WRF model were analysed. The difference in virtual potential temperature, $\Delta\theta_v$, between 10m and 100m was selected as a proxy for the characterisation of atmospheric stability.

Both data sets (Vortex and University of Edinburgh) displayed trends that are consistent with the physical nature of atmospheric stability set out in Chapter 2, specifically in terms of onshore/offshore differences and diurnal/seasonal trends. Maps of the UK and Ireland were generated which can be used as quick-reference guides for identifying regions of high variability or particularly diabatic stability, which might warrant particular attention in terms of flow modelling.

In **Chapter 5**, data were analysed from twelve locations (ten onshore and two offshore) at which measurements of temperature differential had been made for periods spanning at least one year, using a TG01 system. The $\Delta\theta_v$ measurement error was found to lie in the

range 0.02 – 0.11K, depending on instrument configuration, taking into account the need for precise pressure, relative humidity and absolute temperature measurements. This range was deemed to be acceptable for the purposes of measuring atmospheric stability for wind flow modelling.

At nine sites, measurements from a secondary temperature differential measurement system (either 2 x HMP155 sensors or 2 x CS215 sensors) were compared against the primary system (TG01 system). The HMP155 sensors, which had undergone calibration and bias-correction, were found to agree well with TG01 measurements whereas the uncalibrated CS215 sensors were found to disagree significantly, with the magnitude of the measurement error depending on absolute temperature.

Measured $\Delta\theta_v$ was used to categorise time series data sets of wind shear, turbulence intensity and wind speed ratio (between two locations within a few km) as stable, unstable or neutral. Stable periods exhibited high wind shear and low turbulence intensity whereas unstable periods exhibited the opposite, in line with physical theory. This leant confidence to the use of the metric $\Delta\theta_v$ for characterising atmospheric stability.

$\Delta\theta_v$ distributions from Vortex WRF data were then compared against the measured equivalents. Vortex WRF showed a tendency to slightly over-estimate the magnitude of $\Delta\theta_v$ in stable conditions and significantly under-estimate $\Delta\theta_v$ in unstable conditions. At one densely forested site, the inability of Vortex to accurately capture frequently occurring unstable periods resulted in a significant overall deviation between the Vortex and measured distributions. Otherwise, the level of agreement was acceptable and Vortex was judged to be a satisfactory substitute for measured data for the purpose of defining site-specific stability distributions.

**Chapter 6** demonstrated how $\Delta\theta_v$ time series data from the Vortex WRF model can be incorporated into CFD wind flow modelling, this being the key objective of this project. Significant consideration was given to identifying a means of down-sampling time series data into a compact CFD input profile, without losing the key characteristics of the raw data. This resulted in a straight-forward and efficient CFD process for modelling site-specific diabatic

conditions which does not require any additional CFD simulations, compared to the neutral process.

Both neutral and diabatic simulations were completed for six sites and wind maps were created for each. Wind speeds were observed to differ significantly (up to 10%) in the diabatic wind maps – most so at sites with complex terrain and/or highly variable atmospheric stability. Neutral and diabatic CFD predictions of wind shear, turbulence intensity and wind speed ratio were also extracted and compared to measured values, showing improved accuracy at modelling all three variables using the diabatic method.

In **Chapter 7**, neutral and diabatic wind resource grids were generated and the WindFarmer wake/energy modelling software was used to assess the difference between the two in energy terms. For a fixed wind farm layout, diabatic wind modelling led to a significant difference in the evaluated energy yield of 1.4% on average (0.1% to 4.8% across six sites modelled). When wind farm layouts were re-optimised based on the diabatic wind map, this led to an average 0.5% uplift in energy yield (0.1% to 1.1%), compared to layouts optimised on the neutral wind map.

## 8.2 Impact

The impetus for this PhD research lies in the technical requirements of SSE Renewables, the largest renewable energy generator in the UK and Ireland. SSE has a high proportion of sites in complex terrain and forestry and therefore holds a particular interest in accurately modelling complex wind flow.

The method for including atmospheric stability in CFD wind flow modelling described in this thesis has been part of SSE's standard methodology for wind farm layout design and yield assessment since 2017. The implementation phase (Chapter 7) of this thesis focussed on hypothetical turbine configurations, since the details of specific sites under development are obviously commercially sensitive. However, it is anecdotally true that significant value has been added to SSE's project pipeline by implementation of this new methodology.

In broader terms, SSE is currently targeting the development of an additional 1GW of onshore wind, as well as looking further ahead to re-powering opportunities. If the conclusion of this

research holds true, then improved layout designs will lead to an average 0.5% uplift in energy yield across this installed capacity. This would be equivalent to an uplift of approximately 17.5GWh or £0.9M of revenue per year per 1GW capacity and is likely to substantially impact on the viability of certain individual projects.

Outside of SSE, clearly this new methodology can be applied widely and should be of interest to onshore wind farm developers in the UK and beyond. The work will be submitted to relevant journals and will continue to be presented at conferences (having already been well received at two annual ETP conferences).

## 8.3 Key Findings

### 8.3.1 $\Delta\theta_v$ Measurement

This research has robustly established a reliable means of measuring virtual potential temperature differential for the purpose of validating mesoscale data.

Dedicated systems, such as the WindSensor TG01 can achieve greater stated measurement certainty than alternative systems due to their design and calibration process. However, as a general rule, any sensor pair deployed for the task of measuring temperature differential should be of high quality, calibrated at an accredited facility in an appropriate range of ambient temperatures and subsequently adjusted according to the results of the calibration (i.e. bias-corrected).

For reliable conversion of $T$ to $\theta_v$, twin pressure and RH sensors should be installed as close as possible to temperature sensor height.

### 8.3.2 CFD Modelling

Diabatic CFD simulation should be implemented for any site under consideration for layout design and wind resource assessment, with particular emphasis on sites with lower mean wind speed, significant deviation of mean stability from neutral, high variation in stability and/or complex terrain.

Approximating atmospheric stability in CFD by the proxy $\Delta\theta_v$ between 10m and 100m from WRF data and constructing a speed-sorted bin-average profile is an adequate method to achieve accuracy improvements.

To the author's knowledge, this thesis is the first published example of a methodology for incorporating a full range of validated site-specific atmospheric stability conditions into CFD modelling and has demonstrated the value of this improvement via a set of worked example layout designs and energy yield assessments.

It has been shown that an average increase in energy yield of 0.5% can be achieved by using this new method for improved wind farm layout design. However, even greater improvements may be possible, as will be explored in the following section.

## 8.4 Limitations

As with any PhD project, it has been necessary here to strike a compromise between breadth and depth. A start to end process for incorporating validated atmospheric stability values into CFD modelling and energy yield assessment has been demonstrated, resulting in improved energy yield for six re-designed wind farm layouts. That is a key strength of this research.

However, the cost of pursuing such breadth is that investigations into certain aspects of the process were less than comprehensive. It would have been preferable, for example, to thoroughly explore alternative GCMs and planetary boundary layer schemes at the mesoscale modelling stage, in order to find that combination which best described surface-layer stability.

Also, it is accepted that CFX has been utilised to less than its full ability as a software package, in terms of the use of a simple virtual potential temperature offset instead of a high vertical resolution virtual potential temperature profile. The progressed stability input method was selected on the basis that it was the best practically implementable method, rather than the best overall.

Overcoming these limitations, which are detailed further below, will form part of the future work described in 8.5.

### 8.4.1 Stability Definition

A key hypothesis in this research was that $\Delta\theta_v$ between 10m and 100m derived from WRF data should be an adequate proxy for describing atmospheric stability. This is despite the fact that this does not match the input requirements specified by CFX (which is $\Delta\theta_v$ between the surface and $h_{SL}$). To a large extent, this assumption has been validated in that a method using this metric has resulted in clearly improved flow modelling accuracy across numerous sites.

However, a more exhaustive study would have considered alternative metrics, which may have resulted in physically more realistic and even more accurate CFD modelling.

For example, surface temperature values could have been used in place of temperature at 10m (or at least to investigate the difference between the two). Surface skin temperature is an output parameter in the UoE WRF data set. However, no ground temperature measurements were specified in the measurement campaign that would have allowed for validation. Sea-surface temperature measurements are available at the Dogger Bank DBE and DBW masts but these were not investigated due to time constraints.

Additionally, it is likely that the metric chosen does not adequately represent the shape of the $\theta_v$ profile across the entire height of the ABL. It *is* possible to define a $\theta_v$ profile in CFX as a series of vertically distributed values, rather than stating $\Delta\theta_v$ and allowing CFD to assume a logarithmic fit. However, this would involve significant adjustments to the standard CFD configuration which were outside of the scope of this project. Moreover, measured temperature data from three or more heights at multiple sites were not available in order to validate such an approach (see 8.5.2).

Finally, it would have been preferable to more robustly quantify the validity of using Vortex WRF data as an input to the CFD process. This was justified on the basis that the mean biases introduced by using Vortex data as opposed to measured data were ‘small’ relative to the range of $\Delta\theta_v$ being modelled.

An alternative approach would have been to run CFD simulations using $\Delta\theta_v$ profiles from both Vortex and measurements. The error in $\Delta\theta_v$ modelling could then have been quantified in a more useful sense: as a wind speed or energy error. However, this approach was not feasible within the timeframe of the research due to (i) the increased computational resource required to duplicate every CFD run and (ii) the complication introduced by using profiles based on measurements which are not at consistent heights AGL.

### 8.4.2 CFD Input

Section 6.2 concerned how CFD should be run; whether with raw time series $\Delta\theta_v$ data, pre-processed $\Delta\theta_v$ time series data (averaged into diurnal, seasonal or speed-sorted bin-average profiles) or at discrete stability states, the outputs of which could be weighted-averaged to achieve a final solution.

A qualitative case was made for progressing with the speed-sorted bin-average profile approach, on the grounds that it retained the mean value and much of the variability of the time series approach but allowed a vast reduction in computational resource requirements.

Were more time and computational resource available, it would have been preferable to offer a fully quantified argument, having explored some of the alternative methods and conducted a cost/benefit analysis in terms of their increased (or decreased) flow modelling accuracy alongside their additional requirements.

### 8.4.3 CFD Limitations

The limitations of the status-quo CFD configurations were set out previously in Chapter 6. To summarise, there is a risk that running CFD with a fixed boundary layer height (i.e. unchanging $h_{ABL}$ regardless of stability) is a significant deviation from reality (actually, it would be expected that stable conditions would be coincident with low $h_{ABL}$ and with high $h_{ABL}$ in unstable conditions. Neglecting to model this combined effect may have significant implications for flow model accuracy.

Similarly, it is possible that greater improvements in accuracy could be seen if Coriolis effects were enabled within the CFD model.

### 8.4.4 Use of Ultrasonic Anemometers

Initially, it had been envisaged that measurements of eddy covariance and Obukhov length could be compared against temperature gradient measurements, as a means of co-validation via the flux-profile relationships set out in section 2.3. This would have leant confidence to the values of virtual potential temperature used and would have been of interest in terms of comparing the coefficients derived from observations to those derived by others. However, this step was not critical in terms of the development of the new CFD process and as such it was de-prioritised.

It was also the case that due to ultrasonic anemometer instrument failure, there were no data sets longer than one year in duration from any site. This would have compromised the impact of any conclusions of the investigation summarised above. Flux-profile relationships are empirical and therefore benefit from well-populated data sets.

At the time of writing, a number of ultrasonic anemometer data sets have surpassed one year duration so this investigation is proposed as further work.

## 8.5 Further Work

### 8.5.1 Addressing Limitations

Section 8.4 set out some key area of limitation in the research conducted. To recap, these include improving the validation of Vortex WRF data, refining the physical link between the input data and CFD model, reviewing the status-quo CFD physics to better accommodate the modelling of atmospheric stability and co-validating temperature differential measurements with ultrasonic anemometer measurements of Obukhov Length via flux-profile relationships.

The following sections detail proposals for applying the new CFD methodology beyond the original scope of this research.

### 8.5.2 Temperature Profiling

ANSYS CFX allows for implementation of atmospheric stability by definition of a virtual potential temperature profile, rather than simply a temperature offset. If combined with a

variable boundary layer height, this offers a much more realistic representation of the real atmosphere. Mesoscale data could be used to define the $\theta_v$ profile up to the tropopause. However, like in this project, mesoscale data should be validated against measurements in order to provide high-certainty CFD inputs.

Since mast-based measurements for measuring are not practical above 100-200m, alternative techniques could be considered. Radiosonde (weather balloon) readings can be easily acquired – but these typically only measure a single profile at two regular intervals per day (for example, 12AM and 12PM) which is not adequate for capturing the level of variation.

Temperature profilers, such as picture in Figure 8.1, allow for measurement of temperature and humidity up to 5km AGL. However, their vertical resolution and minimum measurement height are such that they would be best used as supplements to conventional mast-based measurements (such as used in this project) in the surface layer.

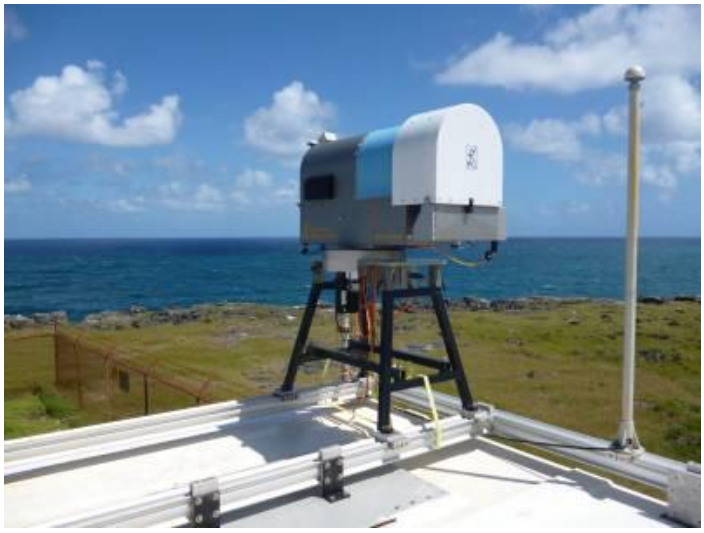

*Figure 8.1: Humidity and Temperature Profiler (HATPRO-SUNHAT) at the Barbados Clouds Observatory [radiometer-physics.de].*

### 8.5.3 Wake Modelling

CFX has been used by SSE Renewables and others to model inter-turbine wake effects, at fixed diabatic stability. Figure 8.2 shows wind speed maps of the same wind farm under stable (-2K; left) and unstable (+1K; right) conditions.

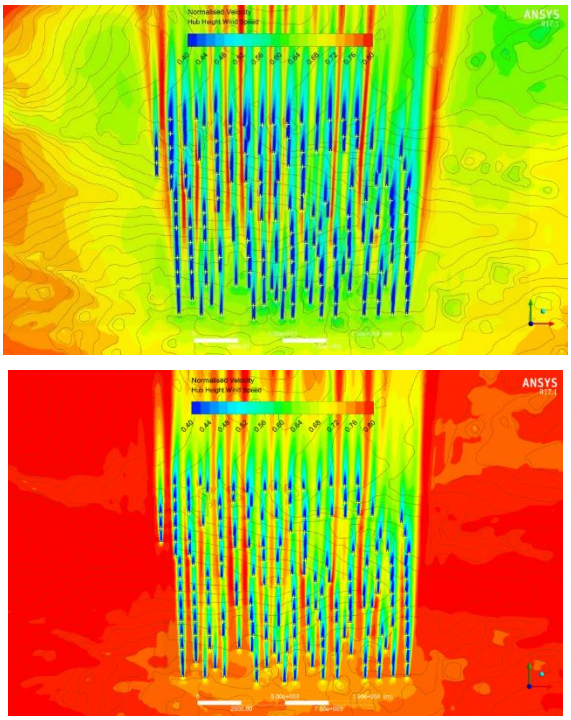

*Figure 8.2: CFD simulations of wind farm wakes including atmospheric stability effects: stable (left) and unstable (right).*

The ability to capture the effect of less prevalent wakes in increasingly unstable conditions (due to greater turbulent mixing) has been demonstrated. The next step, in the context of this project, would be to demonstrate an ability to model an accurate long-term average array efficiency by defining a time-varying $\Delta\theta_v$ input. This would lead to more accurate, while computationally achievable, wake loss calculations.

### 8.5.4 Forecasting

Wind farm operators use meteorological forecasts to predict energy output at various forecast horizons from real-time to multiple days-ahead. Incorrect forecasting leads to financial penalties.

Mesoscale modelling can be used to create wind power forecasts at site-level, using predicted values from GCM models as a basis. At its simplest, the process involves retrieving wind speed and wind direction from WRF and referencing these against a wind farm power output matrix derived from measured data, making adjustments for turbine availability.

A limitation of this approach is that it does not take into account variation in ambient wind flow (or wakes) with atmospheric stability. This research could form the basis of a more sophisticated, and more accurate forecasting approach, whereby $\Delta\theta_v$ from WRF is used as a third variable in the power output reference.

### 8.5.5 Suitability Assessment and Complex Flow

Chapter 7 concentrated on demonstrating an improved ability to model energy yield as a function of hub-height wind speed. However, wind shear and turbulence intensity (TI) can also impact on turbine power output. In brief, high wind shear across a turbine rotor generally results in a greater decrease in wind speed in the lower half of the turbine rotor than there is an increase in the upper half. The Rotor-Equivalent Wind Speed (REWS) is therefore generally lower than the hub-height wind speed.

Turbulence intensity affects power output of wind turbines in the near cut-in and near-rated regions of the power curve. At cut-in wind speed, high TI can lead to greater power output than predicted by the power curve; at rated wind speed, lower output.

In both respects there are also power performance effects which are not simply related to the vertically-varying (wind shear) or time-varying (turbulence) nature of wind speed but also reduced aerodynamic efficiency of wind turbines in non-standard shear and TI conditions.

Improved predictions of wind shear and TI by incorporating atmospheric stability, such as were demonstrated in Chapter 6, would be expected to lead to more accurate energy yield assessment.

## 8.6 Thesis Conclusion

The main output from this research project is a new approach for improving wind farm layout design and energy yield assessment accuracy. In that respect, the research aims set out in Chapter 1 have been well progressed and the technical objective of the research - an efficient, reliable and straight-forward method for modelling atmospheric stability in CFD, as set out in Chapter 3 - has been delivered.

The impact of this work has already been felt within SSE and it is the author's intention to share as much of this knowledge as is appropriate for the benefit of the wider wind industry. The main subject of this research, onshore wind, has a significant role still to play in our energy future and efforts should continue to drive up the efficiency of onshore wind projects, wherever opportunities arise.

# 9 References


[1] International Governmental Panel on Climate Change, “Climate Change 2014 Synthesis Report,” 2013 *[www.ipcc.ch/report/ar5/syr/]*.

[2] UN, “United Nations Framework Convention on Climate Change Paris Agreement.” 2015 [*unfccc.int/process-and-meetings/the-paris-agreement/the-paris-agreement*].

[3] Scottish Government, “2020 Routemap for Renewable Energy in Scotland,” *[https://www2.gov.scot/Publications/2011/08/04110353/0].*

[4] Scottish Government, “Annual Energy Statement 2019,” [ *www.gov.scot/publications /annual-energy-statement-2019/*]

[5] Scottish Government, “Scottish Energy Strategy :The Future of Energy in Scotland,” 2017 [*https://www2.gov.scot/energystrategy*].

[6] The Scottish Parliament, “Climate Change (Emissions Reduction Targets) (Scotland) Bill,” vol. Session 5, pp. 2–5, 2018 [*www.parliament.scot/ parliamentarybusiness/Bills /108483.aspx*]

[7] BEIS, “Contracts for Difference Allocation Round 3 Results.” 2019 [*www.gov.uk/ government/ publications/contracts-for-difference-cfd-allocation-round-3-results*].

[8] International Electrotechnical Commission, “IEC 61400-12-1:2017 Wind Energy Generation Systems - Part 12: Power Performance Measurements of electricity producing wind turbines.” 2017.

[9] R. B. Stull, *An Introduction to Boundary Layer Meteorology*. Springer Netherlands, 1988.

[10] D. G. Andrews, *An Introduction to Atmospheric Physics*. Cambridge University Press, 2010.

[11] O. Tetens, “Über einige meteorologische Begriffe. Z.,” *Geophys 6 207-309.*, 1930.

[12] D. M. Burridge and A. J. Gadd, “The Meteorological Office ten-level numerical weather prediction model,” *Sci. Pap. Met. Off. London*, no. 34, 1975.

[13] R. A. Zhang, Dalin; Anthes, “A High-Resolution Model of the Planetary Boundary Layer--Sensitivity Tests and Comparisons with SESAME-79 Data.,” *J. Appl. Meteorol. vol. 21, Issue 11, pp.1594-1609*, 1982.

[14] R. A. Anthes and E. Hsie, “Description of the Penn State / NCAR Mesoscale Model

Version 4 ( MM4 ),” no. May, 1987.

[15] A. K. Blackadar, “Modelng the nocturnal boundary layer,” in *Preprints, Third Symp. on Atmospheric Turbulence, Diffusion, and Air Quality, Raleigh*, 1976.

[16] J. W. Deardorff, “Efficient prediction of ground surface temperature and moisture, with inclusion of a layer of vegetation,” *J. Geophys. Res. Ocean.*, vol. 83, no. C4, pp. 1889–1903, 1978.

[17] C. Desmond, “The Consideration of Forestry on Wind Energy Resource Assessment,” *PhD Thesis*, 2015.

[18] J. R. Garratt, “Review: The Atmospheric Boundary Layer,” *Earth-Science Rev.*, vol. 37, no. 1–2, pp. 89–134, 1994.

[19] B. Lange, S. Larsen, J. Højstrup, and R. Barthelmie, “The influence of thermal effects on the wind speed profile of the coastal marine boundary layer,” *Boundary-Layer Meteorol.*, vol. 112, no. 3, pp. 587–617, 2004.

[20] J. A. Businger, J. C. Wyngaard, Y. Izumi, and E. F. Bradley, “Flux-Profile Relationships in the Atmospheric Surface Layer,” *Journal of the Atmospheric Sciences*, vol. 28, no. 2. pp. 181–189, 1971.

[21] A. Sathe and W. Bierbooms, “Influence of different wind profiles due to varying atmospheric stability on the fatigue life of wind turbines,” *J. Phys. Conf. Ser.*, vol. 75, p. 012056, 2007.

[22] P. Argyle and S. Watson, “A study of the surface layer atmospheric stability at two UK offshore sites,” *EWEA2012 - Eur. Wind Energy Assoc. Conf. 16-19 April 2012, Copenhagen, Denmark*, p. 929, 2012.

[23] S. A. Hsu, E. A. Meindl, and D. B. Gilhousen, “Determining the power-law wind-profile exponent under near-neutral stability conditions at sea,” *Journal of Applied Meteorology*, vol. 33, no. 6. pp. 757–765, 1994.

[24] L. Prandtl, “Bericht uber Untersuchungen zur ausgebildeten Turbulenz,” *Math. Mech. 5 136-139.*, 1925.

[25] WMO, *Guide to Meteorological Instruments and Methods of observation*, vol. I & II, no. 8. 2008.

[26] W. Paeschke, “Experimentelle Untersuchungen zum Rauhigkeitsproblem in der boden- nahen Luftschicht,” *Z. Geophys. 13, 14–21.*, 1937.

[27] R. J. Barthelmie, “The effects of atmospheric stability on coastal wind climates,” *Meteorol. Appl.*, vol. 6, no. 1, pp. 39–47, 1999.

[28] A. S. Monin and A. M. Obukhov, “Basic laws of turbulent mixing in the surface layer of the atmosphere,” *Contrib. Geophys. Inst. Acad. Sci. USSR*, vol. 24, no. 151, pp. 163–187, 1954.

[29] A. J. M. Van Wijk, A. C. M. Beljaars, A. A. M. Holtslag, and W. C. Turkenburg, “Evaluation of stability corrections in wind speed profiles over the North Sea,” *J. Wind Eng. Ind. Aerodyn.*, vol. 33, no. 3, pp. 551–566, 1990.

[30] A. Peña, *Sensing the wind profile Risø-PhD-Report*, vol. 45, no. March. 2009.

[31] J. S. Rodrigo and P. S. Anderson, “Investigation of the Stable Atmospheric Boundary Layer at Halley Antarctica,” *Boundary-Layer Meteorol.*, vol. 148, no. 3, pp. 517–539, 2013.

[32] R. M. Beljaars, A. C. M., Holtslag, A. A. M. & van Westrhenen, “Description of a software library for the calculation of surface fluxes,” *Tech. Rep. TR-112, KNMI, Bilt, Netherlands.*, 1987.

[33] J. F. Newman and P. M. Klein, “The Impacts of Atmospheric Stability on the Accuracy of Wind Speed Extrapolation Methods,” pp. 81–105, 2014.

[34] International Electrotechnical Commission, “IEC 61400-1:2019 Wind Energy Generation Systems - Part 1: Design Requirements.” 2019.

[35] DNV GL, “WindFarmer v5.3.” .

[36] “Wind Atlas Analysis and Application Program.” [Online]. Available: www.wasp.dk.

[37] O. N. I Katic, J Hojstrup, J Jensen, “A Simple Model for Cluster Efficiency,” *EWEC’86. Proceedings. Vol. 1*, vol. 1, 1987.

[38] J. F. Ainslie, “"Development of an eddy viscosity model for wind turbine wakes,” *Proc. 7th BWEA Wind energy Conf. Oxford.*, 1985.

[39] U. H. and H. B. Ann-Sofi Smedman, “Low Level Jets – A Decisive Factor for Off-Shore Wind Energy Siting in the Baltic Sea,” *Wind Eng. Vol. 20, No. 3 (1996), pp. 137-147*, 1996.

[40] Y. L. Pichugina, R. M. Banta, N. D. Kelley, S. . Sandberg, J. L. Machol, and W. A. Brewer, “Nocturnal Low Level Jet Characteristics Over Southern Colorado,” *PhD Thesis*, 2015.

[41] S. Hawkins, “A High Resolution Reanalysis of Wind Speeds over the British Isles for

Wind Energy Integration," *PhD Thesis*, 2012.

[42] "National Center for Atmospheric Research Staff (Eds). Last modified 11 Nov 2018. 'The Climate Data Guide: NCEP-NCAR (R1): An Overview.' Retrieved from https://climatedataguide.ucar.edu/climate-data/ncep-ncar-r1-overview." .

[43] "National Center for Atmospheric Research Staff (Eds). Last modified 07 Nov 2017. 'The Climate Data Guide: NASA MERRA.' Retrieved from https://climatedataguide.ucar.edu/climate-data/nasa-merra." .

[44] "'The Climate Data Guide: Climate Forecast System Reanalysis (CFSR).'" [Online]. Available: https://climatedataguide.ucar.edu/climate-data/climate-forecast-system-reanalysis-cfsr.

[45] "Bosilovich, Michael, Cullather, Richard & National Center for Atmospheric Research Staff (Eds). Last modified 07 Nov 2017. 'The Climate Data Guide: NASA's MERRA2 reanalysis.' Retrieved from https://climatedataguide.ucar.edu/climate-data/nasas-merra2-reana." .

[46] ECMWF, "ERA-5 Reanalysis Dataset." [Online]. Available: https://www.ecmwf.int/en/forecasts/datasets/archive-datasets/reanalysis-datasets/era5.

[47] B. E. Launder and D. B. Spalding, "The numerical computation of turbulent flows," *Comput. Methods Appl. Mech. Eng.*, vol. 3, no. 2, pp. 269–289, 1974.

[48] D. Wilcox, *Turbulence Modelling for CFD*. 1998.

[49] F. Menter, "Improved two-equation k-omega turbulence models for aerodynamic flows," *NASA Tech. Memo.*, no. 103978, pp. 1–31, 1992.

[50] ANSYS Ltd, "'Atmsopheric Stability,'" *Wind. Doc.*

[51] N. Mittelmeier, T. Blodau, G. Steinfeld, A. Rott, and M. Kühn, "An analysis of offshore wind farm SCADA measurements to identify key parameters influencing the magnitude of wake effects," *J. Phys. Conf. Ser.*, vol. 753, no. 3, pp. 0–12, 2016.

[52] M. Dörenkämper, B. Witha, G. Steinfeld, D. Heinemann, and M. Kühn, "The impact of stable atmospheric boundary layers on wind-turbine wakes within offshore wind farms.," *Jnl. Wind Eng. Ind. Aerodyn.*, vol. 144, pp. 146–153, 2015.

[53] K. S. Hansen, "Calculation of Atmospheric Stability Used For Wake Analysis," 1990.

[54] M. C. Holtslag, W. A. A. M. Bierbooms, and G. J. W. van Bussel, "Wind turbine fatigue

loads as a function of atmospheric conditions offshore," *Wind Energy*, 2016.

[55] E. A. Bossanyi, "GH Bladed User Manual," *Garrad Hassan Bl.*, 2009.

[56] M. Dörenkämper, J. Tambke, G. Steinfeld, D. Heinemann, and M. Kühn, "Atmospheric impacts on power curves of multi-megawatt offshore wind turbines," *J. Phys. Conf. Ser.*, vol. 555, no. 1, 2014.

[57] S. Wharton and J. Lundquist, "Assessing atmospheric stability and its impacts on rotor-disk wind characteristics at an onshore wind farm," *Wind Energy*, vol. 17, no. April 2013, pp. 657–669, 2014.

[58] K. S. Hansen, R. J. Barthelmie, L. E. Jensen, and A. Sommer, "The impact of turbulence intensity and atmospheric stability on power deficits due to wind turbine wakes at Horns Rev wind farm," no. November 2011, pp. 183–196, 2012.

[59] A. C. and A. E. M. Christopher T.M. Clack, Anneliese Alexander, "Demonstrating the effect of vertical and directional shear for resource mapping of wind power," *Wind Energy*, 2015.

[60] C. Montavon, "Simulation of Atmospheric Flows Over Complex Terrain for Wind Power Potential Assessment," *PhD Thesis*, 1998.

[61] O. Texier, T. Clarenc, C. Bezault, N. Girard, and J. Degelder, "Integration of atmospheric stability in wind power assessment through CFD modeling," *Eur. Wind Energy Conf.*, 2010.

[62] T. Koblitz, a Bechmann, J. Berg, a Sogachev, N. Sørensen, and P.-E. Réthoré, "Atmospheric stability and complex terrain: comparing measurements and CFD," *J. Phys. Conf. Ser.*, vol. 555, p. 012060, 2014.

[63] Y. Hristov, G. Oxley, and M. Žagar, "Improvement of AEP Predictions Using Diurnal CFD Modelling with Site-Specific Stability Weightings Provided from Mesoscale Simulation," *J. Phys. Conf. Ser.*, 2014.

[64] C. Montavon, C. Rodaway, P. Housley, and I. Jones, "Sensitivity of wind flow to atmospheric stability for a complex site with multple masts," 2014.

[65] C. J. Desmond, S. Watson, C. Montavon, and J. Murphy, "Modelling uncertainty in t-RANS simulations of thermally stratified forest canopy flows for wind energy studies," *Energies*, vol. 11, no. 7, 2018.

[66] M. Alletto *et al.*, "E-Wind: Steady state CFD approach for stratified flows used for site

assessment at Enercon," *J. Phys. Conf. Ser.*, vol. 1037, no. 7, 2018.

[67] P. A. Taylor and H. W. Teunissen, "The Askervein Hill project: Overview and background data," *Boundary-Layer Meteorol.*, vol. 39, no. 1–2, pp. 15–39, 1987.

[68] C. Y. Chang, J. Schmidt, M. Dörenkämper, and B. Stoevesandt, "A consistent steady state CFD simulation method for stratified atmospheric boundary layer flows," *J. Wind Eng. Ind. Aerodyn.*, vol. 172, no. June 2017, pp. 55–67, 2018.

[69] O. Temel, S. Porchetta, L. Bricteux, and J. van Beeck, "RANS closures for non-neutral microscale CFD simulations sustained with inflow conditions acquired from mesoscale simulations," *Appl. Math. Model.*, vol. 53, pp. 635–652, 2018.

[70] G. Carney, P. Housley, C. Montavon, and I. Jones, "Practical Usage of Cfd for Wake Effects Prediction Within Offshore Wind Farms," *EWEA2012presentation*, 2012.

[71] UL (formerly AWS), "Windographer Version 4.0.17 (Aug 16) - 4.1.11 (Jun 18)." .

[72] "ISO/IEC 17025:2017 General requirements for the competence of testing and calibration laboratories." International Organization for Standardization, 2017.

[73] "SVEND OLE HANSEN APS - SANKT JØRGENS ALLÉ 5 - DK-1615 COPENHAGEN V-DENMARK." .

[74] "Deutsche WindGuard, Oldenburger Str. 65, 26316 Varel, Germany." .

[75] "Vaisala, P.O. Box 26, FI-00421 Helsinki, Finland." .

[76] "Danmarks Tekniske Universitet - DTU, Anker Engelunds Vej 1 Bygning 101A, 2800 Kgs. Lyngby, Denmark." .

[77] Ordnance Survey, "© Crown Copyright and Database Rights 2019 Ordnance Survey 0100031673." .

[78] ANSYS Ltd - Windmodeller Documentation, "Forestry Modelling," pp. 1–12, 2011.

[79] G. Katul, C. I. Hsieh, G. Kuhn, D. Ellsworth, and D. Nie, "Turbulent eddy motion at the forest-atmosphere interface," *J. Geophys. Res. Atmos.*, vol. 102, no. D12, pp. 13409–13421, 1997.